SIMULATIONS FOR THE INTERNATIONAL X-RAY OBSERVATORY

by

Nathan William Slack

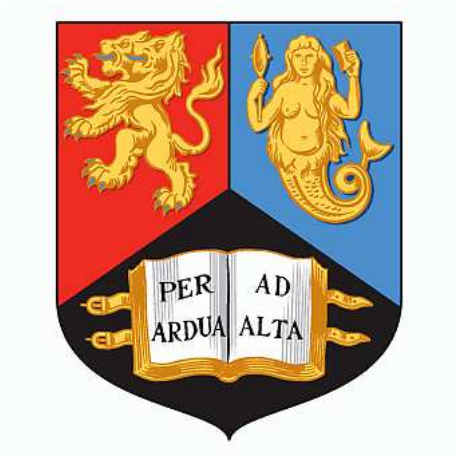

A thesis submitted to
The University of Birmingham
for the degree of
DOCTOR OF PHILOSOPHY

Astrophysics and Space Research Group
School of Physics and Astronomy
The University of Birmingham
May 2011

UNIVERSITY OF
BIRMINGHAM

University of Birmingham Research Archive

e-theses repository

This unpublished thesis/dissertation is copyright of the author and/or third parties. The intellectual property rights of the author or third parties in respect of this work are as defined by The Copyright Designs and Patents Act 1988 or as modified by any successor legislation.

Any use made of information contained in this thesis/dissertation must be in accordance with that legislation and must be properly acknowledged. Further distribution or reproduction in any format is prohibited without the permission of the copyright holder.

Abstract

The subject of this thesis is the simulation of X-ray cluster surveys and related issues, with a focus on the research that can be conducted with the International X-ray Observatory (IXO), or a similar next-generation X-ray observatory.

A general purpose X-ray image simulator has been developed. It uses a modern cosmological simulation and cluster scaling relations to produce simulated cluster images that are well motivated by theory and observation. A distribution of point sources and various instrumental effects are also included. The simulator is complemented by a source identification method.

The IXO selection function is mapped over a varying surface brightness parameter space. Simulated IXO surveys are used to explore the biases present in X-ray cluster surveys. These reveal that it is necessary to correct for biases using a detailed and carefully applied selection function to recover the true evolution of the luminosity-temperature relation. This is crucial for shallow surveys.

Simulations of IXO using different angular resolutions are found to have only a minor effect on the number and distribution of detected clusters.

for Tracey and Michael Slack

Acknowledgements

I am very grateful for the continuous support and inspiration provided by my supervisor, Professor Trevor Ponman, who kept my mind on the big picture when I became lost in the minutiae.

To my parents; thank you for encouraging my every interest. Without you I would not have gotten this far.

To Sarah Kirkham; your love and understanding has gotten me through the past few months unscathed. Your help with proof reading was also very much appreciated.

I would also like to thank Jesper Rasmussen for developing the XMM-Newton image simulator that inspired XIS, Florian Pacaud for useful discussions about the selection function and Will Hartley for help with the Millennium gas run.

Thanks go out to my friends for all the good times over the course of this research, and for your understanding in the final months.

Statement of originality

This thesis consists of an introductory chapter, two methodology chapters (Chapters 2 and 3), two results chapters (Chapter 4 and 5) and a concluding chapter. Where methods have followed or been based on work by other authors, this is stated in the text. Chapter 1 includes Figures from Voit (2005b), Voit (2005a), Pacaud et al. (2007) and IXO development documentation through NASA. Chapter 2 includes a Figure from Snowden et al. (1995). Chapter 3 includes Figures from Vikhlinin et al. (1998). Chapter 2 includes the analysis of data that has been gathered by other authors. The use of these data is made clear in the relevant sections and is expanded on in the appendices.

Elements of Chapters 2, 3 and 4 are used in two papers which are in preparation for submission to Monthly Notices of the Royal Society (MNRAS), titled 'Next-generation X-ray cluster surveys' and 'The impact of survey selection functions on deep X-ray cluster surveys', with appropriate editing.

All unreferenced data analysis has been conducted by myself, with constructive input and suggestions from my supervisor Prof. Trevor Ponman.

Contents

List of Figures

List of Tables

CHAPTER 1

Introduction

Since the 1960s scientists have been studying the wealth of information on the cosmos available at the highest energies of the electromagnetic spectrum. X-ray emission has the energy to penetrate galactic gas, but can be focused and observed by space-borne telescopes which give us a window into the distant Universe. It is associated with the most massive structures known to exist, allowing us to learn about the evolution of the Universe on large scales and the nature of high energy thermal and gravitational physics.

As the current generation of dedicated X-ray observatories approach the end of their mission lifetimes, preparations are being made for an International X-ray Observatory (IXO). This instrument will be considerably more powerful than its predecessors in both imaging and spectroscopy. Its technical capabilities are being driven to achieve numerous scientific goals.

To facilitate this development it is important to predict the output of the observatory under various configurations. This enables the evaluation of its effectiveness at accomplishing the science goals. A detailed prediction of the output can be made through simulation - the production of fake observations which are based on current theory. By producing the end-product of an observation one can perform scientific tests on the sim-

ulated data using established methods. This gives us a true understanding of the science that can be performed with them.

This research is based around the use of simulations to study the imaging capability of IXO in the context of galaxy clusters (hereafter clusters). I develop a flexible X-ray imaging simulator to produce simulations for the evolving design of IXO and the current generation observatories. This is complemented by a source identification process for analysing the simulated images. Together these are the main components in collection of tools known as the X-ray Image Suite (XIS). These are used to predict how effective IXO would be in detecting clusters when different instrument parameters are assumed.

A serious issue when attempting to quantify statistical trends in large samples of sources is survey bias. Certain kinds of sources may be easier to detect than others so the frequency of detection will not necessarily represent the population. If these sources populate a particular region of a trend, and are offset from the mean they will weight it in the direction of that offset. The effect of missing sources must be accounted for in the analysis to recover the true situation. A major part of this research is the study of biases that would affect cluster surveys performed with IXO. This bias study focuses on the relationship between X-ray luminosity and temperature, and its possible evolution with cosmological time.

This chapter begins by reviewing the field of X-ray astronomy and its associated technology. This includes an introduction to IXO and what it will have to offer. It then delves deeper into the physics of the galaxy clusters. To conclude the review the history and methods of conducting X-ray surveys are explored. Chapter 2 goes into detail about the design of the X-ray imaging simulator. Following on, Chapter 3 describes the source identification techniques used on the simulated images. Chapter 4 covers the method and results of the survey bias study. In Chapter 5 the effect of different IXO configurations is explored. Finally, Chapter 6 summarises and discusses the results of this work.

1.1 X-ray Astronomy

1.1.1 The History of X-ray Astronomy

Viewing the Universe in X-rays is nearly impossible from the ground as the Earth's atmosphere absorbs most of the incident radiation. The Sun's corona was revealed as a source of X-rays in the late 1940s when astronomers used rocket flights for their observations. The first extrasolar source of X-ray emission was the X-ray binary Scorpius X-1, detected from a rocket flight by a team directed by Riccardo Giacconi in 1962 (Giacconi et al. 1962).

To make significant progress in X-ray astronomy satellites began to be used to make observations, as they would always be above the interference of the atmosphere. The National Aeronautics and Space Administration (NASA) launched Uhuru in 1970, which had an angular resolution of approximately 30 arcminutes (hereafter arcmin). Its proportional counters found evidence for accreting binary systems and hot gas in galaxy clusters. 1978 saw the launch of NASA's Einstein observatory, which included X-ray mirrors to focus the incident radiation. This was followed by the launch of the European X-ray Observatory Satellite (EXOSAT) by the European Space Agency (ESA) in 1983. X-ray telescopes went on to confirm X-ray emission from the corona of other stars, image supernova remnants and the hot gas in galaxy clusters, and detect bursts of X-rays emitted from what is now believed to be accretion of gas onto black holes.

X-ray telescopes have not always been limited to dedicated satellites. In 1985 the NASA Space Shuttle Challenger orbited for a week with Spacelab 2, which included an X-ray telescope built at the University of Birmingham. Its observations included galaxy clusters and the Galactic centre. An X-ray telescope was also present on the Kvant-1 module of the Russian Mir Space Station, which was added in 1987.

The next major X-ray observatory was the German-British-American Röntgensatellit (ROSAT) in 1990, which was responsible for bringing the number of known X-ray sources

to more than 60,000. With the launch of the Japanese-American Advanced Satellite for Cosmology and Astrophysics (ASCA) and NASA's Rossi X-ray Timing Explorer (RXTE), in 1993 and 1995 respectively, information was gathered on the distribution of X-ray energies and the the variability of sources with time. Launched in 1996, the Italian Space Agency (ASI)'s BeppoSAX covered a wide spectral range from 0.1 to 200 keV. Important outcomes for BeppoSAX included high precision studies of the position of X-ray sources caused by Gamma-ray bursts and investigation of their X-ray afterglow.

Scientists wanted to be able to measure X-ray sources more precisely and study even fainter sources. To meet these needs two even more powerful observatories were placed in orbit in 1999. NASA's Chandra observatory has an angular resolution of 0.5 arcsec, which is over a thousand times better than that of the first orbiting X-ray telescope. This allowed it to resolve complex gas distributions in cluster cores. Its time resolution of 16 μs has been very useful for investigating the production of X-ray bursts around black holes. ESA's XMM-Newton uses three telescopes which together gather 5 times as many X-ray photons as Chandra, but are restricted to an angular resolution of 6 arcsec. This enables detailed X-ray studies of star-forming regions and cluster populations. A more recent X-ray observatory is Suzaku, launched by Japan Aerospace Exploration Agency (JAXA) in 2005. Its five telescopes each focus onto a detector, and contain nested mirrors to maximise photon collecting power at the cost of angular resolution. All three facilities continue to observe a wide variety of sources.

Again, the need arises for greater sensitivity in X-ray observations. The earliest supermassive black holes are beyond the observational reach of the current generation of X-ray telescopes, and further study into the properties of galaxy clusters is required. To meet these desires an ESA-NASA collaboration has proposed IXO - an X-ray observatory designed to be 25 times as sensitive as XMM-Newton.

Figure 1.1: Composite image of galaxy cluster Abell 1689, combining optical data from the Hubble Space Telescope (yellow) with X-ray data from Chandra (purple). The image is 3.2 arcmin across. Figure credit: X-ray, NASA/CXC/MIT/E.-H. Peng et al.; optical, NASA/STScI.

1.1.2 Extragalactic X-ray Sources

The most massive objects in the Universe are the source of many of the X-ray detections. An example of this is a galaxy cluster, the largest known gravitationally-collapsed structure in the Universe. These groups of hundreds or thousands of galaxies are gravitationally bound in a volume of order 1 Mpc^3,[1] and contain large amounts of hot gas at temperatures generally between $2 - 10$ keV (Bothun 1998, 3.2.2). This gas was heated as it fell into the gravitational potential well of the cluster, becoming almost entirely ionised. It emits photons via bremsstrahlung (free-free) radiation whilst maintaining hydrostatic equilibrium within that potential well. This radiation is in the X-ray range due to the temperature of the hot gas. By measuring the X-ray emission the distribution of mass within a cluster can be estimated. An example of a galaxy cluster is shown in Figure 1.1.

The energetic hot gas of a cluster is assumed to be contained within the potential well through gravitational attraction. Studies of cluster masses and temperatures have shown that there is insufficient gas mass to confine gas of a particular temperature to a cluster

[1] $1 \text{ pc} = 3.086 \times 10^{16}$ m.

(Liddle 2003, pp 66-67). Only $\sim 17\%$ of the required mass is present in gas and stars. It is widely believed that the other mass does exist in the system in the form of non-baryonic dark matter, which only interacts gravitationally. The most popular models for a universe with dark matter assume it is non-relativistic and refer to it as Cold Dark Matter (CDM). Evidence for the presence of dark matter includes studies of the rotational velocity profiles of galaxies, which do not have the expected drop in the outer radii predicted from the visible matter, as well as the existence of gravitational lensing and studies of the Bullet cluster (Rubin et al. 1980; Bosma 1981; Markevitch et al. 2006). The presence of such a large amount of dark matter in clusters makes them useful laboratories for dark matter studies.

Due to the large scale of galaxy clusters, their evolution is dominated by gravity and significantly affected by the geometry of the Universe. Their presence at a wide range of distances allows them to be used in studies of the expansion of the Universe. This can provide valuable information on the curvature of the Universe and its dark energy content. Dark energy is a theoretical component of the Universe that produces a negative pressure, used to explain the observed acceleration of the expansion of the Universe (Riess et al. 1998; Sefusatti et al. 2006).

Low luminosity, poor galaxy clusters are known as galaxy groups (hereafter groups) (Price et al. 1991). Observations have shown the relations between different properties to be different for groups and clusters. Also, these scaling relations appear to be evolving over time. Scaling relations are described in more detail in Section 1.3.3. Measurement of cluster properties can be difficult to do accurately, and use assumptions such as spherical symmetry and hydrostatic equilibrium. Some of these assumptions become inadequate when the non-gravitational effects of the baryon content of a cluster are taken into account. For example, complicated and not very well understood physics in the cores of clusters can lead to inaccuracies with the determination of cluster mass (Sanderson et al. 2003). The strength of these non-gravitational effects is expected to be stronger in galaxy groups, where sources of heating are more significant compared to the scale of the structure

(Finoguenov et al. 2003).

Galaxies themselves are sources of X-rays, especially those that have recently gone through an intense period of star formation (known as starburst galaxies). The origin of these X-rays includes emission from the hot gas trapped in the potential well, star-forming regions and supernova remnants (Fabbiano 1989). The combined luminosity of the galaxies in the Universe contributes greatly to the faint part of the X-ray sky, producing a huge number of low luminosity point sources (Ranalli et al. 2003).

Another significant source of X-rays is compact objects, such as black holes and neutron stars. When matter is accreted around a compact object, friction causes its temperature to greatly increase and it begins to emit X-rays. By observing the X-ray spectrum from this accretion to obtain temperature information, the mass of the object can be determined (Shrader & Titarchuk 2003). A low luminosity form of this emission comes from stellar-mass black holes or neutron stars paired with a companion star, known as X-ray binaries. The matter that comprises the accretion disk is pulled off the companion star by the gravitational attraction of the compact object (Guseinov 1971). Dozens of X-ray binaries may exist in a galaxy, and this contributes to their X-ray emission.

At the centre of most large galaxies there is believed to be a supermassive black hole. These objects have been detected though visual and radio observations, where Doppler shift measurements of material near the centre of a galaxy have shown the orbital velocity of stars to increase significantly. The orbits indicate a central body that contains millions of Solar masses, which images show to be no larger than the Solar system (Kormendy & Richstone 1995). Supermassive black holes can also be detected from X-ray emission. When a significant quantity of matter is infalling onto the supermassive black hole it can produce powerful X-ray emission from interactions near the centre of the accretion flow, and the black hole is said to be in an active state (Zentsova 1980). These Active Galactic Nuclei (AGN) are observed as point sources, some of which rival clusters in brightness (Hasinger et al. 2005).

There are various theories for the formation of such a massive object. Great quantities

of matter could have been pulled into a stellar-mass black hole, or many stellar-mass black holes may have merged, or they may form from the gravitational collapse of a very dense region of gas during the formation of a galaxy (Schulz & Komossa 1999). High energy jets have been observed from supermassive black holes. It is thought that these jets are caused by accumulation of matter by the black hole, and that they eventually stop the accumulation of matter by the galaxy and black hole until the jets dissipate and the region cools. The result would be a cycle of growth, shared by the galaxy and its central black hole. The relation between the mass of the central black hole and the velocity dispersion of the stars in a galaxy also suggests co-evolution in the early Universe (Volonteri 2006). X-ray observations of sufficient sensitivity would make it possible to study the first supermassive black holes at the edge of the observable Universe.

Strong gravitational fields, like those near black holes, provide good opportunities to test the principles of general relativity. This includes analysing the event horizon around a black hole, where the escape speed equals the speed of light (Menou et al. 1997). The accretion of matter onto a compact object, such as a neutron star or black hole, results in the emission of X-rays, as mentioned previously. Consequently, X-ray observations can be used to study the behaviour of matter within a strong gravitational field. Investigating the accretion disk in this way allows the parameters of a compact object to be constrained. X-ray observations could also be used to complement gravitational wave detectors.

In addition to studying matter within a strong gravitational field, neutron stars provide a way to study matter under extreme conditions. Matter near a neutron star is under the influence of its very strong magnetic field of around 10^{12} G , which is a result of the star's magnetic field acting over a much smaller surface area when it collapsed to form the neutron star (Anderson & Cohen 1970). Also, matter within the neutron star is very dense and is theorised to be in a super-fluid state. Investigating the X-ray emission around neutron stars yields data on their mass and radius (Fujimoto & Taam 1986). Therefore, it could help reveal more information on their composition and equations of state.

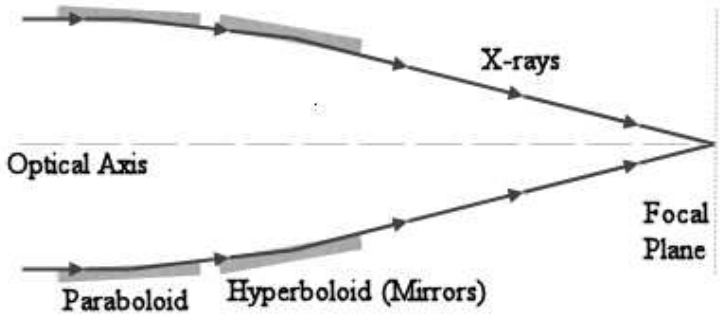

Figure 1.2: Reflection of photons in X-ray telescopes.

1.1.3 X-ray Telescopes

The two main types of X-ray telescopes are grazing mirrors and coded apertures. The design of mirror-based X-ray telescopes is quite different to that of their optical counterparts. X-ray photons have high energy, and pass through mirrors, rather than reflecting off them, if they impact a mirror at any significant angle. To bring the X-rays to a focal point they must hit the mirrors at a small grazing angle, which will slightly alter the direction of the photons (Culhane & P W Sanford 1981, pp 38-43). This process is imperfect; it results in loss of photons at every reflection. The telescopes have a barrel shaped appearance and contain very smooth mirrors. The Chandra X-ray observatory uses two reflecting surfaces to bring the X-rays to a focal point, similar to the configuration shown in Figure 1.2.

One problem that arises from the focusing of the X-rays is vignetting. The X-ray brightness reduces towards the outer regions of the detector. This is caused by a reduced efficiency in the reflection of photons the further they are from the central axis of the telescope, so they have less chance of reaching the focal plane. The effective area of a telescope therefore decreases with off-axis angle. The strength of this effect also depends on the energy of the incident photon. The amount of vignetting is specific to the design of the mirror assembly. A good X-ray mirror would have a high effective area in the energy range where the spectrum of the target source peaks.

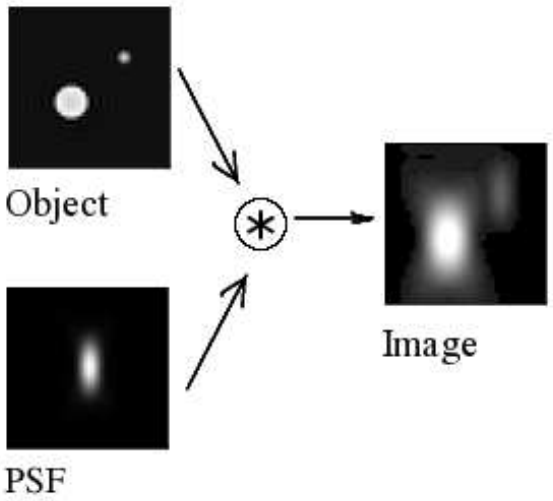

Figure 1.3: Example of how convolution with the PSF affects the appearance of two sources.

Another problem with mirrors is the Point Spread Function (PSF). At each point in the mirror incident photons have a probability of being reflected at a slightly different angle than that intended. This results in some of the photons from a point source impacting the detector at a different location to the majority of the source photons, leading to a blurred appearance (see Figure 1.3). The PSF for a location on the mirror is defined by the probability of a photon being detected at each position on the detector. This blurring limits the spatial resolution of the observatory, so it is usually used to define its angular resolution. The mirror on Chandra has been finely ground to give it an angular resolution of ~ 0.5 arcsec at the centre, allowing it to resolve the cores of clusters (Weisskopf et al. 2002). The further a photon is from the centre of the mirror, the worse its PSF tends to be, leading to a reduction in telescope ability with off-axis angle.

Coded aperture telescopes are based around a mask containing varied arrangement of opaque and transparent elements. X-ray sources project a shadow of the aperture on to a position-sensitive detection plane, producing a mask pattern (Caroli et al. 1987). This pattern must then be processed to reconstruct the distribution of sources that produced it.

1.1.4 X-ray Detectors

A variety of different X-ray detectors have been designed to capture the focused X-ray photons. The two broad tasks performed by X-ray telescopes are imaging and spectroscopy. The former prioritises good spatial resolution whilst the latter focuses on good energy resolution. Two other detector properties that play an important role are time resolution and quantum efficiency, which is the probability of a detection occurring as a function of photon energy.

Proportional counters use gas-filled chambers (Tananbaum & Kellogg 1970). Within these chambers, incident X-rays produce ion pairs in the gas particles through photoionisation. An electric field is applied, causing the electrons to move towards a readout electrode (anode). The change in voltage across the chamber is then used to determine the amount of incident radiation. Proportional counters possess a large surface area but their accuracy is limited by their energy resolution.

Another detector type is a microchannel plate (Henry et al. 1977). A reactive metal is divided into many channels, each with a diameter on the order of tens of μm (Fraser et al. 1982). When an X-ray photon is incident on one of the channels, the photoelectric effect causes an electron to be emitted from the channel wall. A potential difference across the channel causes the electron to accelerate and collide with the wall, producing more free electrons. This process continues until thousands of electrons reach the plate at the end of the channel, resulting in a charge pulse. This signal is confined to the channel, allowing the location and energy of the photon to be measured. The lowest energy detectable is when all the energy of the photon is used in freeing the electron in the channel. As with proportional counters, microchannel plates can be made to cover a large surface area but have very poor energy resolution. However, they have superior temporal resolution.

A detector technology which has become more popular in recent years is the Charge-Coupled Device (CCD). A semiconductor surface is used to connect an array of capacitors, which act as pixels. Incident X-rays create electron-hole pairs in the silicon of the CCD

pixels. Applying a voltage to the CCD allows the electrons to be read off as a charge. Read outs are done by shifting a charge down a row of pixels until it reaches the edge of the CCD. The photon impacts registered are referred to as counts or events, and regular readouts result in good timing for the detected X-rays. However, the small size of a CCD limits their photon collecting area. Therefore, it is important to have X-ray mirrors focus the X-ray radiation onto them. They can be constructed into arrays large enough to be used for imaging observations, and also make capable spectral instruments. The energy resolution is mainly limited by the electronic noise within the CCD, but statistical fluctuations from the ionisation process also play a part (Wilson 2003). Another problem is that a bright source can cause a CCD pixel to receive more than one count before it is read out. The energy of these photons is then summed (or lost), an effect known as pile-up (Ballet 1999).

Due to the penetrating power of high energy photons, CCDs are only useful for detecting soft X-rays (< 10 keV). Hard X-rays are better absorbed by Cadmium-Telluride (CdTe) semiconductor detectors, one of which was used to detect hard X-rays and γ-rays on the INTEGRAL mission (Tadayuki et al. 2005). These can be used effectively in combination with CCDs by placing them behind the CCD array to catch the hard X-rays that pass through the first detector.

A common method of enhancing the spectral resolution of X-ray detectors is to place a reflection grating in path of the photons after reflection by the mirrors. The light is subject to wavelength-dependent dispersion and captured by a detector, which can be a linear array of CCDs. This can increase the spectral resolution (often quoted as $E/\Delta E$, the photon energy divided by resolution in energy) by an order of magnitude (Brinkman et al. 1998).

Very small detectors with excellent energy resolution are becoming available. These operate at very low temperatures and are referred to as Cryogenic Imaging Spectrometers (CIS). One such detector is a Transition Edge Sensor (TES), used as part of a microcalorimeter (Kilbourne et al. 2007). The microcalorimeter is composed of an ab-

sorber, which contains a resistive thermometer (the TES) on a circuit, and a heat bath. When an X-ray is absorbed it thermalises, causing the temperature of the detector to rise in less than 1 μs. The resulting thermal energy causes a transition out of the superconducting state. The positive coefficient of resistance of the TES results in a voltage bias between the sensor and the bath, resulting in feedback. To read out the thermometer the current in the circuit is measured.

A problem that X-ray detectors have to endure is false readings caused by impacts from high energy particles. These can be divided into two categories: solar protons and internal, cosmic-ray induced particles (Read & Ponman 2003). The former is the result of solar flares and can sometimes render large periods of an observation too noisy to use. The latter is more regular and predictable, so can be removed from an observation along with the X-ray background. The Earth's magnetic field can provide some protection against the particle background, but can also trap solar protons which are then gathered by the X-ray mirrors. Observatories have shields around their focal plane assemblies to reduce the number of particle impacts on the detectors.

1.1.5 Current Generation X-ray Observatories

There are currently three general purpose X-ray observatories that focus on low to medium energies: Chandra, XMM-Newton and Suzaku. Their improvement in effective area and resolution over previous observatories has allowed discoveries and advances in numerous areas, including:

- X-ray emission from planets
- accreting gas in star forming regions
- enrichment of the intergalactic medium by starburst galaxies
- the evolution of supernova remnants
- the resolution of a large quantity of the X-ray background into discrete sources

- feedback between supermassive black holes and the galaxies and clusters they inhabit
- estimation of the amount of dark matter in galaxy clusters

(Santos-Lleo et al. 2010; Swartz et al. 2010).

The Chandra observatory consists of a single X-ray telescope with a focal length of 10 m, orbiting Earth with a period of 64.2 hours (Smithsonian Institution 2008). The use of 4 highly ground and polished mirrors give Chandra an impressive angular resolution of 0.5 arcsec Full Width at Half Maximum (FWHM) at the centre of its 30 arcmin diameter field of view. This has allowed it to observe cavities in the X-ray halos of clusters caused by bubbles rising from a central AGN (Fabian et al. 2000). Two detection instruments are placed at the focal plane, the Advanced CCD Imaging Spectrometer (ACIS) and the High Resolution Camera (HRC). ACIS is made up of 10 CCDs, divided into two subsets (ACIS-I and ACIS-S), and is used for a wide range of observing tasks. HRC uses a pair of microchannel plates to give a high time resolution of 16 μs but with a lower received count rate than ACIS. Either instrument can produce high resolution spectral data by use of one of two transmission gratings, which can give an energy resolution of over 1000 $E/\Delta E$.

XMM-Newton is a powerful counterpart to Chandra. The spacecraft consists of three X-ray telescopes of 7.5 m focal length, orbiting with a period of 48 hours (Ehle et al. 2007). Each telescope is constructed from 58 concentric mirrors, which give a combined effective area much greater than that of any other X-ray observatory. The quality of the mirror assembly gives an angular resolution of $\sim$ 6 arcsec FWHM, allowing it to resolve bright point sources, but restricting it from studying features in the same detail as Chandra. However, its greater collecting area allows it to gather more photons for use in analyses. All three telescopes are equipped with a European Photon Imaging Camera (EPIC), which are CCD detectors designed to cover most of their 30 arcmin diameter field of view. Two of these are EPIC Metal Oxide Semi-conductors (MOSs) and the other is called EPIC pn. The MOS cameras have half of their incident flux diverted to the Reflection Grating Spectrometers (RGS) with only 44% reaching the detectors, while the

pn detector uses a larger number of smaller CCDs and has a higher timing resolution of 7-30 μs (Turner et al. 2001; Strüder et al. 2001). The RGS consist of a line of 9 MOS CCDs with an energy resolution of upto 800 $E/\Delta E$. XMM-Newton is also complemented by a small optical/UV monitoring telescope.

The latest X-ray observatory is Suzaku (ASTRO-E2). It operates five X-ray telescopes with a maximum focal length of 5 m and 17 arcmin field of view, each in front of an instrument (ISAS/JAXA 2010). Four are aligned with imaging spectrometers. The other telescope is in front of a high throughput microcalorimeter with $\Delta E = 7$ (~ 1400 $E/\Delta E$ at 10 keV), which unfortunately failed a month after launch. The angular resolution of $\sim$ 2 arcsec FWHM is in between that of Chandra and XMM-Newton, and so is the effective area of each imaging spectrometer. Suzaku also operates a non-imaging hard X-ray detector, allowing it to study higher energies (up to 700 keV) than Chandra and XMM-Newton.

1.1.6 The IXO Mission

IXO is being designed as the successor to the Chandra and XMM-Newton observatories (Parmar 2009; Bookbinder 2010). It will feature revolutionary mirror and detector technology which will give IXO a significant increase in capability over previous X-ray observatories. The mission is being developed by a coalition of the space agencies ESA, NASA and JAXA, and is competing for an $\sim$ 2021 launch in the category of large missions. Its primary science goals are:

- studies of strong gravity,
- measuring black hole spin,
- the neutron star equation of state,
- growth of supermassive black holes,
- evolution of galaxy clusters and feedback,

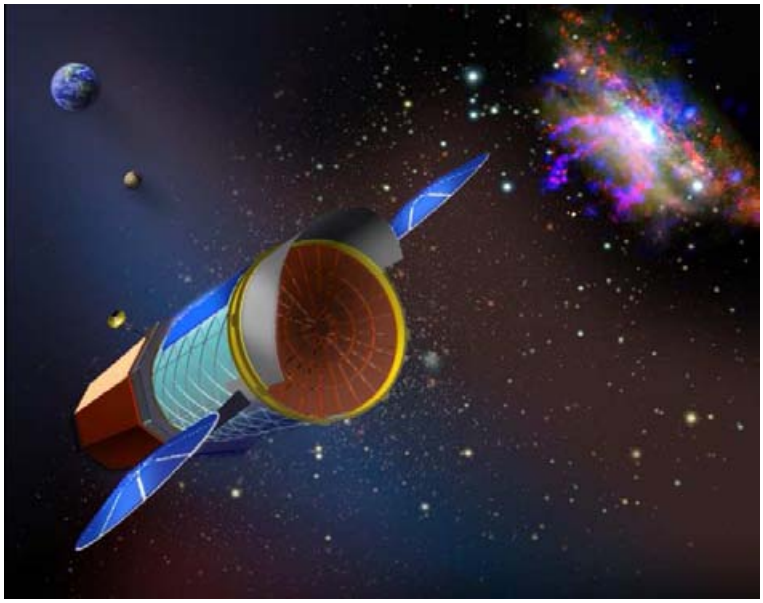

Figure 1.4: An artist's conception of the IXO spacecraft. Figure credit: NASA.

- cosmology,
- the cosmic web of baryons.

There is also the possibility of unexpected new science topics being discovered. The research covered here is focused on the goal 'evolution of galaxy clusters and feedback'.

The IXO concept originated from the merging of ESA's X-ray Evolving Universe Spectroscopy (XEUS) mission and NASA's Constellation-X, previous designs for next generation X-ray observatories. It consists of a single spacecraft capable of being launched from either an Atlas V or Ariane V rocket. A transfer trajectory will place it into orbit around the 2nd Lagrange (L2) point, where it will deploy from its compact form. The L2 point is an unstable location of zero potential gradient in the Earth-Sun system, therefore the spacecraft will only have to make occasional corrections to its position. Its position away from Earth orbit means it can observe continuously, but lacks the protection from energetic particles offered by the Earth's magnetic field. Once fully deployed, IXO will have a 20 m focal length from its grazing incidence mirrors. Having a longer focal length than previous observatories increases the effective area, especially at high energies, but reduces the field of view for a detector of fixed size.

To achieve its scientific aims IXO is being designed to meet certain requirements. To observe the first supermassive black holes, IXO needs to be able to measure spectra out to a redshift z of 10. The flux levels of the objects at this redshift are around 10^{-17} erg cm^{-2} s^{-1}, one hundred times fainter than the XMM-Newton limit of approximately 10^{-15} erg cm^{-2} s^{-1}. To make sure that the specific source of such faint emission can be detected, a spatial resolution of better than 5 arcsec FWHM will be required at 1 keV. For spectroscopic studies of redshifted line profiles to be sufficiently detailed to accomplish the science goals, an energy resolution of only 1 eV at around 1 keV is being aimed for. The effective area goal for IXO is 3 m^2 at 1.25 keV. A more detailed summary of the IXO science goals can be found in Appendix B.2.

Previous X-ray observatories used thick, and thus heavy, mirror shells. However, the length and weight limit of IXO requires the use of large numbers of thin, segmented mirrors, assembled into a radial structure. There are two mirror technologies being developed in parallel for use on IXO: segmented glass and silicon micro-pore optics. The former is a development of proven X-ray mirror technology used on previous observatories. It uses thin glass sheets (≈ 0.4 mm), which are heated and slumped over a cylindrical mould to form a curved shape, then cooled and cut (Zhang et al. 2009). The problem with this technology is mounting them together without distorting them. The alternative technology involves very flat and polished silicon wafers with 0.6 mm pores that are chemically formed into a stiff rib-structure (Collon et al. 2009). These ribbed plates are then stacked into modules and mounted into a petal segment of the mirror, and the resulting mirror modules are assembled radially.

The 20 m focal length of IXO means that the plate scale will be ~ 2.7 times smaller than that of XMM-Newton, so a larger detector area would be required to cover the same field of view. Unfortunately, a larger detector is subject to a greater bombardment of particles from the telescope environment, adding more unwanted background to any observations. It would also require more resources to operate. This makes detectors with a smaller field of view more preferable. Also, due to the increased effective area of the

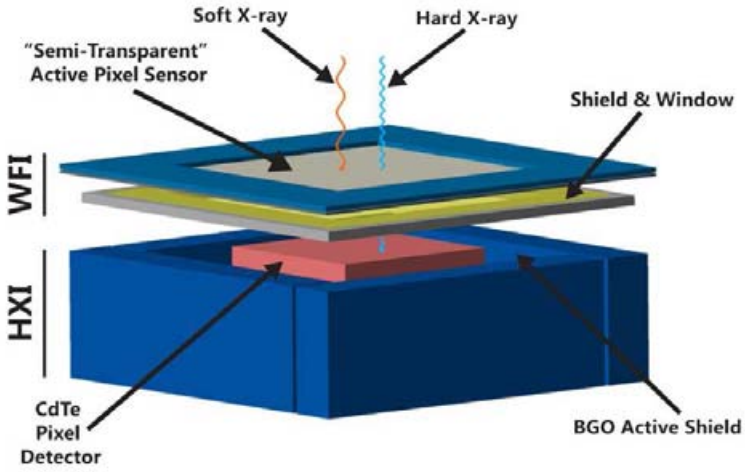

Figure 1.5: The layout of the X-ray imaging detectors proposed for IXO. Figure credit: NASA.

mirrors, the detectors will need to be capable of handling a much higher count rate than those on previous X-ray observatories.

Numerous detectors have been outlined for IXO. One of these is known as the Wide Field Imager (WFI). The WFI is a single Depleted P-channel Field Effect Transistor (DePFET) active pixel sensor (Treis et al. 2009). This is an advancement in CCD technology in which each pixel can be read out individually, resulting in faster readout speeds. Other advantages of this sensor include higher energy resolution and larger array sizes. It will cover a field of view of 18 arcmin diameter (approximately 2.8 times smaller than that of the Chandra and XMM-Newton) and operate in the $0.1 - 15$ keV range. Pixels will be 100×100 μm^2 in size, corresponding to 1 arcsec on a side, so will not limit the spatial resolution of the observatory. A CdTe detector covering an 8×8 arcmin^2 field will be mounted behind the WFI to function as a Hard X-ray Imager (HXI), expanding the imaging capability of IXO to 40 keV. Also, two layers of Double-sided Silicon Strip Detector (DSSD) will be placed between the WFI and HXI to detect the particle background and cover the energy range in which both imagers have a lower effective area. The configuration of the imagers is illustrated in Figure 1.5.

Three spectrometers are planned for IXO. One is an X-ray Grating Spectrometer (XGS), with a performance requirement of 5000 $E/\Delta E$ for its spectral resolution within

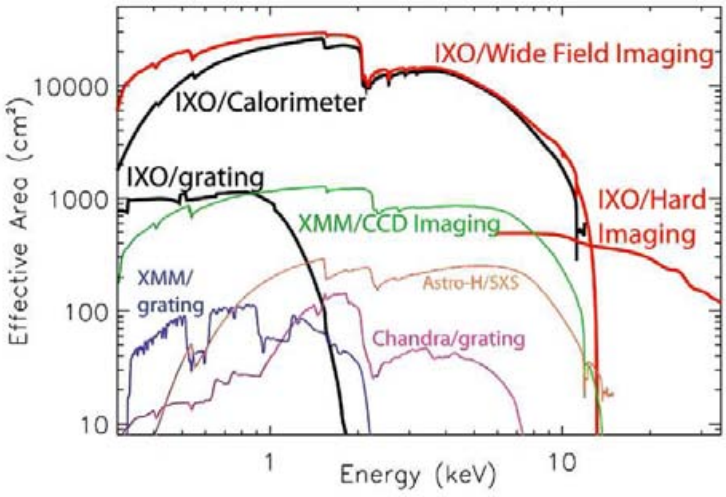

Figure 1.6: The effective area against energy as predicted for four IXO detectors, along with those of other observatories. Figure credit: NASA/GSFC.

the $0.3 - 1$ keV band. A dedicated array of between 9 and 32 CCDs will be used to capture the dispersed X-rays. Covering a higher energy range of $0.3 - 7$ keV is an X-ray Microcalorimeter Spectrometer (XMS), providing 2.5 eV resolution imaging spectroscopy in its central 2×2 arcmin^2, and at least 10 eV in the whole 5.4×5.4 arcmin^2 field of view. The final spectral instrument is a High Time Resolution Spectrometer (HTRS), capable of observing 10^6 cts s^{-1} in the $0.3 - 10$ keV band with an optimal resolution of 40 $E/\Delta E$ at 6 keV. This will be an array of 31 silicon drift diodes, a semiconductor technology which uses increasingly negatively biased rings to drive impact-generated electrons towards a readout (Barret et al. 2008). They can have a small physical size, and thus anodes with small capacitance, allowing for very high readout speeds along with good energy resolution.

The final proposed instrument is an X-ray polarimeter. It uses a gas pixel detector to track the direction of the electron produced by X-ray photoionization, which gives polarisation information about the incident radiation (Muleri et al. 2008). The aim is for a polarisation sensitivity of 1% in the $2 - 10$ keV band, with a field of view of 2.5×2.5 arcmin^2 and a spectral resolution of 5 $E/\Delta E$ at 6 keV.

The XGS CCDs will be placed on a fixed platform, while the other detectors will be mounted on a Mobile Instrument Platform (MIP). This allows one of the five MIP instruments to operate at a time while the XGS operates simultaneously. The effective area predicted for IXO instruments, along with those from several other X-ray observatories, are shown in Figure 1.6. A table summarising the proposed detector specifications and their main science drivers is available in Appendix B.1.

1.1.7 Observatory Simulators

An important stage in planning an observation is developing a simulator that will give scientists an idea of what the telescope may detect in different situations. This helps to evaluate possible instrument configurations, and is also useful for optimising the allocation of time with the instrument between different research projects. Some X-ray detectors are created for a specific observatory, while others are capable of performing less detailed simulations for a variety of X-ray telescopes and detectors. Observatory simulators take their input from an artificial sky. How well each aspect of the sky is modelled depends on the research for which the simulator is intended. This artificial sky may have been generated semi-analytically, or have been taken from an N-body simulation, depending on the physical properties and level of detail that the simulator considers important. Examples of outputs from observatory simulations include data tables, images, spectral files and photon event datasets. More specific formats are sometimes output for analysis with other software packages. For example, a Chandra event file may be useful if the researcher intends to use routines within the Chandra Interactive Analysis of Observations (CIAO) package.

The ASI Science Data Center (ASDC) X-ray events simulator was developed for the BeppoSAX observatory (Giommi 2000). One of several different satellite-detector combinations can be selected. The program is capable of handling up to 10,000 point sources and 100 extended sources, which can either be randomly generated or input by the user using an ASCII file. A variety of functions are available for the spectral distributions

of the sources. The simulator deals with each source separately, using flux and spectral information to determine the number of counts and photon energies. It then convolves each photon with the PSF for the chosen satellite to create an event file. Since the PSF describes how the X-rays propagate through the optics of the telescope it is different for each observatory. This simulator was adapted to run simulations for the Swift-XRT observatory (Giommi 2005). Additions include the simulation of gamma ray bursts and X-ray afterglows, and the output of an event file for a situation of ideal photon counting.

Marx is a software package used to simulate observations from the Chandra observatory (Ishibashi 2006). There are options for the various detector and grating types on Chandra. It begins with chosen source spatial and spectral models. The specific emission of each body is projected along the line of sight, a process known as ray-tracing. Marx will account for the positions of the spacecraft and detector, as well as dithering of the spacecraft's line of sight. The effects of vignetting and the PSF are also included, along with several other aspects of the detectors. Multiple simulations can be combined, and the results are stored in a Flexible Image Transport System (FITS) file for use with a variety of other astronomy tools.

Simulations for Chandra have also been generated using a private software package called X-ray Map Simulator (X-MAS) (Gardini et al. 2004). The input used is a hydro-N-body simulation, and the processing conducted is divided into two stages. In the first stage, for each energy channel, ray-tracing is performed for each body. This creates an array of angular position and energy, and is independent of the properties of the telescope. The second stage uses position-dependent Ancillary Response Files (ARFs) and Redistribution Matrix Files (RMFs), which determine the number of detector events for photons incident on the observatory mirrors. A routine called `FAKEIT`, in the software package XSPEC (Arnaud 1996), uses these two files and the array to generate an event file. Noise is also added by the routine, based upon the specified integration time.

A program called SciSim is available for making simulated XMM-Newton observations (XMM-Newton Team 2005). SciSim contains a 'cosmic simulator', which provides

the input for the simulation. It allows point sources to be manually positioned, chosen from a star catalogue or generated by the program. SciSim then performs ray-tracing of the photons through the telescope and detector. The resulting array is then processed according to the PSF, vignetting and detector response of XMM-Newton. Also taken into account are bad pixels, readout effects and the gaps between the CCD chips.

Due to the long processing time when running SciSim, a simpler simulator was developed known as QuickSim (Arida 2001). One of the key differences in increasing the speed of the simulations is the lack of ray-tracing. Other simplifications include less accurate vignetting and PSF calculations, and no representation of the gaps between the CCD chips. QuickSim can create its own input files for point and extended sources, using its SimSource and SimExtend programs, respectively.

Many of the principles for creating an IXO simulator are similar to those in the simulators mentioned above. The methods used should be carefully considered, as using processes such as ray-tracing can significantly increase the time required to run a simulation. Specific information about the performance of IXO, such as vignetting and detector response, would allow the simulator to produce a more accurate representation of its capabilities. Before the desired level of detail can be determined, the purpose behind creating the simulator should be discussed. It is the physical properties under investigation that will guide the development of the simulator.

1.2 Non X-ray Methods

Galaxy clusters can be detected in many other wavelengths, both directly and indirectly. The most obvious of these is discovering overdensities of galaxies found by the optical light from their stars. Distant galaxies can also be detected through X-ray or radio emission from an AGN. By using them to direct optical searches, small groups at high-z can be found (e.g. Pascarelle et al. 1996; Fabian et al. 2001). Clusters can also be studied through gravitational lensing. The concentration of mass within a cluster perturbs the

light from a source behind it. By including the distortion of background galaxy shapes in a model, the mass of the lensing structure can be inferred (reviewed in Mellier 1999). Lensing can also amplify flux from a background galaxy, allowing the study of distant galaxies that would otherwise be too faint.

Another method of detecting clusters is the Sunyaev-Zel'dovich (SZ) effect. This involves looking for distortion of the Cosmic Microwave Background (CMB) from the inverse-Compton scattering of CMB photons off the energetic electrons of the intracluster medium (reviewed in Birkinshaw & Lancaster 2007; Sunyaev & Zeldovich 1980). It can be divided into thermal and kinetic SZ effects caused by the temperature-related motion and bulk motion of the cluster electrons, respectively. An important feature of the SZ effect is that its amplitude is independent of redshift, which makes it of great interest in cosmological studies. Originally limited to the most massive clusters due to other CMB effects and background noise, improvements in measurement accuracy have produced several new cluster detections (e.g. Staniszewski et al. 2009).

1.3 Group and Cluster Physics

1.3.1 Cosmology

Both the formation and observation of clusters are dependent on a number of cosmological parameters which govern the behaviour of the Universe on large scales. Those relevant to this research are defined below:

H_0, the Hubble constant. This parameter relates the recession speed v of a body in an expanding Universe at redshift $z = 0$ to its distance d away: $H_0 = v/d$. This expansion is known as the Hubble flow, as it was discovered by Hubble (1929).

ρ_c, the critical density. Density of the Universe required to make its geometry flat.

Ω_m, the matter density. This is the fraction of ρ_c that is baryonic and dark matter.

Ω_Λ, the dark energy density. This is the fraction of ρ_c that is dark energy.

σ_8, the fluctuation amplitude at 8 h^{-1} Mpc. This is a measure of the normalisation of the density perturbations from which clusters grow (explained in Section 1.3.2).

These have long been subject to a great deal of uncertainty. To allow for the uncertainty in the Hubble constant, it is often parametrised as

$$H_0 = 100h \text{ km s}^{-1} \text{ Mpc}^{-1} \tag{1.1}$$

where h is a dimensionless number used to insert the researcher's choice of H_0. An estimate of the age of the Universe can be obtained by inverting H_0 to give the Hubble time

$$t_H \equiv \frac{1}{H_0} = 9.78 \times 10^9 h^{-1} \text{yr} \tag{1.2}$$

In 2001, measurements with the Hubble space telescope found $H_0 = 72 \pm 8$ km s^{-1} Mpc^{-1} (Freedman et al. 2001). This gives an age of the Universe of ~ 13.6 billion years.

Since the all points in space are expanding apart with the Hubble flow, it is often useful to remove this expansion from measurements to study the gravitational movement of structures in the Universe. This leads to the definition of comoving coordinates, where the separation s between two objects independent of the Hubble flow

$$s_{\text{CM}} \equiv s\frac{a_0}{a} \equiv s(1+z) \tag{1.3}$$

where a is the scale factor of the Universe at the epoch of interest and a_0 is that at the present epoch. Cosmological distances are often given in units of h^{-1} Mpc. Measurements of certain parameters of astronomical bodies are dependent on the value of H_0, so it can be preferable to express them in units of h.

The Hubble constant is only valid for $z = 0$, and defines the Hubble parameter $H(z)$. The evolution of the Hubble parameter is dependent on the density of the different constituents of the Universe. Observations of the CMB, distant supernovae and cluster

evolution support a cosmology that includes dark energy, with $\Omega_m \sim 0.3$ and $\Omega_\Lambda \sim 0.7$ (Vikhlinin et al. 2003). This is known as the ΛCDM model.

A combination of more recent studies has produced the following estimates for key cosmological parameters: $H_0 = 70.4^{+1.3}_{-1.4}$ km s^{-1} Mpc^{-1}, $\Omega_m = 0.272 \pm 0.016$, $\Omega_\Lambda = 0.728^{+0.015}_{-0.016}$, $\sigma_8 = 0.809 \pm 0.024$ (Komatsu et al. 2010). These are based on constraints from a combination of the following:

- the polarisation of the CMB from the integration of 7 years of data from the WMAP satellite,
- baryonic acoustic oscillations in the distribution of galaxies,
- measurements of the Hubble constant using Cepheid variables and Type Ia supernovae.

These constraints continue to support ΛCDM.

1.3.2 Cluster Formation

Clusters of galaxies exist inside massive halos that are presumed to be mostly comprised of dark matter. Theory suggests that these halos collapsed from gravitational instabilities (density perturbations) in an almost flat matter distribution sometime after the epoch of recombination, when protons and electrons formed the first hydrogen atoms (Peebles 1965; Press & Schechter 1974). Recombination occurred at $z \sim 1000$, when the Universe was around 400 million years old (Peebles 1968). The gravitational attraction within a perturbation slows down the expansion rate of the matter within it, eventually separating it from the Hubble flow and causing it to fall inwards. The development of these halos can be derived, allowing their abundance and even their large scale spatial distribution to be modelled (Press & Schechter 1974; Sheth & Tormen 1999).

Modern structure formation models make use of a primordial power spectrum to represent the growth of perturbations on different scales. The perturbations are described

by an overdensity field $\delta(\mathbf{x})$, which is assumed to be isotropic and also a Gaussian random field. Spherically integrating $\delta(\mathbf{x})$ over some radius r gives the mass perturbation $\delta M/M(r)$. The normalisation of the power spectrum can only be determined through observation (Voit 2005b). Since the measured mass fluctuation at the current epoch is $\delta M/M \approx 1$ inside comoving spheres of radius 8 h^{-1} Mpc, this normalisation is expressed as σ_8. The other two parameters used to define the power spectrum are its slope, n_s, and its shape parameter Γ, the latter of which is used to include the minor effects of baryons and massive neutrinos. An increase in either Ω_m or σ_8 will increase the number of high mass halos in the model.

While a numerical approach is required to accurately model the process of cluster collapse, a useful simplification is a spherical collapse model (Gunn & Gott 1972). Spherically symmetric shells of matter collapse to the centre of the density perturbation with a predictable motion. Since the majority of the mass is collisionless dark matter, these shells can interpenetrate and oscillate about their origin. The oscillations slowly decrease in amplitude as the growing mass increases the depth of the potential well (Gunn 1977).

A more realistic approach to the accretion model involves matter falling in as clumps. This creates a time-varying gravitational potential that randomises the particle motions, producing a Maxwell-Boltzmann distribution (Lynden-Bell 1967). This results in virial equilibrium, with

$$E_G + 2E_K = 4\pi P_b r_b^3 \tag{1.4}$$

where E_G is the gravitational potential energy, E_K is the kinetic energy, and P_b is the effective pressure at the boundary r_b of the halo (Voit 2005b). From the virial theorem a proportionality relation can be established between the mass of a system and its temperature. This is explored further in Section 1.3.3.

The scale on which the mass is measured can be important for comparing cluster properties. It is conventional to define the scale in terms of the mean matter density of the cluster within it. These density scales are often stated as a multiple of the critical density of the Universe. Common overdensity scales used are $\Delta = 200$, 500 and 2000. A

scale of $\Delta = 200$ encompasses most of the cluster, containing regions where the matter is only just virialised. It contains most of the cluster mass, but the the assumption of hydrostatic equilibrium may not be valid over the entire enclosed region. A scale of $\Delta = 500$ is often used when comparing cluster properties, where symmetrical models better represent the data. A useful model for estimating the location of the boundary of a cluster is the spherical top-hat. This assumes that a perturbation which will form a cluster is a spherical, constant density region, and all of the mass shells collapse to the origin in unison. For a universe with a non-zero cosmological constant, the spherical top-hat model leads to the redshift dependent virial scale

$$\Delta_v = 18\pi^2 + 82[\Omega_m(z) - 1] - 39[\Omega_m(z) - 1]^2 \tag{1.5}$$

where $\Omega_m(z)$ is the matter density as a function of redshift (Bryan & Norman 1998). Therefore, for the $\Omega_m = 0.3$, ΛCDM model of the Universe the present mean density within which a cluster is virialised is $\simeq 101$ times ρ_c.

Approximately 17% of the matter in the Universe is in the form of baryons ($\Omega_b \simeq 0.045$). Of this, just over one tenth is in the form of stars, and even less is made up from neutrinos (Liddle 2003). The remaining mass is free hydrogen and helium atoms, which gain a significant amount of kinetic energy when they collapse into a gravitational well of a halo. Much of this matter is ionised and emits X-ray photons via a bremsstrahlung process.

1.3.3 X-ray Scaling Relations

A useful way to explore the properties of galaxy groups and clusters is to define some quantitative parameters, e.g. gas density, and then to relate them to each other using simple physics within a chosen cosmology. The resulting equations take the form of proportionality relations, scaling one parameter with respect to another. Using a CDM cosmology, the assembly of dark matter halos through hierarchical structure formation

produces a population of clusters that is self-similar (Navarro et al. 1995; Voit 2005a). This means that the same scaling relations should be applicable to clusters of all sizes. In reality, the poorly understood baryon physics causes these clusters to deviate from being strictly self-similar.

Self-similar scaling relations can be defined by assuming that the evolution of cluster properties has a simple dependence on cosmological parameters. By taking the density profiles for dark matter and intracluster gas to be self-similar, the following relations can be defined:

$$r \propto M^{1/3}\rho^{-1/3}$$
$$T \propto Mr^{-1} \propto M^{2/3}\rho^{1/3}$$
$$\rho_g \propto \rho$$
$$M_g \propto M \propto T^{3/2}\rho^{-1/2}$$
$$L_{\rm X} \propto \rho_g M_g T^{1/2} \propto T^2\rho^{1/2}$$

where r is the radial size of the cluster, M is the cluster mass, T is the cluster temperature, ρ is the total matter density, ρ_g is the gas density, M_g is the cluster gas mass, and $L_{\rm X}$ is the cluster's X-ray luminosity in free-free emission (Voit 2005a). The derivation of these relations and the assumptions involved can be found in Appendix C.1.

Simulations of hierarchical structure formation which neglect processes such as radiative cooling and feedback result in clusters which approximately follow these self-similar scaling relations at $z = 0$ (Navarro et al. 1995). These scaling relations can be compared with observations of clusters at low redshifts to see how well they hold up. Observations to date have produced the following relations:

$M \propto T^{1.5-1.8}$ (Horner et al. 1999; Nevalainen et al. 2000; Finoguenov et al. 2001a) (Arnaud et al. 2005; Vikhlinin et al. 2006; Sun et al. 2009);

$M_g \propto T^{1.8-2.0}$ (Mohr et al. 1999; Neumann & Arnaud 2001);

$L_{\rm X} \propto T^{2.6-3.4}$ (Edge & Stewart 1991; Markevitch 1998; Arnaud & Evrard 1999)
(Maughan 2007; Pratt et al. 2009);

These show steeper scaling relations than those predicted by self-similarity. Results differ depending on the regions measured and the techniques used (e.g. see Pratt et al. 2009; Vikhlinin et al. 2006). Different results can be obtained from a sample when the cluster cores are excluded. Including the core region may break the self-similarity due to the effects of baryon physics, which will be covered in the next section.

These scaling relations have been observed down into the galaxy group regime, where low brightness increases measurement errors. The $M-T$ relation for groups appears to be consistent with that for clusters (Sun et al. 2009). However, many studies have indicated a steepening of the luminosity-temperature ($L_{\rm X} - T$) relation:

$L_{\rm X} \propto T^{2.5-6.0}$ (Helsdon & Ponman 2000; Xue & Wu 2000; Osmond & Ponman 2004)

This represents a greater deviation from self-similarity in groups and is a strong indication that they are not just scaled down clusters. Before the causes of these differences can be inferred, it is necessary to understand the baryon physics taking place within groups and clusters.

1.3.4 Underlying Baryon Physics

While constituting only a small fraction of its total mass, which is dominated by non-baryonic dark matter, the baryons within a cluster play an important role in producing the cluster scaling relations observed. Unlike the dark matter, which only interacts gravitationally, the baryons can collide and produce photons via a variety of mechanisms. There are two main components to the baryon content of a cluster: the stars that make up the galaxies with the cluster, and the hot gas trapped inside the cluster's gravitational potential well (Liddle 2003, pp 66-67). The latter is known as the Intracluster Medium (ICM), and contains about 5 to 10 times more mass than the stellar content of the cluster. The X-ray emission associated with a cluster is a combination of bremsstrahlung radiation

and atomic emission lines from elements in the ICM. Also present are black holes at a variety of mass scales, including AGN. The presence of stars and AGN in the ICM can have a significant effect on its emission, which will be explored shortly.

A useful cluster property to study is entropy, both because it traces the structure of the ICM and because it holds information about the thermodynamic history of the cluster gas. One definition of entropy is

$$K \equiv \frac{k_B T}{\mu m_p \rho_g^{2/3}} \tag{1.6}$$

and is directly related to thermodynamic entropy. High entropy gas floats, while low entropy gas sinks. Convection continues until constant entropy (isentropic) surfaces align with the dark matter equipotential surfaces. The gas density profile $\rho_g(r)$ and temperature profile $T(r)$ are expressions of the entropy distribution.

In the hierarchical merging model of cluster growth, galaxies and groups from the field are pulled into the gravitational potential wells of clusters (Katz & White 1993). When one of these dark matter subhalos merges with the cluster halo, the baryons bound to each halo become compressed, causing shocks that increase the entropy of the gas within the cluster in predictable way. Numerical simulations have shown that the entropy distribution of clusters is approximately self-similar if only these gravitationally driven processes take place (Navarro et al. 1995). Other processes taking place will affect the entropy of the cluster gas. Deviations from self-similarity have been observed, with the normalisation of the entropy profiles scaling as $T^{2/3}$ rather than T (Pratt & Arnaud 2003; Ponman et al. 2003; Pratt et al. 2010).

Bremsstrahlung emission from the ICM is in the X-ray energy range and gives us the opportunity to detect the cluster in X-ray observations, along with X-ray luminosity from any unresolved X-ray point sources present. Emission of radiation from the cluster gas causes it to cool. The radiative cooling rate is a sum of the rates from bremsstrahlung emission, recombination radiation, and line emission caused by electron impact excitation (Kafatos 1973). The rate at which the ICM radiates energy can be represented by a cooling function $\Lambda_c(T)$, usually defined so that $n_{\rm e} n_{\rm ion} \Lambda_c(T)$ equals the $L_{\rm X}$ per unit volume (Voit

2005b). This assumes collisional ionisation equilibrium. Initially, this loss of thermal energy would appear to result in a simple decrease of the temperature expected for given mass in a scaling relation. However, the cooling of cluster gas has consequences that further complicate the matter.

1.3.5 Cooling Flows and Feedback

High gas density near the centre of a cluster causes a high rate of radiation, which can result in a radiative cooling time less than the Hubble time, and this time decreases at smaller radii (Fabian 1994). Energy is removed efficiently from the gas in the core, and without a heat source to establish balance within the region, a subsonic inflow develops to maintain enough pressure to support the weight of the gas overlying the central region. This is known as a cooling flow.

XMM-Newton and Chandra have allowed observers to search for evidence of cooling flows. While the cores of clusters have been shown to often have lower X-ray temperature plasma than the outer regions, the amount and location of the cooling flow by-products is uncertain (Peterson et al. 2003). Gas that has cooled from X-ray temperatures should be present. There is some evidence for cool gas from UV and Hα emission (O'Dea et al. 2004; Hicks & Mushotzky 2005; Wilman et al. 2006). However, there is a lack of OVII and Fe line emission expected from the spectra of cool gas in clusters where cooling has been observed (Tamura et al. 2001; Peterson et al. 2001; Kaastra et al. 2001). CO emission indicates an order of magnitude less cold molecular material than predicted (Edge 2001).

However, the observed cooling rates give mass losses of tens to hundreds of $M_\odot$ yr^{-1}, whilst the observed star formation rate is only a few tens of $M_\odot$ yr^{-1} (Fabian et al. 1982; Fabian 1994; McNamara 2004; O'Dea et al. 2004). This indicates that much of the cooling gas does not collapse into stars. This is supported by studies of the Initial Mass Function (IMF), which characterises how the initial mass of a star forming region is distributed between different masses of stars. With a normal IMF, the galaxies in the centre of these clusters would be brighter and more blue than they are observed to be.

A consequence of forming stars is the possibility of supernovae occurring (Pen 1999; Voit & Bryan 2001). This would become a source of energy for the region, resulting in feedback to the ICM. The energy contribution from supernova feedback can be calculated by modelling their iron production and the energy that they emit (Domainko et al. 2004). Observational data is used to estimate the excess iron in the region, allowing a supernova rate and hence a heating rate to be calculated. This heating would act to reduce the loss of ICM temperature from radiative cooling. However, current models of supernova feedback indicate that there is insufficient heating to counteract the cooling rate (Valdarnini 2003; Kay et al. 2004; McNamara et al. 2004).

Another potential source of heating within the centre of a cluster are AGN. These active central black holes produce jets which inject mass and energy into the surrounding region and cause shock heating (Binney & Tabor 1995). The jets can produce powerful radio emission, so a host galaxy is often known as a radio galaxy. Also, radio bubbles from AGN may pull filaments of cool gas away from the central reservoir (Fabian et al. 2003). Observations suggest that optical and radio AGN have different accretion mechanisms (Best et al. 2005). Powerful radio outbursts have the potential to support against the cooling flow for several Gyr (McNamara et al. 2005). However, a true feedback system would involve the regulation of the AGN output by the influence that output has on the cluster gas. Simulations indicate that this AGN self-regulation may be effective, but several different AGN feedback mechanisms are required to produce the variety in radio emission observed (Cattaneo & Teyssier 2007; Croston et al. 2006).

Feedback has become a popular solution for providing heating within clusters, but many alternatives have been suggested. The dynamical friction of galaxies moving through the ICM is a supplier of heat to the cluster, although it is unlikely to produce the heating required to solve the cooling flow problem (Kim et al. 2005). Another theory is that the action of heat conduction, the transportation of heat from a hot gas reservoir to the cluster core, could offset cooling. Conduction has been shown to be effective in regions of hot gas ($T \gtrsim 5$ keV), but fails to offset cooling in cool clusters and the inner, cooler regions

of hot clusters (Voigt & Fabian 2004). Merging has also been suggested as the cause of the observed state of high mass cool core clusters (Motl et al. 2004). Despite these alternatives, the absence of evidence for strong cooling flows remains strong motivation for the presence of feedback in cluster environments.

Another problem relating to radiative cooling models is overcooling. These models produce a universe where too high a fraction of the baryon content would have cooled into low mass halos before clusters formed (Cole 1991; White & Frenk 1991; Blanchard et al. 1992). Overcooling must be dealt with when generating a cosmological simulation (Balogh et al. 2001).

1.3.6 Similarity Breaking

Previously it was mentioned that the physics of the cluster gas affects the entropy profile of the cluster, causing the cluster properties to not scale in a self-similar manner. This similarity breaking will now be discussed in more detail.

An early attempt to explain the similarity breaking involved pre-heating the gas before it contracted into clusters, imposing a minimum 'entropy floor'. Higher entropy means that less gas is compressed in the cluster cores. This causes reduced core densities, especially in low temperature clusters which have shallower potential wells. Lower core density leads to less X-ray emission, resulting in a steepening $L_{\rm X} - T$ relation, similar to that observed. Measurements of low temperature clusters at R_{200} suggested an entropy floor of ~ 135 keV cm^{-2} (Lloyd-Davies et al. 2000). However, the preheating model also predicts isentropic cores in low temperature clusters (Balogh et al. 1999), while observations show an entropy threshold with a weak dependence on temperature (Ponman et al. 2003).

An alternative scenario for similarity breaking has it originating from radiative cooling. Assuming pure bremsstrahlung cooling for $\Lambda_c(T)$, Voit (2005b) derives the cooling threshold

$$K_c(T) \approx 81 \text{ keV cm}^2 \left(\frac{t_0}{14 \text{ Gyr}}\right)^{2/3} \left(\frac{T}{1 \text{ keV}}\right)^{2/3} \tag{1.7}$$

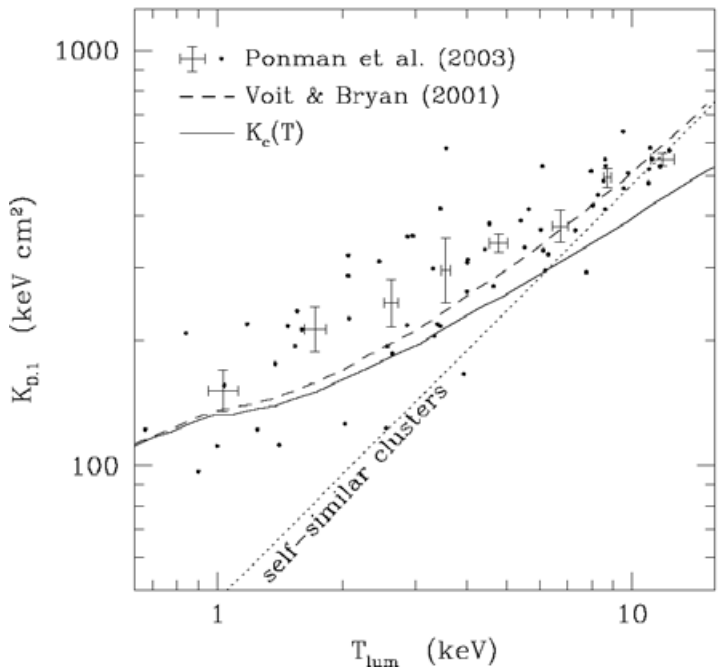

Figure 1.7: Plot of entropy at 0.1 R_{200} ($K_{0.1}$) against temperature from Voit (2005b), with data points from Ponman et al. (2003). The solid line shows the cooling threshold for heavy-element abundances of 0.3 Solar and $t_0 = 14$ Gyr. The dashed line is $K_{0.1}$ from the analytical model of Voit & Bryan (2001). The dotted line shows the mean entropy from the self-similar prediction. Figure taken from Voit (2005b).

where t_0 is the time the gas at temperature T has radiated. This entropy threshold for radiative cooling is close to the observed entropy floor mentioned previously. Measured core entropies also scale as $T^{2/3}$ (illustrated in Figure 1.7), although these data have significant scatter (Ponman et al. 2003). This solution still has a major problem, which can be seen in the dimensionless form of Equation 1.7:

$$\frac{K_c(T)}{K_{200}} \approx 0.2\,(Ht)^{2/3}\left[\frac{H(z)}{H_0}\right]^{2/3}\left(\frac{T}{1\,\mathrm{keV}}\right)^{-1/3} \tag{1.8}$$

where K_{200} is the entropy at a $\Delta = 200$, Ht is the Hubble parameter multiplied by time (2/3 in a matter dominated Universe), and both $H(z)$ and H_0 have their previous definitions (Voit 2005b). This shows that the cooling threshold is $\sim 20\%$ of K_{200}, and it becomes greater at earlier epochs. With such a high cooling threshold, a much larger proportion of the baryons should have condensed into stars than that observed in the

mass ratio of stars to the total baryons within clusters, which appears to be in the range $0.09 \lesssim f_* \lesssim 0.14$ for rich to poor clusters (Lin et al. 2003). This is the overcooling problem again, where cosmological models produce too many stars and/or cold gas clouds.

Voit & Bryan (2001) proposed a method for radiative cooling to determine the entropy scale of similarity breaking. It highlighted feedback as a mechanism which would prevent gas entropy from remaining below $K_c(T)$ indefinitely. Consider an ICM divided into independent gas parcels, which have changing entropy with time. Parcels below the cooling threshold will cool. This either cools out and disappears from the system, condenses to form stars or falls onto AGN. The latter two processes lead to supernova and AGN feedback, respectively, which raise the entropy and push the gas parcels out to higher radii. Low entropy gas flows in to replace high entropy gas. The recent results of Pratt et al. (2010) imply that observed entropy distributions are caused by variations in the gas mass fraction. These radiative cooling and feedback processes break the self-similarity. By accounting for them in simulations, the clusters have reproduced the shape of the observed $L_{\rm X} - T$ relation (Tornatore et al. 2003; Borgani et al. 2004).

Cluster entropy can be used to define a new set of scaling relations. Since the entropy threshold for radiative cooling can be calculated by equating the gas cooling time with the age of the Universe, it can be used to substitute out ρ in the self-similar relations. With this new scaling method, Voit (2005a) derives the following low redshift scaling relations:

$$\rho_g \propto T^{1/2}$$
$$M_g \propto T^2$$
$$L_{\rm X} \propto T^3$$

Whilst they are more consistent with the observed clusters than the previous relations, they are still inappropriate to describe galaxy groups with their steeper $L_{\rm X} - T$ relation. Other non-gravitational process appear to have a significant effect.

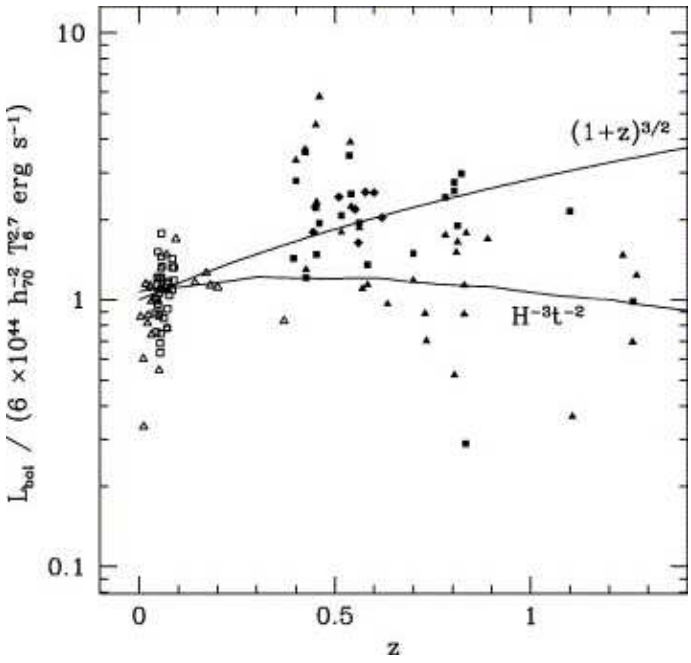

Figure 1.8: Plot of bolometric luminosity against redshift from Voit (2005a). Bolometric luminosity has been divided by the low-redshift fiducial relation $L_{\rm X} = 6 \times 10^{44} h_{70}^{-2} T_6^{2.7}$ erg s^{-1}. The sources of the data points are as follows: hollow triangles from Arnaud & Evrard (1999), hollow squares from Markevitch (1998), solid squares from Vikhlinin et al. (2002), solid diamonds from Lumb et al. (2004), and solid triangles from Ettori et al. (2004). The large error bars are suppressed for clarity. Figure taken from Voit (2005a).

1.3.7 Evolution of Scaling Relations

The scaling relations dealt with so far describe clusters at low redshifts. Evolving scaling relations have been approached in several different ways. The model of Kaiser (1986) had clusters to be self-similar with respect to the Universe's mean matter (background) density. This has the $M - T$ and $L_{\rm X} - T$ relations take the form:

$$M \propto T^{3/2}(1+z)^{-1}$$

$$L_{\rm X} \propto T^{2}(1+z)^{3/2}$$

A tight virial relation between M and the dark matter velocity dispersion suggests that ρ_c has a greater impact than background density on cluster substructure (Evrard 2004). Thus, clusters can be defined to be self-similar with respect to ρ_c, in which case their

evolution scales with the Hubble parameter:

$$M \propto T^{3/2} H(z)^{-1}$$
$$L_{\rm X} \propto T^2 H(z)$$

The evolving scaling relations for both of these models are derived in Appendix C.2. Another solution includes the redshift dependent density scale Δ_v of the top-hat collapse model (Bryan & Norman 1998). For a ΛCDM cosmology, this produces evolution intermediate between the previous two models. The corresponding $M-T$ and $L_{\rm X}-T$ relations are:

$$M \propto T^{3/2} \Delta_v^{-1/2} H(z)^{-1}$$
$$L_{\rm X} \propto T^2 \Delta_v^{1/2} H(z)$$

A scaling relation that is non-monotonic with redshift has also been considered for the $L_{\rm X} - T$ relation. This comes about from the inclusion of the cooling threshold. By including both the Hubble parameter time-scale for structure formation and another time-scale for the cooling of baryons, one obtains:

$$M \propto T^2 H(z)^{-3} t^{-1}$$
$$L_{\rm X} \propto T^3 H(z)^{-3} t^{-2}$$

(Voit 2005a). A model of this evolution is plotted in Figure 1.8. For redshifts increasing from $z = 0$, the rise in ρ_g dominates, causing $L_{\rm X}$ to increase, but after $z \approx 1$, the effects of cooling and feedback processes begin to dominate, causing $L_{\rm X}$ to decrease.

Evidence for evolution has been found in the observed scaling relations (Gioia et al. 1990a; Henry et al. 1992; Mullis et al. 2004b). Observations at high redshift, mostly of relaxed clusters, show a self-similar $M - T$ evolution that approximately scales with the Hubble parameter (Kotov & Vikhlinin 2006; Maughan et al. 2006), but there is a

large fraction of disturbed clusters at higher redshifts that need to be sampled more thoroughly before this is conclusive. Evolution in the $L_X - T$ relation has been more difficult to constrain, as evident in Figure 1.8. Studies have been hindered by large scatter in both parameters and biases that result from sample incompleteness (further explored in Section 1.4.5).

Cosmological simulations can be used to predict the form of the scaling relations when different non-gravitational processes are in effect, such as feedback (Muanwong et al. 2006). At higher redshifts, the lower amount of cluster gas entropy means that a higher proportion of gas is below the cooling threshold. The self-similar model of the $L_X - T$ relation is expected to be inappropriate for these higher redshifts, as cooling and feedback processes become dominant over gravitational processes. High redshift observations can be used to constrain these processes, so long as the cluster selection function is well understood. The subject of cluster selection functions and survey biases is covered in the next section.

Current knowledge of how clusters evolve is hindered by the lack of detailed cluster studies in the high redshift Universe. Of particular importance are the low temperature clusters, as the effect of non-gravitational processes is more prominent in clusters with low mass. IXO should prove useful in furthering research into group and cluster scaling relations, and baryon physics. Its sensitive spectral resolution should help to resolve cluster properties more accurately. A large effective area will allow IXO to study clusters out to higher redshifts, as well as increasing the number of clusters which can have their properties dissected radially, separating out the physics of the core. One of the current scientific aims proposed for IXO is to study the evolution in cluster properties in the range $0.1 < z < 2$ (Bookbinder 2010). These studies will require a PSF of no greater than 5 arcsec to resolve interesting features in nearby clusters and to resolve the core in distant clusters. Field of view is also important when mapping large clusters.

1.4 X-ray Surveys

Whilst X-ray observatories are sometimes pointed in a certain direction in the sky with a particular target in mind, they are also used to perform surveys of whole regions of the sky. It is useful to divide these into three broad categories: wide-angle surveys, with short amounts of telescope time being allocated to each observation to cover a larger area; deep surveys, which carry out long exposures over a much smaller region in an attempt to reach lower fluxes; and serendipitous surveys, the use of existing observations to compile a catalogue for study. All these survey types have their own advantages, but with the general aim of obtaining useful catalogues of data for statistical analysis. This section gives examples of X-ray surveys and their methodology. All flux limits quoted in this section are for the clusters in the $0.5 - 2$ keV energy band. Note that flux limits are subjective due to the different methods used to extrapolate the total X-ray flux $S_{\rm X}$.

1.4.1 Identifying Clusters

Two important stages in the analysis of an observed image are the detection of sources and the determination of whether or not a source is truly extended. The former requires the identification of regions with a statistically-significant increase in photon count rate compared to the background. The latter is more difficult. Due to the PSF of the telescope mirror, point sources usually appear to extend over several pixels on the detector. Various methods have been devised to discriminate between these smeared point sources, such as AGN, and actual extended sources, such as groups and clusters. In the early days of X-ray astronomy, clusters had to be identified by either time-consuming optical spectroscopy follow-up, or crude checks of the consistency of its X-ray spectrum with a thermal profile. Since ROSAT the PSF of X-ray telescopes has been narrow enough to allow clusters to be identified from their extent alone (Rosati et al. 2002). To do this, observers must compare the source extent with that of the PSF, then make a quantitative judgement based on that comparison. Optical follow-up is still popular for confirming those identifications

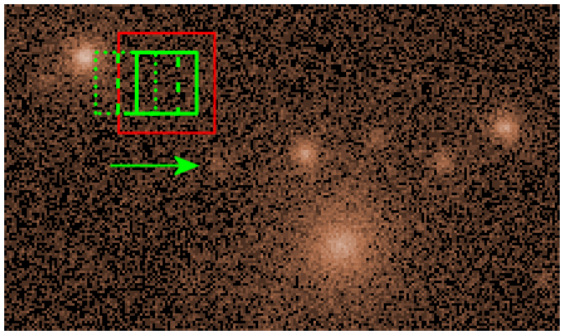

Figure 1.9: Sliding cell method of source detection. Broken green lines show the movement of the detection cell. The background frame is shown in red.

(e.g. McHardy et al. 1998). Some of the methods used for extended source identification in X-ray images are described below.

The sliding cell, or sliding window, technique has been used in analysis packages such as XIMAGE (Giommi et al. 1992), and was included in the ROSAT Standard Analysis Software System (SASS) (Voges 1993). A detection cell is moved across the image in small steps, and the signal-to-noise ratio of the contents of the cell is compared to the local background, assuming Poisson statistics. Estimates of source positions and intensities come from the regions with maximum signal-to-noise. The CIAO version of this technique uses cell that is some fraction of the PSF in size, and slides it across the image in steps of one-third the cell width (Calderwood et al. 2001). This cell is surrounded by a frame of approximately equal area, which is used to measure the local background (see Figure 1.9). That background is then subtracted from cell counts. A source is detected if the number of remaining cell counts is significantly greater than the background. This background can also be supplied through a background map or single value input. The sliding cell technique is optimised towards point sources and has become less common in cluster surveys (Voges 1993; Ebeling et al. 1996; Scharf et al. 1997).

Voronoi Tessellation and Percolation (VTP) combines the analysis of a set of convex cells with a friends-of-friends algorithm, creating a method of detecting non-Poissonian structures (Ebeling & Wiedenmann 1993). Each cell is a polygon that contains only one

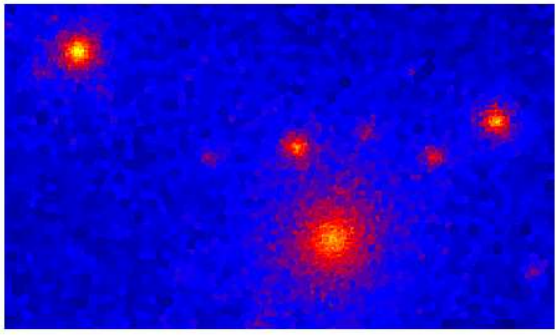

Figure 1.10: Sample of an image with a high number of counts that has been binned using weighted Voronoi tessellations generated by the Diehl & Statler (2006) generalisation of the Cappellari & Copin (2003) algorithm.

photon, with an area defined by the outermost points of the distribution. The flux for each cell is calculated from the inverse of the product of the area and exposure time. The cumulative distribution of the inverse of the areas of the cells is calculated and compared with a model of the expected Poisson distribution. A background density cut-off is established from the minimum of the residual (data minus model). Cells are then linked to neighbouring cells to form the object, with the cut-off replacing the standard maximum allowed separation in the friends-of-friends algorithm. The background cut-off calculation and cell linking can be performed iteratively (Scharf et al. 1997). The user will usually determine the minimum number of counts for a true source to remove background fluctuations, and this establishes the false source identification probability as a function of area.

A problem with identifying extended sources is distinguishing between individual extended sources and bends of sources. Scharf et al. (1997) used a method of source deblending by performing VTP with three different surface brightness thresholds and carrying out a visual inspection on the results.

Weighted Voronoi Tessellation (WVT) has been used to adaptively bin data to give it a constant signal-to-noise ratio S/N per bin (Diehl & Statler 2006; Cappellari & Copin 2003). This does not suffer from loss of small scale structure unlike fixed binning techniques, nor from presenting misleading structure, an issue that afflicts other adaptive bin-

ning and smoothing techniques. An example of an image binned with weighted Voronoi tessellations is given in Figure 1.10.

The previously described methods do not take into account the PSF, which can have a significant effect in making a point source appear to be extended, especially off-axis. The first method devised around the PSF was the Steepness Ratio Technique (SRT) (de Grandi et al. 1997). Assume that the surface brightness profile can be approximated by an isothermal β-model:

$$S(r) = S(0)\left[1 + \left(\frac{r}{r_c}\right)^2\right]^{0.5-3\beta} \tag{1.9}$$

with normalisation $S(0)$, core radius r_c and slope β (Cavaliere & Fusco-Femiano 1976; Jones & Forman 1984). A normalised β-model is convolved with the PSF of the telescope, and then integrated over both a circle of fixed angular size and a surrounding annulus. The steepness ratio is defined as the integral of the annulus divided by that of the circle. By assuming a fixed value of β and calculating the steepness ratio as a function of r_c, the r_c of an observed source can be derived. The significance of the measured r_c compared to that from the random fluctuations of a point source can be used to judge the source extent. A method of detecting sources must be used first to obtain the locations to perform the SRT.

An improvement on the SRT is Growth Curve Analysis (GCA) (Böhringer et al. 2000), which involves two procedures. For the first procedure, a model of the surface brightness profile with fixed β is convolved with a vignetting-corrected PSF. Next, a χ^2 fit to the differential count rate profile of a source is performed with the azimuthally integrated model. Normalisation is a free parameter, while r_c varies in fine steps. This gives a measure of the size of the source. The second procedure relies on a Kolmogorov-Smirnov (K-S) test to examine the probability that a source has extent. The expected cumulative count rate profile of a PSF convolved point source is compared with the observed source profile out to a radius which contains more than 90% of the PSF. This point source model includes

background. Böhringer et al. (2000) base their K-S probility for an extended source on a false identification percentage. They prefer GCA over VTP due to its simplicity to reproduce in simulations, yielding of count rates that relate to known apertures, and the output of essential diagnostic plots.

A significantly different approach to the problem of source detection and identification is the use of wavelet transforms. A signal is convolved with a chosen wavelet function, also referred to as a kernel. The wavelet must be a localised function with a mean of zero (Grebenev et al. 1995). The localisation, smoothness and oscillating properties of the wavelet decomposes the signal into space and scale dimensions (Slezak et al. 1990; Rosati et al. 1995). This can be interpreted as a multi-scale filtering process in Fourier space. Sources can be identified by finding the image pixels where the correlation with the wavelet is above a certain threshold (Romer et al. 2000; Freeman et al. 2002), and then percolation can be used to extract emission relating to a source past the threshold. The observer can recover the flux and extent of a source by fitting the wavelet-convolved source with a convolved source model at the local maximum (Rosati et al. 1995). Use of anisotropic wavelets also allows ellipticity and orientation to be measured.

Wavelet transforms have numerous advantages. They can identify sources on a range of scales, with blending effects limited by the angular resolution of the telescope. A wavelet transform algorithm, `WAVDETECT`, is included in CIAO (Freeman et al. 2002). It is not dependent on a fixed analysis region chosen by the user, as the scale sizes are related to the pixel size by powers of two. Also, a varying background does not significantly effect the detection efficiency or ability to recover parameters (Rosati et al. 1995). A popular choice of wavelet is the Mexican hat, which is the second derivative of a Gaussian. This is influenced by the similarity between the ROSAT and Chandra PSFs and a Gaussian. Its positive core and negative outer ring result in an integral of zero in the spatial plane Other advantages of this wavelet include two moments where the correlation with a linear function is zero, which helps to suppress the background, and its width of 2σ (Gaussian standard deviation) at its zero-crossing points, which is useful for determining the extent

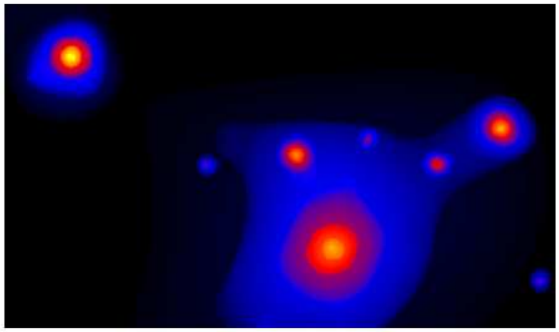

Figure 1.11: Sample of an image that has been decomposed using wavelets and then recombined. Generated using the wavelet decomposition code `Wvdecomp` in zhtools (Vikhlinin 1999).

of a source (Freeman et al. 2002; Romer et al. 2000).

Grebenev et al. (1995) used the wavelet transform technique to analyse the small scale structure in a cluster. The use of wavelets to decompose structure was exploited by Vikhlinin et al. (1998). Images were broken down into components by using a 'family' of wavelets covering six different scales, keeping all structures where the flux exceeded half the detection threshold and had a maximum above that threshold. All structures on the smaller three scales were attributed to point sources, which could then be removed from the analysis. They set their detection threshold low, maximising the detections with the intent of screening out false detections at a later stage. Finoguenov et al. (2007) took into account the changing shape of the XMM-Newton PSF with off-axis angle by requiring that extended sources had a small ratio of the sum of the flux on the smallest two scales to the flux on larger scales. An example of a recombined image after wavelet decomposition is shown in Figure 1.11.

The next stage of the Vikhlinin et al. (1998) analysis involved fitting a β-model to the source by minimising the Cash statistic C (Cash 1979), which was derived to apply the likelihood ratio to photon counting statistics:

$$C = -2 \ln P = -2 \sum_{i=1}^{N} (d_i \ln m_i - m_i) \tag{1.10}$$

where P is probability, d_i and m_i are the data and model for pixel i, respectively, and N is the total number of pixels. This β-model is convolved with the PSF and includes background. By fixing the flux to zero (creating a background model) and calculating the difference between the two fits ΔC, the significance of source existence is obtained. The significance of extent is found by refitting the model with $r_c = 0$ (i.e. a PSF model) and comparing it to the original fit. ΔC significance thresholds are set for the two statistics, along with the requirement for a minimum number of counts due to the non-linearity of the model. A normalisation-independent variant of this extent test is used by Pacaud et al. (2006), who ran simulations to find the ΔC thresholds that created the largest uncontaminated extended source sample.

Many more variants of the methods mentioned above exist in the literature, due to a combination of author preference and the needs of the survey. These techniques continue to be developed in effectiveness, and are especially important with an ever-increasing amount of archival data becoming available for study. Their use has already identified many hundreds of optically-confirmed clusters, enabling surveys to produce a wealth of information.

1.4.2 Wide-angle Surveys

Wide-angle surveys are useful for creating a shallow map of the X-ray sky. They can involve many exposures (known as pointings) over a large area, often to create a mosaic map, or they can continuously scan across the sky as the telescope slews. They were more popular with previous generations of observatories due to their wide field of view but poor resolution. The large solid angle covered means that many bright sources are detected, although a great many faint ones will be lost in the X-ray Background (XRB) due to the high level of noise in short exposures. This leads to incompleteness in a sample, where the source population is sparsely sampled past a certain limiting flux. However, the sheer number of detections through the observation of a large part of the sky gives these surveys great statistical power. Having a large number of pointings also helps with studies of the

XRB, allowing for a more accurate correction for its effects on observations performed by a particular instrument (e.g., Read & Ponman 2003).

There are several examples of wide-angle surveys in the literature. An early X-ray survey was the Einstein Extended Medium Sensitivity Survey (EMSS). Performed using the Einstein X-ray observatory, it obtained a flux-limited sample of 835 sources over 778 degree^2. After imposing a flux limit of 1.33×10^{-13} erg cm^{-2} s^{-1} and performing optical follow-up, a subsample of 93 clusters was used to examine the evolution of the cluster X-ray Luminosity Function (XLF) (Gioia et al. 1990b; Henry et al. 1992). Shortly after ROSAT became operational, the ROSAT All Sky Survey (RASS) was conducted. Its mean exposure time of 0.4 ks corresponds to a limiting X-ray flux $S_{\rm X} \simeq 5 \times 10^{-15}$ erg cm^{-2} s^{-1}. By combining a VTP analysis of this data with the Abell et al. (1989) all-sky optical cluster catalogues, the X-ray-Brightest Abell-type Clusters of galaxies (XBACs) sample was assembled for use in modelling the XLF and investigating optical correlations above 4.45×10^{-12} erg cm^{-2} s^{-1} (Ebeling et al. 1996, 1997).

More recent ventures include the XMM Large Scale Structure (XMM-LSS) survey and the Cosmic Evolution Survey (COSMOS). While considerably smaller than ROSAT surveys, these XMM-Newton surveys cover a field that is wide with respect to the field of view of the observatory, and their exposure times would classify them as medium-deep. XMM-LSS aims provide a well defined statistical sample of clusters, and has so far resulted in 29 spectroscopically confirmed clusters over 5.2 degree^2 (Pacaud et al. 2007). When completed, this survey will have covered 10 degree^2. COSMOS is made from XMM-Newton pointings in field being covered by observations at multiple wavelengths, of which the first 36 contained 72 optically-confirmed clusters with $S_{\rm X} \geq 3 \times 10^{-15}$ erg cm^{-2} s^{-1} in 2.1 degree^2 (Finoguenov et al. 2007).

Wide-angle surveys have been evolving toward more sensitive, smaller coverage surveys. In part, this is a consequence of the longer focal lengths of the current generation of observatories. A longer focal length gives increased effective area, but reduces the field of view for a detector of fixed size. This change can be seen in the data above, with later

surveys finding a higher density of sources. The surveys need to catalogue their data before any kind of analysis can be performed. Source types can be sorted using their likelihood of being extended, based on the methods described earlier. If available, data from other wavelengths, such as radio and infra-red, may also be compiled to get a more complete picture of the physics taking place. X-ray observations can be a useful addition to other surveys, such as the multi-wavelength COSMOS, due to their effectiveness in identifying and localising AGN and distant clusters (Hasinger et al. 2006). X-rays are not significantly affected by starlight or by the obscuring dust in the Galactic plane, both of which cause bias in optical selection.

1.4.3 Serendipitous Surveys

With many archives now containing a few decades worth of X-ray pointings, the serendipitous survey is a popular way to create a representative catalogue, i.e. a well defined sample which accurately characterises the underlying population. A collection of images can be gathered from pointed surveys and one-off pointings, and the data analysed in bulk. These surveys may detect new sources in pointings where the observers were interested in other targets. They can be used obtain a statistically comparable catalogue where the same detection techniques and criteria have been used on all sources, including those previously known.

Many serendipitous surveys have made use of ROSAT pointings. These include the ROSAT Deep Cluster Survey (RDCS) (Rosati et al. 1995), ROSAT International X-ray Optical Survey (RIXOS) (Carrera et al. 1996), Wide-Angle ROSAT Pointed X-Ray Survey (WARPS) (Scharf et al. 1997; Perlman et al. 2002), WARPS-II (Horner et al. 2008), 160 square degree (160d) survey Vikhlinin et al. (1998), 400 square degree (400d) survey (Burenin et al. 2007), Southern Serendipitous High-redshift Archival ROSAT Cluster (SHARC) (Collins et al. 1997), Bright SHARC (Romer et al. 2000), and ROSAT ESO Flux-Limited X-Ray (REFLEX) (Guzzo et al. 1999; Böhringer et al. 2004). These surveys approach the available data in different ways. Designed to complement each other,

Southern SHARC was a deep survey that used a combination of the sliding cell technique and the Cash statistic, while Bright SHARC covered a wide field using a wavelet transform method. In contrast, REFLEX reanalysed the sources from the third reprocessing of the RASS using GCA, creating a large X-ray selected sample.

The surveys listed above have been used in many studies that require large samples. Several have been used to study the cluster XLF and its evolution, including RDCS (Rosati et al. 1998), RIXOS, 160d survey, and Southern SHARC Burke et al. (1997). The 400d clusters, which were found using wavelet decomposition, were augmented with data from the Chandra archive and used to measure the cluster mass function to constrain cosmology (Vikhlinin et al. 2009a). The evolution of cluster scaling relations has been studied with WARPS (Maughan et al. 2006), which identified clusters with VTP. 3 sources from Bright SHARC were reported to be 'fossil groups', which form from a relaxed group merging to form a single bright elliptical galaxy (Ponman et al. 1994).

REFLEX enabled the Representative XMM-Newton Cluster Structure Survey (REXCESS). This is a medium-deep survey performed on clusters selected from REFLEX, with the goal of creating an unbiased, representative sample of clusters with $z \leq 0.2$ and temperature > 2 keV (Böhringer et al. 2007). They have been selected to provide nearly homogeneous coverage of the X-ray luminosity range, to be detectable with XMM-Newton out to a radius of $\sim R_{500}$ and to have distances that optimise the use of the field of view and angular resolution of XMM-Newton. Such an approach is necessary to correctly understand any trends discovered. The issue of biases is discussed further in Section 1.4.5. REXCESS has been used to study the radial distribution of cluster gas (Croston et al. 2008).

Serendipitous surveys have begun on the wealth of data from the two current X-ray observatories. The XMM Cluster Survey (XCS) is a project to analyse the XMM-Newton archival data. Sahlén et al. (2009) reported that XCS had obtained $\sim$ 2000 cluster candidates over 132 degree^2 using more than 2000 pointings, of which 125 have redshift measurements and > 500 counts. They made a conservative estimate of reaching

500 degree^2 with the XMM-Newton mission lifetime extending to 2013. The catalogue is expected to be used to constrain cosmological parameters and scaling relations.

Modern serendipitous surveys consider using large-scale automated routines for their analysis due to the large volume of data. The procedures established to analyse the data are often known as a pipeline, with new information being gained at each stage. When conducting a survey of this nature it is important to make sure the observing conditions of each pointing are accounted for correctly. The analysis process needs to have a way of determining background affecting the image, and requires accurate PSF models for the relevant observatory. If pointings performed with multiple observatories are to be used, the pipeline also needs to be able to handle the raw data from each one, which may be formatted differently.

1.4.4 Deep Surveys

In comparison to the surveys mentioned previously, deep surveys focus their available exposure time over a much smaller number of fields. This can allow them to detect fainter and higher-z objects. The XRB is still a limiting factor, but the effect of Poisson noise is reduced, and the smaller field of study can permit them to avoid regions of high local XRB, which varies in intensity in different parts of the sky (Markevitch et al. 2003). Unfortunately, covering such a small area can result in the sample being biased by the underlying large scale structure, which is particularly important to remember when surveying the cluster mass function to constrain cosmology.

Two extremely deep surveys were Chandra Deep Field North (CDFN) (Brandt et al. 2001) and Chandra Deep Field South (CDFS) (Giacconi et al. 2002), each only covering 0.11 degree^2. These reached flux limits of 3.1×10^{-16} and 9.5×10^{-17} erg cm^{-2} s^{-1}, finding 6 and 19 clusters using VTP and WAVDETECT, respectively. Observations in the $2-10$ keV energy band have resolved a significant amount of the cosmic XRB, confirming that most of the contribution in this band was caused by unresolved AGN (Gilli 2003). Chandra deep surveys have been used to probe AGN properties and redshift distributions

Table 1.1: Summary of the survey examples given here. Brackets for WARPS indicate the statistical sample.

Survey	Observatory	Area (deg^2)	Sources	Confirmed Clusters	Flux limit (erg cm^{-2} s^{-1})
EMSS	Einstein	778	835	93	1.33×10^{-13}
RASS	ROSAT	All sky			5×10^{-15}
XMM-LSS	XMM-Newton	5.2		29	1.1×10^{-14}
COSMOS	XMM-Newton	2.1		72	3×10^{-15}
RDCS	ROSAT	48	160	70	4×10^{-14}
RIXOS	ROSAT	20.4	385	264	3×10^{-14}
WARPS	ROSAT	72.9(70.8)		159 (124)	$3.5\ (6.5) \times 10^{-14}$
160d	ROSAT	158	203	98%	2×10^{-13}
400d	ROSAT	397	287	93%	1.4×10^{-13}
Southern SHARC	ROSAT	17.7		35	3.9×10^{-14}
Bright SHARC	ROSAT	178.6	374	40	1.63×10^{-13}
REFLEX	ROSAT	13924		447	3×10^{-12}
XCS	ROSAT	132	> 2000	125	
CDFN	Chandra	0.109		6	3.1×10^{-16}
CDFS	Chandra	0.109	346	19	9.51×10^{-17}

(Georgakakis et al. 2006). The purpose of some deep surveys is to obtain detailed X-ray data for a single structure, such as a star cluster (Pillitteri et al. 2006). Larger deep surveys have been used to produce useful statistical samples with a low flux limit. For example, a survey with ROSAT has been used to constrain Ω_m using the evolution of cluster luminosity distributions (Borgani et al. 2001).

An important effect that needs to be considered when performing long exposures is source confusion. At first, increasing the exposure time will decrease the limiting flux. However, the effect of angular resolution eventually becomes significant. Once this confusion limit is reached, sources will start to be missed. Two sources in close proximity on the sky may fail to be resolved from each other. Higher angular resolution results in a more clear separation of the components of the XRB, allowing a lower limiting sensitivity to be reached before source confusion takes effect. Separating sources is also important to obtain more accurate data about an otherwise contaminated object.

1.4.5 Survey Bias

A summary of the survey examples given above is compiled in Table 1.1, and their flux limits are shown in Figure 1.12. While these flux limits are sometimes associated with the

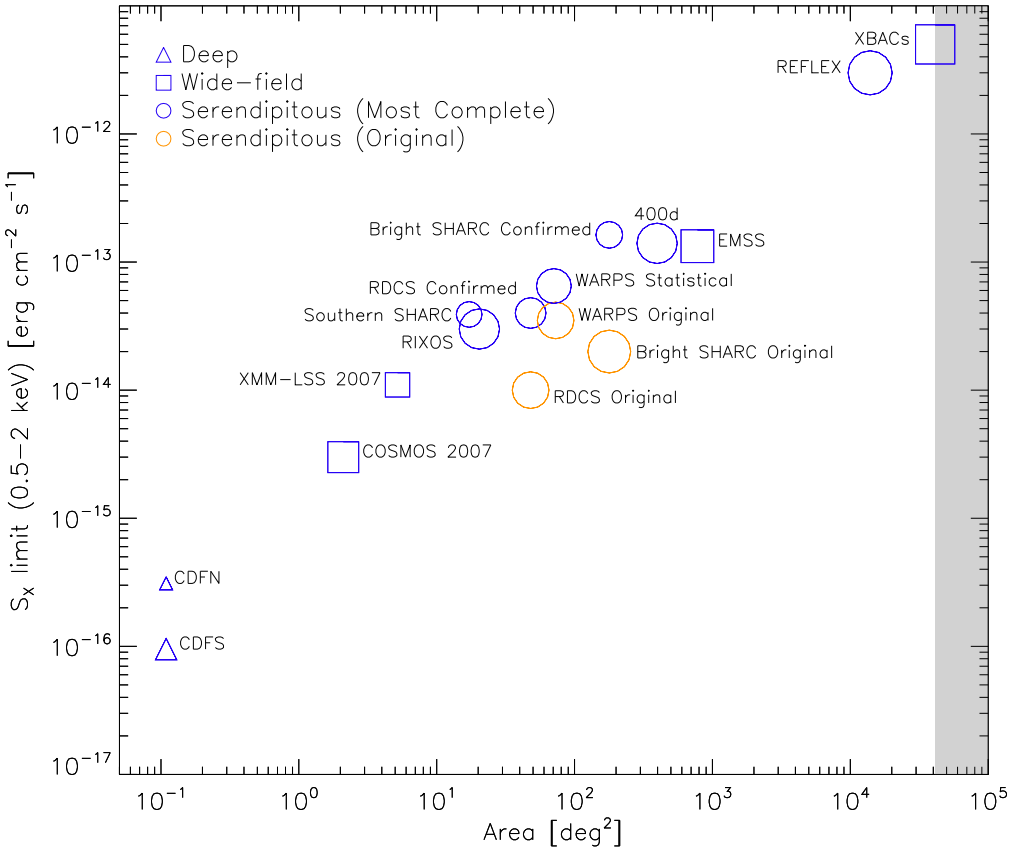

Figure 1.12: Plot of flux limit against area for several X-ray surveys. Triangles, squares and circles represent the surveys classified here as deep, wide-field and serendipitous, respectively. The most complete samples stated in the publications are indicated in blue, while the original sample selections are shown in yellow. Flux limit for the original sample is usually the flux of the faintest cluster. Symbol size has been scaled logarithmically by the number of sources. Note that the error in the flux measurements is higher for surveys conducted with ROSAT than those performed by the modern observatories.

faintest detected source, many surveys place flux cuts at a level where they consider the survey statistically complete. When conducting a survey it is important to understand the nature of its flux limit so the use of the data is statistically meaningful. It is unlikely that the survey has detected all of the clusters that are brighter than the faintest system. The reasons for this are described below.

It is obvious that performing X-ray follow-ups of clusters that have been optically selected produces a sample that is not representative of an X-ray population. Those conducting X-ray selected surveys must take care when making judgements about how effectively the surveyed area has been covered, known as sky coverage. This is often stated

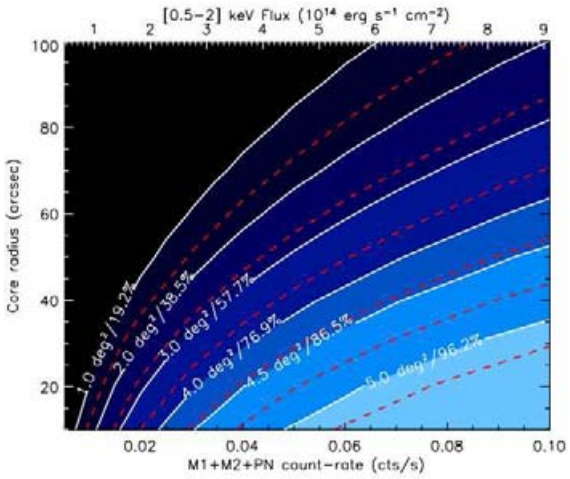

Figure 1.13: XMM-LSS coverage is displayed in a 2D parameter space: the sky coverage is a function of both cluster flux and extent. The dashed lines are the result of extensive 10ks simulations. The slightly shifted white lines are the analytical corrections accounting for exposure variations across the surveyed area, hence indicating the effective selection function of the current data set. The sample completeness corresponding to each line is indicated in terms of both the sky coverage and the percentage of detected sources. Extent values correspond to the core radius of a β-model with $\beta = 2/3$. The count-rate to flux conversion assumes a 2 keV spectrum at $z = 0$. Figure and caption taken from Pacaud et al. (2007).

as a function of the limiting flux. To calculate the sky coverage, an astronomer must take into account many factors such as exposure time, background levels, vignetting and the off-axis PSF. The true extent of some groups and clusters can be difficult to quantify sometimes due to background noise in the image, with only their brighter centres being resolved. This means that the detection of extended sources is not only limited by flux but also by the surface brightness distribution of the emission. All of these factors determine the selection function of a survey - the probability of detecting a cluster with a certain set of properties and with certain observational parameters (such as exposure time and background).

Understanding the selection function has started to become a serious issue for surveys. The primary limit for XMM-LSS is surface brightness, rather than flux. Simulations were used to map the cluster selection function for a range of count rates and angular core radii, using a fixed physical radius and slope, creating an assumed selection function (see Figure 1.13). XCS have attempted a more thorough parametrisation of the selection function. They find the statistical likelihood of a particular catalogue of clusters from a

model which includes many factors such as the mass function, scaling relations and the distribution of errors in T and z. REXCESS are attempting to control their selection function by using a well defined and understood sample.

Systematic effects from observational selection are often referred to as Eddington or Malmquist bias due to their work on the subject (Hendry et al. 1993; Eddington 1913; Malmquist 1920). Consider two luminosity-based source populations with scattered luminosity distributions that overlap. If more sources are present in one population, the size of that population may be underestimated due to the more systems scattering out than scattering in. This is Eddington bias. Another consequence of scatter is the possibility of overestimating the mean luminosity due to a portion of the (scattered low) distribution being too faint to detect.

Some of the problems that can occur from failing to correctly account for the selection function when studying the $L_{\rm X} - T$ relation are illustrated by Pacaud et al. (2007). For example, only the most luminous part of the low luminosity end of the $L_{\rm X} - T$ relation may have been adequately sampled, causing a bias. The majority of the detections are sources which are above the mean. Observations of the $L_{\rm X} - T$ relation produce a shallower slope than in reality, as illustrated in Figure 1.14.

This bias moves higher up the $L_{\rm X} - T$ relation at higher redshifts due to the detection limit moving to higher $L_{\rm X}$. Therefore, when the $L_{\rm X} - T$ relation includes a range of different redshifts the combination of the slope bias across the relation creates a bias towards a higher normalisation. Increasing the redshift range of a sample would reduce the slope bias but increase the normalisation bias. The bias also affects the recovered evolutionary trend.

Another problem which affects studies is Malmquist bias, the trend to detect more luminous systems at higher redshift. More luminous systems are easier to detect at higher redshift, and therefore they are sampled over a larger volume. This makes them appear more numerous than they actually are, compared to the fainter systems. This does not apply to volume-limited samples.

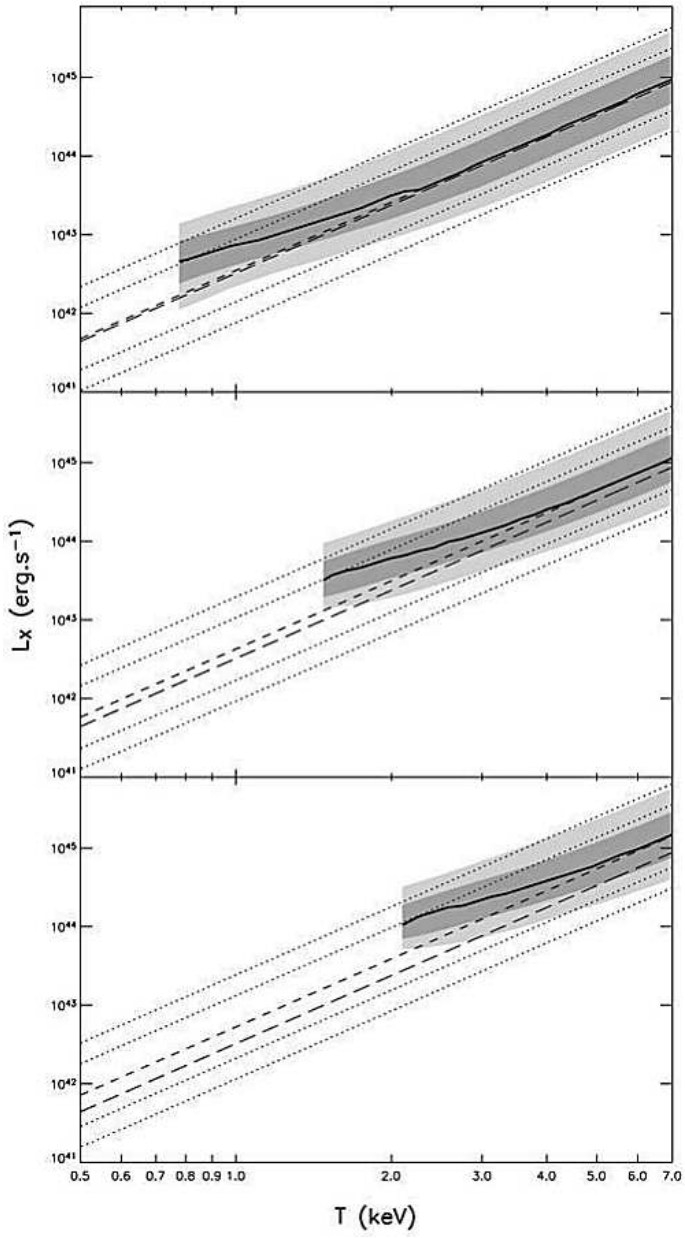

Figure 1.14: Comparison of the Pacaud et al. (2007) modelled $L_{\rm X} - T$ distribution with and without selection effects for several redshifts, assuming self-similar evolution. The light and dark shaded regions show, for each temperature, the luminosity interval that contains respectively 95.5 and 68.3% of the expected detections. The solid line gives the maximum of the luminosity PDF for each temperature; it is cut at the temperature for which the detection probability (integrated over $L_{\rm X}$) falls to 5%. For comparison, the local Arnaud & Evrard (1999) relation, evolved according to the self-similar model, is indicated by the short dash line, and the 1 and 2 bounds arising from the scatter model are shown by dotted lines. The long dash line is the local relation. Figure taken and caption adapted from Pacaud et al. (2007).

Cosmological distance also affects the observed size of a cluster, which would change its detectability. All these biases lead to a misleading amount of evolution in the $L_X - T$ relation. Both luminosity and size are linked with cluster mass, which evolves with time, further complicating matters. It is clear that creating and applying an assumed selection function is necessary to make reasonable judgements about an observed population, but the quality required of this correction and how close it needs to be to the true survey selection function are unclear.

1.4.6 Surveys with IXO

When the IXO observatory is operational it will allow for X-ray surveys of even greater quality to be performed. The WFI will have a smaller field of view than Chandra and XMM-Newton, so the practical area of the sky that a wide-field survey could cover would be further reduced from that of the previous observatories, if the same exposure times were used for a pointing. However, the significant increase in effective area would allow much shorter pointings when conducting a survey of a certain limiting magnitude, compensating for the difference in the field of view, and also reducing particle contamination in the observations. If similar duration pointings to those in previous wide-field surveys were to be used, then the increased effective area whilst maintaining good angular resolution will allow fainter detections within the survey, as well as producing higher quality data for the brighter sources. When performing deep surveys, IXO will be able to see out to greater redshifts than ever before, hopefully revealing the first AGN in the Universe. The spectral instruments could provide detailed follow-up data on objects detected in surveys.

Part of the preparation for IXO should be to predict its selection functions. Only with this knowledge can large samples of data be used to make statistically valid conclusions about the state of the Universe at different epochs. One of the aims of this research is to generate a cluster selection function for IXO and to understand its effects on the study of cluster evolution.

It is the scientific goals of the IXO mission, such as those mentioned at the end

of Section 1.3.7, that drive the technical capabilities which are being worked toward (see Appendix B.2). The effect of the instrument properties on the studies of evolution of galaxy clusters and feedback is another focus of this research. The IXO technical requirements may be ambitious, but they will help push back the boundaries of the X-ray exploration of the Universe.

CHAPTER 2

Image Simulation

The focus of this work is the science that can be performed with X-ray images. To facilitate this the X-ray Image Suite (XIS) has been developed. This powerful collection of tools includes an image simulator and a source identification process. The simulator is designed to represent current and future X-ray observatories. Of particular interest is the predicted output from the IXO Wide Field Imager (WFI), the most effective instrument of those proposed for IXO for imaging galaxy clusters. In this chapter I present the simulator component of XIS, which is customised to represent the current design of the WFI and is adaptable to future developments.

The output of an X-ray observatory is, overall, dependent on two very different factors: the X-ray emitting sources that populate the sky, and the properties of the mirrors and detectors within the observatory. This chapter covers the simulation of both factors, dividing the former into galaxy clusters (the sources of interest) and other X-ray sources. Also described are some of the programmed structures and algorithms used to implement a simulation.

The simulator is designed to facilitate the objectives of this research. One of these is to predict the cluster selection function for IXO and use it to determine the bias

when recovering scaling relations. For a practical method of creating a detailed selection function, control over the cluster properties is required. Study of survey bias requires creating a simulated cluster population which is strongly supported by both theoretical and observational research. Another objective is to study how varying the technical specifications of IXO would affect the quality of cluster imaging. This requires flexibility in the simulation process, with the option of changing important instrument properties. The result is a highly adaptable X-ray image simulator, which will now be described.

2.1 Implementation

Before delving into the scientific basis for each element of the simulator, this section gives a brief overview of its structure and the tools used in its construction.

2.1.1 Interactive Data Language

All of the programmed routines used in the simulator, and the majority of those used in XIS, are written in the Interactive Data Language (IDL). The language has been developed for easy handling and analysis of data, and has proven popular in space science. IDL is vectorised, which allows rapid processing of multi-dimensional arrays, hence it is useful in image processing. It also includes object-orientated programming features, flexible graphical capabilities, and a wide variety of statistical tests. The Astronomy User's Library (AUL) (Landsman 1993) is used for line fitting and FITS file handling. FITS files are used to store simulated images and data structures.

Line fitting in this research is performed using Bayesian approach to linear regression included within the AUL (`LINMIX_ERR`, see Kelly 2007). This is an orthogonal regression method that uses Markov Chain Monte Carlo (MCMC) to sample the posterior distribution via Gibbs sampling. When this method is applied to a dataset, the standard deviation of that dataset is assumed to follow a single Gaussian distribution.

A further set of statistical routines used in the development of XIS are `MPFIT` and

its related routines (Markwardt 2009). `MPFIT` performs least-squares fitting using the Levenberg-Marquardt technique. This is an iterative procedure which uses the gradient of the function with respect to the free parameters to step those parameters from their initial guesses to a solution. The process allows parameters to be limited and fixed as required.

2.1.2 Simulator Design

In its simplest form, the simulator needs to take an expected distribution of X-ray sources and convert it into an image. Further development of this idea depends on what the simulator needs to achieve. Two overall goals have been established for this research: predict the IXO cluster selection function for the current IXO design, and discover what impact changing the design of IXO's instruments has on cluster detection. To accomplish these, we define the following goals:

- include a representation of the Universal cluster population that agrees with the observed flux distribution;
- include masses on group scales, out to $z \sim 3$;
- use observed cluster scaling relations, but be free to alter them;
- have the capability to create clusters with customised properties;
- include the observed distribution of X-ray flux which is in the form of point sources;
- use a reasonable prediction of the response of IXO to an X-ray photon in the $0.5 - 2$ keV energy band, in which cluster emission has the strongest contrast;
- include estimates of significant time-independent background signals;
- include all significant image degradation caused by the observatory (e.g. the PSF);
- have the capability to alter several key observatory properties which affect the image quality;

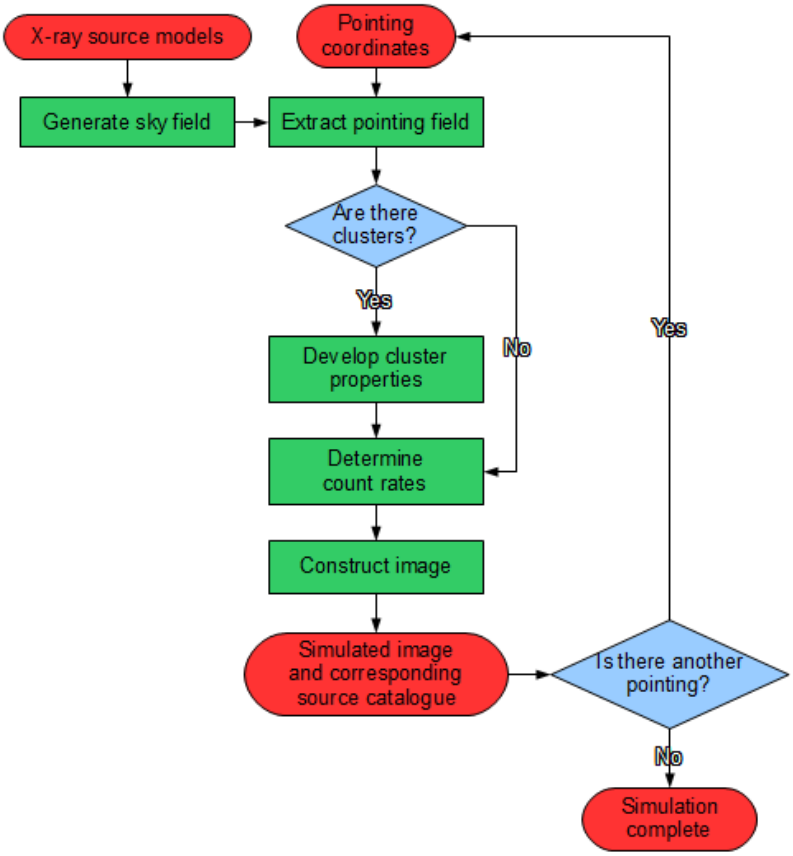

Figure 2.1: An overview of the process by which simulations are generated.

- have the capability to automatically create multiple simulations with different centres and exposure times (i.e. different pointings).

The ways in which the simulator achieves these goals are explained throughout this chapter.

The simulator is structured into five stages. The first stage is the creation of a simulated distribution of X-ray sources on the sky, which is referred to as a 'sky field'. It consists of thousands of sources which are each described by numerous properties. These sources can be drawn from an analytical model, a survey catalogue or another simulated distribution. The second stage involves the extraction of a chosen sub-field from the sky field, which is known as a 'pointing field'. This only includes sources that are required to generate a simulated pointing at that location. In the third stage the properties of the

clusters in the pointing field are expanded on using a number of observationally supported relations and cosmological effects. The fourth stage consists of modelling the spectral profiles of each source and calculating the response of the observatory. Finally, the fifth stage constructs an image by combining all of the pointing field sources onto an array resembling the detector layout while applying any instrumental effects. If multiple pointings have been input, the simulator repeats all relevant stages. A flowchart summarising the overall design of the simulator is shown in Figure 2.1. Data structures used to control its operation are defined in Appendix D.

Due to rapidly developing constraints on cosmological parameters, the simulator is designed to operate with H_0, Ω_m, Ω_Λ and σ_8 as variables. The default values used for these parameters are based on constraints from numerous studies (see Section 1.3.1): $H_0 = 70.4$ km s^{-1} Mpc^{-1}, $\Omega_m = 0.272$, $\Omega_\Lambda = 0.728$ and $\sigma_8 = 0.809$ (hereafter the XIS cosmology). For a significant reduction in complexity, the simulator uses cosmological formulae that assume a flat Universe (curvature $k = 0$). Observational constraints support a curvature extremely close to zero (Komatsu et al. 2010).

The number of sources processed for a particular pointing depends on the field of view of the observatory configuration. For efficiency, only sources which appear within the field of view are simulated. Some clusters with centres away from the field of view could extend into the visible region. To include such clusters an extraction field is defined. The radius of this field is set to 2 arcmin greater than the field of view. Once the cluster radii have been calculated, any clusters which have no emission within the field of view are removed from the source list for the pointing.

2.2 Clusters

In this section we cover how the simulated X-ray emission from galaxy clusters is derived. The initial cluster mass and position distribution is created by extracting dark matter halos within a lightcone through a cosmological simulation. Scaling relations are used to

calculate baryonic properties such as temperature and surface brightness profiles.

By using a mass distribution instead of a luminosity distribution, cluster temperatures are obtained using the $M - T$ relation rather than the $L_{\rm X} - T$ relation, which appears to have higher scatter (see Section 1.3.3). This improves the accuracy of all properties which relate to T. By using a theoretical mass distribution instead of an observed one, observational bias does not affect this aspect of the simulations.

An alternative would be to use gas simulations to produce the clusters and their baryonic properties. This would have the advantage of directly relating those properties to physical processes taking place. However, the number of possible mass distributions, scaling relations and evolutionary scenarios that could be explored would be limited to those that occur within the gas simulations. Use of custom scaling relations allows for more flexibility.

The cosmological effects of luminosity distance and angular diameter distance, appropriate for an expanding Universe, are included to appropriately calculate how these properties appear when observed. Finally, each cluster is given an isothermal spectral profile. For the purpose of simulations, groups are included within the category of clusters as the low mass, low temperature end of the parameter space.

A few useful overdensity scales were discussed in Section 1.3.2. Two of these are used in XIS to describe both the shape of the cluster and the scaling properties: $\Delta = 200$ and $\Delta = 500$. An overdensity region of $\Delta = 500$ with respect to the critical density is commonly used when measuring the baryonic properties of clusters through observations, as emission beyond this radius can be difficult to detect. Cluster parameters in XIS are those corresponding to $\Delta = 500$ unless stated otherwise. Logarithms are base 10 unless stated otherwise (e.g. as natural logarithm ln).

2.2.1 Cosmological Simulation

In a CDM Universe, the dominant mass component of a cluster is its dark matter halo. These halos are believed to grow from density perturbations in an otherwise smooth

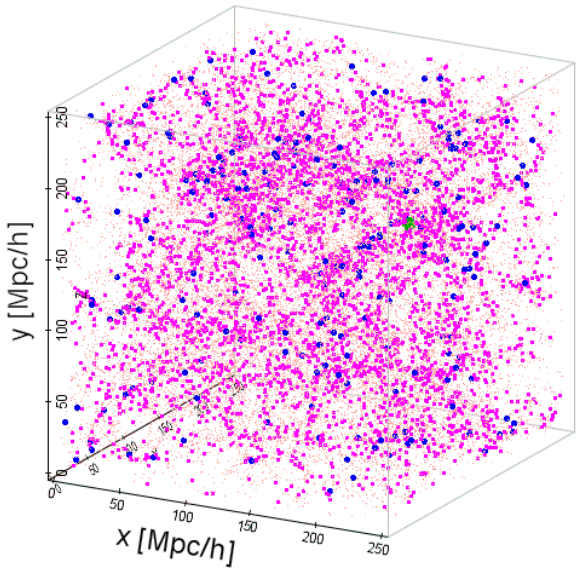

Figure 2.2: Distribution of halos within one-eighth of the Millennium Simulation $z = 0$ snapshot. The colour key is as follows: pink for $10^{12} < M_{200} \leq 10^{13}\ h^{-1}\ \mathrm{M}_{\odot}$, magenta for $10^{12} < M_{200} \leq 10^{13}\ h^{-1}\ \mathrm{M}_{\odot}$, blue for $10^{14} < M_{200} \leq 10^{15}\ h^{-1}\ \mathrm{M}_{\odot}$ and green for $M_{200} > 10^{15}\ h^{-1}\ \mathrm{M}_{\odot}$. The one green point is a halo of $M_{200} = 1.2 \times 10^{15}\ h^{-1}\ \mathrm{M}_{\odot}$.

distribution of matter after the Big Bang. The time scale over which these halos form and their distribution in mass has long been predicted by theory (Press & Schechter 1974). With improvements in the speed of computers, simulations using tens of thousands of particles were used to model this formation (Davis et al. 1985). An advantage of using one of these cosmological N-body simulations is that they produce a distribution of matter in space which comes from the simulated gravitational attraction between the particles, mimicking the structure of the Universe on both galaxy and cosmological scales. Outputs from these simulations are usually produced at a number of different cosmological times and are known as snapshots.

The last decade has seen the number of particles in cosmological simulations grow into the billions. In 2005 the Millennium Simulation (MS) was published (Springel et al. 2005). This was an N-body simulation of 10^{10} particles within a comoving cube 500 h^{-1} Mpc in length. MS dark matter halos were identified using a friends-of-friends algorithm (Davis et al. 1985) with a linking length of 0.2 times the mean particle separation. The number of particles gave it a mass resolution of $8.6 \times 10^{8}\ h^{-1}\ \mathrm{M}_{\odot}$. With this mass reso-

lution, halos with $M \geq 1.7 \times 10^{10}\ h^{-1}\ \mathrm{M}_{\odot}$ were well sampled at $z \leq 12$. This meant that mass evolution on galaxy scales was simulated thoroughly. See Springel et al. (2005) for a full description.

The MS is chosen as the source for the clusters masses and positions in the XIS sky field. It contains very well resolved group scale halos over the required redshift range, along with other benefits of cosmological simulation such as large scale structure. The final 37 snapshots of the cube are used, covering a redshift range of $0 \leq z \leq 3.06$ in the MS cosmology. The masses are used to generate X-ray properties using empirical scaling relations.

There are several issues with using the MS for this research. One of these is the absence of M_{500} masses in the halo catalogues, which provide masses as M_{200}. An estimation of M_{500} could be obtained by assuming a density profile, such as that of Navarro, Frenk, & White (1997) (NFW), along with a concentration for each halo. The concentration of a halo depends on the density of the Universe at the time of its formation and the accumulated mass since then. No concentration information available for the halos, so a different approach is required.

An empirical relation between M_{200} and M_{500} is derived from a related cosmological simulation. The Millennium Gas Simulations (MGS) are lower resolution re-simulations of the original MS with added gas dynamics (Gazzola & Pearce 2007; Hartley et al. 2008). The halo catalogues for the MGS have been generated for several overdensities, which include $\Delta = 200$ and $\Delta = 500$. We calculate M_{500}/M_{200} for every halo in each snapshot of the MGS. Halos from the $z = 0$ snapshot are used to determine the mass thresholds for 8 mass bins, with the number per bin inversely proportional to the mass. This gives ~ 5000 halos in the lowest mass bin and 17 in the highest. Defining $\mu = M_{500}/M_{200}$, a least-squares fit is performed on the $z = 0$ halos with a customised power law function, obtaining

$$\mu(M_{200}) = 16.54(\ln M_{200} - 22.83)^{-2.506} + 0.5387 \tag{2.1}$$

with a standard deviation of 0.01153. The 120 snapshots are divided into 5 redshift bins of

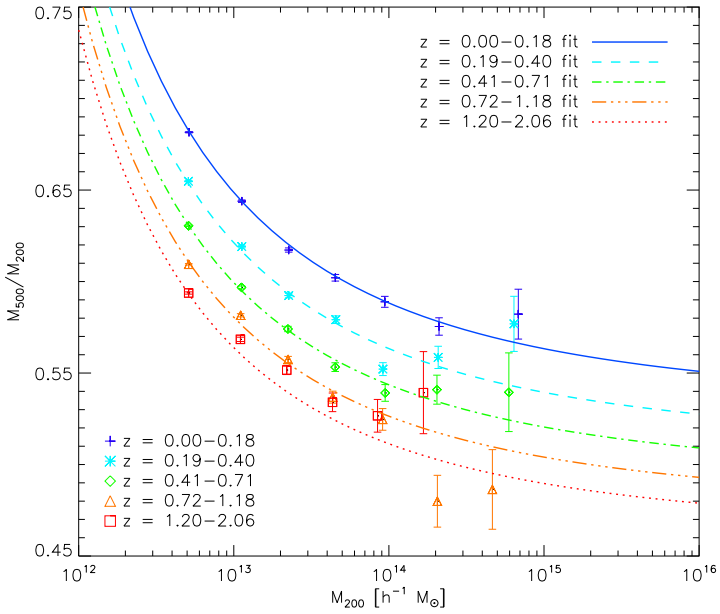

Figure 2.3: M_{500}/M_{200} as a function of M_{200} and redshift as found in the Millennium gas run (Gazzola & Pearce 2007). Data points mark the mean mass in each of the 5 redshift bins, and errors are the standard error on the mean. The increasingly broken lines show the fit to the data points as a function of increasing redshift.

equal number. The evolution of the mass conversion is then modelled by minimising the standard deviation between the 40 $\mu(M_{200}, z)$ bins and $\mu(M_{200})$ multiplied by a redshift dependent power law. This gives the function

$$\mu(M_{200}, z) = \mu(M_{200}) \times [0.1998(1+z)^{-1.517} + 0.8036] \tag{2.2}$$

with a standard deviation of 0.05403. The M_{500}/M_{200} bins and the evolving fit is shown in Figure 2.3. This function is used to estimate the M_{500} for all clusters. The fit becomes poorer with increasing redshift. It appears to underestimate M_{500} by $\sim 2\%$ for systems with $M_{200} \gtrsim 10^{13}\ h^{-1}\ \mathrm{M}_\odot$ at $z \gtrsim 1.2$.

Another problem using the MS is the accuracy of its space density of halos of different masses, known as the mass function. When the MS was created it used cosmological parameters that were based on evidence available at the time. These included $H_0 = 73$ km s^{-1} Mpc^{-1}, $\Omega_m = 0.25$, $\Omega_\Lambda = 0.75$ and $\sigma_8 = 0.9$. As discussed in Section 1.3.1,

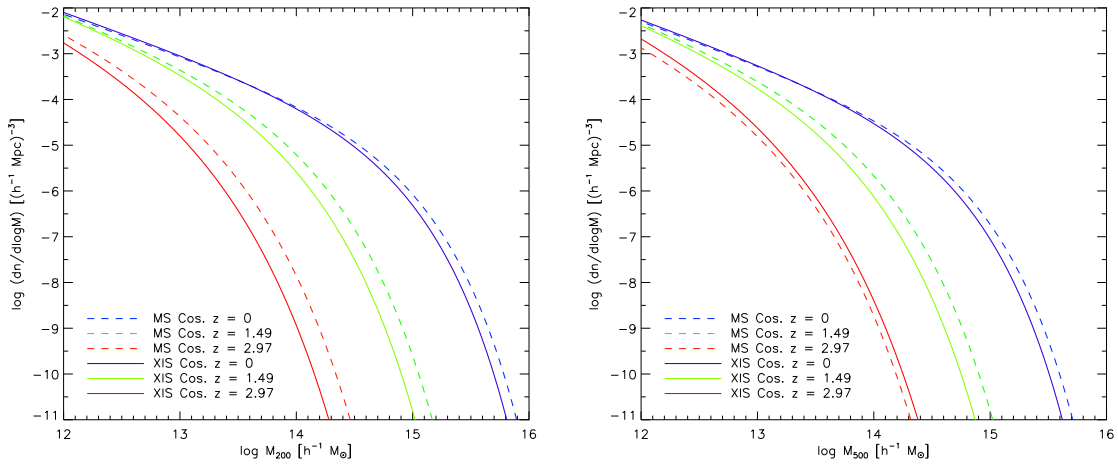

Figure 2.4: *Left:* Comparison of two different Tinker et al. (2008) halo mass functions with $\Delta = 200$. Solid lines represent the XIS cosmological parameters, while dash lines represent the Millennium Simulation cosmology. Blue, green and red indicate $z \approx 0$, 1.5 and 3, respectively. *Right:* The same as left but with $\Delta = 500$.

recent constraints indicate $H_0 = 70.4^{+1.3}_{-1.4}$ km s^{-1} Mpc^{-1}, $\Omega_m = 0.272 \pm 0.016$, $\Omega_\Lambda = 0.728^{+0.015}_{-0.016}$, $\sigma_8 = 0.809 \pm 0.024$ (Komatsu et al. 2010). This difference has a noticeable effect on the mass function. The number of massive halos is scaled upwards with increasing σ_8 and downwards with increasing Ω_m. Unfortunately, these parameters change the shape of the mass function in different ways and affect the spatial clustering of galaxies. Spatial clustering can be maintained at a fixed mass scale if $\sigma_8 \propto \Omega_m^{-0.5}$. However, this condition pivots the halo space density around $M \approx$ several $\times 10^{14}$ h^{-1} M$_\odot$, and the only way to realign the mass function is to change its slope or shape parameters (Zheng et al. 2002).

It is important to have a mass function that closely resembles reality as this affects the number of clusters expected in a particular survey and their flux distribution. The masses determine the baryonic properties of the clusters. The number of clusters and their size, which is also mass-related, affects the chance of contamination by point sources. Since it is difficult to correct the number density of halos without radically changing the large scale structure, the MS halo space density is adjusted by changing the mass of each halo.

To convert the MS mass function into one based on current cosmological constraints, a mass-dependent mass change is applied to each halo taken from the snapshots. The form of this mass change is taken from comparisons of the Tinker et al. (2008) mass function

model using the MS cosmology and the XIS cosmology with $\sigma_8 = 0.809$. Tinker et al. (2008) used simulations to calibrate their mass function to $\lesssim 5\%$ in the range $10^{11} \leq M \leq 10^{15}\ h^{-1}\ \mathrm{M}_\odot$, and derived it for a wide range of overdensities. The Tinker et al. (2008) mass function is used to calculate $\log(dn/d\log M)$ for 601 mass values in the range $11 \leq \log M \leq 17$. These overdensities are with respect to the mean matter density of the Universe $\overline{\rho}$, so the evolving mean matter density is calculated for the evolving critical density:

$$\overline{\rho}(z) = \overline{\rho_0}(1+z)^3 = \rho_{c,0}\Omega_{m,0}(1+z)^3 \tag{2.3}$$

$$\Delta'(z) = \Delta\frac{\rho_c(z)}{\overline{\rho}(z)} = \frac{\Delta(z)}{\Omega_{m,0}(1+z)^3}\frac{H^2(z)}{H_0^2} \tag{2.4}$$

where Δ' is the mean matter overdensity equivalent to Δ. The two mass functions are generated for $\Delta = 200$ and $\Delta = 500$ at 101 different redshifts in the range $0 \leq z \leq 4$, divided into equal comoving distances. Calculations are performed with an edited version of the Reed et al. (2007) mass function software.

In Figure 2.4 the MS and XIS mass functions are compared at both critical overdensities. In general the MS cosmology predicts more high mass halos. At $z \sim 3$ the MS cosmology gives fewer high M_{500} halos. This could indicate lower concentrations than in the XIS cosmology, or inaccuracies in the method that are significant at high redshift.

For each mass and redshift, the XIS mass that gives the MS value of $\log(dn/d\log M)$ is found using logarithmic interpolation, and then used to calculate $M_{\mathrm{XIS}}/M_{\mathrm{MS}}$. This correction is then applied to both of the mass scales.

The difference between the MS mass function models and the MS snapshots can be seen in Figure 2.5. There is a slight disagreement for M_{200} and a more significant one for M_{500}. Since only the change in the mass function is required, these disagreements do not prevent the correction from being applied. However, it is important to apply the correct amount of mass shift. Therefore, $\log M_{200} + 0.06$ is used to calculate the magnitude of the correction to better align with the model. For $\log M_{500}$ the disagreement increases

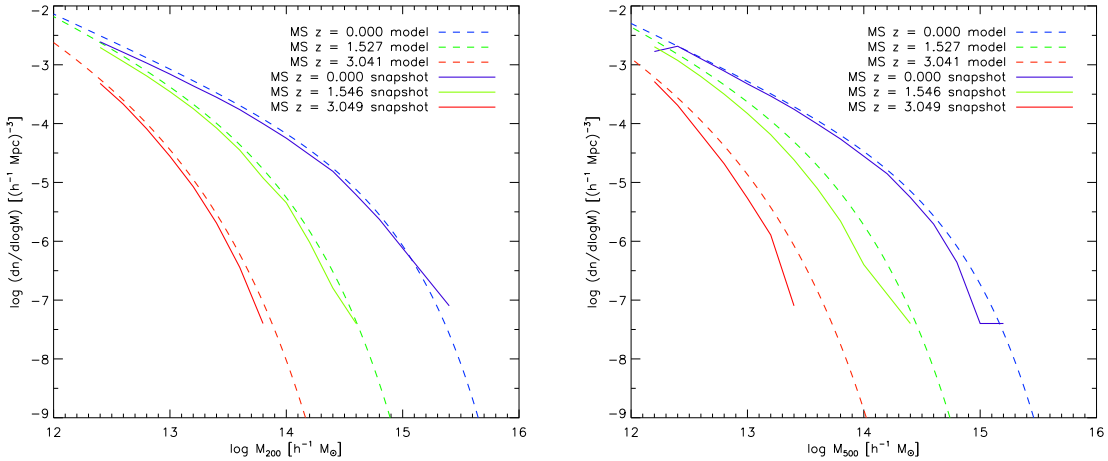

Figure 2.5: *Left:* $\Delta = 200$ comparison of the MS snapshots with the Tinker et al. (2008) halo mass function model using the MS cosmological parameters. Solid lines represent the snapshots, while dashed lines represent the mass function model. Colours as Figure 2.4. *Right:* The same as left but with $\Delta = 500$.

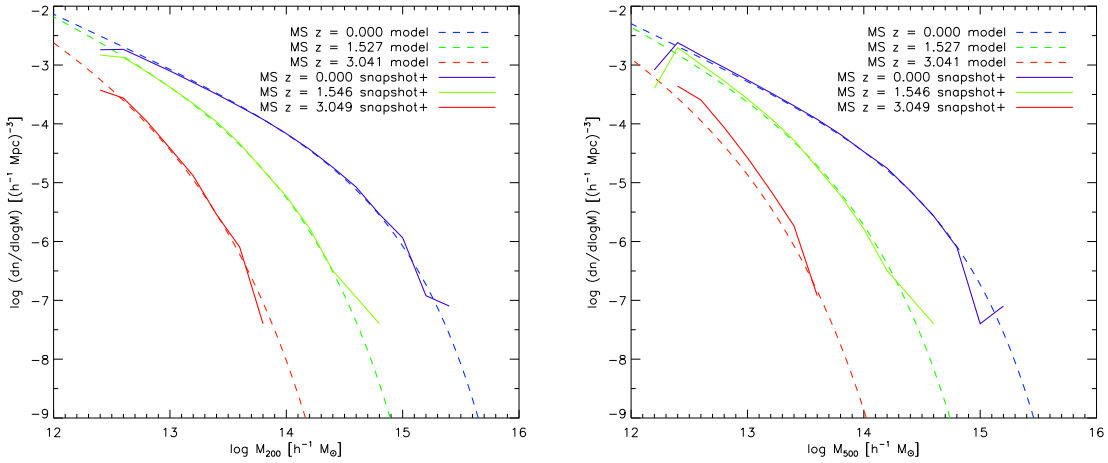

Figure 2.6: As Figure 2.5, but with snapshot masses rescaled by $\log M_{200} + 0.06$ and $\log M_{500} + 0.06(1+z)$. These changes are not permanently applied to the simulated masses, they are used to calculate the amount of mass function correction to apply.

with redshift, so an artificial addition of $0.06(1 + z)$ is used. Again, these 'corrections of corrections' are only used to determine the amount of mass shift, the shift itself is applied to the original MS halo mass. The effect of these corrections is shown in Figure 2.6.

The mass function-corrected MS snapshots can be seen in Figure 2.7, which is expected to have a similar shift to Figure 2.4. There remains a slight under-correction of high M_{500} masses at high redshifts, which would result in a slight lack of distant clusters too large

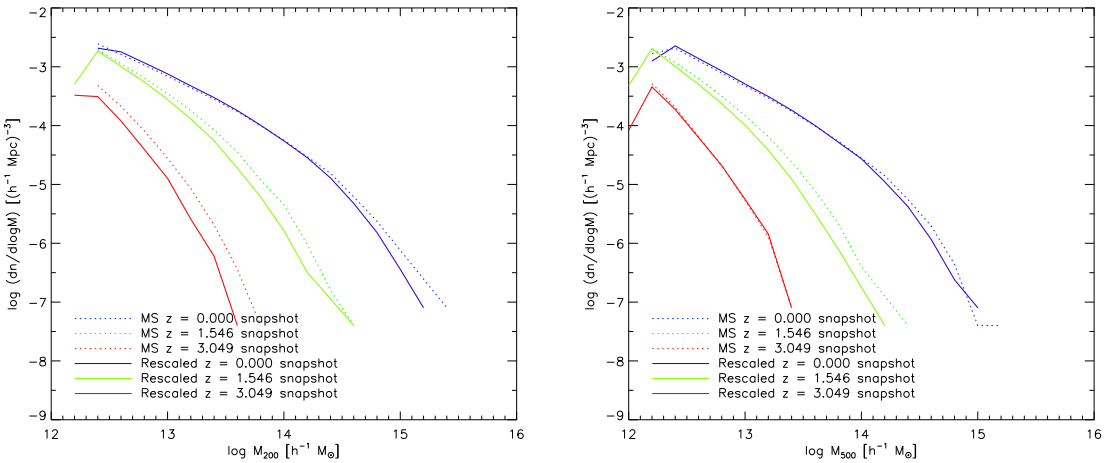

Figure 2.7: *Left:* $\Delta = 200$ comparison of the MS snapshots before and after correction using the M shift in Figure 2.4. Solid lines represent the corrected snapshots, while dotted lines represent the original snapshots. Colours as Figure 2.4. *Right:* The same as left but with $\Delta = 500$

and bright. However, accuracy of the XIS mass function at this stage is questionable as indicated earlier.

With the differing behaviour of the high redshift models for the two overdensities, the corrected M_{500} is greater than M_{200} at very low masses. To prevent this, M_{500}/M_{200} is never allowed to become greater than the $z = 0$ value (i.e. the maximum) at the mass cut selected for simulation.

Using a non-uniform scaling of mass affects the accuracy of a simulated distribution of clusters. The halos would have different relative velocities, leading to different positions in the snapshots and different merging times. However, for the purpose of this research, which deals with cluster detection, it is more important to have an accurate mass function than accurate cluster positions. Positions do not need to be rigorous, it is the masses that matter as they determine the baryonic properties of the clusters. The adjusted MS still provides a reasonable representation of the cluster spatial distribution.

It should be noted that the MS includes no baryon physics, only gravitational physics. Baryon physics can have an effect on the halo mass function. This was evidenced by Stanek et al. (2009) in the MGS. When comparing the gravitational-only simulation with one which included preheating, they saw a 15% suppression in the halo masses

at 10^{-14} h^{-1} $M_\odot$ due to a reduction in their baryon fraction. However, estimates from a simulation which includes cooling and star formation predict an enhancement of halo mass, caused by an increased baryon fraction and subsequent deepening of the potential well. With feedback processes also taking place, the truth likely lies between these two models. No evidence is available to suggest the magnitude of this correction, so the effect of baryon physics on the halo mass function is not modelled within the XIS simulator.

Only halos with $M_{500} \geq 2{\times}10^{12}$ h^{-1} $M_\odot$ are included in XIS simulations. This excludes typical galaxies, so that the scaling relations are applied to just groups and clusters. This is discussed further in Section 2.3.1.

2.2.2 Lightcones

A lightcone is constructed to transform the halo catalogues from each MS snapshot into a distribution of masses on an observed sky. Lightcones represent a distribution of sources in four-dimensional space-time, taking into account the time taken for emitted photons to cross the distance to the observer. A more distant source will be viewed at a higher redshift, determined by the cosmology. The method used to create a lightcone is based on that used by Kitzbichler & White (2007) to produce simulated observations of galaxies from the MS.

Before constructing a lightcone it is necessary to understand how cosmology affects distance scales. Section 1.3.1 introduced the concept of comoving space. The line-of-sight comoving distance to an object can be found by integrating all of the distance contributions along a light ray between it and $z = 0$. For a ΛCDM Universe with zero curvature, the line-of-sight comoving distance to an object

$$D(z) = \frac{c}{H_0} \int_0^z \frac{\mathrm{d}z'}{E(z')} \tag{2.5}$$

where c is the speed of light, z' is the redshift of the redshift interval dz', and

$$E(z) = \sqrt{\Omega_m(1+z)^3 + \Omega_\Lambda} \tag{2.6}$$

(Hogg 1999). Expressed in terms of h, the constant $c/H_0 \equiv 2.998 \times 10^3\ h^{-1}$ Mpc. A similar method can be used to find the lookback time t_L for a given redshift:

$$t_L(z) = t_H \int_0^z \frac{\mathrm{d}z'}{(1+z')E(z')} \tag{2.7}$$

For consistency with the change in cosmology applied to the mass function, the lookback time for each snapshot is converted to a redshift using the XIS cosmology. Hence the redshift given here for each snapshot is slightly different to that in the MS database.

The Millennium Simulation snapshots represent the matter within a comoving cube, 500 h^{-1} Mpc on each side. Under the XIS cosmology, a lightcone 'drawn' through the length of a snapshot would reach $z = 0.173$. With clusters observed to $z > 1$, simulated cluster masses present at $z > 2$ and group masses at $z > 3$, this redshift limit is obviously inadequate. Kitzbichler & White (2007) dealt with this problem by progressing the lightcone through a periodically replicated grid of simulated cubes, at an angle that would avoid reusing the same region for several cube lengths. A similar approach is followed for XIS and is described in detail in Appendix A.1. While this method limits the amount of structure replicated, it still results in a discontinuity in large scale structure every time the cube is reused. Therefore, it would be inappropriate to use this method in a study that focuses on large scale structure.

Each MS snapshot has a redshift, which is equivalent to a comoving distance from the point of observation. When searching for halos that belong in the lightcone, the process always uses the MS snapshot with the comoving position nearest to that of the lightcone. This relates the properties of the halos to their position within the lightcone and their observed redshift. When the lightcone would traverse a previously used region of the MS the cube is rotated. Therefore, no structure is viewed more than once from a particular

angle.

The output of the lightcone construction process is a halo catalogue with Right Ascension (RA), Declination (Dec), D, z, M_{200} and M_{500}, referred to as the cluster sky field. This work uses lightcones which have an area of 4.77×3.18 degree^2 and reuses regions of the MS at $z > 1.80$. Four lightcones are generated, originating from a different corner of the MS. One for the studies in Chapter 4 and Chapter 5 another is for source identification method calibrations, referred to as primary and secondary, respectively. The other two are to increase the sample size for the cluster population checks in Section 2.2.8. The maximum M_{500} within the sky fields are 2.52×10^{14} and 3.41×10^{14} h^{-1} $\mathrm{M}_{\odot}$, respectively. The lightcone of the primary sky field is shown in Figure 2.8 and Figure 2.9.

As a consistency test between the sky field and the expected cluster space density, one can count the number of low redshift halos. By assuming the mass function of the $z = 0$ snapshot approximates that in the range $z < 0.5$, then above the mass cut one expects $N(> M) \approx 10^{-3}$ h^3 Mpc^{-3}. The comoving volume within the full sky out to $z = 0.5$ is approximately 10^{10} h^{-3} Mpc^3. The sky field represents 0.037% of the sky and hence contains a volume of $\sim 3.7 \times 10^6$ h^{-3} Mpc^3. This gives an expected halo count of $N(z \leq 0.5) \sim 3700$. Within the primary sky field $N(z \leq 0.5) = 3971$, whilst the secondary sky field has $N(z \leq 0.5) = 3413$. This confirms that the mean cluster space density within these lightcones is reasonable.

2.2.3 Cluster Radii

Cluster size is usually defined by an overdensity with respect to the critical density

$$\rho_c(z) = \frac{3H(z)^2}{8\pi G} \equiv 277.3 \left(\frac{H(z)}{100}\right)^2 \ \mathrm{M}_{\odot}\ \mathrm{kpc}^{-3} \tag{2.8}$$

where G is the gravitational constant. This convention is followed in XIS, allowing the radius of a cluster to be derived from the masses provided by the MS. Assuming spherical symmetry, the radius of a cluster within a given overdensity can be found from its mass

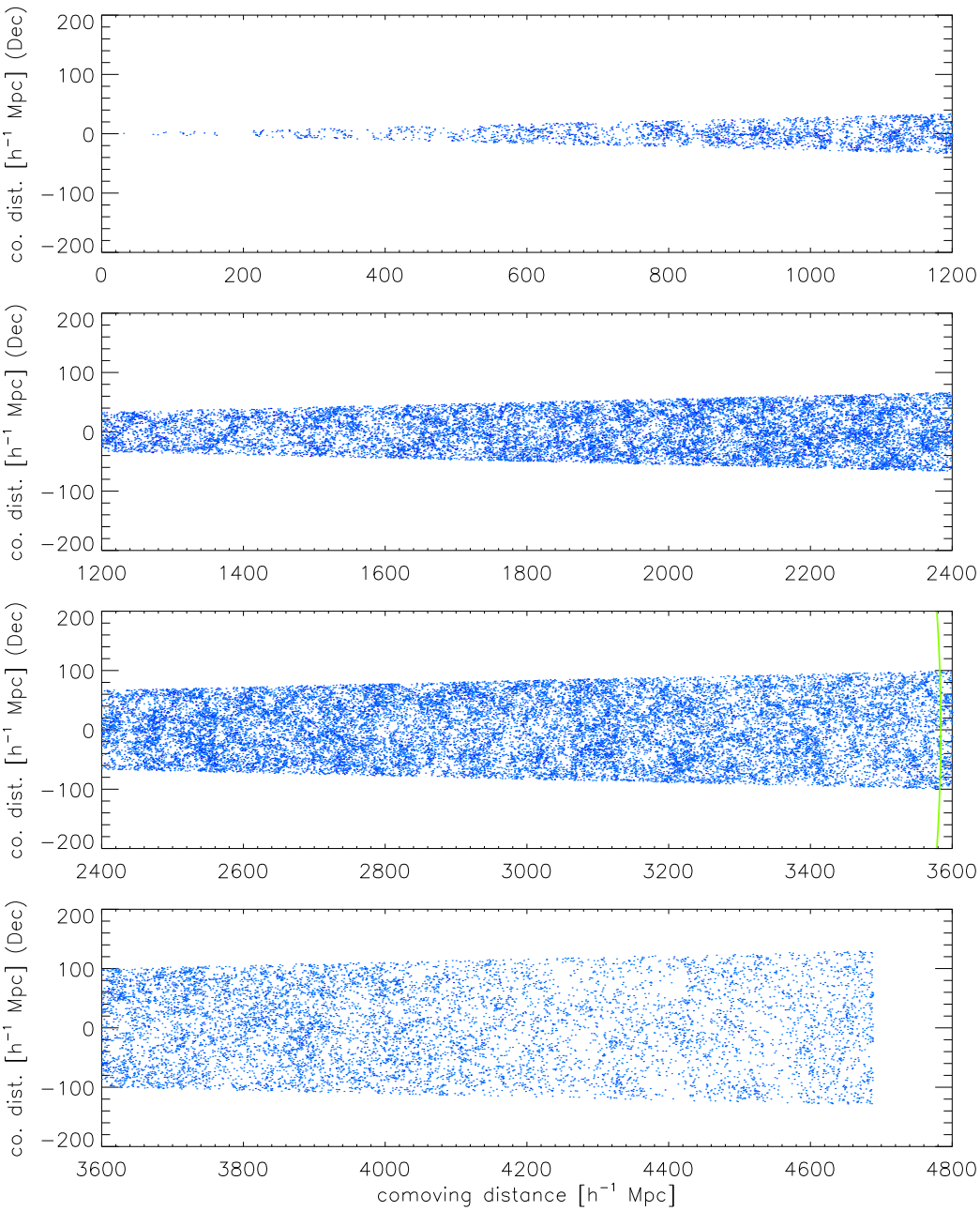

Figure 2.8: The cluster halo lightcone drawn through the Millennium Simulation which forms the XIS primary cluster sky field, as seen 'side-on' (i.e. viewed along its Right Ascension axis). The solid line indicates the distance at which the simulation had to be rotated before re-use. Colour scale of clusters from light blue to dark blue is proportional to $\log M_{500}$.

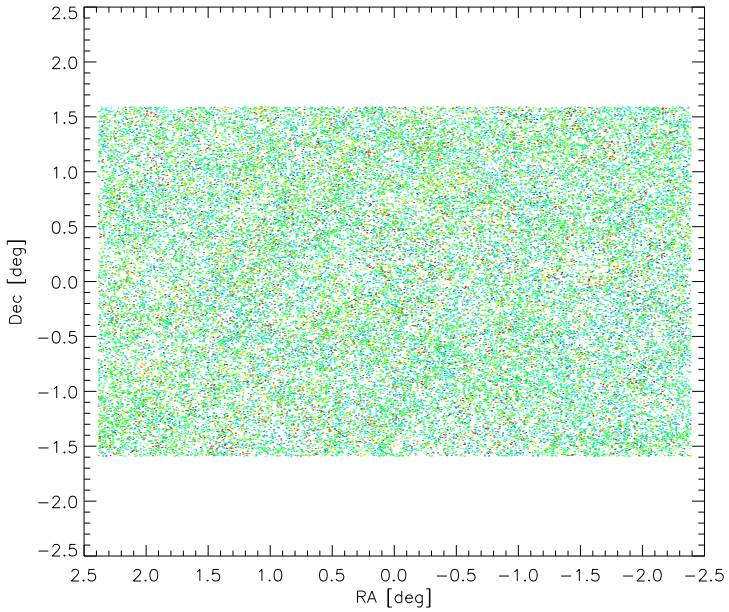

Figure 2.9: Angular distribution within the primary cluster sky field (i.e. the lightcone from an observer's point of view). Colour scale of clusters from blue to red indicates redshift.

and redshift:

$$R_\Delta = \left(\frac{3M_\Delta}{4\pi\rho_c(z)\Delta} \right)^{1/3} \tag{2.9}$$

where M_Δ is the mass within overdensity Δ. Both the R_{200} and R_{500} radii of the clusters are calculated. R_{200} is used as the extent of the cluster surface brightness profiles, which describe the shape given to emission from the clusters.

2.2.4 Scaling Relations

A set of four empirical scaling relations are used to relate several of the baryonic properties of a simulated cluster to its temperature and redshift. Two of these were discussed in Section 1.3.3: mass-temperature $M_{500} - T$ and luminosity-temperature $L_{\mathrm{X},500} - T$ (hereafter $L_{500} - T$). The other two represent trends found in observed surface brightness profiles: fractional core radius-temperature $r_{cf} - T$ and surface brightness profile slope-

temperature $\beta - T$. The first three of the scaling relations take the form:

$$\log X = \log \left[N \left(\frac{T}{P} \right)^{\alpha} (1+z)^{u} E(z)^{v} \tau(z)^{w} \right] \pm \sigma_{\log X} \tag{2.10}$$

where X is the temperature-related cluster property, T is its temperature, z is its redshift, $E(z) \equiv H(z)/H_0$, and $\tau(z) = t(z)/t_0$, with $t(z) \equiv t_0 - t_L(z)$. The $\beta - T$ relation differs slightly in that $\beta \equiv \log X$. The parameters N, P, α, u, v, w and σ describe the relation and its evolution. The distributions adopted for these parameters are derived from observed cluster scaling relations as described below.

Population scatter is allowed for using random deviates from mean relations following a normal distribution with standard deviation σ. To accommodate variable scatter about the relation, σ can be represented by a power law:

$$\sigma_{\log X} = N_{\sigma} \left(\frac{T}{P} \right)^{\alpha_{\sigma}} \tag{2.11}$$

where N_{σ} and α_{σ} are the normalisation and slope of the scatter. These scaling relations are based on properties extracted within a cluster radius of R_{500}. The MS provides M_{200} for each simulated cluster, which is converted to a value of M_{500} using the method described in Section 2.2.1, allowing T to be calculated. With T available the other three parameters can be calculated.

To define best values for the free parameters in these relations, we gather the results of several observational studies of groups and clusters, rescale them to have similar definitions and then fit them with the scaling relation model. The values derived in this way are summarised in Table 2.1. Thus, the observed scaling relations provide the distribution of baryonic properties for the cluster halos that originate from the MS.

The goal is to obtain relations that reproduce the general behaviour of the cluster population and not to produce an accurate study of scaling relations, which are sensitive to the choice of sample. These cluster samples are constructed to provide scaling relations that represent groups and clusters over a wide dynamic range, rather than attempting

Table 2.1: Default values used for the scaling relation variables in XIS.

	$M_{500} - T$	$L_{500} - T$ [a]	$r_{cf} - T$	$\beta - T$
P[b]	3	3	4	4
log	Both	Both	Both	Only T
N_c[c]	$1.22^{+0.04}_{-0.03} \times 10^{14}$	$1.81^{+0.13}_{-0.12} \times 10^{44}$	$0.0888^{+0.0082}_{-0.0075}$	0.598 ± 0.009
N_g[c]	. . .	6.35×10^{43} ($1.27^{+0.19}_{-0.16} \times 10^{44}$)[e]	. . .	. . .
$N_{\rm NCC}$[c,d]	. . .	1.53×10^{44}	0.129	. . .
$N_{\rm CC}$[c,d]	. . .	3.70×10^{44}	0.0549	. . .
α_c	1.62 ± 0.04	2.76 ± 0.16	1.07 ± 0.10	0.160 ± 0.021
α_g	. . .	4 (3.17 ± 0.29)[e]	. . .	. . .
$\log(T_0/P)$	. . .	-0.203 (0.376)[e]	. . .	. . .
d	. . .	0.413 (0.430 ± 0.053)[e]	. . .	. . .
u	0	0[f]	0	0
v	-1.0	0[f]	0	0
w	0	0[f]	0	0
N_σ[g]	(0.0766)[h]	0.327 ± 0.087	0.521	0.105
$N_\sigma(CC)$[g]	. . .	0.265	0.267	. . .
α_σ	0	-0.208 ± 0.207	0	0
$\alpha_\sigma(CC)$	0	-0.168	0	0
$\sigma^2_{{\rm s},X}/\sigma^2_{{\rm o},X}$	0.808	0.025	0.085	0.308
$\sigma^2_{{\rm s},T}/\sigma^2_{{\rm o},T}$	0.193	0.152	0.018	0.090

NOTE. - All scaling relations are derived within $r < R_{500}$.
[a] Luminosity is bolometric.
[b] Units of keV.
[c] Units - M_{500}: h^{-1} $M_\odot$, $L_{\rm X}$: erg s^{-1}.
[d] Normalisation when the evolving cool core model is used. Offset of $N_{\rm NCC}$ (or $N_{\rm CC}$) from N_c is used as the offset from N_g.
[e] Value selected for consistency with $\log N - \log S$ (see Section 2.2.8). Value in brackets is the fit to the observational data in Section 2.2.4.2.
[f] No evolution was assumed when deriving the $L_{\rm X} - T$ relation, but it could be added during simulations as part of this research.
[g] When the dependent parameter is logarithmic, the scatter is given as $\sigma_{\log}$. N_σ (CC) and α_σ (CC) are the values used for the $r_{cf} - T$ relation when the evolving cool core model is used.
[h] Scatter is dominated by measurement errors and not used.

to create a statistically complete sample. It is more useful to have good estimates for properties over the entire sky field mass range than to have very well defined relations at just the high mass end. This is because the survey bias study focuses on the ability to distinguish between different scaling relations, and the IXO trade-offs study is more relevant at the low mass end. The following data sources are used provide samples for each scaling relation:

$M_{500} - T$**:** Arnaud et al. (2005); Kotov & Vikhlinin (2005); Vikhlinin et al. (2006); Kotov & Vikhlinin (2006); Sun et al. (2009).

$L_{500} - T$**:** Helsdon & Ponman (2000); Mulchaey et al. (2003); Osmond & Ponman (2004); Pacaud et al. (2007); Maughan et al. (2008); Pratt et al. (2009).

$r_{cf} - T$**:** Helsdon & Ponman (2000); Mulchaey et al. (2003); Osmond & Ponman (2004); Kotov & Vikhlinin (2005); Johnson et al. (2006); Maughan et al. (2006); Chen et al. (2007).

$\beta - T$**:** Same as for $r_{cf} - T$.

The methods used by each study to obtain the properties, and the ways in which they are scaled, are given in Appendix C.3. r_{cf} and β samples are only taken from studies which give both parameters. These sources are restricted to the range $0.2 < \beta < 0.9$ for $T < 2$ keV and $0.2 < \beta < 1.0$ for $T \geq 2$ keV to reduce the number of poor fits that are included due to degeneracy in the β-model. Where the cosmology assumed is significantly different from that used here, attempts are made to correct for it. Where R_{500} is required for the $L_{500} - T$ and $r_{cf} - T$ relations but is unavailable or inappropriate, it is derived from the source temperature using the $M_{500} - T$ relation presented in this section. To represent the whole cluster population, no attempt is made to exclude mergers or distinguish between Cool Core (CC) and Non Cool Core (NCC) clusters in the initial scaling relation fits. However, additional $r_{cf} - T$ relation fits of CC and NCC samples are performed using available data.

2.2.4.1 Temperature

It is important to obtain reasonable evaluation of the $M_{500} - T$ relation as temperature determines the other simulated scaling properties. The $M_{500} - T$ relation is found from a sample of 51 objects, composed of both groups and clusters. All masses are derived from best-fit T and ρ profiles with the exception of those from Arnaud et al. (2005), which use NFW profiles (see Appendix C.3).

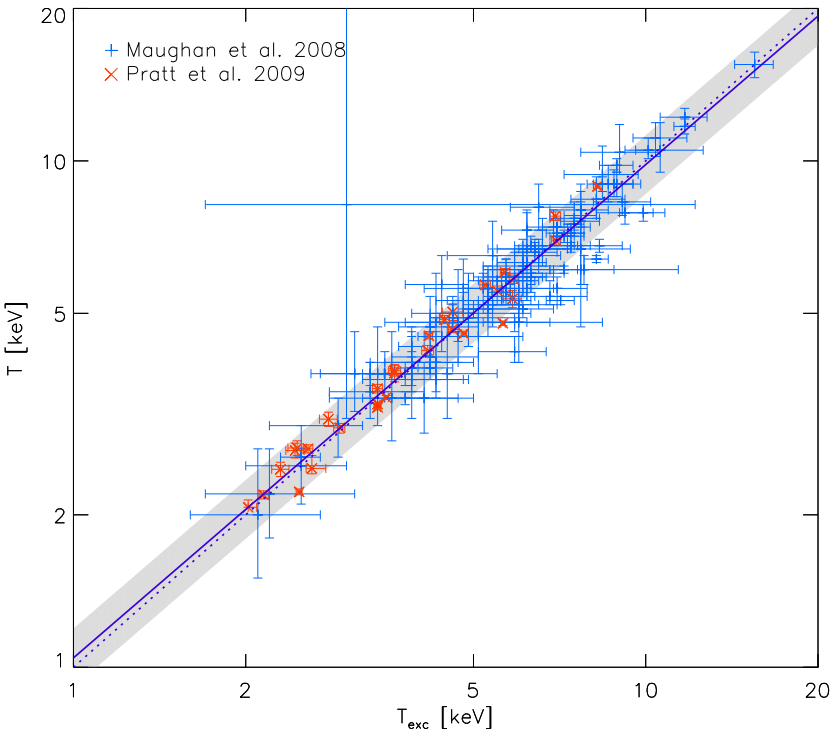

Figure 2.10: Total integrated temperature versus core excluded temperature (x-axis) from a compilation of data which originated from Kotov & Vikhlinin (2005); Maughan et al. (2008); Pratt et al. (2009). The dotted line represents a 1:1 relation. The solid line shows the fit to the data: $T = (5.98 \pm 0.06)(T_{\rm exc}/6)^{(0.97\pm0.2)}$. The shaded region shows its 1σ standard deviation of 0.0579 keV.

Masses are compared with spectral temperatures extracted by excluding the core, which have been derived in many recent mass studies. This is due to the large amount of scatter in T present in a mix of CC and NCC clusters. There can often be significant radiative cooling taking place in the core, which causes a drop in temperature and breaks the self-similarity. Removing a CC increases the integrated T, while removing a NCC causes it to decrease (e.g. see Pratt et al. 2009). Excluding the core gives a temperature that better reflects the halo mass.

To obtain a large sample with which to construct the other scaling relations over a T range which includes groups and clusters, we are required to use samples that mostly consist of core-included temperatures. The samples used for the other relations consist of a mix of CC and NCC groups and clusters, and some core-excluded groups. We test for a possible offset in the $L_{500} - T$ relation using the samples that have measurements for both

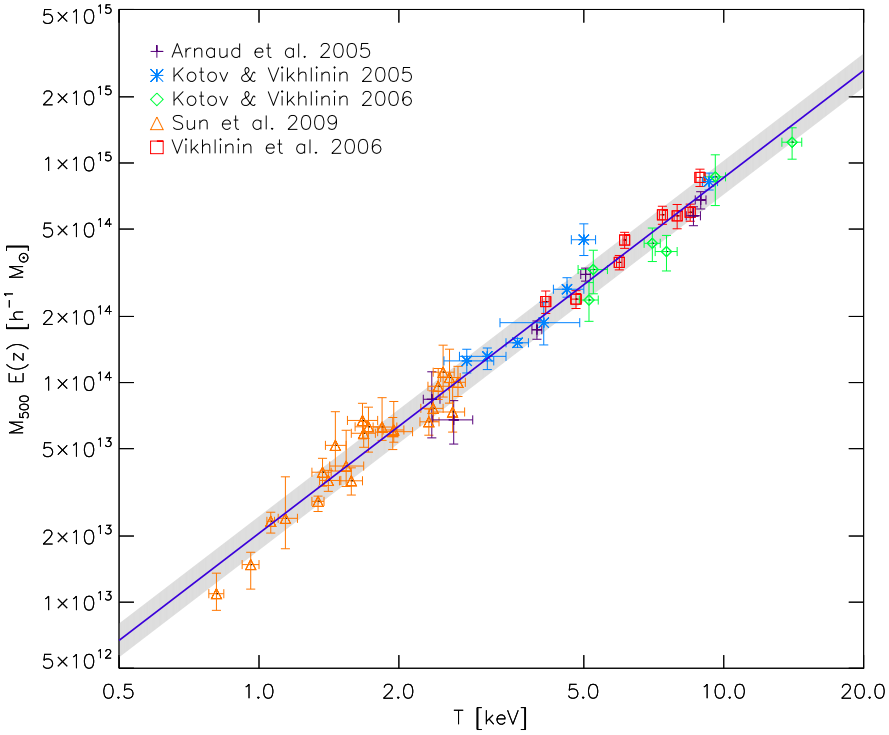

Figure 2.11: $M_{500} - T$ relation from a compilation of data which originated from Arnaud et al. (2005); Kotov & Vikhlinin (2005); Vikhlinin et al. (2006); Kotov & Vikhlinin (2006); Sun et al. (2009). The solid line shows the power law fit to the data and the shaded region shows its 1σ standard deviation, used for the scaling relation scatter.

temperatures (96% of the sample over $T > 2$ keV). The overall relationship between the two temperatures in the subsample is consistent with unity (see Figure 2.10). Therefore, the use of core-included T should not create a significant T offset in $L_{500} - T$ or other relations.

We normalise temperatures to a value near the median of the sample so that the estimates for N and α are almost independent, following the approach of Vikhlinin et al. (2006). This gives temperature normalisation factor $P = 3$ keV. The $M_{500} - T$ relation is assumed to evolve in a self-similar fashion with respect to the critical density as suggested by the results of Kotov & Vikhlinin (2006), therefore $u = 0$, $v = -1$ and $w = 0$. All of the cluster masses in the sample are converted to $z = 0$ by multiplying by $E(z)$. The data are fitted with a power law by using orthogonal regression (see Section 2.1.1) on the renormalised logarithms. The $M_{500} - T$ relation can be seen in Figure 2.11 and

Table 2.1. This observation-based relation is used determine the temperatures of XIS simulated clusters.

Scatter in the scaling relations is based on the observed standard deviation σ_o of the sample. A proportion of this scatter is due to statistical measurement errors σ_s. It would be inappropriate to assume scatter in the underlying population if the measurement errors produce a scatter that is significant with respect to σ_o. To test this, the observed variance about the scaling relation needs to be decomposed into the real variation in the population and the contribution from measurement errors.

We define the variance of the measurement errors of the relevant scaling property and temperature as $\sigma^2_{\mathrm{s},X}$ and $\sigma^2_{\mathrm{s},T}$, respectively. We compare these with the respective variances of the residuals between the scaling relation model and the observed data, $\sigma^2_{o,X}$ and $\sigma^2_{\mathrm{o},T}$. Values are calculated in log space for the appropriate scaling relations. If $\sigma^2_{\mathrm{s},X}/\sigma^2_{\mathrm{o},X} \ll 1$ and $\sigma^2_{\mathrm{s},T}/\sigma^2_{\mathrm{o},T} \ll 1$ then the scatter is considered significant enough to include as population scatter. This is not the case for the $M_{500} - T$ relation, where the statistical scatter in M_{500} dominates (see Table 2.1). Therefore, no population scatter is included in the simulated $M_{500} - T$ relation.

2.2.4.2 Luminosity

Since this work aims to study the $L_{500} - T$ relation with a variety of evolutionary models, it is inappropriate to assume any particular evolutionary model for the accumulated luminosity data. To minimise the effect of evolution on the fitted $L_{500} - T$ relation, the only objects included in the sample are those for which their maximum evolved L_{500} would fall well within the scatter in the sample. The strongest evolution considered here is self-similar evolution with respect to the background density of the Universe, where $L_{\mathrm{X}} \propto (1+z)^{1.5}$ (Voit 2005a). The fitting procedure described below is continuously repeated on a subsample defined by an upper-limit on z which decreases with every iteration. This process terminates when the standard deviation of the subsample from the model is twice the maximum amount of evolution that would be present if $L_{\mathrm{X}} \propto (1+z)^{1.5}$ is as-

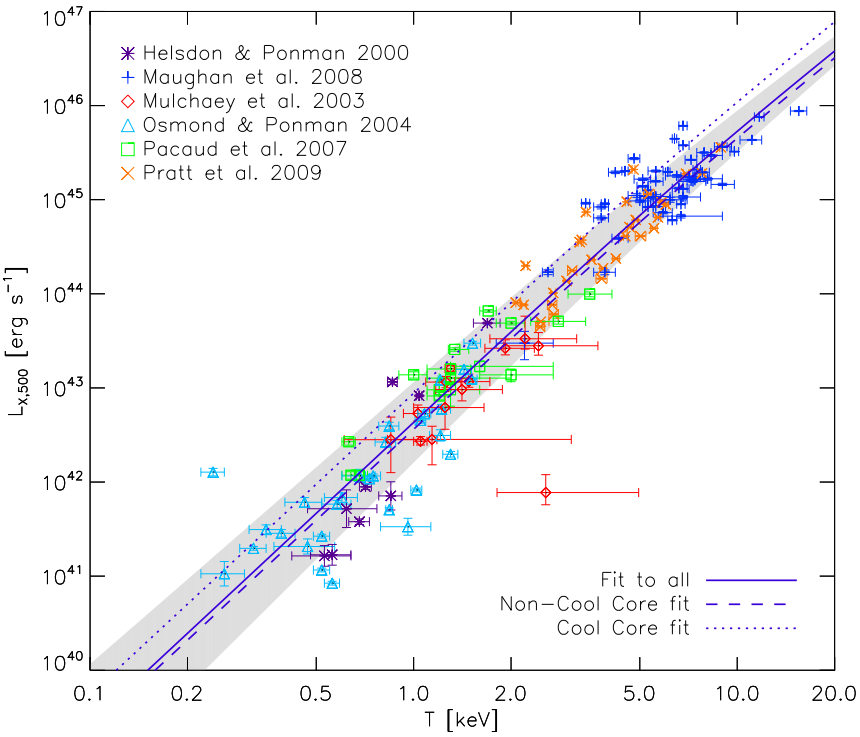

Figure 2.12: $L_{500} - T$ relation from a compilation of data which originated from Helsdon & Ponman (2000); Mulchaey et al. (2003); Osmond & Ponman (2004); Pacaud et al. (2007); Maughan et al. (2008); Pratt et al. (2009). The solid line shows the sigmoid-based two power law fit to the data and the shaded region shows its 1σ standard deviation, used for the scaling relation scatter. The dashed and dotted lines show the renormalisations of the fit for the non-cool core and cool core samples of Pratt et al. (2009), respectively.

sumed. The final sample contains the 154 objects with $z < 0.33$, which have $\sigma_{\log L} \sim 0.373$ and a pivot at 3 keV.

Observations have revealed a possible change in the slope of the $L_{500} - T$ relation at low temperatures (Helsdon & Ponman 2000). To accommodate this, we represent the relation by joining two power laws with a sigmoid function:

$$S = \frac{1}{1 + e^{-[\log(T/P) - \log(T_0/P)]/d}} \tag{2.12}$$

where $\log(T_0/P)$ is the centre of the sigmoid and d is the width of the transition. Omitting

the evolution and scatter, the form of the $L_{500} - T$ relation is

$$L_{500} = (S-1)N_g\left(\frac{T}{P}\right)^{\alpha_g} + SN_c\left(\frac{T}{P}\right)^{\alpha_c}$$

where the subscripts g and c denote the power law parameters at the group and cluster ends of the relation, respectively. For a more robust fit, the normalisation and slope in the group and cluster regimes are found using power law fits to sub-samples from the respective studies. Since the Pacaud et al. (2007) sample covers both of these regimes, those objects from this study with $T < 2$ keV are defined here as groups. The group sample of 64 objects has $P = 1$ keV, while the cluster sample of 90 objects has $P = 5$ keV. The normalisations are rescaled for use with the 3 keV pivot of the whole sample. For the sigmoid fit the normalisations and slopes are fixed and T_0 is set at the value where the two power laws intersect, 7.13 keV. This high transition point suggests that the relation may only asymptote to the cluster slope deep into the cluster regime. `MPFIT` is used to fit the sigmoid to the data by minimising the residuals weighted by the errors in both dimensions, giving $d = 0.430 \pm 0.053$. The $L_{500} - T$ relation is plotted in Figure 2.12 and the best-fit parameters are given in Table 2.1.

Scatter in $L_{500} - T$ appears to increase towards the group regime. Some of this trend may be caused by measurement bias, as it is more difficult to constrain the T and $L_{\rm X}$ of less luminous systems. However, since the observed scatter is less than the statistical scatter, we include the increased scatter at low T in the simulations. The σ is fitted as a decreasing function of temperature. σ is found for 7 bins in $\log T$ containing 22 objects each. Bins are assigned their mean T. The results for N_σ and α_σ are shown in Table 2.1, and give our simulated clusters T-dependent scatter in $L_{\rm X}$ as shown by the shaded region in Figure 2.12. Both the $M_{500} - T$ and $L_{500} - T$ relations shown here have gradients that lie within the ranges found the other studies mentioned in Section 1.3.3.

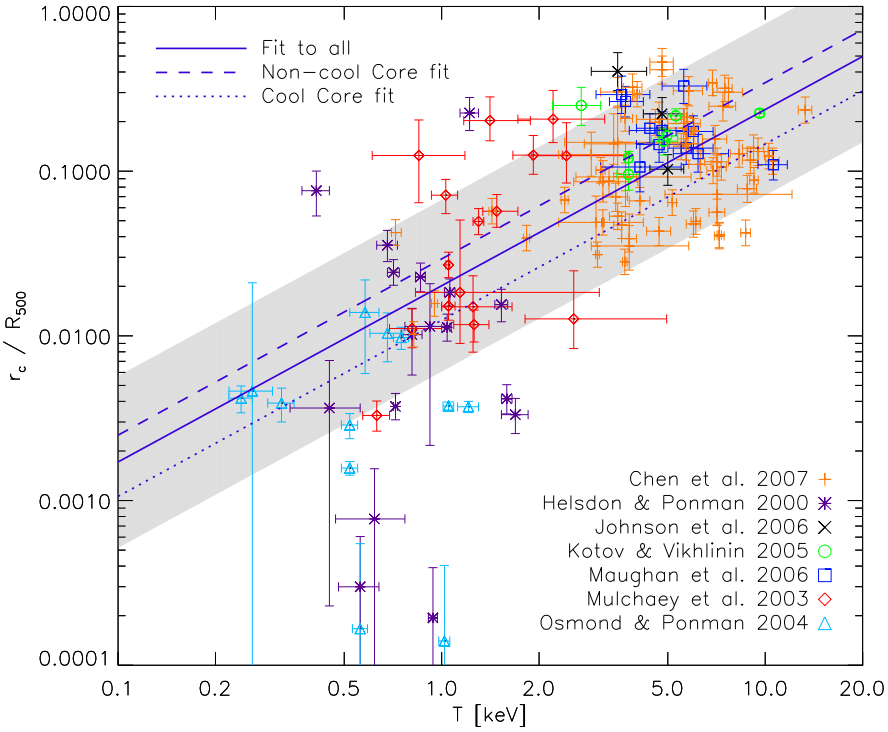

Figure 2.13: $r_{cf} - T$ relation from a compilation of data which originated from Helsdon & Ponman (2000); Mulchaey et al. (2003); Osmond & Ponman (2004); Kotov & Vikhlinin (2005); Johnson et al. (2006); Maughan et al. (2006); Chen et al. (2007). The solid line shows the power law fit to the data and the shaded region shows its 1σ standard deviation, used for the scaling relation scatter. The dashed and dotted lines show the renormalisations of the fit for the non-cool core and cool core samples of Chen et al. (2007), respectively.

2.2.4.3 Surface Brightness

R_{500} is used to compute the radius of the constant density core r_c of each simulated cluster. This is usually defined as the core radius of a β-model, as discussed in Section 1.4.1. The results of Sanderson & Ponman (2003) indicated a significant change in the fractional size of the core between the group and cluster regimes. Excluding cool cores, the observed relation for clusters was $r_c \approx 0.1\ R_{200}$, but at temperatures of < 1 keV they found $r_c \approx 0.01\ R_{200}$. Instead of a sudden change in core radius fraction, an attempt is made to model the relationship between r_c/R_{500} and T (hereafter $r_{cf} - T$) by compiling 133 β-model fits from the studies mentioned earlier. Since these are single β-model fits, the entire gas distribution (including any CCs) is represented. This maintains consistency with the

$L_{\rm X} - T$ relation, which provides the integrated luminosities for the whole $r < R_{500}$ region. At this stage no evolution is assumed. The fitted $r_{cf} - T$ relation can be seen in Figure 2.13 and Table 2.1.

The large amount of scatter is likely a combination of several factors. The sample includes a mix of CC and NCC systems, which have differently shaped profiles in the core regions and thus different results from single β-model fits (discussed further below). Another factor could come about from observational bias at low temperatures. Bias to lower r_c can be expected in the low T systems due to the difficulty in detecting the more extended low luminosity systems. A power law fit may not be the most appropriate way to fit the $r_{cf} - T$ trend, especially with this bias. Also, r_c and β are degenerate within the β-model, which would broaden the deviation from the relation.

Another important factor to note is the plausibility of the core radii of group sample, which were obtained from ROSAT data. Many of these systems have much smaller core radii than the PSF of the data (which is $\gtrsim 20$ arcsec), and 5 groups have a r_c fit less than one tenth of the PSF size. These 5 systems, which have the smallest r_{cf} values of our dataset, also have physical core radii ranging from $70 - 276$ pc, considerably smaller than galaxy sizes. For these reasons it is likely that their true core sizes are much larger.

Another parameter used to define a cluster surface brightness profile is β. A trend to find smaller β values (i.e flatter profiles) for cooler systems has been observed in both nearby and distant clusters (Mohr & Evrard 1997; Schindler 1999; Croston et al. 2008). Croston et al. (2008) also observe an entropy excess at intermediate radii and a steep relationship between gas mass and temperature, suggesting that gas has been displaced outwards from the centres of the lower temperature systems. To model the $\beta - T$ relation a line is fitted to β and $\log T$. The result is shown in Figure 2.14 and Table 2.1. It should be noted that the degeneracy between r_c and β causes their measurements to be correlated outside of their relationship with temperature.

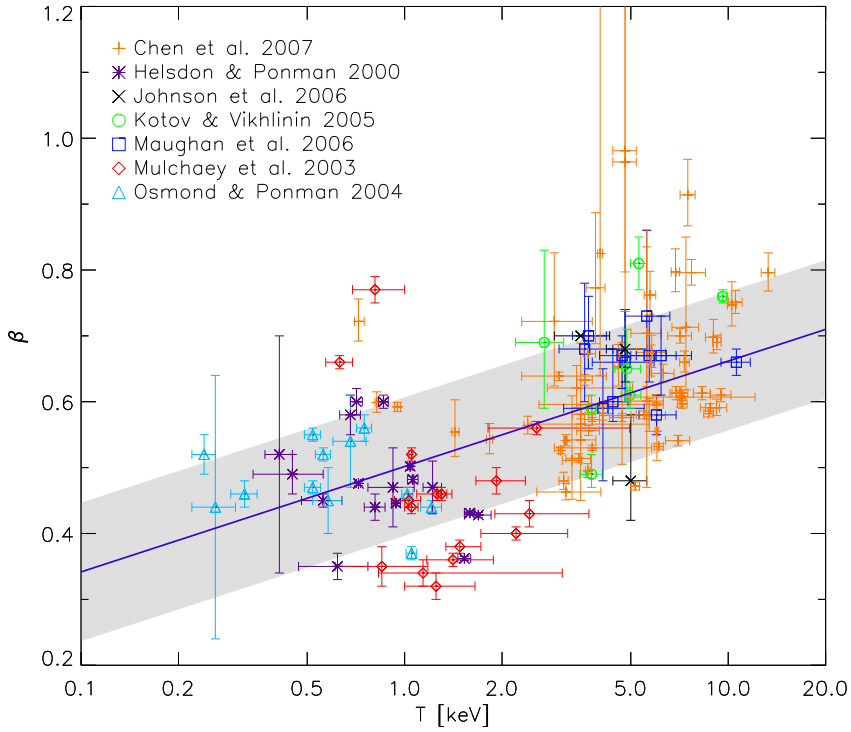

Figure 2.14: As Figure 2.13, but showing the $\beta - T$ relation from the that sample. The solid line shows the linear fit to $\beta - \log T$.

2.2.4.4 Cool Cores

The empirical scaling relations discussed above include the effects of cool cores. We also wish to address the impact of CCs on the cluster selection function. CCs raise the central surface brightness, improving the chance of detection, but this also puts the cluster in danger of being identified as a point source.

Several features with a variety of strengths have been used to classify clusters as CC, including central cooling time, mass deposition rate and the presence of a central cusp in the surface brightness profile (Vikhlinin et al. 2007). The latter feature provides a simple way to address the detectability of CCs using XIS. It has also been used to study the evolution of the CC population. Another distinction between CC and NCC populations is the mean $L_{\rm X}$ for a given T (see Pratt et al. 2009).

Optional renormalisations of the $L_{\rm X} - T$ relation and $r_{cf} - T$ relation are used to

represent changes the surface brightness of clusters when separate CC and NCC populations are required. The systems used to determine the $L_{\rm X} - T$ renomalisation are those of Pratt et al. (2009), while the $r_{cf} - T$ relation uses the sample of Chen et al. (2007) (see Appendix C.3). No attempt is made to include the effect of cool cores on the $\beta - T$ relation due to the uncertainty caused by the correlation between r_{cf} and β.

The $L_{\rm X} - T$ relation is renormalised to fit only the 21 NCC systems, resulting in $\log N = 44.186 \pm 0.005$, and then again for the 10 CC systems, obtaining $\log N = 44.569 \pm 0.005$. We also renormalise the $r_{cf} - T$ relation to fit the 32 NCC and 35 CC systems, giving $\log N = -0.889 \pm 0.048$ and $\log N = -1.26 \pm 0.05$, respectively. The corresponding relations for NCC and CC clusters are shown in Figure 2.12 and Figure 2.13.

The $r_{cf} - T$ scatter N_σ for both system classifications is set to the mean standard deviation of these subsamples, 0.267. For the $L_{\rm X} - T$ scatter the mean standard deviation of the subsamples is 81% of the standard deviation of the full sample. We rescale the T-dependent $L_{\rm X} - T$ scatter by this amount, giving $N_\sigma = 0.265$ and $\alpha_\sigma = -0.168$.

Observations have shown cool cores to be common at low redshift, but have indicated that they are rare at high redshift (Ettori et al. 2004; Bauer et al. 2005; Vikhlinin et al. 2007; Santos et al. 2008). Bauer et al. (2005) determined that at least 20 of their sample of 38 X-ray-selected clusters had mild or stronger cool cores. These were luminous clusters at redshifts of $0.15 < z < 0.4$. A study by Vikhlinin et al. (2007) found evidence for a lack of strong CC clusters at $z > 0.5$, with only 3 of 20 clusters exceeding their cuspiness criterion. The lack of CCs has been attributed to more frequent merger activity (Santos et al. 2008).

More recently, Samuele et al. (2011) searched for evidence of cooling flows a sample of Brightest Cluster Galaxies (BCGs) from the 160d survey at $z < 0.7$ by measuring nebula emission-line strengths. The X-ray selected sample contained no sign of strong cooling flows. They compared this with the Crawford et al. (1999) analysis of the RASS Brightest Cluster Sample (BCS), which contained systems at $z \lesssim 0.3$ with emission lines for 30% of the BCGs from the most X-ray luminous clusters and 16% for the least luminous. Samuele et al. (2011) conclude that this difference is significant and is not greatly

affected by projection or selection effects. It suggested a rapid evolution in the number of established strong cooling flows within $0 < z < 0.5$.

Santos et al. (2010) investigated the surface brightness concentration of three representative cluster samples with median redshifts of 0.08, 0.59 and 0.83, taking advantage of the high spatial resolution of Chandra. This revealed a well defined population of CCs at $z \sim 1.3$, but lacking strong CCs. Interestingly, comparing with WARPS, it appeared that 400d survey selected systems might be biased against concentrated morphologies. Such a bias would have affected the 160d survey-based results of Samuele et al. (2011) and may be responsible for the lack of CCs.

Another discrepancy from earlier studies comes from the work of Alshino et al. (2010), who found evidence that CCs are more prominent at higher z in cool systems. These studies highlight the importance of understanding the survey selection effects when studying CC populations. In Chapter 4 we use an evolving cool core model to explore how biases affect the recovery of the CC fraction with redshift.

In order to investigate the impact of potential evolution of CCs on cluster surveys, each cluster that we simulate is assigned as either CC or NCC based on a simple redshift-dependent probability. Clusters with $z \leq 0.5$ have a 50% probability of being CC, with all others designated as NCC. This probability is decreased in a linear fashion to 0% at $z = 1.5$. The $L_{\rm X} - T$ and $r_{cf} - T$ relations are modified to be cool core dependent, thus a CC cluster has its r_c calculated from a different distribution than a NCC cluster. Standard XIS simulations are without CC evolution and use the standard $L_{\rm X} - T$ and $r_{cf} - T$ relations unless otherwise stated.

2.2.4.5 Sample Bias

The samples that establish the scaling relations discussed above are by no means representative and likely include several biases. Inclusion of only objects with constrained β-model fits introduces a bias at the extreme ends of the $r_{cf} - T$ and $\beta - T$ relations, and biases upwards the poor end of the $L_{\rm X} - T$ relation. This bias is reinforced by an

observational selection bias due to the difficulty in detecting low $L_{\rm X}$ groups. A noticeable change in $L_{500} - T$ slope is found in the group regime, although both slopes could be reconciled within errors. Using biased observational data to produce simulations could harm the attempt to study the effects of bias, and produce unrealistic predictions for the performance of IXO in the group regime. Therefore, we consider an adjusted $L_{\rm X} - T$ relation to reduce the amount of bias present in the simulated datasets. This is covered in Section 2.2.8.

These scaling relations are derived from observed group and cluster samples which are biased towards a more relaxed state, which produce X-ray emission that is easier to both detect and analyse. This is especially true for the $M_{500} - T$ relation, due to the difficulty of obtaining accurate mass estimates and the samples selected for such work. This means that the scaling relations here do not represent the Universal cluster population, but provide reasonable estimates of cluster parameters for the purpose of studying the bias caused by selection effects. Accuracy in the high redshift Universe is questionable due to a smaller fraction of the population being sampled, and the less relaxed state of that population. The ability of IXO to recover the evolution of the $L_{500} - T$ relation through observations is explored in Chapter 4. To attempt to improve their accuracy, one could include the results of detailed numerical simulations supported by data from non X-ray methods.

2.2.5 Cosmological Distance Effects

In an expanding Universe both the calculation of incident flux from a luminous source and the angular size for a given physical size are non-trivial. Focusing on the former, the X-ray flux $S_{\rm X}$ received from a source of luminosity $L_{\rm X}$ at distance D in a static Universe is:

$$S_{\rm X} = \frac{L_{\rm X}}{4\pi D^2} \tag{2.13}$$

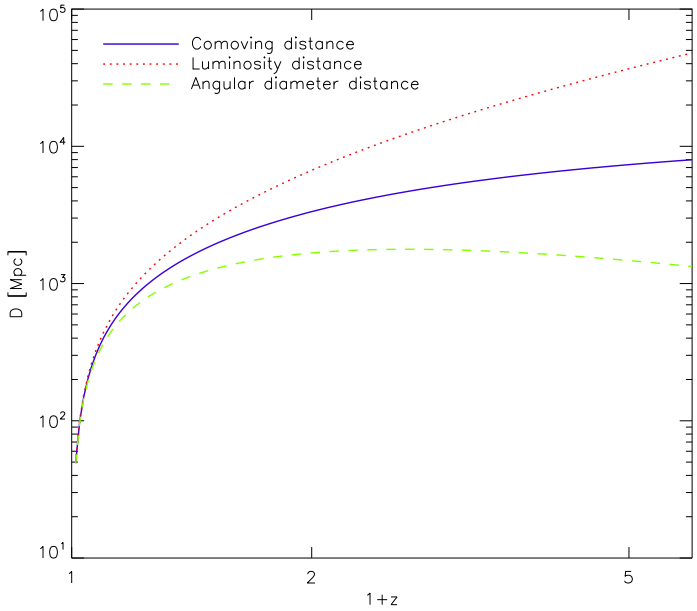

Figure 2.15: Comparison of three cosmological distance scales using the XIS cosmology. Comoving distance is given by the solid blue line, luminosity distance by the dotted red line, and angular diameter distance by the dashed green line.

per unit solid angle observed. However, less flux is received in an expanding Universe due to photons losing energy $\propto (1+z)$ and arriving less frequently $\propto (1+z)$ (Liddle 2003, pp 129). A cosmological distance scale known as luminosity distance D_L can be defined, relating to the expansion of the Universe using the comoving distance D:

$$D_{\mathrm{L}} = (1+z)D \tag{2.14}$$

Note that this is only true in a flat Universe, where the transverse comoving distance is equivalent to the line-of-sight comoving distance (Hogg 1999). An X-ray source in an expanding Universe is observed with an $r < R_{500}$ X-ray flux

$$S_{500} = \frac{L_{500}}{4\pi D_{\mathrm{L}}^2} \tag{2.15}$$

The flux S_{500} of each simulated cluster is calculated in units of erg cm^{-2} s^{-1} by converting D_{L} from h^{-1} Mpc to cm using H_0.

A contrasting distance scale emerges for angular separations, known as angular diameter distance D_A. Consider two light rays emanating from either side of a distant extended object towards an observer. In a static Universe, as the rays propagate radially towards the observer the distance between them reduces. This distance is equivalent to an angular separation on the sky. The expansion of the Universe increases the distance between the light rays, acting to preserve the angular separation. The object appears larger, and hence closer, than it actually is. For a comoving distance D in a flat Universe,

$$D_{\mathrm{A}} = \frac{D}{1+z} \tag{2.16}$$

Due to the huge distances involved, the angular extent of an object can be determined from the small-angle approximation. Hence for a physical radius R the angular radius

$$R' \simeq \sin R' = \frac{R}{D_{\mathrm{A}}} \tag{2.17}$$

in radians. This is applied to the R_{200}, R_{500} and r_c of each cluster to calculate their angular sizes. The different distance scales are compared in Figure 2.15. It is interesting to note that above a certain redshift the angular size of an object of fixed physical size becomes larger with redshift. Thus, discounting structure formation, clusters tend be smaller with redshift up to a certain distance, and then larger. Beyond this distance, the combination of angular diameter distance and luminosity distance effects leads to a significant decrease in surface brightness. The result is clusters becoming increasingly difficult to detect.

2.2.6 Surface Brightness Profiles

With most of the independent variables established for the cluster sky field, the next topic is the shape given to emission from the clusters, the surface brightness profile. Observations have shown clusters to be elliptical in shape more often than circular (Mohr et al. 1995). To distribute the X-ray emission across a cluster in an elliptical way, a two-

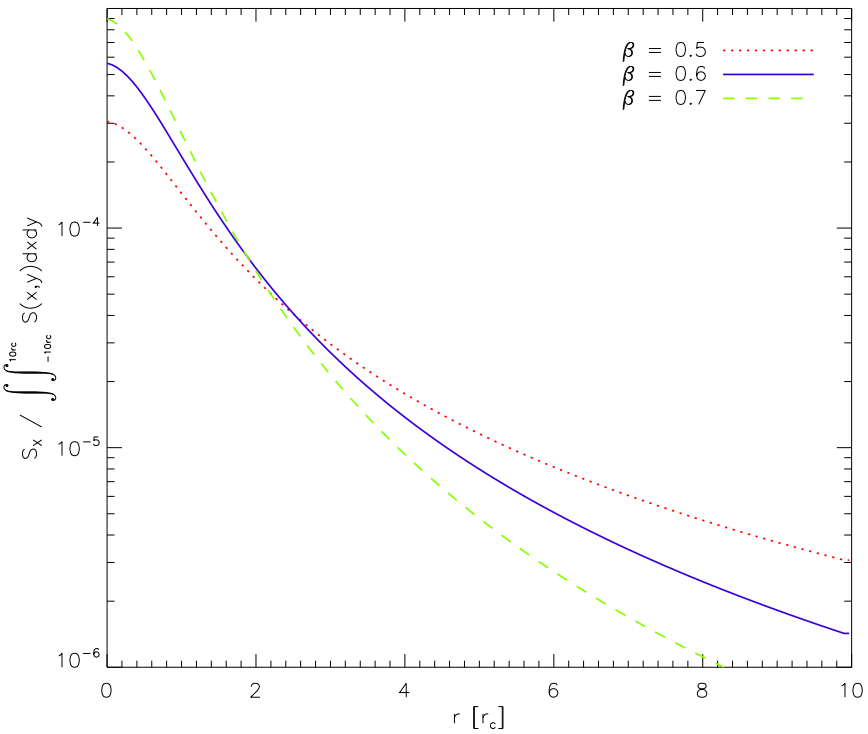

Figure 2.16: Radial profile of a circular two-dimensional β-model for three different values of β: 0.5 (dotted red line), 0.6 (solid blue line) and 0.7 (dashed green line). The plot is normalised by the sum of the flux within the profile out to a radius of 10 r_c.

dimensional surface brightness profile is required. Cluster morphology can be approximated by an elliptical β-model of the form

$$\left[1 + \left(\frac{x}{r_{c,m}}\right)^2 + \left(\frac{y}{\eta r_{c,m}}\right)^2\right]^{0.5-3\beta} \tag{2.18}$$

where x and y are the distance from the centre along the major and minor axes, respectively, $r_{c,m}$ is the major axis core radius, η is the minor to major axis ratio and β defines the gradient of the model (Cavaliere & Fusco-Femiano 1976; Jones & Forman 1984; Mohr et al. 1995). This is based on the King (1972) approximation to an isothermal sphere. Examples of three different β-models are shown in Figure 2.16. Some studies fit their clusters with double β-models (e.g. Mulchaey et al. 2003; Chen et al. 2007). This allows for a better fit of clusters with more complicated profiles, such as cool core clusters. However, for the purpose of this research a single β-model is adequate. A double β-model

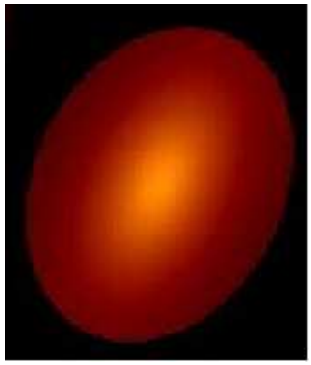

Figure 2.17: An example of a two-dimensional surface brightness profile generated by the XIS simulator.

approach would add a significant amount of extra complexity to the selection function calculations. Also, due to its simplicity for deprojecting into 3D to calculate the gas density distribution, β-model fits are widely available in the literature for use in relating the fit parameters to other cluster properties.

Each cluster profile is rotated to a random angle θ. Performing a rotation on the image of a profile using interpolation would reduce the accuracy of the profile due to the resolution of the image. To overcome this issue and optimise the speed with which profiles are generated, a rotated 2D surface brightness profile is generated analytically. Consider a 2D Cartesian coordinate system (x, y) with its origin at the centre of the cluster. First, two 2D arrays of displacements in x and y are created, Δx and Δy, respectively. These are used to calculate an array of radial coordinates. The ellipticity and rotation of the cluster is represented by a change in the effective radial position:

$$
\begin{aligned}
r &= \sqrt{(\Delta x)^2 + (\Delta y)^2} \\
\Theta &= \arctan\left(\frac{\Delta y}{\Delta x}\right) + 2\pi\theta \\
r' &= \sqrt{(r\eta^{0.5}\cos\Theta)^2 + (r\eta^{-0.5}\sin\Theta)^2}
\end{aligned}
$$

where Δx and Δy are displacements on their respective axes, and Θ is effective angle of each coordinate within the cluster in radians. The full derivation is given in Appendix A.2.

The X-ray flux S_{X} as a function of radius is then defined by

$$S_{\mathrm{X}}(r) = S_{\mathrm{X},0}\left[1 + \left(\frac{r'(r)}{r_c}\right)^2\right]^{0.5-3\beta} \tag{2.19}$$

where $S_{\mathrm{X},0}$ is the flux at the centre of the profile, and r_c is the core radius of a 1D surface brightness profile, available from the $r_{cf} - T$ relation. Figure 2.17 gives an example of how this profile appears. Clusters are given a lower limit of $\beta = 0.3$ due to the extreme behaviour of the β-model below this value and the lack of such systems in the $\beta - T$ relation dataset.

When Mohr et al. (1995) analysed the ellipticities of their cluster sample, they found $\overline{\eta} = 0.80$ with a scatter of 0.12. This distribution is applied to the simulated clusters. For convenience when assessing cluster statistics, the axial ratio is stored as the ellipticity parameter $\epsilon = 1 - \eta$.

For bright clusters with unusually shallow surface brightness profiles, the emission cut-off at R_{200} can sometimes cause a sharp drop in flux, even after the PSF blurring. This unrealistic feature can confuse source detection algorithms. Increasing the cut-off radius is undesirable due to the significant increase in the time required to generate the profile. To create a smooth transition between the cluster edge and the background, the surface brightness in the range $R_{500} < r < R_{200} + 0.5$ arcsec is multiplied by a factor which scales linearly from 1 to 0 with radius. This ensures a low surface brightness at R_{200} for nearby clusters, and preserves the luminosity within R_{500} which relates to the cluster properties. It should be noted, however, that it would reduce the amount such a cluster contaminates the emission from other objects at its perimeter.

While the simulated clusters are given radially-dependent fluxes, isothermal profiles are assumed for the purpose of deriving count rates. Cluster temperature profiles would add a significant amount of extra complexity to the calculation of the count rate profile without a great gain in accuracy.

Even a double β-model does not describe all clusters well. Mergers can cause the gas

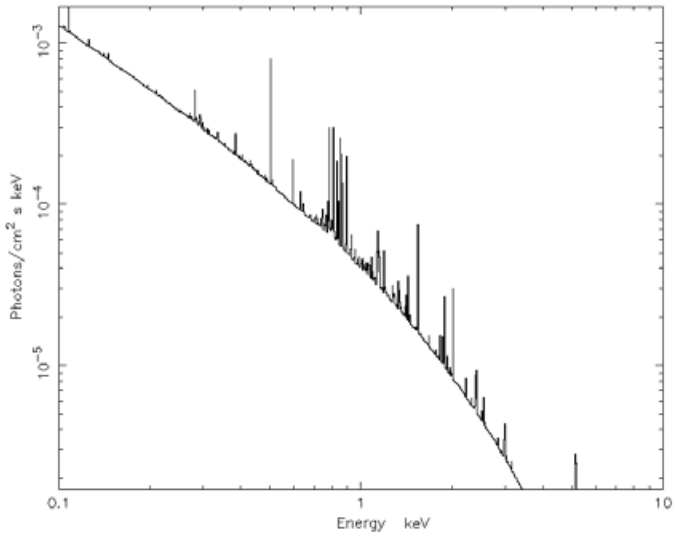

Figure 2.18: Example of an APEC spectral model used for the clusters in XIS. This model has $z = 0.3$, $S_{\mathrm{SX}} = 10^{-13}$ erg cm^{-2} s^{-1}, $T = 2$ keV and $Z = 0.3$ Z$_{\odot}$.

density profile of a cluster to become disrupted, resulting in an irregular X-ray emission profile. Another set of features identified in cluster profiles are cavities caused by bubbles, believed to be formed by the powerful jets of an AGN. These features are beyond the scope of this research.

2.2.7 Spectra

The final aspect of cluster emission that needs to be determined is the spectrum. This spectral model should be based on the emission of the hot plasma in the cluster. This is a combination of bremsstrahlung and line emission. Three spectral models are commonly used in the literature: Raymond-Smith (Raymond & Smith 1977), Mewe-Kaastra-Liedahl (MEKAL) (Mewe et al. 1985; Kaastra & Mewe 1993; Liedahl et al. 1995) and APEC (Smith et al. 2001). The major differences between these models lie in their inclusion of different spectral lines. Raymond-Smith is the simplest with emission lines not calculated in fine structure, which mostly affects the iron lines. However, their overall flux as a function of temperature, known as the cooling curve, is very similar. While the

spectral information is not a significant factor in this work, using one of the more detailed spectral models is preferred for consistency with the data used to derive the scaling relations. The APEC model is sufficient for the cluster spectra in XIS, with the MEKAL model also requiring the hydrogen density. An example of this model is presented in Figure 2.18.

The amount of line emission is dependent on the metallicity Z of the cluster gas. The simulator only requires the integrated count rate the detector receives for each source. No further use is made of the spectral profiles. Higher Z produces a higher count rate. The relative strength of spectral lines is greater for lower temperature systems due to the steep relation between bremsstrahlung luminosity and temperature. For an increase from 0.2 $Z_\odot$ to 0.4 $Z_\odot$, the integrated count rate increases by 17%, 9% and 2% for $T = 0.5$ keV, 1 keV and 2 keV, respectively. The probability of detecting a cluster depends on its count rate. Consequently, metallicity has an effect on the overall detectability of low temperature systems.

Maughan et al. (2008) found evidence for a trend of decreasing Z with increasing redshift, which follows predictions based on supernova rates. Z decreases from ~ 0.4 $Z_\odot$ to 0.2 $Z_\odot$ within $0 < z \lesssim 1$. Given the effect of metallicity at low temperatures, this trend would have an effect on the detectability of groups with redshift. However, including such a trend would add an extra dimension of complexity to the selection function. We follow the common practice of fixing Z at 0.3 $Z_\odot$, which matches the metallicity assumed for many of the objects used to derived the scaling relations (see Appendix C.3).

Spectra are also affected by the local velocity of the source. Movement of a cluster towards or away from the observer relative to its local recession velocity would blueshift or redshift its spectrum, respectively. This is in addition to the redshift from cosmological expansion. No attempt is made to include the local velocities of X-ray sources in spectral redshifting.

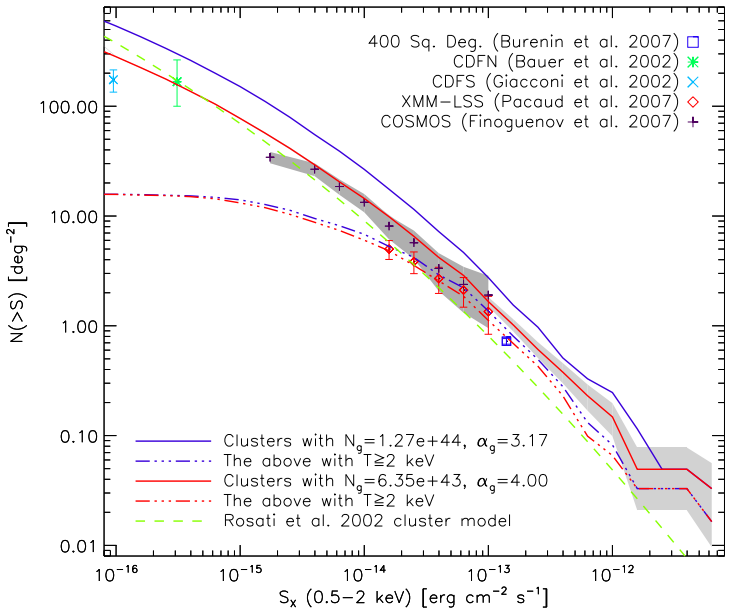

Figure 2.19: Cumulative $\log N - \log S$ plot for a compilation of 4 cluster sky fields (cumulative number of clusters as a function of soft X-ray flux). The solid dark blue and red lines show the sky field clusters with the observed and adjusted $L_{500} - T$ relations, respectively. The triple-dot-dash blue and red lines show clusters with $T \geq 2$ keV, and the dashed green line represents the non-evolving SXLF of Rosati et al. (2002) derived above 10^{41} erg cm^{-2} s^{-1}. The points show the results of cluster surveys by Bauer et al. (2002); Giacconi et al. (2002); Burenin et al. (2007); Finoguenov et al. (2007); Pacaud et al. (2007). Error bars give Poissonian 1σ confidence levels for the observational data. The light shaded area shows the 1σ confidence interval around the $L_{500} - T$-adjusted, simulated sky field clusters, while the dark shaded area shows that around the Finoguenov et al. (2007) clusters.

2.2.8 Cluster $\log N - \log S$

The cumulative flux function $\log N - \log S$ from a compilation of 4 simulated cluster sky fields using the models described above is shown in Figure 2.19. Surveys often try to estimate the total flux $S_{\rm X}$ of a cluster, rather than presenting the flux within an overdensity. For a more accurate comparison with observations, we approximate the $S_{\rm X}$ of the simulated clusters by assuming $S_{\rm X} \sim S_{200}$. This is extrapolated from S_{500} using a low resolution β-model and the XIS scaling relations, including scatter where appropriate. Poissonian counting errors are included in Figure 2.19 to highlight the low number of clusters available at the high flux end. Cosmic variance means the number of clusters in 2 different sky fields differs for $S_{200} \gtrsim 10^{14}$ erg cm^{-2} s^{-1}.

For comparison with observational data, the $\log N - \log S$ also includes results from

the recent surveys 400 square degree (Burenin et al. 2007), COSMOS (Finoguenov et al. 2007) and XMM-LSS (Pacaud et al. 2007), along with two Chandra deep field surveys (Bauer et al. 2002; Giacconi et al. 2002). It should be noted that the limited area covered by the deep surveys (~ 0.11 degree^2) means that cosmic variance could significantly affect the number density. For consistency, the fluxes of COSMOS and XMM-LSS are extrapolated to $S_{\rm X}(< R_{200})$ using the XIS β-model and the $r_{cf} - T$ and $\beta - T$ relations. Also included is the Soft X-ray Luminosity Function (SXLF) of Rosati et al. (2002). This function is valid for low redshift, bright clusters and is based on $S_{\rm X}$ extrapolations that used a model with $\beta = 2/3$. Its representation of systems with $T < 2$ keV is very limited.

The blue lines in Figure 2.19 represent the simulated clusters using the observational $L_{500} - T$ relation from Section 2.2.4.2. Clusters with $T > 2$ keV (broken blue line) appeared to follow the observed data well. When the group regime is included (solid blue line) the flux function rises significantly above the observed data. Disagreement is expected at low fluxes due to the selection function. However, at high fluxes the number of clusters is approximately twice as high as that observed.

It is likely that this cluster model over-predicted the flux due to bias in the $L_{500} - T$ relation, and possibly other group-related selection effects. The group sample has a lower mean redshift than the cluster sample. Therefore, evolution in the $L_{500} - T$ relation could have biased high T systems to higher $S_{\rm X}$, but the magnitude of such an effect should be small due to the redshift limit of $z < 0.33$ in the $L_{\rm X} - T$ relation sample. However, this redshift limit still suffers from volume-related normalisation bias due to a 3 order of magnitude variation in $S_{\rm X}$ due to D_L.

The scale of the $L_{\rm X} - T$ bias expected in the XMM-LSS data can be seen in the models of Pacaud et al. (2007) (see Figure 1.14, Section 1.4.5). This estimated bias (which used an observed $L_{\rm X} - T$ relation) was a factor 2 or more when close to the detection limit at a given redshift. To attempt to compensate for some of the bias that is expected in the $L_{500} - T$ relation, the normalisation of the group regime is halved and the slope is fixed at 4. Note that, although the mean redshift of the $L_{\rm X} - T$ relation group sample is

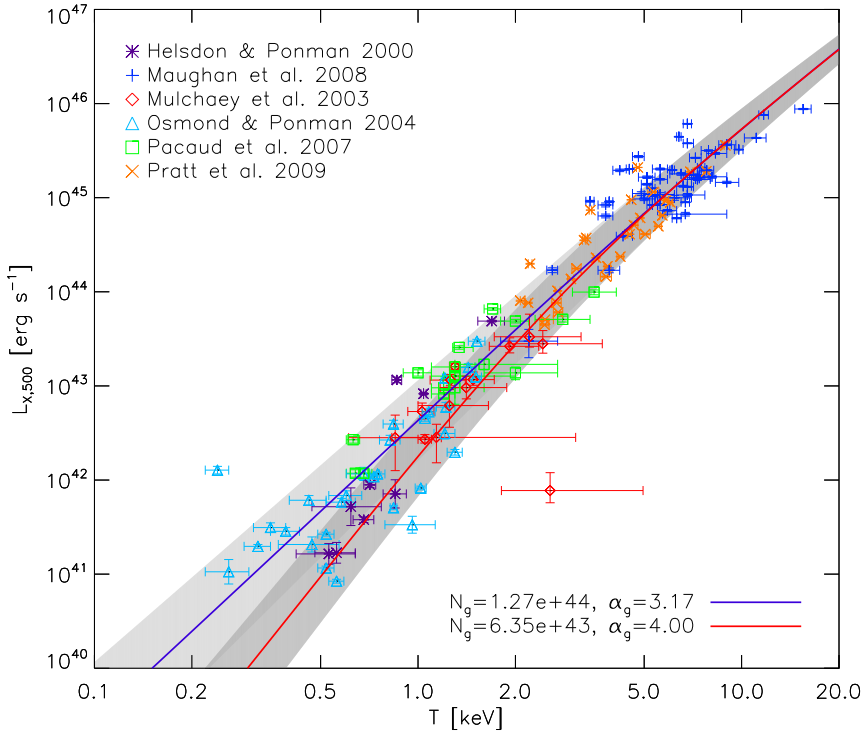

Figure 2.20: $L_{500} - T$ relation from Figure 2.12 with an adjusted group relation and sigmoid fit, shown by the red line, used in XIS to compensate for some of the expected bias in the group regime. The darker shaded region shows the 1σ standard deviation of this new $L_{500} - T$ relation.

$z = 0.057$, it still covers the full $z < 0.33$ range. Therefore, some of the slope bias will have been integrated into an overall normalisation bias. The slope change given here is only a rough correction.

This change is presented by the red lines in Figure 2.19 and Figure 2.20. It brings the total cluster $\log N - \log S$ (solid red line) into the Poisson errors of the COSMOS data (dark shaded region), deviating no more than 25% above the COSMOS number counts at $S_{\rm X} > 3 \times 10^{-15}$ erg cm^{-2} s^{-1}.

Also note that Malmquist bias means that the normalisation of $L_{\rm X} - T$ in the cluster regime is biased high. However, the limited number of high mass clusters present in the MS means that this bias should only have a small effect on XIS simulations. A more accurate approach to correcting all of the biases would have been to produce selection functions for all of the surveys included in the $L_{500} - T$ relation. However, such a large

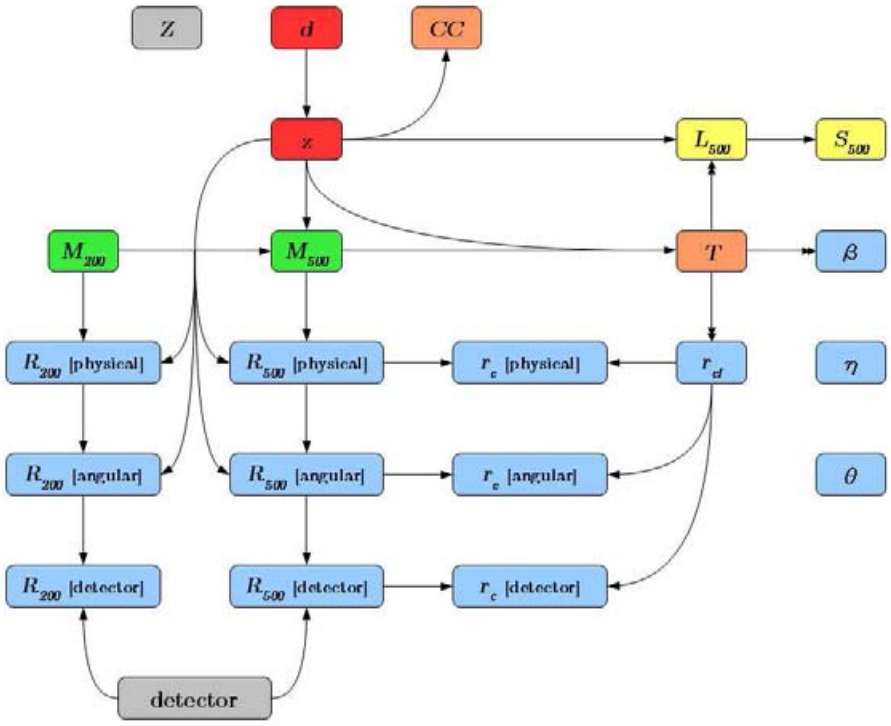

Figure 2.21: Diagram showing which cluster properties were used to derive others. Double arrows indicate relations with simulated scatter. Shape-related properties are coloured in blue.

undertaking is beyond the scope of this research. Later in this work we create an IXO selection function for a survey using 10 ks pointings (Section 4.1.2). A prediction of the recovered $\log N - \log S$ based on this selection function is available in Appendix F, Figure F.2. This shows that the recovered $\log N - \log S$ is expected to drop significantly below the simulated $\log N - \log S$ at $S_{\rm X} \lesssim 10^{-14}$ erg cm^{-2} s^{-1}.

2.2.9 Review of Cluster Properties

To review, the position and mass of each cluster is extracted from the Millennium Simulation by defining a lightcone through the simulation snapshots. This method includes an estimation of how mass changes with scale radius and a correction for the mass function. The mass determines the size of the cluster. Each cluster is given a 2D surface brightness profile with a random ellipticity and rotation. The luminosity, core radius and slope of the profile are found from the cluster temperature using scaling relations, which is itself

related to the mass. Luminosity is converted to a bolometric flux while accounting for cosmological effects. The calculation of flux as a count rate will be covered in Section 2.4. Finally, a standard metallicity is assigned to each cluster for use in an APEC spectral model. The properties of each cluster are stored in an IDL structure, and an array of these structures contains the whole sky field cluster catalogue. A flowchart presenting how the cluster properties are derived is given in Figure 2.21. A summary of the properties stored can be found in Appendix D, Table D.1.

2.3 Other X-ray Sources

Cluster emission makes up a large fraction of the total X-ray emission in the sky at low energies, but even below 2 keV it is only the dominant population at $S \gtrsim 10^{-13}$ erg cm^{-2} s^{-1}. The other extrasolar sources of X-ray emission consist of:

- AGN, galaxy thermal sources, X-ray binaries and stars seen as resolved sources;
- the unresolved cosmological (extragalactic) X-ray background, which is significant at ≥ 2 keV, also known as the hard X-ray Background (XRB);
- the local Diffuse Soft Background (DSB), significant at $\lesssim 2$ keV.

AGN are overwhelmingly the dominant population outside the plane of the galaxy, with a contribution from galaxies at very low fluxes. It is important to include these sources in simulations when doing cluster research as they can contaminate the cluster emission. Galaxies and AGN in XIS are based on Soft X-ray Luminosity Functions (SXLFs) included in the Gilli, Comastri, & Hasinger (2007, hereafter GCH07) analysis of the cosmological XRB. The galaxies in XIS represent the non-nuclear components of galaxy emission and are based on star forming galaxies. Emission from different classifications of AGN is represented by different levels of source obscuration. All galaxy emission is assumed to be outside of the local Universe, so both galaxies and AGN are included as point sources

in the sky field. Conversely, the X-ray background is represented as a flux over the whole field. This section describes the models used for these sources.

2.3.1 Galaxies

Star-forming galaxies without an X-ray emitting nucleus still produce low luminosity X-ray emission. This is generated by mixture of hot plasma (similar to that in clusters), X-ray binaries and supernova remnants, with negligible emission from stars (Fabbiano 1989). The flux distribution of X-ray emitting galaxies is modelled using the method of Ranalli, Comastri, & Setti (2003, hereafter RCS03), which combines the galaxy radio flux density model of Richards (2000) with a radio to X-ray relationship. A 1.4 GHz radio survey of the Hubble Deep Field (HDF) by Richards (2000) recovered 371 sources, which gave a number density $n(S) = (8.25 \pm 0.42)S^{-2.38}$ sr^{-1} Jy^{-1}. Therefore, the 1.4 GHz differential number density of galaxies in XIS is represented by:

$$n(S_{1.4}) = (2.51 \times 10^{-3})S_{1.4}^{-2.38} \tag{2.20}$$

in units of degree^{-2} Jy. RCS03 compared galaxy 1.4 GHz emission with X-ray fluxes from ASCA and BeppoSAX. They modelled the $0.5 - 2$ keV X-ray fluxes (hereafter $S_{\rm SX}$) using a two-component model consisting of a hot plasma model and a power law, or just a power law when analysing poor quality data (see RCS03 and references therein). Using the local and supplementary sample they produced the following relation between the soft X-ray and 1.4 GHz luminosity:

$$\log L_{\rm SX} = \log L_{1.4} + 11.10 \tag{2.21}$$

with a dispersion of 0.24.

For simplicity the RCS03 $\log N - \log S$ model assumed all sources were at $z = 1$ based on the peak of the distribution of sub-mJy galaxies in Windhorst et al. (1990), which span the range $0.5 \leq z \leq 1.5$. The XIS model uses a normal distribution of redshifts with a

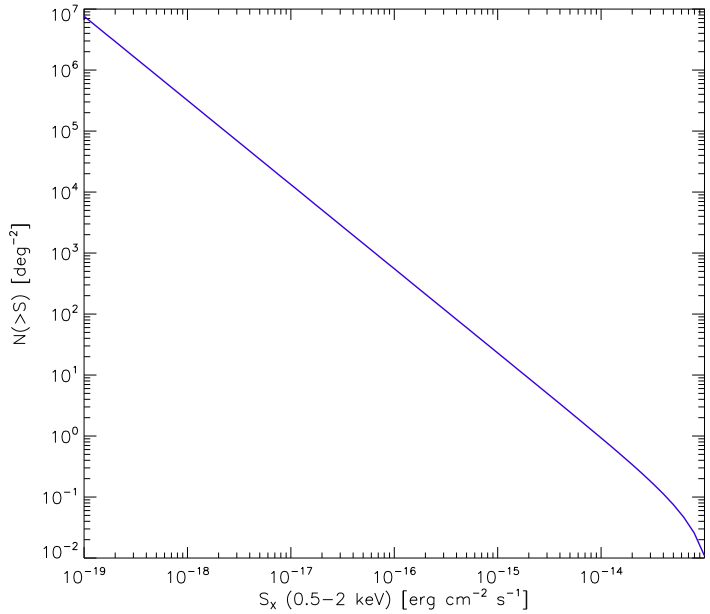

Figure 2.22: Cumulative $\log N - \log S$ of simulated X-ray emitting galaxies using the 1.4 GHz radio emission number density model of Richards (2000), along with the relationship between 1.4 GHz emission and soft X-ray luminosity from RCS03.

$\overline{z} = 1$ and $3\sigma_z = 0.5$. Following the RCS03 method, the redshifts are used to calculate a K-correction of

$$K^{\mathrm{X}}_{1.4}(z, \alpha, \Gamma) = \frac{L_{\mathrm{SX}}}{L_{1.4}}(1+z)^{-(\Gamma-1)+\alpha} \tag{2.22}$$

where X-ray spectral index $\Gamma = 2.1$ and radio spectral index $\alpha = 0.5$ are assumed. By applying this K-correction, the soft X-ray number density is determined:

$$n(S_{\mathrm{SX}}) = n(S_{1.4}K^{\mathrm{X}}_{1.4}) \tag{2.23}$$

A logarithmic distribution of 1.4 GHz fluxes is created by assuming a luminosity distribution of $27 \leq \log L_{1.4} \leq 31$ (in erg s^{-1} Hz^{-1}) which spans the range $0 < z \leq 2$ (encompassing the z distribution to 6σ). The corresponding number density is calculated and the K-correction is used to convert the fluxes into a matrix of soft X-ray fluxes. These number densities are sorted into bins of width $\Delta \log S_{\mathrm{SX}} = 0.1$ and $\Delta z = 0.2$ in the ranges $-19 \leq \log S_{\mathrm{SX}} \leq -13$ and $0.1 \leq z \leq 1.9$, respectively. The resulting $\log N - \log S$,

integrated over z, is shown in Figure 2.22.

To generate a galaxy sky field the $N(S_{\rm SX}, z)$ model is sampled as a Poisson distribution of expectation $N \times area$ for each point in $(S_{\rm SX}, z)$, where $area$ is the sky area of the cluster sky field. Each galaxy is assigned a random RA and Dec coordinate from the same distribution used for the AGN positions, described in the next section. This produces a correlation with the cluster positions. An alternate approach would be to position the galaxy emission at the locations of the MS halos below the mass cut. However, the method used in XIS allows for a wide variety of point source distributions to be created, and point source positions to be correlated to clusters which are not sourced from a cosmological simulation.

The contribution from the different emission components varies for different galaxy types, and is also dependent on star formation activity. A two-component spectral model is adopted for all simulated galaxies, consisting of an APEC hot plasma model and a power law, which are each allocated 50% of the flux. The thermal model used $T = 0.6$ keV and $Z = 0.8$ $\rm Z_\odot$, based on the best fitting diffuse single component model of Kobulnicky & Martin (2010) after their removal of compact sources from a starburst galaxy. The spectral index of the power law component is fixed at $\Gamma = 2.1$ following RCS03.

From an X-ray perspective, the distinction between emission from small galaxy groups and individual galaxies is unclear. The emission from the gravitational well of a cluster scales down for smaller halos (although not necessarily in a self-similar fashion). No obvious distinction exists in the MS halo catalogue. To avoid having too many faint sources in the sky field due to an over-abundance of galaxy-size X-ray emitting halos it is important to set a sensible cut-off mass in the cosmological simulation. A mass cut of $M_{500} = 2 \times 10^{12}$ h^{-1} $\rm M_\odot$ excludes large spiral galaxies from the cluster sky field and, via the local $M_{500} - T$ relation, is associated with the lowest temperature source used to derived the $L_{500} - T$ relation. However, it should be noted that the most luminous galaxy in the RCS03 full sample had an equivalent mass of $M_{500} \sim 5 \times 10^{12}$ h^{-1} $\rm M_\odot$ via the XIS

Table 2.2: The number of galaxy X-ray halos that it might be possible to resolve in IXO simulations, assuming that the $M_{500} - T$, $r_{cf} - T$ and $\beta - T$ relations[a] remain valid for these galaxy-scale masses. Halos are counted in 4 logarithmic M_{500} bins below the mass limit of the lightcone. The top row gives the number per square degree, while the bottom row gives the number as a fraction of all the systems (resolved or not) within this bin.

$\log M_{500}$[b]	$11.5 - 11.7$	$11.7 - 11.9$	$11.9 - 12.1$	$12.1 - 12.3$
N (deg^{-2})	5	257	469	428
Fraction	0.019	0.035	0.066	0.119

[a] β values have a lower limit of $\beta = 0.3$.
[b] M_{500} is in units of h^{-1} M$_\odot$.

cluster scaling relations, so some overlap between the galaxy and cluster sky fields may be present.

To test the validly of only including point-like galaxies, a lightcone with a lower mass limit is used to examine the X-ray emission of MS halos with $M_{500} < 2 \times 10^{12}\ h^{-1}$ M$_\odot$. Since the distribution of the flux is important, the cluster β-model is used to determine the FWHM of each system. We then count the number of systems that exceed 1 arcsec FWHM in a range of M_{500} bins. This width is one-fifth of the IXO PSF FWHM and approximately the size of one detector pixel, making such extended sources difficult to resolve. The results are given in Table 2.2. Immediately below the mass limit $\sim 12\%$ of the halos meet this size criterion. This number drops to half for halos appoximately half this massive. Therefore, the number of galaxy-size halos that we expect to be noticably extended is a small fraction of the population. Note that there is a flux element to detecting an object as extended, so with this taken into account the difference between the mass bins would be greater.

Representing galaxies as extended sources would spread their flux over more of an image. This would make the population slightly more difficult to detect, but some systems may become more distinguishable from AGN. Since the flux from undetected systems effectively becomes part of the X-ray background, spreading this flux out would increase the homogeneity of the background.

The properties of galaxies in XIS are summarised in Table D.2 (Appendix D).

2.3.2 Active Galactic Nuclei

X-ray emission from AGN is often divided into two categories: unobscured and obscured (also known as type-1 and type-2). This obscuration comes in a variety of strengths, and highly obscured AGN are sometimes described as Compton-thick due to a diffusive process increasing the absorption of X-rays (Lamastra et al. 2006). The difference between sources with obscured and unobscured emission was believed to be a matter of viewing angle relative to a dusty torus which surrounds the AGN, which re-emits in the infrared (Barvainis 1987; Barthel 1989; Nenkova et al. 2002). However, this 'standard model' is insufficient to explain the variety of AGN that have been discovered (Hardcastle et al. 2006; Ogle et al. 2006), and both mass and accretion rate have been suggested as main drivers (Hardcastle et al. 2007). While the exact nature of the emission remains unclear, observation-based luminosity models provide a sufficient representation of the AGN population for use in these imaging simulations, especially since they are only required as a contaminating source.

The distribution of unobscured AGN in XIS is modelled using the best-fit evolving SXLF of Hasinger, Miyaji, & Schmidt (2005, hereafter HMS05):

$$\frac{d\Phi(L_{\rm SX},z)}{d\log L_{\rm SX}} = A_{44}\left[\left(\frac{L_{\rm SX}}{L_{\rm SX,*}}\right)^{-\gamma_1}+\left(\frac{L_{\rm SX}}{L_{\rm SX,*}}\right)^{-\gamma_2}\right]^{-1} e_d(z,L_{\rm SX}) \tag{2.24}$$

They obtained a number counts normalisation $A_{44} = (2.62 \pm 0.16) \times 10^{-7}\ h_{70}^3\ \mathrm{Mpc}^{-3}$ (defined at $\log L_{\rm SX} = 44$), pivot $\log L_{\rm SX,*} = 43.94 \pm 0.11\ h_{70}^{-2}$ erg s^{-1}, and gradients $\gamma_1 = 0.87{\pm}0.10$ and $\gamma_2 = 2.57{\pm}0.16$. They used Luminosity Dependent Density Evolution (LDDE), as suggested by Schmidt & Green (1983), with the $L_{\rm X}$ dependent z_c form of Ueda et al. (2003) with $z_{c,44} \equiv z_c(L_{\rm SX} = 10^{44}\ \mathrm{erg\ s^{-1}})$:

$$e_d(z,L_{\rm SX}) = \begin{cases} (1+z)^{p1} & (z \le z_c) \\ e_d(z_c)[(1+z)/(1+z_c)]^{p2}] & (z > z_c) \end{cases} \tag{2.25}$$

where

$$z_c(L_{\rm SX}) = \begin{cases} z_{c,44}(L_{\rm SX}/L_{{\rm SX},c})^{\alpha} & (L_{\rm SX} \leq L_{{\rm SX},c}) \\ z_{c,44} & (L_{\rm SX} > L_{{\rm SX},c}) \end{cases} \tag{2.26}$$

HMS05 expanded the formulation to allow p_1 and p_2 to be dependent on luminosity:

$$p1(L_{\rm SX}) = p1_{44} + \beta_1(\log L_{\rm SX} - 44) \tag{2.27}$$

$$p2(L_{\rm SX}) = p2_{44} + \beta_2(\log L_{\rm SX} - 44) \tag{2.28}$$

Their best fitting model had $z_{c,44} = 1.42 \pm 0.11$, $\log L_{\rm SX} = 44.67\ h_{70}^{-2}$ erg s^{-1}, $\alpha = 0.21 \pm 0.04$, $p1_{44} = 4.7 \pm 0.3$, $p2_{44} = -1.5 \pm 0.7$, $\beta_1 = 0.7 \pm 0.3$, and $\beta_2 = 0.6 \pm 0.8$. This function fits the observed flattening of the low luminosity end of the SXLF at high redshift.

The SXLF is used to generate an unobscured AGN $N(S, z)$ function for use in XIS. A matrix of $41 \leq \log L_{\rm SX} \leq 48$ and $0 < z \leq 4.8$ is established and used to calculate the corresponding fluxes, based on the limits of the HMS05 sample but extrapolated one decade lower in luminosity. The SXLF is then integrated over bins of width $\Delta \log S_{\rm SX} = 0.1$ and $\Delta z = 0.2$ with centres the ranges $-18 \leq S_X \leq -9$ and $0.1 \leq z \leq 4.7$, respectively, using the volume per square degree in each redshift bin to convert to a number density on the sky. The AGN SXLF and derived $\log N - \log S$ are shown in Figure 2.23. As an additional consistency check the $\log N - \log S$ is compared with that from the recent AEGIS-X (Laird et al. 2009), corrected for Galactic absorption.

GCH07 performed the same extrapolation of the low-end of the SXLF and found that it over-predicts the number of unobscured AGN observed by HMS05 with $S < 10^{-16}$ erg cm^{-2} s^{-1}. However, a comparison with the local optical luminosity function by Schulze et al. (2009) revealed considerably more low luminosity AGN than predicted by the SXLF. They suggested that either the assumed luminosity-dependence of the optical/X-ray ratio was too strong, or that the faint-end of the X-ray sample is incomplete. Also the presence of only broad-line AGN in both samples meant that any incompleteness should be independent of obscuration. Due to the uncertainty at the faint-end of the

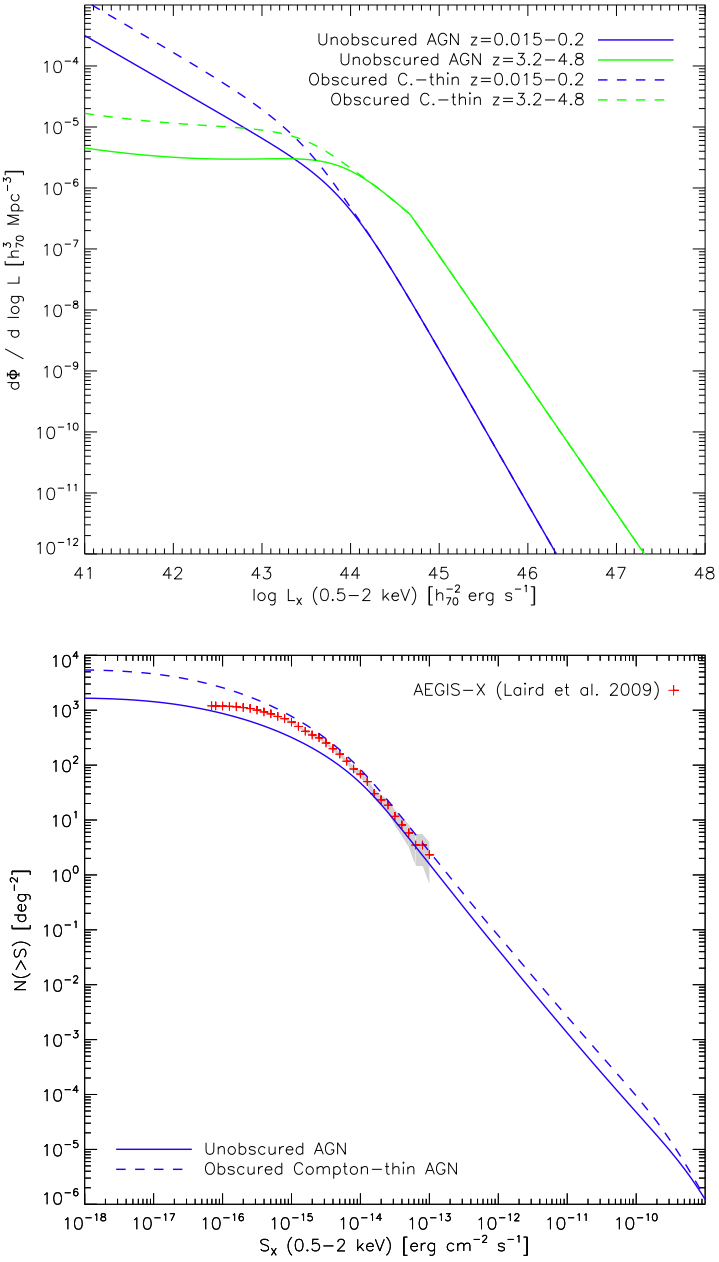

Figure 2.23: Top: AGN evolving SXLF using the best-fitting model of HMS05 (solid lines), along with the distribution of Compton-thin ($21 < \log n_H < 24$) sources from GCH07 (dashed lines). Blue lines show the mean density for $0.15 \leq z \leq 0.2$, whilst the green lines show that for $3.2 \leq z \leq 4.8$. Bottom: Lines show the cumulative unabsorbed $\log N - \log S$ from the above model, integrated over the entire redshift range. Data points show the results of AEGIS-X (Laird et al. 2009), with Poissonian counting errors given by the shaded region.

SXLF, we make no attempt to adjust the HMS05 model.

To create a distribution of obscured AGN, the SXLF is augmented with the ratios stated in GCH07. The amount of obscuration of each source is represented by a neutral hydrogen column density n_H, with unobscured sources having negligible n_H compared to the Galactic absorption. Defining $21 < \log n_H < 24$ as obscured Compton-thin and $\log n_H > 24$ as obscured Compton-thick, the ratio R of obscured Compton-thin AGN to unobscured AGN was given as:

$$R(L_{\rm SX}) = R_S e^{-L_{\rm SX}/L_{{\rm SX},c}} + R_Q(1 - e^{-L_{\rm SX}/L_{{\rm SX},c}}) \tag{2.29}$$

where R_S is the ratio in the Seyfert regime, R_Q is the ratio in the Quasi-stellar Object (QSO) regime, and $\rm L_{SX}$ is the characteristic $0.5 - 2$ keV luminosity that separated the two regimes. For a fixed $\log L_{{\rm SX},c} = 43.5$, their model, which fits both the soft and hard XLF well, has best fitting values of $R_S = 3.7$ and $R_Q = 1.0$. They calculate the fraction of sources which are present in bins of width $\Delta \log n_H = 1$ with centres of $\log n_H = 21.5, 22.5, 23.5, 24.5, 25.5$. The respective results are $R(n_H) \simeq 0.05, 0.35, 0.60, 0.50, 0.50$ as a ratio to the number of Compton-thin AGN (i.e. the total of the first 3 bins equals 1). These ratios are used to add an n_H dimension to the AGN distribution in XIS, with 5 values that matched the same bin centres as stated above along with the original $n_H = 0$ distribution of HMS05. The result is a coarse distribution function $N(S_{\rm SX}, z, n_H)$.

As with a galaxy sky field, an AGN sky field is created by sampling the $N(S_{\rm SX}, z, n_H)$ model as a Poisson distribution of expectation $N \times area$ for each point in $(S_{\rm SX}, z, n_H)$. The RA and Dec of each source is assigned using the method discussed below.

The gravitational instability paradigm of structure formation in the Universe involves the collapse of matter into halos, within which galaxies form and cluster. Consequently, unless the dense environment suppresses the accretion mechanisms, one would expect a correlation between the positions of clusters and the positions of AGN, which reside inside galaxies. Overdensites of AGN have been observed in the outer regions of clusters

(Henry & Briel 1991; Cappi et al. 2001), and measurements of the spatial correlation between AGN have been measured (Mullis et al. 2004a; Gilli et al. 2005; Basilakos et al. 2005).

The results of Cappelluti et al. (2007) are used to weight the randomly assigned positions of the simulated AGN in XIS, correlating them to the 3D cluster positions. They calculated the three-dimensional cross-correlation between the positions of AGN and those of clusters in the ROSAT North Ecliptic Pole (NEP) survey:

$$\xi_{\rm CA}(s) = \left(\frac{s}{s_0}\right)^{-\gamma} \tag{2.30}$$

where s_0 and γ are free parameters, and ξ_{CA} is defined by the joint probability of finding, at distance s, both one cluster and one AGN in the infinitesimal comoving volume elements $\delta V_{\rm C}$ and $\delta V_{\rm A}$, respectively,

$$\delta P = n_{\rm C} n_{\rm A}[1 + \xi_{\rm CA}(s)]\delta V_{\rm C}\delta V_{\rm A} \tag{2.31}$$

where $n_{\rm C}$ and $n_{\rm A}$ are the mean comoving number densities of clusters and AGN, respectively. Their best-fit values were $s_0 = 8.7^{+1.2}_{-0.3}$ Mpc and $\gamma = 1.7^{+0.2}_{-0.7}$, and they considered no data with $s < 2.5$ Mpc.

The 3D probability distribution for AGN in the cluster lightcone is produced by combining the probability distributions around each cluster. A matrix is generated representing (RA,Dec,z) space equivalent to the cluster sky field, with coarse elements of ΔRA and ΔDec = 30 arcsec, and $\Delta z = 0.2$. The choice of redshift binning is for consistency with the AGN distribution, whilst the angular resolution is to keep memory usage reasonable. A corresponding flat probability matrix is created. These coordinates are converted into comoving positions and then into comoving displacements from each cluster, which are then used to calculate the enhanced probability P in each element. Defining $s_{\rm min} = 1.75\ h^{-1}$ Mpc and using $s_0 = 6.09\ h^{-1}$ Mpc and $\gamma = 1.7$, the cross-correlation

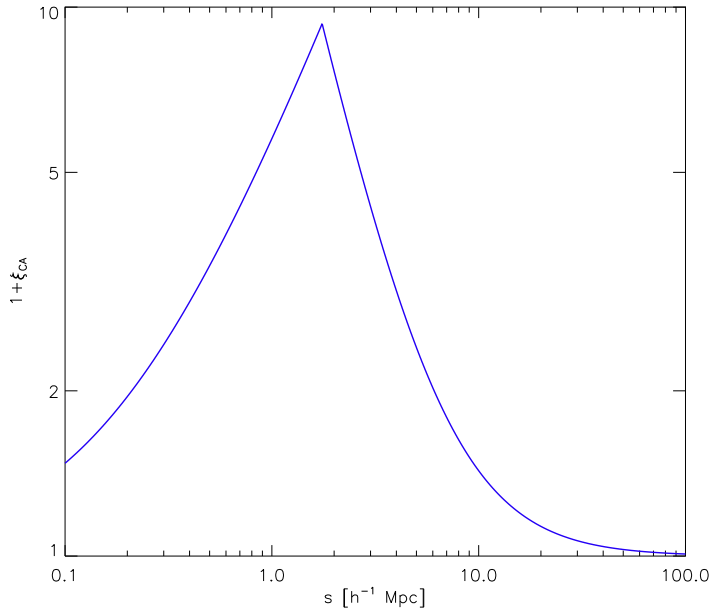

Figure 2.24: Cluster-AGN spatial cross-correlation function in XIS, using the best-fitting model of Cappelluti et al. (2007) and a linear decrease to $\xi = 0$ from their minimum considered distance to $s = 0$.

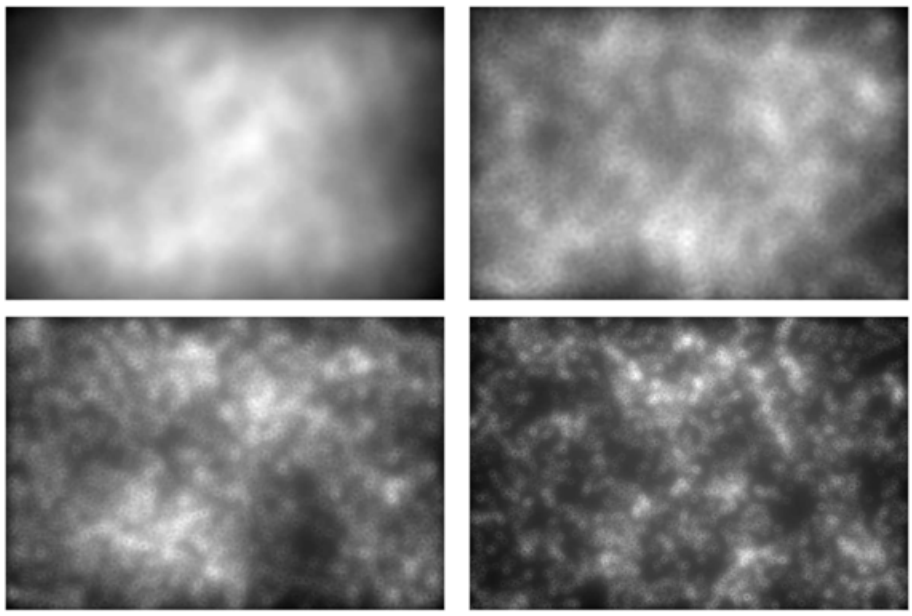

Figure 2.25: AGN position function generated by the XIS application of the spatial cross-correlation model shown in Figure 2.24 to the primary cluster sky field, which has an angular size of 4.77×3.18 degree^2. Each image is an example of one redshift bin of size $\Delta z = 0.2$, centred on *from top-left to bottom-right:* $z = 0.1$, 0.7, 1.3 and 1.9, with equivalent physical sizes of 22.2×14.8, 87.1×58.1, 103×68.6 and 104×69.1 h^{-2} Mpc^{-2}, respectively. The grey scale represents the probability of an AGN occupying that position (brighter is more probable), normalised to the maximum within the z bin.

function is defined as

$$\xi_{\rm CA}(s) = \begin{cases} \xi_{\rm CA,max} s/s_{\rm min} & s \leq s_{\rm min} \\ (s/s_0)^{-\gamma} & s > s_{\rm min} \end{cases} \tag{2.32}$$

where

$$\xi_{\rm CA,max} = (s/s_{\rm min})^{-\gamma} \tag{2.33}$$

i.e. it includes a linear decrease to zero below the minimum considered value of $s = 2.5$ Mpc. This function can be seen in Figure 2.24. To ensure that each cluster is fairly represented in the low resolution redshift space it is assumed to be at the redshift of its nearest z bin. For efficiency, the effect of a cluster is only calculated in its redshift bin. The smallest separation between bins in comoving space is $> 100\ h^{-1}$ Mpc, therefore clusters within one bin have a negligible effect on the other bins. Due to computing requirements, the integration of $\xi_{\rm CA}$ for each cluster is limited to the resolution of the coordinate matrix. The position of each AGN is decided using rejection sampling of a randomly generated (RA,Dec,P) within the appropriate z bin. As the redshifts of each AGN are defined by the $N(S_{\rm SX}, z, n_H)$ model, each redshift bin of the probability matrix is normalised to the maximum value within that bin.

A sample of the resulting correlation for the primary cluster sky field is presented in Figure 2.25. A more plausible AGN placement method would include higher probabilities at $s < 1$ Mpc (see Gilmour et al. 2009). This is discussed in detail in Appendix A.3.

The Cappelluti et al. (2007) study had a flux limit of 2×10^{-14} erg cm^{-2} s^{-1}, and included only clusters with $z \leq 0.81$ and AGN with $z \leq 1$. Assuming hierarchical structure formation, it is quite possible that the cross-correlation has a dependence on mass and redshift. However, with no strong evidence to support such evolution, the same correlation function is applied across the entire mass and redshift range of the sky field.

The same probability 'map' is used to correlate the galaxy positions with those of the clusters, defining $\xi_{\rm CG}$. The spatial position of galaxies and cluster are, by definition, linked and positive spatial correlations have been measured between different source selections (Lilje & Efstathiou 1988; Mo et al. 1993; Sánchez et al. 2005). The cross-correlation

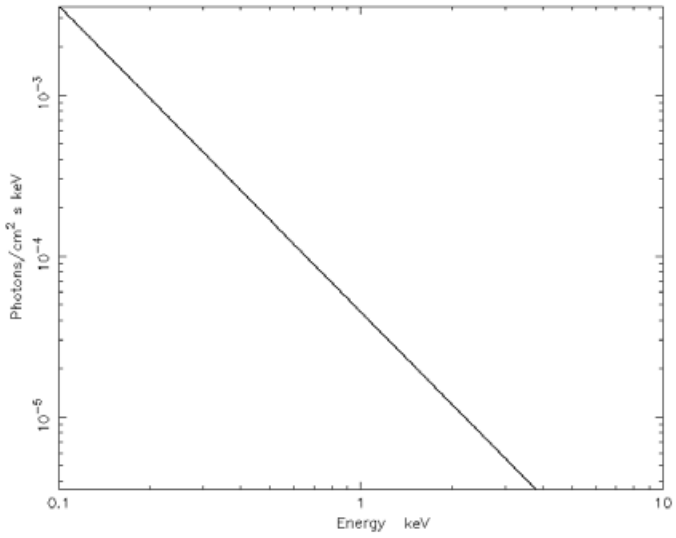

Figure 2.26: Example of a power law spectral model used for the AGN in XIS. This model has $z = 0.3$, $S_{\rm SX} = 10^{-13}$ erg cm^{-2} s^{-1} and $\overline{\Gamma} = 1.9$.

length and slope between infrared galaxies and Abell clusters measured by Mo et al. (1993) are similar to that for the $\xi_{\rm CA}$ of Cappelluti et al. (2007). For these reasons a spatial correlation is included between galaxies and clusters, and for simplicity $\xi_{\rm CG} = \xi_{\rm CA}$.

The X-ray spectrum of an AGN is usually represented as a power law with an optional obscuring component. For $z \lesssim 5$, the slope of this power law is not significantly redshift dependent and has a mean of $\overline{\Gamma} \approx 1.9$ (see GCH07 and references therein). The dispersion around this mean is $\sigma_\Gamma \simeq 0.2 - 0.3$. A hardening of the spectrum above $8 - 10$ keV and a 6.4 keV iron line are also significant features, but well above the energy band covered in this research. To simulate the spectra of AGN, XIS uses a simple model consisting of a redshifted power law multiplied by a redshifted absorption component. Each AGN is assigned a spectral index Γ from a normal distribution with $\overline{\Gamma} = 1.9$ and $\sigma_\Gamma = 0.2$, as assumed by GCH07. To allow for bulk spectral calculations, these values are rounded to the nearest bin with centres from $\Gamma = 1.5$ to $\Gamma = 2.3$ and width $\Delta\Gamma = 0.1$. An example of a power law spectral model is given in Figure 2.26.

The properties of AGN in XIS are summarised in Table D.3 (Appendix D).

2.3.3 Cosmological X-ray Background

A large portion of the hard XRB has been found to be a result of unresolved point sources, such as AGN. This is often modelled as a power law, hence it is known as the Extragalactic Power-Law (EPL) (Kuntz & Snowden 2000). The cosmological X-ray background can be accounted for at medium and high fluxes by using the AGN model described above, and accuracy at low fluxes can be improved by adding the galaxy model described in Section 2.3.1 (Gilli et al. 2007; Ranalli et al. 2003).

Since these models are used to generate point sources in the simulator, the amount of flux that becomes unresolved depends on the angular resolution of the simulated observatory. With the theoretical angular resolution of IXO subject to change, individual point sources provide a more appropriate model than representing the background as a flat X-ray flux across the whole image. For efficiency when producing IXO simulations, point sources below $S_{\mathrm{X}} = 10^{-17}$ are represented by a flat background. This is covered further in Section 2.4.10, when observatory simulation is discussed.

2.3.4 Diffuse Soft Background

Very low energy X-ray emission can be observed over the entire sky, producing background counts in all images. The Diffuse Soft Background (DSB) is comprised of diffuse emission from the Galactic disk and halo, and possibly from the local hot bubble (Read & Ponman 2003). It could also contain intergalactic warm gas (Cen & Ostriker 1999). A complication of the DSB is the variation in its intensity over the sky (Snowden et al. 1995; Markevitch et al. 2003) (see Figure 2.27). The coordinates of simulated sources in XIS have no relation to real positions on the sky, so we treat the diffuse soft background as spatially invariant. This invariance is mirrored in the fixed Galactic n_H used in these simulations.

We assume that all simulated observations in this work are pointed towards regions of low DSB. The intensity of the DSB is estimated from the results of a Chandra-based

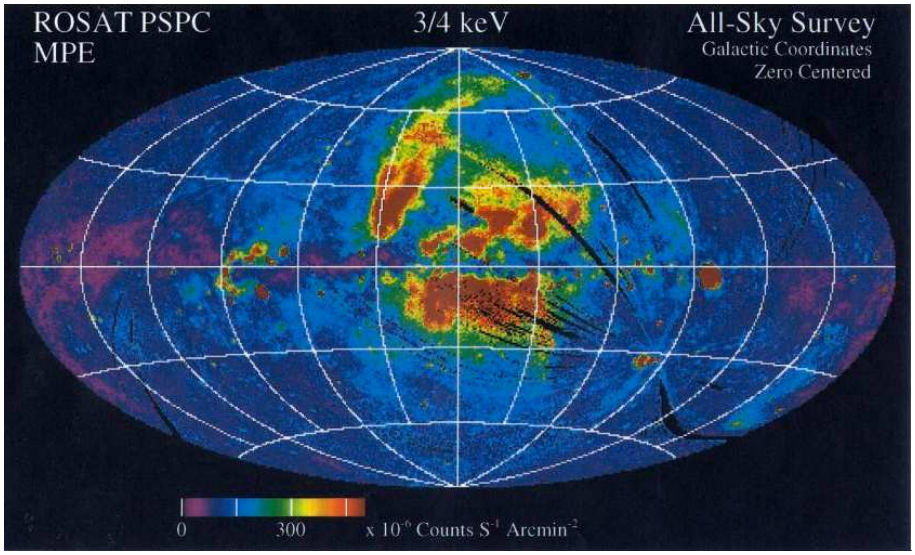

Figure 2.27: All-sky map of the DSB from ROSAT PSPC observations in its $\frac{3}{4}$ keV band. Figure credit: Snowden et al. (1995).

study by Markevitch et al. (2003). They estimated the flux of the diffuse background from two deep observations away from bright features, obtaining $S_{\rm X}$ = (2.5 and 1.7) $\times 10^{-15}$ erg cm^{-2} s^{-1} arcmin^{-2} in the $0.3-2.0$ keV energy band. For use in XIS, these results are converted into the $0.5-2$ keV band using their best-fit spectral models. This gives a mean value of $S_{\rm X} = 3.86 \times 10^{-19}$ erg cm^{-2} s^{-1} arcsec^{-2}, which is used as the flat DSB. Using only measurements away from bright features means that all simulated pointings, and hence the sky fields, are assumed to be similar low background regions of the sky.

All simulations within this research include the DSB. We represent it with a Raymond-Smith thermal plasma model with the mean properties of the Markevitch et al. (2003) fits: $T = 0.185$ K, Solar abundance and no Galactic absorption.

2.3.5 Total Source $\log N - \log S$

The cumulative flux function $\log N - \log S$ result of the completed primary and secondary sky fields is shown in Figure 2.28. These plots display the relative contributions of flux that are present in XIS simulations. By comparing the number of high flux sources in the

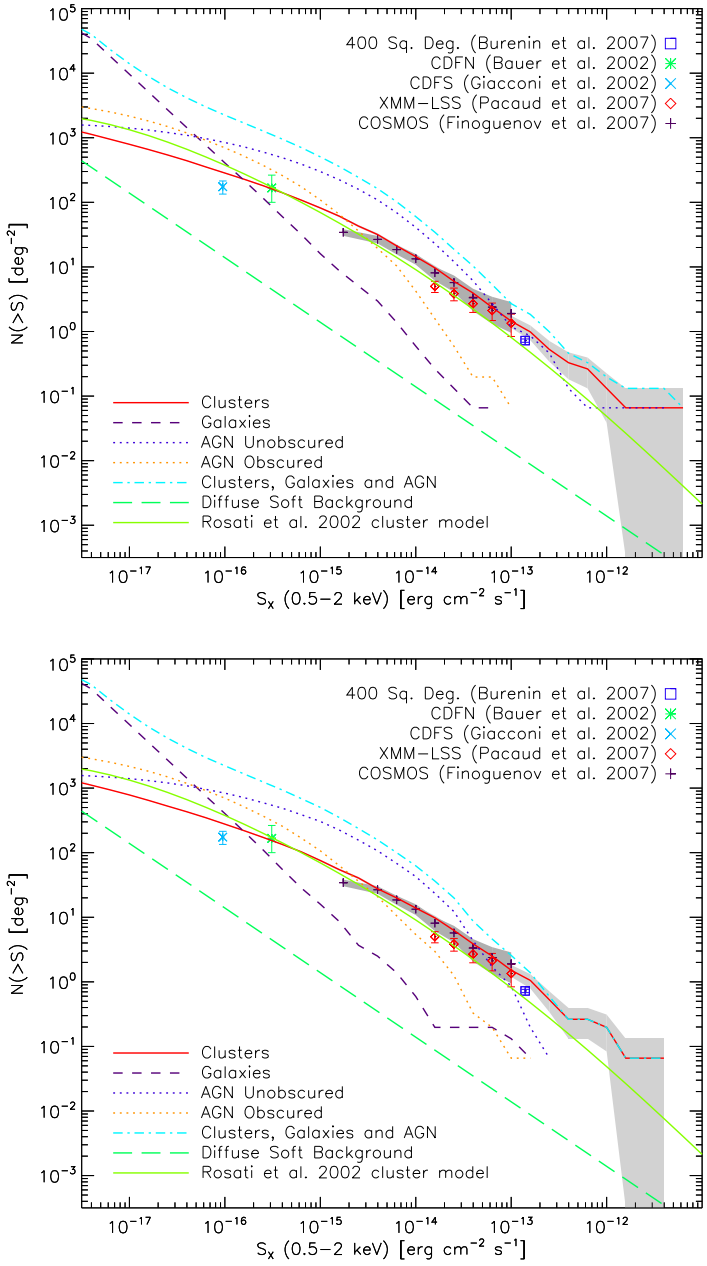

Figure 2.28: *Top:* Cumulative $\log N - \log S$ plot comparing the various source types in the primary sky field and observational results. The solid red line shows the sky field clusters and the solid green line represents the non-evolving SXLF of Rosati et al. (2002) derived above 10^{41} erg cm^{-2} s^{-1}. The points show the results of cluster surveys by Bauer et al. (2002); Giacconi et al. (2002); Burenin et al. (2007); Finoguenov et al. (2007); Pacaud et al. (2007). Error bars give Poissonian 1σ confidence levels for the observational data. The light shaded area shows the 1σ confidence interval around the sky field clusters, while the dark shaded area shows that around the Finoguenov et al. (2007) clusters. The dashed purple line shows the sky field galaxies, whilst the dotted dark blue and orange lines show the sky field unobscured and obscured AGN, respectively. Flux shown here for the obscured AGN is that after obscuration, which reflects its relative contribution to observations. The total flux density of sources in the sky field is given by the light blue dash-dot line, and the effective DSB is represented by the dashed green line (assuming 1 source with the flux of the DSB). *Bottom:* As above but for the secondary sky field.

two fields the effect of cosmic variance becomes evident. Galaxy flux does not become significant until $S \lesssim 10^{-16}$ erg cm^{-2} s^{-1}, whilst unobscured AGN flux density dominates from $S \lesssim 10^{-13}$ erg cm^{-2} s^{-1}.

Note that galaxy and AGN flux is concentrated into point sources, whilst cluster flux is distributed over the region within R_{200} based on the surface brightness profiles. Therefore this plot does not directly give the relative detection probability of each source. The recovered $\log N - \log S$ for different IXO configurations is investigated in Chapter 5.

2.4 Instrumental Effects

The final section of this chapter covers the simulation of the technical aspect of X-ray observations. Instrumental effects separate how the different observatories perceive sources in the sky. Several of these were covered in sections 1.1.3 and 1.1.4, including the vignetting, PSF and particle background. This section describes all of the instrumental effects that are included in XIS simulations.

To begin the simulation process we calculate the expected count rate for each source, based on the effective area of the mirror and detector combination. A vignetted background image is created and convolved with the PSF. Vignetted point source models are added to the image using the shape of the PSF, followed by cluster models using vignetted β-models convolved with the PSF. The image is placed onto a simulated detector layout and particle background is added. Poisson noise is applied to finalise the image. These stages are described in more detail below.

2.4.1 Review of Observatory Design

XIS is capable of simulating images for any X-ray observatory, provided the instrument response is available. For this research, the observatory properties of interest are those of, or coupled with, the IXO WFI within the $0.5 - 2$ keV energy band (the band most sensitive to cluster emission). We also simulate the Chandra and XMM-Newton observatories

Table 2.3: Summary of the two IXO and WFI configurations used in this research, along with the comparison instruments Chandra ACIS-I and XMM-Newton EPIC pn.

Configuration	Focal length (m)	Effective area (m^2)	Field of view (arcmin)	Pixel size (μm)	Pixel size (arcsec)	PSF FWHM (arcsec)
ACIS-I	10.066	0.08 @ 0.25 keV	30	24	0.49179	0.425
EPIC pn	7.5	0.155 @ 1.5 keV	30	150	4.1253	6.677
IXO-09	25	3 @ 1.25 keV	14	99.42468	0.82031	5
IXO-10	20	3 @ 1.25 keV	18	100	1.0313	5

for comparison. The concept of IXO was reviewed in Section 1.1.6 and the missiontarget properties of the WFI are available in Appendix B.1. However, due to the continuously changing nature of the IXO design, two different configurations are used in this research, which are referred to as IXO-09 and IXO-10. The former is based on design studies available in 2008 and early 2009, whilst the latter uses the properties covered in Section 1.1.6. Development of the simulator during the course of this research also has an effect on the implementation of those properties. IXO-09 assumes a 25 m focal length and field of view radius R_{FoV} of 7 arcmin, while IXO-10 has a 20 m focal length and $R_{\mathrm{FoV}} = 9$ arcmin.

The IXO-09 design is used for the survey biases study, whilst IXO-10 is used for exploring the instrument trade-off, i.e. the change in observatory effectiveness when changing the instrument properties.

The concept for the WFI is a single CCD consisting of approximately 1024×1024 pixel^2. Based on a more simplistic simulation of the WFI, the IXO-09 configuration in XIS assumes that the 14 arcmin field of view is entirely covered by the WFI, and therefore has a pixel size of approximately 0.8203 arcsec $\equiv$ 99.425 μm. The more developed IXO-10 configuration uses the design reviewed in Treis et al. (2009), with 100 μm pixels. This is equivalent to 1.0313 arcsec/pixel and means that the WFI covers 17.6 arcmin of the 18 arcmin diameter field of view.

Detectors from two current generation observatories are also set up for accuracy checks and comparison with IXO: Chandra ACIS-I and XMM-Newton EPIC pn, referred to by their detector names. These are chosen because of their simple detector layouts and common use in imaging. The EPIC pn response we use is that for the thin filter. A

summary of all the configurations is presented in Table 2.3.

2.4.2 Effective Area and Detector Response

The first stage of simulating an observatory in XIS is to calculate the count rate for each source based on the mirror on-axis effective area and detector response. A count rate model is preferred over the ray-tracing simulation approach due to the high throughput of IXO, which would result in a very large number of photons to process. While the simulation process attempts to mirror the workings of an X-ray observatory by applying effects in the same order as occurs in reality, the approach described below requires the detector response to be determined before the optical effects of vignetting and PSF are applied. The scaling nature of these effects and the level of detailed used in XIS means that this order does not significantly effect the accuracy of the results. In reality the response of a detector CCD can vary from position to position. This variation is not applicable to IXO at this time and is not included in XIS.

The tool used for the count rate calculation procedure is the X-ray spectral fitting package XSPEC 11.3.1 (Arnaud 1996), which can simulate the response of an observatory to a complicated X-ray spectrum. For efficiency, the count rate output is the integrated count rate within an energy band, rather than that within each detector channel or a smooth continuum. Three energy bands are made available: $0.5-2$, $2-5$ and $5-10$ keV; referred to as soft, medium and hard, respectively. The latter two are not used in this research.

To produce the simulated count rate XSPEC usually requires two files. One of these is the Ancillary Response File (ARF), which contains the effective area as a function of energy for the mirror and detector combination. This includes the mirror effective area, detector quantum efficiency and, if applicable, bad pixel locations. The other requirement is a Redistribution Matrix File (RMF), which gives the detected properties of an incoming photon based on its physical properties. Both files can be combined into a single response file.

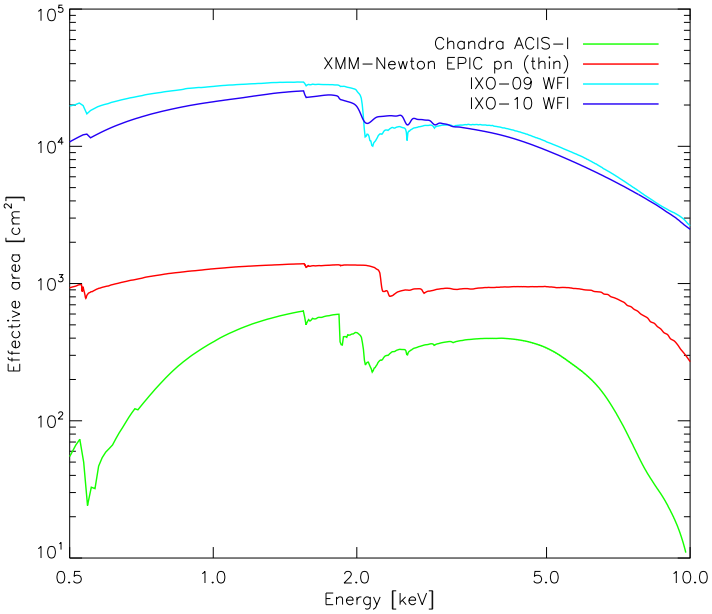

Figure 2.29: Effective areas of the observatory configurations used in XIS.

Several response files have been made available for IXO design studies, representing different mirror and instrument technologies. This work uses the response files of the silicon pore optics design, the European mirror system. For IXO-09, simulations are performed using the WFI response file dated 30/10/08. IXO-10 uses the response file dated 27/05/10 which includes a thick optical blocking filter. The response of both IXO configurations is shown in Figure 2.29.

Each different spectral model among the sources within the pointing field is processed through XSPEC. The spectra of all extragalactic sources are multiplied by a `wabs` photo-electric absorption model (Morrison & McCammon 1983) to represent Galactic absorption. This model uses the same absorption column n_H for all regions on a pointing. $n_H = 10^{20}$ cm^{-2} for all simulations in this work.

To decrease the time taken per simulation, a set of pre-calculated count rate tables are utilised. The cluster tables contains 250 logarithmic redshifts with $0 \leq z \leq 3.5$ and 1000 logarithmic temperatures with $0.05 \leq T \leq 20$ keV. An example is presented in Figure 2.30. Interpolation on this table gives an approximate count rate for the source.

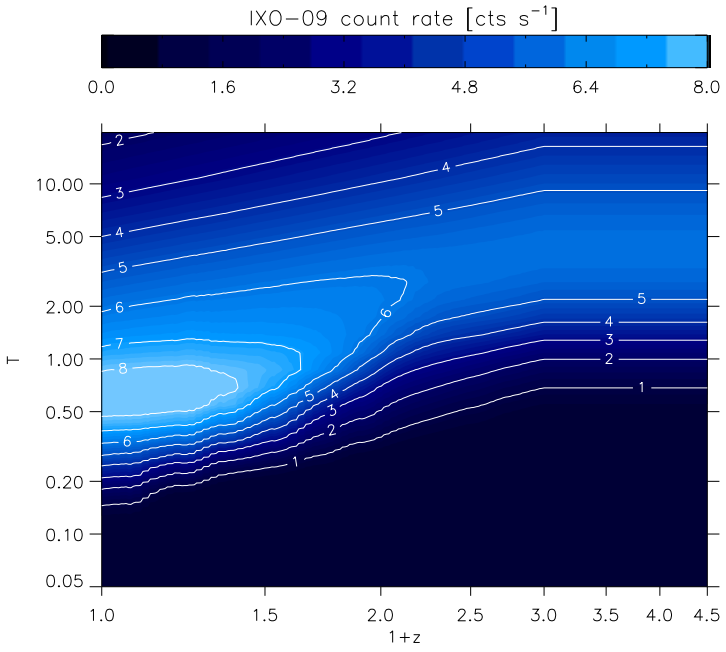

Figure 2.30: IXO-09 $0.5-2$ keV count rate for an unabsorbed bolometric flux of 10^{-12} erg cm^{-2} s^{-1} as a function of redshift and temperature. Spectrum is an APEC model with $Z = 0.3$ multiplied by an absorption component with $n_H = 10^{20}$ cm^{-2}. The maximum value in the table is 8.709 cts s^{-1}.

Galaxy, AGN and DSB tables include all permutations that are present in the XIS models. For all sources except clusters, these tables are used every time. The cluster table is only used when processing a large number of pointings (i.e. > 10).

Using the default XIS model, the IXO-09 $0.5-2$ keV cluster count rate peaks for low redshift systems with $T \approx 0.6$ keV. However, the majority of such systems are dim due to their low luminosity.

2.4.3 X-ray Background

With the count rates for each source available, the next step is to build an image of the extraction field, defined in Section 2.1.2. This starts as a square array with sides equivalent to the extraction field diameter and pixel size equivalent to that of the detector. The first component we add is the DSB. Since a spatially-invariant DSB is used, a single count rate is added to the entire array, which is then referred to as the background image. The DSB model gives the following $0.5-2$ keV rates in cts s^{-1} arcsec^{-2} for the four configurations:

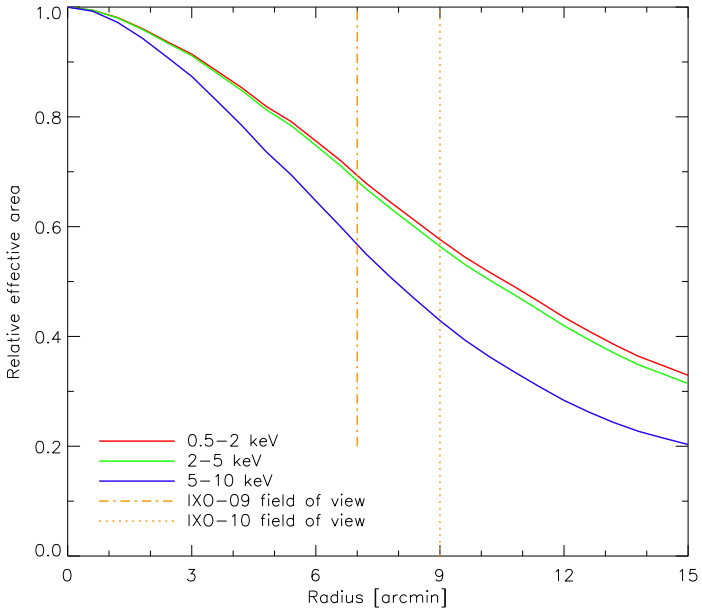

Figure 2.31: Off-axis effective area fraction as a function of energy as used in XIS. Red, green and blue solid lines show the profile for the soft, medium and hard bands, respectively. These profiles are used for all observatory configurations. Orange dash-dot and dotted lines indicate the field of view for IXO-09 and IXO-10, respectively.

ACIS-I 3.10×10^{-8}; EPIC pn 2.39×10^{-7}; IXO-09 6.93×10^{-6}; and IXO-10 5.21×10^{-6}.

A procedure to treat some point sources as cosmological XRB is also implemented. This is covered in Section 2.4.10.

2.4.4 Vignetting

Like other X-ray telescopes, we assume that the effective area of IXO is radially dependent, and this off-axis degradation is energy-dependent. No vignetting profile is available for IXO, so that of XMM-Newton is used with no rescaling. This is taken from the X-ray simulator QuickSim (Arida 2001). With the energy information of each source collapsed, the energy-dependence of the vignetting could not be applied accurately. For the purpose of vignetting, the energy of each photon is assumed to be at the middle of the energy band, e.g. 1.25 keV for $0.5 - 2$ keV. See Figure 2.31 for the form of these profiles. At the R_{FoV} of XMM-Newton, difference in effective area at 2 keV is 0.4% less than at 0.5 keV, so the difference across the soft band is considered to be negligible.

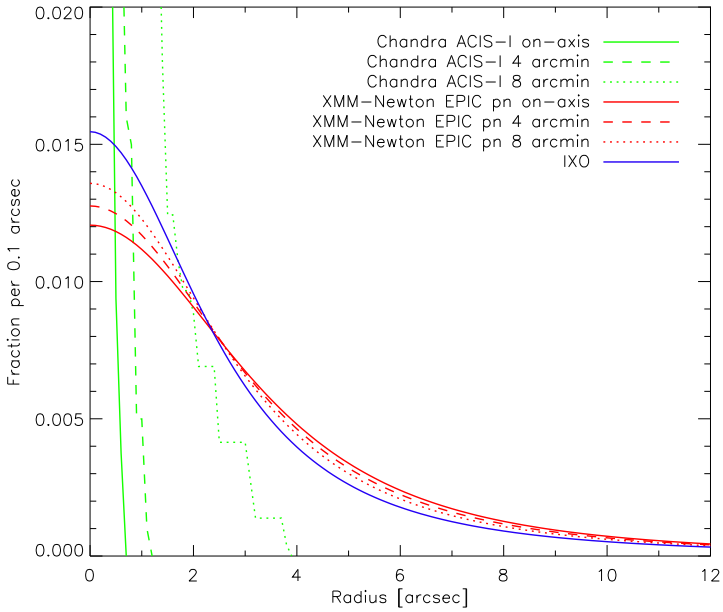

Figure 2.32: $0.5-2$ keV on-axis PSFs for all observatory configurations in XIS, shown by the solid lines, along with off-axis profiles for ACIS-I and EPIC pn at 4 and 8 arcmin, given by the dash and dotted lines, respectively. Note that the y-axis scale is for a 1D PSF.

At $r > R_{\rm FoV}$ the vignetting coefficient is set to zero, producing an edge to the field of view. The radially-calculated vignetting coefficient is applied to the background image and to each source. Point sources have their count rates reduced at this stage, whilst clusters have their surface brightness profiles vignetted during the process covered in Section 2.4.6.

2.4.5 Point Spread Function

Another effect of imperfect X-ray reflection is the Point Spread Function (PSF). The IXO PSF is modelled with a King function, which closely represents the XMM-Newton PSF:

$$\mathrm{PSF}(r) = \left[1 + \left(\frac{r}{r_c}\right)^2\right]^{-\beta} \tag{2.34}$$

where core radius

$$r_c = \frac{\mathrm{FWHM}}{2\sqrt{2^{1/\beta}-1}} \tag{2.35}$$

Expectations for IXO suggest that a FWHM = 5 arcsec and $\beta = 1.4$ are reasonable assumptions. A spatially invariant PSF is used for both IXO-09 and IXO-10. Spatial dependence is implemented for the other two configurations.

The PSF of XMM-Newton EPIC pn is based on the Read (2004) King function calibration data. This model uses a radially dependent r_c and β based on a mean of the values relevant to the energy band, and the enclosed energy fraction varies little with off-axis angle. No azimuthal modulation is included.

The Chandra ACIS-I PSF is spatially dependent and utilises the model of Laird et al. (2009), which is generated using Marx. This takes the form of a set of energy band tables containing profiles for many different physical coordinates on ACIS-I. Each profile is defined by 6 ellipses which represent the $50, 60, 70, 80, 90, 95\%$ enclosed energy radii. In XIS these ellipses are formed into a weighted stack to produce a PSF model. The soft band on-axis and off-axis PSFs are shown in Figure 2.32.

To carry out the research goals, the PSF needs to be applied considerably more quickly than by a pixel-by-pixel calculation. To facilitate this, each source is convolved with the PSF using a Fast Fourier Transform (FFT). This approach is fast but has two main disadvantages: no spatial dependence can be present in a convolution, and blurring that crosses one image edge appears on the opposite one. To partially-solve the former, each source has its own image generated and uses a PSF based on its location. Point sources use the PSF at their location as their image model, whilst cluster surface brightness profiles are convolved with the PSF of their centre. The background image is convolved with the PSF for $R_{\rm FoV}$, as the edge of the field of view is where the blurred background is most noticeable. For efficiency, the size of each source image is based on the extent of the source, with 129×129 pixel^2 used for all point sources and the PSF r_c added to the radius of cluster images. This cluster padding is implemented to limit the edge-effects of the FFT. The background image is given no padding due to the size of the extraction field.

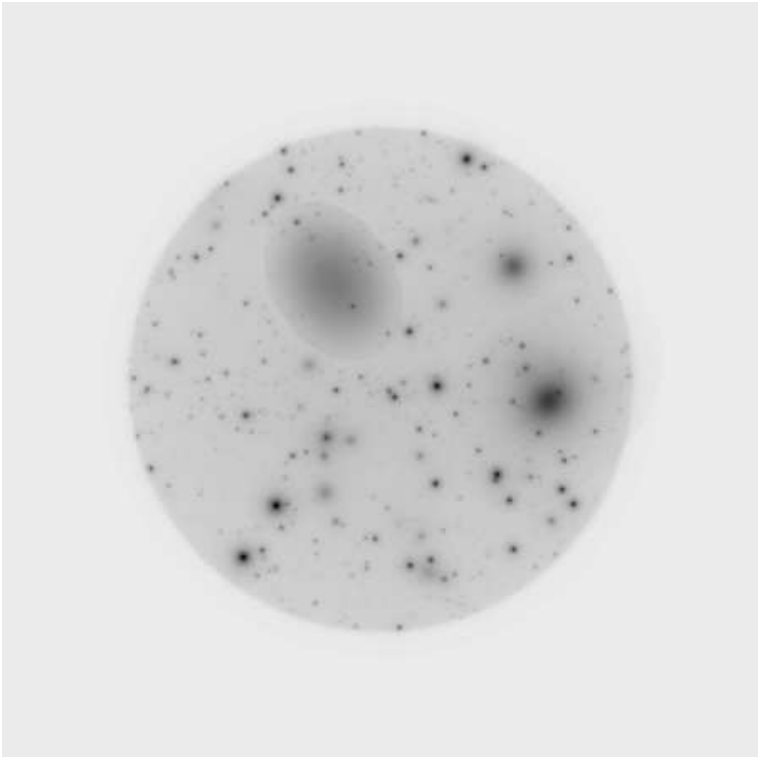

Figure 2.33: Mid-simulation $0.5 - 2$ keV IXO-10 image at the pre-CCD stage. Shown inversed (darker is a higher count rate) in a logarithmic scale.

2.4.6 Generating Source Models

As mentioned above, each source has its own image generated to allow for rapid off-axis PSF convolution. These images are created to align with the pixels of the background image for efficient addition of the source count rates to the total within that region. The centre of each source model is offset from the centre of the central pixel so that the astrometry is accurate. Point source images are PSF images of fixed size, whilst cluster images are 2D β-models large enough to have a radius of R_{200} plus the PSF padding.

Convolution of the clusters with an empty background produces an unrealistic reduction in flux at the surface brightness profile edge. To solve this, the β-model has a flat XRB rate added and is multiplied by an appropriate vignetting profile before applying the PSF. A matching PSF convolved XRB image is then subtracted from the cluster image.

Once all sources have been added, the background image is redefined as the 'field image'. An example of a simulated IXO-10 image at this stage is presented in Figure 2.33.

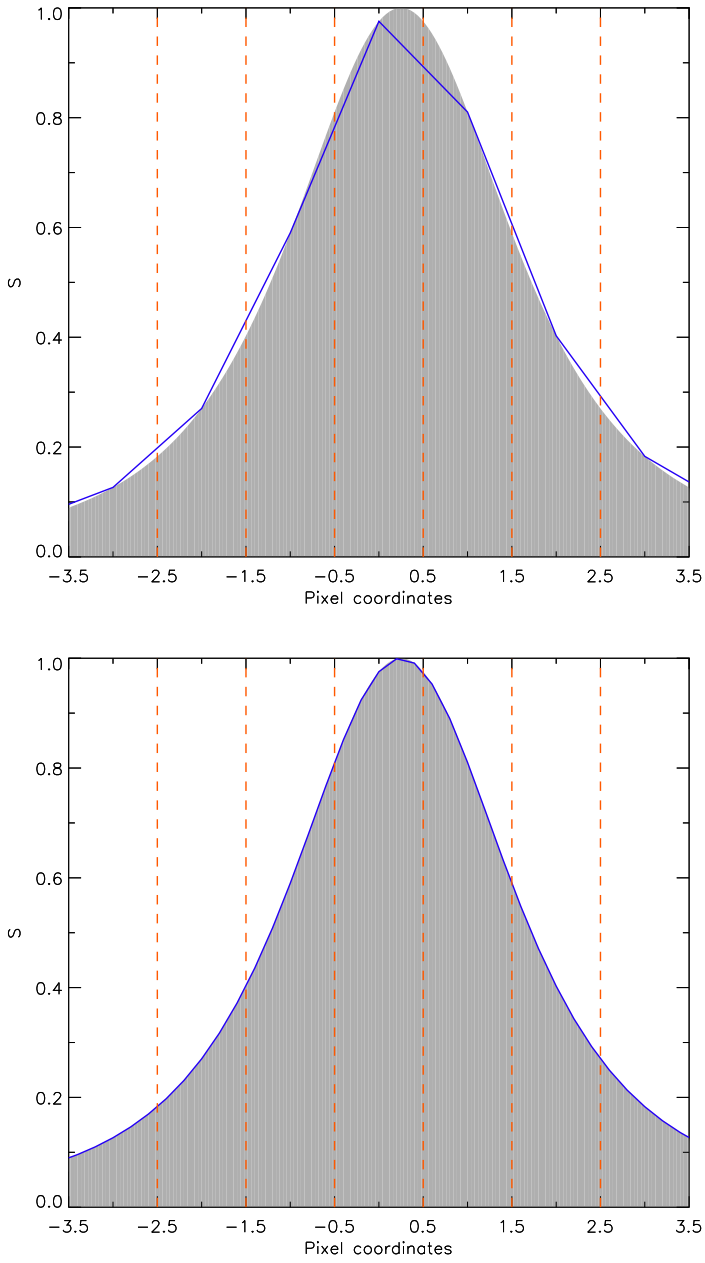

Figure 2.34: Effect of subgridding on model generation. Top: Pixel-resolution sampling of a β-model with $r_c = 2$ pixels and $\beta = 0.7$, offset from the centre of a pixel by 0.25 pixels. Shaded region gives the accurate β-model. Both models are normalised to the maximum of the shaded region. Pixels are divided by the dashed lines. Bottom: Same model with the sampling done using one-fifth of a pixel subgridding.

Use of a finite grid in the modelling of a source leads to inaccuracies analogous to a poorly resolved integration process. The effect of these inaccuracies is more serious when modelling extended sources with r_c similar to that of the PSF or similar in magnitude to the pixel size. Consider a β-model on finite pixel array, where the flux assigned to each pixel is based on the radial distance to the centre of that pixel. When the gradient of a source profile causes its flux to change significantly from one pixel to the next, the flux assigned to a pixel does not represent the integral of the model within the pixel, as illustrated in one dimension in Figure 2.34. The significance of this problem is amplified when a source is convolved with the PSF. This leads to poorly represented point sources and problems with the recovery of source properties.

To limit the significance of the inaccuracies caused by the effect described above, we implement a subgridding method. Each source is generated on a high resolution 2D array with pixel width equal to one fifth of the detector pixel width. This is re-binned to the detector pixel width before being added to the composite image. A further subgrid of 5×5 is used at the centre of the subgridding for increased accuracy with small sources. The background requires no subgridding due to its spatially-invariant origin and the shallow gradient of the vignetting profile. To significantly decrease the time taken to generate very extended clusters, the subgrid resolution is reduced if the padded profile exceeds 1024×1024 pixel^2.

2.4.7 Detector Layout

The completed optically-processed X-ray field image is placed onto a simulated array of CCDs. No interpolation is required since the pixel size of the field image matches that of the detector. For each configuration a detector coordinate layout is defined relative to the centre of the pointing, consisting of CCD origins and dimensions in units of pixels. IXO-09 is a simple square array of 1024×1024 pixel^2, while IXO-10 uses the more complicated 'cross' layout presented in Treis et al. (2009) without the extended components. The chip gaps of EPIC pn and ACIS-I are rounded to the nearest equivalent number of pixels in

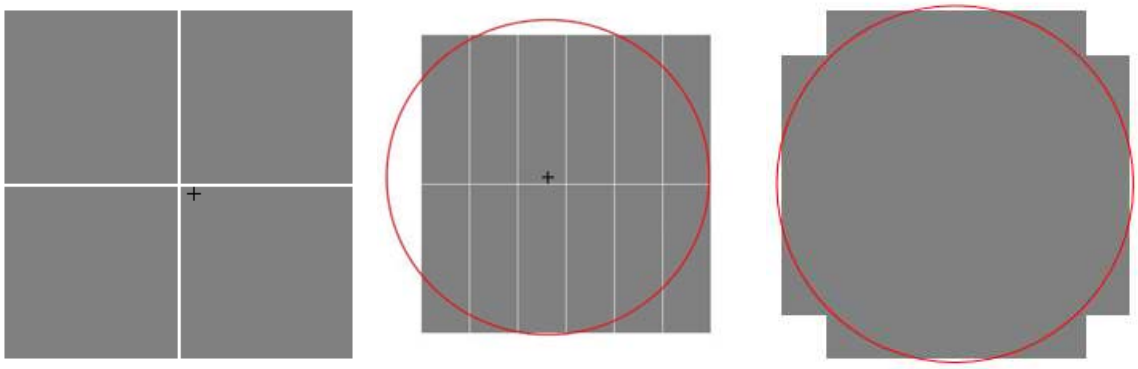

Figure 2.35: Layouts of detector CCDs in XIS. *From left to right:* ACIS-I, EPIC pn and IXO-10. Crosses indicate the aim point when off-centre and circles indicate the field of view when it crosses the array.

size. Layouts of three of the detectors are shown in Figure 2.35.

For each CCD the corresponding region on the field image is found and extracted, creating a set of CCD images (or one in the case of IXO). The IXO-10 layout is applied as a mask to remove the corner regions. All detectors are assumed to have no bad pixels.

2.4.8 Particle Background

The next step is to add count rates from non-X-ray sources to the image. Particles that impact a detector can be divided into two categories: solar protons and internal, cosmic-ray induced particles (Read & Ponman 2003). The amount of background caused by the former is unpredictable, with solar flares causing large spikes in intensity. The remainder of the particle background is a more continuous source of noise. The amount of particle background experienced is also dependent on the orbital radius of the observatory (Hall et al. 2008).

It is difficult to predict the particle background rate for IXO due to its use of new technology and its target location of the L2 point. Current observatories operate at different levels of Earth orbit. An observatory operating at L2 would be in a different environment, outside the magnetic field protection and not subject to trapped particles (Barth et al. 2000; Ambrosi et al. 2005). Position relative to the magnetotail could also be an issue.

Table 2.4: Particle background rates of each configuration in the three energy bands.

Configuration	Energy band (keV)		
	$0.5-2$	$2-5$	$5-10$
	(10^{-6} cts s^{-1} arcsec^{-2})		
ACIS-I	0.417	0.393	2.49
EPIC pn	0.167	0.269	0.384
IXO-09	3.73	6.02	8.58
IXO-10	2.39	3.85	5.49

Flare events reduce the useful exposure time of an observation, therefore it is not appropriate to simulate such interference for this investigation. The cosmic-ray induced particle background is obtained by extrapolating from the simulated estimates of the rates afflicting the XMM-Newton telescopes:

EPIC pn: $0.0087E^{-0.2}$ cts s^{-1} keV^{-1} cm^{-2}

EPIC MOS: $0.0029E^{-0.2}$ cts s^{-1} keV^{-1} cm^{-2}

where E is the energy registered by the detector (Hall 2007, private communication). These physical count rates are given here as angular sizes, based on the plate scale of the telescope, for easier comparison with other incident count rates. The 7.5 m focal length of XMM-Newton means 1 arcsec^2 $\equiv 1.32 \times 10^{-5}$ cm^2. Therefore the prediction for EPIC pn in the $0.5-2$ keV band is 1.67×10^{-7} cts s^{-1} arcsec^{-2}. By analysing the background from observations, Read & Ponman (2003) found a particle rate of $(5.4\pm3.8)\times 10^{-7}$ cts s^{-1} arcsec^{-2} for EPIC pn with the thin filter and $(4.3\pm2.1)\times10^{-7}$ cts s^{-1} arcsec^{-2} with the medium filter. This indicates that true particle background may be twice as high as the predictions.

Both IXO configurations use double the EPIC pn values for a conservative approach to the background rate. Focal lengths of 25 and 20 m for IXO-09 and IXO-10 give 1.47×10^{-4} and 9.40×10^{-5} cm^2 arcsec^{-2}, respectively. Rough estimates of 0.0175, 0.0165 and 0.104 cts s^{-1} cm^{-2} in the three increasing energy bands are used for ACIS-I, based on the ACIS stowed position spectra (Smithsonian Institution 2008). Table 2.4 gives

the estimated particle background rates for all configurations. The appropriate particle background rate is applied to every pixel in all CCD images.

2.4.9 Exposure and Output

To finish the simulation, the affects of exposing the image are applied. We do not attempt to simulate observatory drifting. The images are multiplied by the exposure time of the pointing to give an expected number of counts in each pixel. Each counts value is used as the expectation number λ in a Poisson distribution:

$$P(k, \lambda) = \frac{\lambda^k e^{-k}}{k!} \tag{2.36}$$

where P is the probability of k counts occurring when λ counts are expected. This creates the Poisson noise in each CCD image.

With a completed simulated image generated for each CCD, the images are combined onto a single array at the appropriate locations to create a final image. Example soft band images for each configuration can be seen in Figure 2.36 and a true-colour image is shown in Figure 2.37 (more examples can be found in Appendix E). All CCD images and the final image are output as FITS files. Simple FITS header astrometry is appended to the final image, utilising the same format as recognised by SAOImage DS9 (Joye & Mandel 2003) and CIAO. This allows for some compatibility between the simulated images and these analysis tools.

To complement the simulated image an exposure map is produced in parallel. It originates as a copy of the vignetting profile, then has appropriate regions extracted for each CCD, which get multiplied by the exposure time and combined to represent the exposure over the detector. The exposure map is output in the same format as the final image. A prominent example of one of these maps, that of EPIC-pn, is given in Figure 2.38.

Some simulations are repeated at a variety of exposure times. To decrease the time it

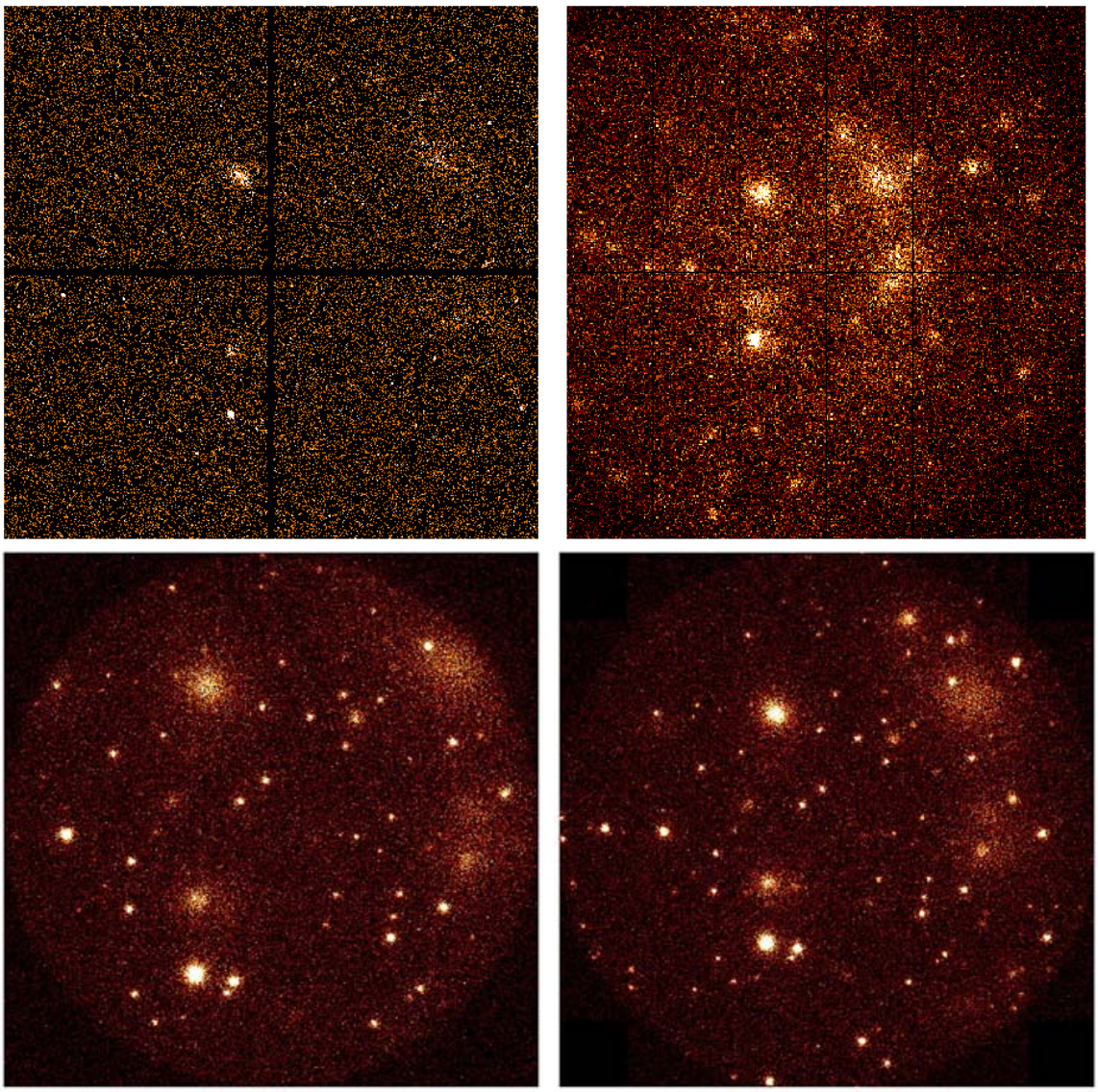

Figure 2.36: Final 100 ks, $0.5-2$ keV images for each configuration, targeted at the centre of the primary sky field. *From top-left to bottom right:* ACIS-I, EPIC pn, IXO-09 and IXO-10. The ACIS-I image has been re-binned by a pixel length of 4:1 due to oversampling. For clarity, each image is scaled separately with a 99.5% linear scale.

takes to perform such a batch of simulations, a 'pre-CCD' image can be output, containing the optically-processed sky. XIS will then resume from this point if repeating a simulation with a different exposure time.

To check the background levels present in the simulated images, those of EPIC-pn and ACIS-I are compared with real observations. Simulated EPIC-pn images have a total soft background of 8.18×10^{-6} cts s^{-1} pixel^{-1} (from the DSB, below flux limit X-ray sources

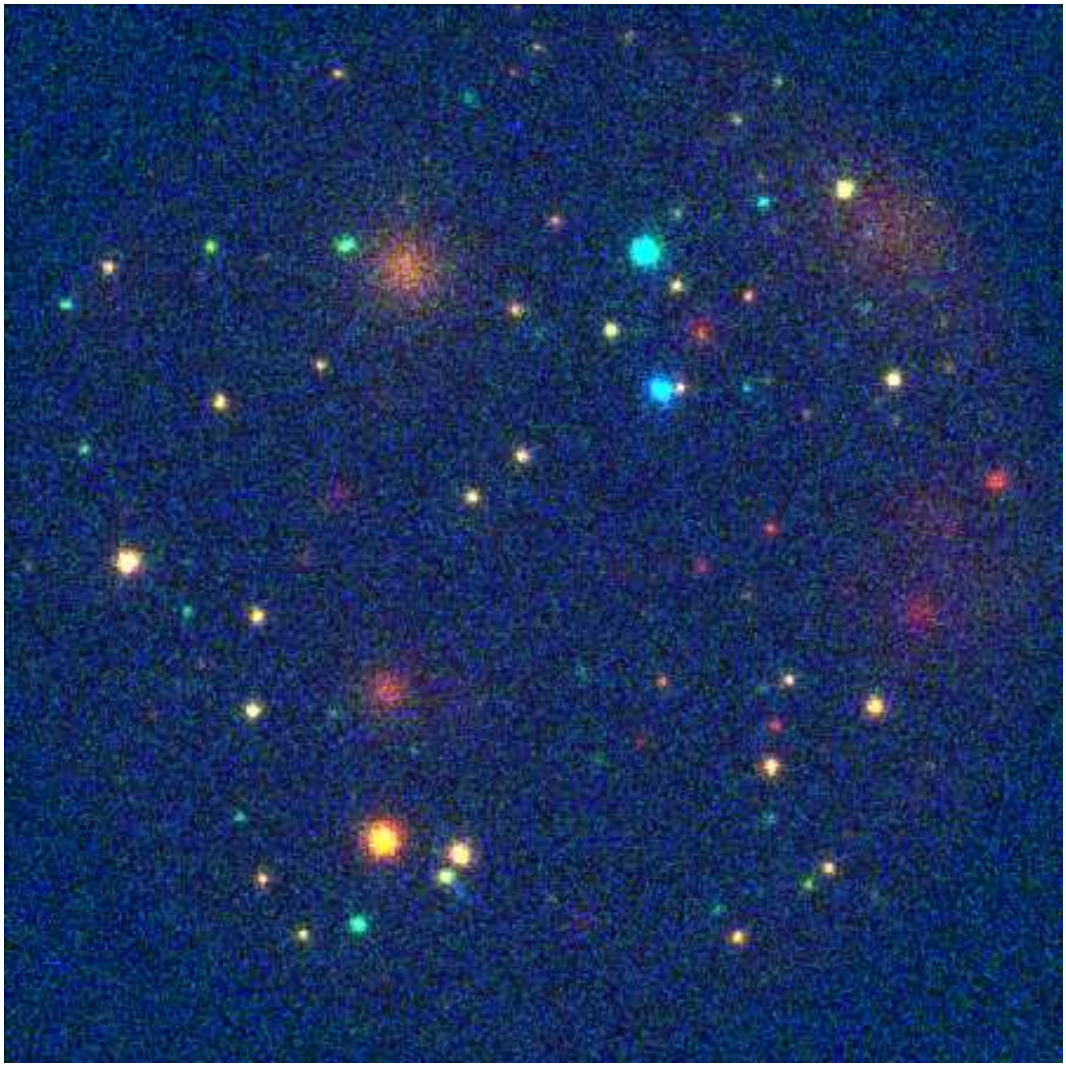

Figure 2.37: Simulated 100 ks, true-colour image of IXO-09. It is a composite of the soft, medium and hard band simulated images at the same coordinates as Figure 2.36. Gaussian smoothing of 2 pixel radius has been applied to improve clarity.

and particles). Since some of the input X-ray sources may be unresolved, the mean background estimation method described in the next chapter is used on the image shown in Figure 2.36. This gives $(1.2 \pm 0.1) \times 10^{-5}$ cts s^{-1} pixel^{-1}. The equivalent background from the Read & Ponman (2003) analysis is $(2.1 \pm 1.3) \times 10^{-5}$ cts s^{-1} pixel^{-1}, consistent with the XIS value but suggesting that the background may have been underestimated.

Note that Read & Ponman (2003) find a higher particle background than the XIS value. Also, the XIS pointings are assumed to be towards a region of low DSB. The high DSB estimates by Markevitch et al. (2003) are ~ 3 times greater, which would give

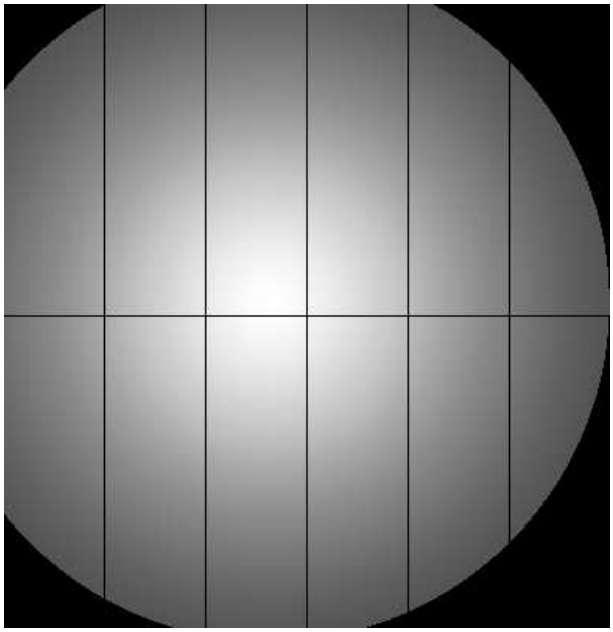

Figure 2.38: Exposure map for EPIC-pn simulations.

a simulated total background of $\sim 2 \times 10^{-5}$ cts s^{-1} pixel^{-1}, increasing the agreement between simulations and observations.

Simulated ACIS-I images have a total soft background of 1.16×10^{-7} cts s^{-1} pixel^{-1}, and the estimate from the Figure 2.36 image gives $1.6 \pm 0.3 \times 10^{-7}$ cts s^{-1} pixel^{-1}. Use of the same background estimation method on a soft band ACIS-I image from observation 2320 (containing cluster A383) gives a mean background estimate of $(8.4 \pm 4.6) \times 10^{-8}$ cts s^{-1} pixel^{-1}. The Giacconi et al. (2002) analysis of CDFS gave a soft background of $(6.3 \pm 1.0) \times 10^{-8}$ cts s^{-1} pixel^{-1}. Therefore it appears that, in contrast to XMM-Newton, XIS simulations overestimate the Chandra background. This background is dominated by the particle contribution, indicating that the Chandra particle background estimate is up to twice as high as it should be.

2.4.10 Flux Limits

The nature of the XLF for all of the cosmological sources means that there is a large number of very faint sources present in the simulations. Many of these sources will become the unresolved cosmological XRB. To enhance the speed of the simulations, flux

cuts are imposed on the galaxy and AGN samples. For both source types, the flux of all sources in the sky field that are below the cut is summed and converted to a count rate per unit area using the most common spectral model. This count rate is then added to the DSB during the stage covered in Section 2.4.3 to create a general X-ray background.

The levels of these cuts are based on the uncertainty in the fully simulated background for the configuration used in the selection function calculations: IXO-09 for $0.5 - 2$ keV. This has a DSB count rate of 4.66×10^{-6} cts s^{-1} pixel^{-1} and a particle background count rate of 2.51×10^{-6} cts s^{-1} pixel^{-1}. Assuming a maximum exposure time of 1 Ms and Poisson errors on the number of counts, the minimum error on the total background count rate is 2.68×10^{-6} cts s^{-1} pixel^{-1}. The centre pixel of the IXO-09 2D PSF model contains approximately 1% of the total flux, therefore $S_{\rm X} \approx 2.7 \times 10^{-4}$ cts s^{-1} is required for a point source to be greater than the background error at the peak of the profile.

The most common spectral profile for galaxies has $z = 1$ and all other parameters as defined in Section 2.3.1. For AGN, the most common spectral profile has $z = 0.8$, $\Gamma = 1.9$ and no obscuration. For $S_{\rm X} = 2.7 \times 10^{-4}$ cts s^{-1}, the equivalent fluxes are (1.8 and 1.9) $\times 10^{-17}$ erg cm^{-2} s^{-1} for galaxies and AGN, respectively. Therefore, a flux limit of 1×10^{-17} erg cm^{-2} s^{-1} is imposed.

For the primary sky field, the flat background flux added to the XRB as a result of the source cuts is 1.58×10^{-19} erg cm^{-2} s^{-1} arcsec^{-2} for galaxies and 7.27×10^{-23} erg cm^{-2} s^{-1} arcsec^{-2} for AGN.

2.5 Summary

In this chapter an X-ray image simulator is presented, with a focus on galaxy clusters and the IXO WFI. The simulator is designed to use theoretically and observationally inspired cluster distributions to investigate IXO's capabilities and survey biases. These are complemented by a less sophisticated distribution of X-ray point sources and background noise. The most significant optical and instrumental effects are applied to the simulations,

imitating the appearance of real extragalactic X-ray observations.

The simulator, written in IDL, takes cluster halos from a cosmological simulation, and combines them with star-forming galaxies and AGN generated from a redshift-dependent $\log N - \log S$. These form a sky field, which represents the X-ray sources on small region of the sky. Cluster properties are expanded using scaling relations and cosmological effects are accounted for. The detector response is calculated for each source, which are then assembled onto an image array as instrumentally-distorted surface brightness profiles. This process sacrifices some small-scale effects for efficiency, enabling the simulation of a large X-ray survey in a matter of days on a single, modern computer. Source and instrumental properties can also be manually configured, allowing specific scenarios to be examined.

Cluster halos are drawn from the Millennium simulation with a lightcone generation method, which uses halos from different regions of the same comoving box to produce a catalogue of masses and redshifts on a simulated sky. Halo masses are adjusted to account for change in the 'best-buy' cosmology since the creation of the Millennium simulation. We use observed $M_{500} - T$, $L_{\rm X} - T$, $r_{cf} - T$ and $\beta - T$ relations with scatter to determine the emission from and surface brightness profile of each cluster. Difference between the observed and simulated cluster $\log N - \log S$ is primarily assumed to be caused by the expected bias in the observed $L_{\rm X} - T$ relation. The group end of the simulated $L_{\rm X} - T$ relation is steepened to bring the cluster number counts into agreement.

Star-forming galaxies are randomly sampled from an SXLF, which comes from the 1.4 GHz radio $\log N - \log S$ of Richards (2000) and the 1.4 GHz to X-ray conversion of Ranalli et al. (2003). Similarly, AGN are sampled from the SXLF of Hasinger et al. (2005) with a distribution in obscuration and power law slope following Gilli et al. (2007). The randomly generated positions of point sources are correlated with the positions of clusters in the lightcone. For efficiency, we remove point sources below 10^{-17} erg cm^{-2} s^{-1} from the source list and replace them with an equivalent flat background. A spatially invariant diffuse soft background is added to the simulations, and is based on estimates

by Markevitch et al. (2003).

Four telescope-detector combinations are implemented for the simulator: Chandra ACIS-I, XMM-Newton EPIC pn, and two IXO WFI designs from different stages of development. Image generation begins by applying the effects of vignetting, field of view and PSF to the X-ray background, creating an initial 'field image'. Individual, spatially-dependent images are then produced for each source and added to the field image. The vignetting profile is that of XMM-Newton, whilst all other effects are instrument-specific. The appropriate regions of the field image are then extracted onto simulated CCD images, and subjected to a particle background rate. Once Poisson noise has been added the CCD images are combined. This produces a final image which resembles an observation with the selected observatory.

CHAPTER 3

Source Identification

The previous chapter established the method for simulating images. To make use of these images for cluster studies, a reliable method of detecting and discriminating between clusters and point sources is required. A procedure to do this has to perform four general tasks:

- source detection, i.e. finding regions with a greater number of counts than expected from the background;
- source verification, i.e. assessing the likelihood that the source is not concentrated background noise;
- determination of extent, i.e. assessing how broad the source is compared to the PSF of the telescope; and
- source matching, i.e. linking the detected sources with those input into the simulation.

No spectral information is available and no optical follow-up can be assumed. Recovering the properties of each cluster surface brightness profile is also desirable.

This chapter is about the source identification process that is included in XIS. To begin, the method of detecting source candidates is described. This is followed by descriptions of the techniques used to measure some of the properties of those candidates. The final section covers the procedure used to link identified sources with the sources that are present in a simulation.

3.1 Detection

A good source detection method is essential in any survey. The basic concept is to search for regions in an image where the number of counts (the signal) is significant compared to the background noise. Several methods used in the literature were discussed in Section 1.4.1. The source detection techniques that perform well at finding extended sources are VTP, WVT and wavelet decomposition. The latter is chosen for its ability to separate an image onto different spatial scales, which efficiently locates smaller sources within the emission of larger ones and allows appropriate analysis regions to be assigned to each source. It also opens up the possibility of analysing morphology on different spatial scales.

The source detection procedure begins with two different decompositions, one configured to produce a list of source candidates on different scales and the other a background estimate. Source positions are then correlated to match up those that appear on multiple scales, and a number of spatial properties are identified for each candidate. The final list is then filtered to remove some common false detections.

3.1.1 Wavelet Decomposition

The software that performs wavelet decomposition within XIS is `Wvdecomp` from the package zhtools (Vikhlinin 1999). This was originally applied by Vikhlinin et al. (1998). An *à trous* wavelet kernel is used as it removes some of the problems with associated with wavelet convolutions, including translation variance (see Slezak et al. 1994). For a scale

a, *à trous* is the difference between the functions f_a and f_{a+1}, which are approximately Gaussian of width 2^{a-1} in form.

When an image is convolved with the kernel κ, structures of size $\sim 2^{a-1}$ are accentuated (Vikhlinin 1999). Decomposition begins on the smallest chosen scale, and all identified structures are removed from the image before moving onto the next scale size. This allows small structures to be recovered from within larger ones. Sources can be reconstructed by combining the structures from each scale.

Sources can be detected by finding regions where the number of counts is significant compared to the background noise in the image. The output from `Wvdecomp` is a set of images displaying structures detected above a certain significance threshold, which is derived from an error map. An approximation is used to estimate the error map in the case of Poisson noise, based on Gehrels (1986):

$$\hat{n}(i,j) = \frac{1 + \sqrt{\mathrm{Bkg}(i,j)s + 0.75}}{s} \tag{3.1}$$

where $\mathrm{Bkg}(i,j)$ is the background in pixel (i,j), s is the effective area under the kernel, $S = 1/\sigma_a^2$, and

$$\sigma_a = \left(\sum \kappa_a^2(i,j)\right)^{0.5} \tag{3.2}$$

Bkg is estimated by convolving the image with the function representing the negative part of the kernel. For a threshold level of τ sigma, the significance threshold is given by $\tau\hat{n}\sigma_a$. Two thresholds are used: a detection threshold, which the maxima of a convolved structure must lie above; and a filtering threshold, above which the pixels of convolved structure are returned in the significance images. The filtering threshold can be used to recover more signal around a maxima.

The application of `Wvdecomp` in XIS involves decomposing an image over $a = 1 \ldots 7$, and the process is performed twice. The first implementation is designed to produce a background map. For source modelling it is important to have a good estimate of the background. A background map can be created by subtracting all detectable sources from

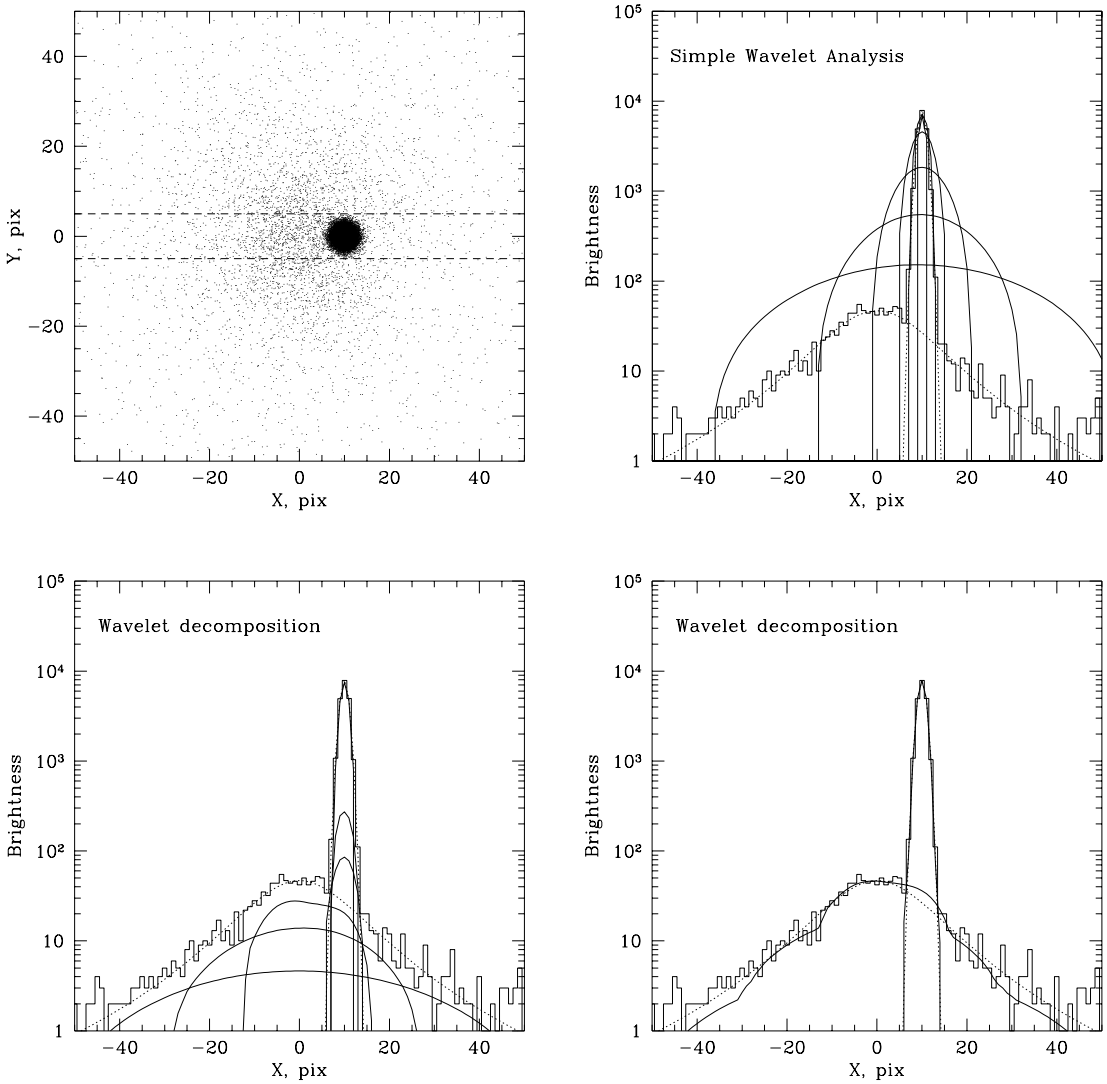

Figure 3.1: Advantage of the wavelet decomposition algorithm. *Top-left:* A bright point source is located in the vicinity of a cluster. Dashed lines show the strip in which brightness profiles (latter three panels) were extracted. *Top-right:* The result of convolution of this image with wavelet kernels with scale sizes of $1, 2, 4, \ldots, 32$ pixels. The data profile is shown by the solid histogram, and the profiles of convolved images by solid lines. At all scales, the convolution is dominated by the point source and there is no separate peak corresponding to the cluster. Therefore, the cluster remains undetected by this simple analysis. *Bottom-left:* The Vikhlinin et al. (1998) method provides a decomposition of the original image into components with the characteristic size 1, 2, 4, ..., 32 pixels. Small-scale components model the point source. The cluster becomes apparent and well-separated from the point source at large scales. *Bottom-right:* The sum of the three smallest and three largest scales of the wavelet decomposition provide almost perfect decomposition of the raw image into its original components. Figures taken and caption adapted from Vikhlinin et al. (1998).

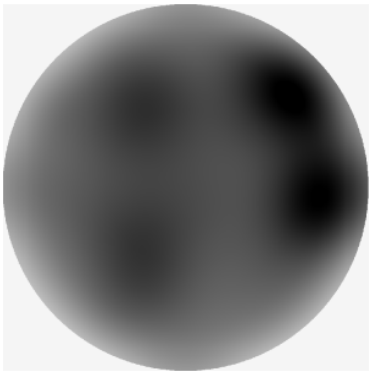

Figure 3.2: Wavelet decomposition generated background image of the IXO-09 image from Figure 2.36. Shown with a negative count scale.

the image, smoothing across it, and correcting for exposure. This is done automatically at the end of the wavelet decomposition process. A detection threshold of $\tau = 6\sigma$ is used for the first scale. This threshold is decreased by 0.5σ for each subsequent scale. This gives increased sensitivity to larger scale structures, which are less likely to originate from Poisson fluctuations. A filtering threshold is used to decide the region out to which a structure is extracted. The filtering threshold is set to 1σ less than the detection threshold. These values originate from an iterative approach, designed to maximise the number of real structures removed from the image. This allows for an effective estimation of the background in most cases.

An example background map is shown in Figure 3.2. A perfect background map will resemble the exposure map in shape. Unfortunately, if large scale sources are not fully subtracted, leaving non-background related structures, then using the background map in the source modelling can be detrimental to the fitting of small scale sources. For this reason, the background map is replaced with a flat background value taken from the mean count rate of the background map $\overline{\mathrm{Bkg}}$.

The second decomposition process is configured to optimise the number of sources detected, including contaminating sources, while minimising the number of false sources detected from rapid fluctuations in signal. The first scale detection threshold is set to 7σ to limit the number of single pixel structures recovered. It is decreased by 0.5σ for

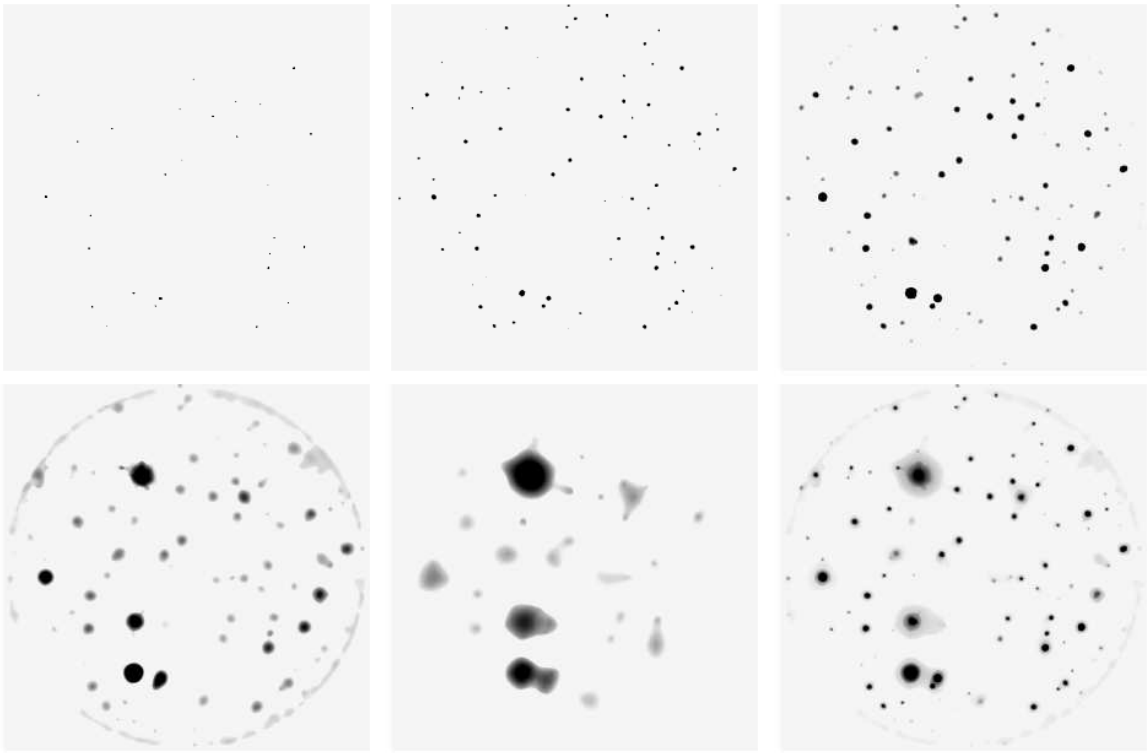

Figure 3.3: Source detection implementation of the wavelet decomposition of the IXO-09 image from Figure 2.36. Scale a increases from 2 to 6 from *top-left* to *bottom-middle*. The field of view edge artifact seen on scale 5 does can appear on other scales. The recombined image is shown *bottom-right*.

each subsequent scale, but not allowed to drop below 4.5σ. The filtering threshold is set equal to the detection threshold. It is not important to maximise the recovered flux in the decomposition process as the source analysis procedure uses the original image data. We are primarily interested in the scale on which a source appears most strongly. An example of a set of decomposed images produced with this method is presented in Figure 3.3.

3.1.2 Candidate Selection

To produce a list of candidates, we assume that every local maximum in a decomposed image is related to a different source. Each decomposed image is searched for maxima, resulting in a list of centroids relating to different spatial scales. Sources will usually appear on multiple scales and need to be connected to prevent duplicate detections. The candidate centroids are matched to any on the next largest scale that are within the radius

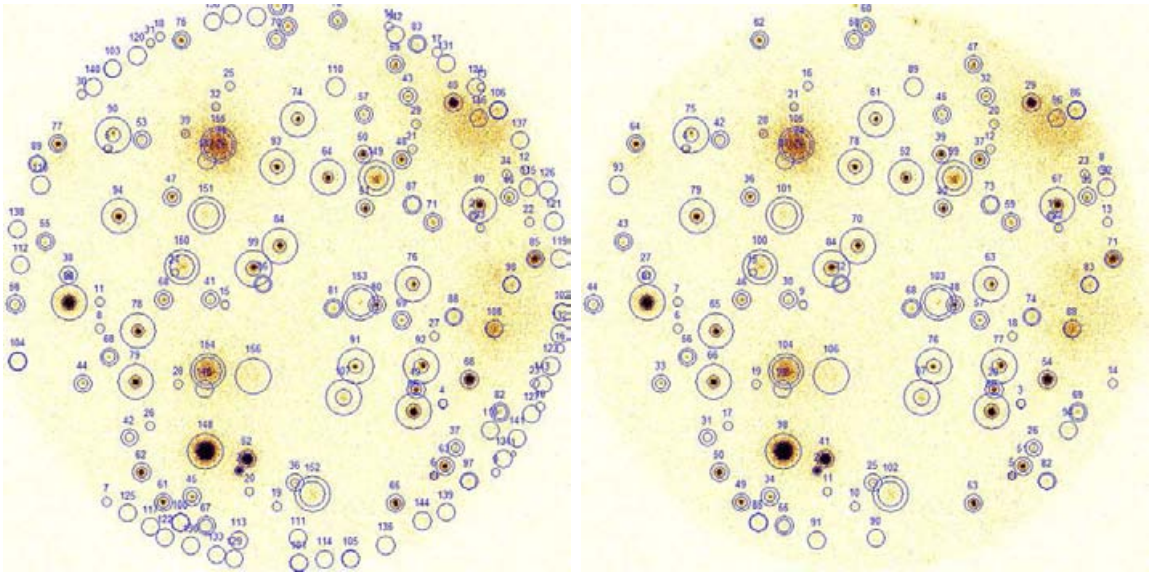

Figure 3.4: *Left:* Source candidates detected from the wavelet decomposition in Figure 3.3. Inner and outer circles show the extraction and contamination radii, respectively. *Right:* Same as left but after the filters have been applied (see text).

associated with the next largest scale. The position of a merged candidate is the mean of its components.

Each candidate is assigned a magnitude $\mathcal{M}$, extraction radius $r_{\rm ext}$ and contamination radius $r_{\rm con}$. $\mathcal{M}$ is the sum of the amplitude of the candidate within the scale radius on each scale it appears on. Its $r_{\rm ext}$ is the mean scale radius of its component candidates, weighted by their strength on their scales. $r_{\rm ext}$ is used to decide the initial region used in measuring source properties. $r_{\rm con}$ is the radius of the largest scale the candidate appears on. It is used when analysing other sources to locate pixels that might be unsuitable for use in measurements.

Due to the large number of simulated pointings that need to be analysed in this research, it is useful to minimise the number of false detections at this stage. To this end, a number of filters are applied to the sources. Any source which appears on only scale 1 or only scale 7 is assumed to be a background fluctuation and ignored. Numerous false detections can occur in the high contrast regions at the edge of the field of view, so any sources that appear on the edge of the field of view and have less counts per pixel than $\overline{\rm Bkg}$ are ignored. An example of a set of source candidates before and after filtering is

given in Figure 3.4.

3.2 Source Measurement

With a list of source candidates available, the next stage is to measure their morphological properties, recovering their surface brightness profiles. The main aim of this process is to assess the extent of each candidate to identify the clusters. Obtaining good measurements of each profile is also useful for accurately applying a selection function correction to a survey. The measurement process and extension testing are based on fitting source models to the candidates and applying statistical tests. Both are designed to operate rapidly to make it feasible to analyse multiple wide-angle surveys.

The method begins by extracting an appropriate set of pixels for a source candidate. We then fit both a point source model and a cluster surface brightness model to the source using a maximum likelihood statistic. A Bayesian marginal likelihood method is used to evaluate the extent of the source. This process repeats for all candidates, from smallest to largest.

3.2.1 Datasets and Models

Model fitting is performed on the original 'raw' image data. An alternative would be to use the wavelet reconstructed images for model fitting, however this would prevent the use of Poisson-based statistics. Source images are extracted from the main image. Pixels included within circle of radius $r_{\rm ext}$ define the initial region used for fitting, and have total number $n_{\rm ext}$. Four sets of imaging data are required for each candidate: raw image data d, background model Bkg, exposure model Exp and a PSF model. d_i defines the number of counts in pixel i.

Initially the fitting region contains $n_{\rm fit} = n_{\rm ext}$ pixels. Any pixels with $\mathrm{Exp}_{ij} = 0$ are removed from the fitting region. If pixels within $r_{\rm con}$ of another source are inside the fitting region then the following test is performed. If the number of 'contaminated' pixels

is $\leq n_{\rm ext}/2$, then these pixels are removed from the fitting region. Otherwise, the fitting region is kept and the source is scheduled to be refit once the best-fit models for all other sources are known. This refitting procedure is not as precise as simultaneously fitting both sources but is significantly less computationally intensive.

Each source is fitted with two models. The first is a model of the PSF with an added, exposure map multiplied background. This represents a point source and is referred to as the 'exposed PSF model'. The second contains symmetric β-model convolved with the PSF, representing a cluster, which is referred to as the 'exposed β-model'. The two can be compared to judge if a source is extended. A 1D β-model is preferred to the 2D case as it is both significantly faster and performs better on poor quality data. This means that no ellipticity or rotation information can be recovered. The form of the exposed β-model is

$$m_i = \left(N \frac{b_i}{\sum_{i=1}^{n_{\rm ext}} b_i} {\rm Exp}_i \right) \otimes {\rm PSF}_i + {\rm Bkg}_i {\rm Exp}_i \tag{3.3}$$

where N is the normalisation of the model (which is also defined by $n_{\rm ext}$), and

$$b_i = \left[1 + \left(\frac{r_i}{r_c} \right)^2 \right]^{0.5-3\beta} \tag{3.4}$$

All other parameters have their previous definitions. The exposure map includes the effect of vignetting. The exposed PSF model is equivalent to setting r_c to its lower fitting limit and β to its upper limit. This means that there can be a case where the two models are identical, giving a more valid comparison.

An ideal model would include two background components, representing vignetted and non-vignetted background. However, such a model would require reliable particle background measurements in every image, independent of observatory. The particle background in IXO is approximately one quarter of the total background, and the vignetting is shallow. Thus, the single Bkg model is considered to be an acceptable representation of the background for our purposes.

These models suffer from the same resolution problems as discussed in Section 2.4.6.

Using the same subgridding system is too time consuming for a large number of simulated pointings. A less accurate alternative, subpixel-shifting, is used to improve model quality. All models are initially centred when generated, then a sub-pixel shift is applied to change the centre co-ordinates of the model. Subpixel-shifted, centred models closely resemble the simulated point sources and require substantially less time to generate. The background component of the model is added after this subshifting to make sure that no regions of the model have a value of zero. Subgridding is still used for the centre pixel to improve accuracy for small scale sources.

3.2.2 Model Fitting

To measure the 'goodness' of a fit, XIS applies the Cash statistic C. Cash (1979) derived a statistic from the probability of obtaining a Poisson expected number of counts in a finite number of bins:

$$C = -2 \ln P = -2 \sum_{i=1}^{n_{\mathrm{fit}}} (d_i \ln m_i - m_i - \ln d_i!) \tag{3.5}$$

where d and m are the data and model, as previously defined, and n_{fit} is the number of pixels in the fitting region. A derivation of this statistic can be found in Appendix A.4. The best-fit parameters can be found by minimising $-2 \ln P$. The $-\ln d_i!$ component remains constant during fitting and is omitted. This statistic or variants on it have been used in surveys such as the 160d survey (Vikhlinin et al. 1998) and XMM-LSS (Pacaud et al. 2006). Note that C is not a likelihood function and only the difference between two values of the C statistic (ΔC) have meaning.

Fitting is performed using the general non-linear function minimisation routine `TNMIN`, similar in implementation to `MPFIT` (see Markwardt 2009). This Truncated-Newton method uses an iterative approach to perform Newton's method, which calculates a step

Table 3.1: Order of source parameter fitting for both model types. 1 indicates a free parameter, 0 a fixed one. The final two fits are only used for sources greater than 500 counts within the fitting region.

	PSF model		β model			
	x & y	$\log N$	X & Y	$\log N$	r_c	β
1	1	0	0	1	0	1
2	0	1	1	0	1	1
3	1	1	1	0	1	0
4			1	1	0	1
5			1	1	1	0
6			0	1	0	1
(7)			1	1	1	0
(8)			0	1	1	1

p_k as the solution to the linear system

$$\nabla^2 f(x_k)p = -\nabla f(x_k) \tag{3.6}$$

and sets $x_{k+1} \leftarrow x_k + p_k$ (Nash 2000). The Truncated-Newton approach allows an approximate solution, which increases the chance of convergence. Numerical derivatives are calculated within `TNMIN` by finite differencing.

The exposed PSF model is fitted in 3 dimensions: the coordinates of the centre of the model x and y, along with $\log N$. With sources encompassing several orders of magnitude in flux, fitting is found to perform more efficiently using a logarithmic step. By fixing $\log(r_c = 0.1 \text{ pixels})$ and $\beta = 1.4$, the model represents an IXO-09 point source with a maximum error of $< 0.001\%$ in any pixel. The initial coordinates are the centre of the extraction region, and the initial normalisation N_0 is the sum of the counts in the fitting region after correcting for exposure and background. The fitting ranges are $x_0 - 3 \leq x \leq x_0 + 3$, $y_0 - 3 \leq y \leq y_0 + 3$ and $(\log N_0) - 1 \leq \log N \leq (\log N_0) + 1$. The order of parameter fitting is given in Table 3.1. When fitting fails to converge the process continues onto the next stage.

Next the exposed β-model is fitted in 5 dimensions, releasing the other two parameters within the ranges $-1 \leq (\log r_c \text{ pixels}) \leq 2$ and $0.3 \leq \beta \leq 1.4$. A logarithmic step is used for r_c due the large dynamic range and the increased sensitivity of the model at the small r_c end. Starting parameters for x, y and $\log N$ match those of the best-fit exposed PSF

model. Initial guesses for $\log r_c$ and β are obtained from a uniform grid of 11 and 13 values, respectively. The order of fitting is given in Table 3.1.

The value of C is also calculated for a background model, which is equivalent to a model with $N = 0$. This allows the significance of source existence to be judged, which gives us another way to remove false detections on top of the detection thresholds of the wavelet decomposition.

Source candidates are fitted in the order of smallest scale to largest scale. The best-fit model of that source is added to the background map. This helps to increase the accuracy of modelling sources which have non-excluded contaminated regions. If a source is refit then this model is removed immediately before the refit takes place.

1σ errors on fitted parameters can be calculated using the χ^2 distributed nature of ΔC (Lampton et al. 1976). The value of a parameter is changed until C is offset by ΔC_σ greater than the best-fit (minimum) value. For the full exposed β-model with 5 degrees of freedom this equates to an offset of $\Delta C_\sigma = 5.8876$. Note that the true error in each parameter may be greater if the background is poorly estimated.

Examples of 4 source images are shown in Figure 3.5, and the radial profiles of their fits are given in Figure 3.6. For the radial profile of the bright cluster (top right), the exposed PSF model and exposed β-model fits are clearly distinct. However the faint cluster (bottom right) is less distinguishable from a point source. It is important to quantify the difference between the two models to rationally identify extended sources.

3.2.3 Extent from Maximum Likelihood

The procedures described above allow the recovery of best-fit β-model parameters for the source candidates, but it is not clear what values should be used to define a source as either point-like or extended. One method of measuring the significance of source extent is to compare C of the best-fit of a PSF model with that of a best-fit β-model:

$$C_{\rm x} = \Delta C = C_{\rm PSF} - C_\beta \tag{3.7}$$

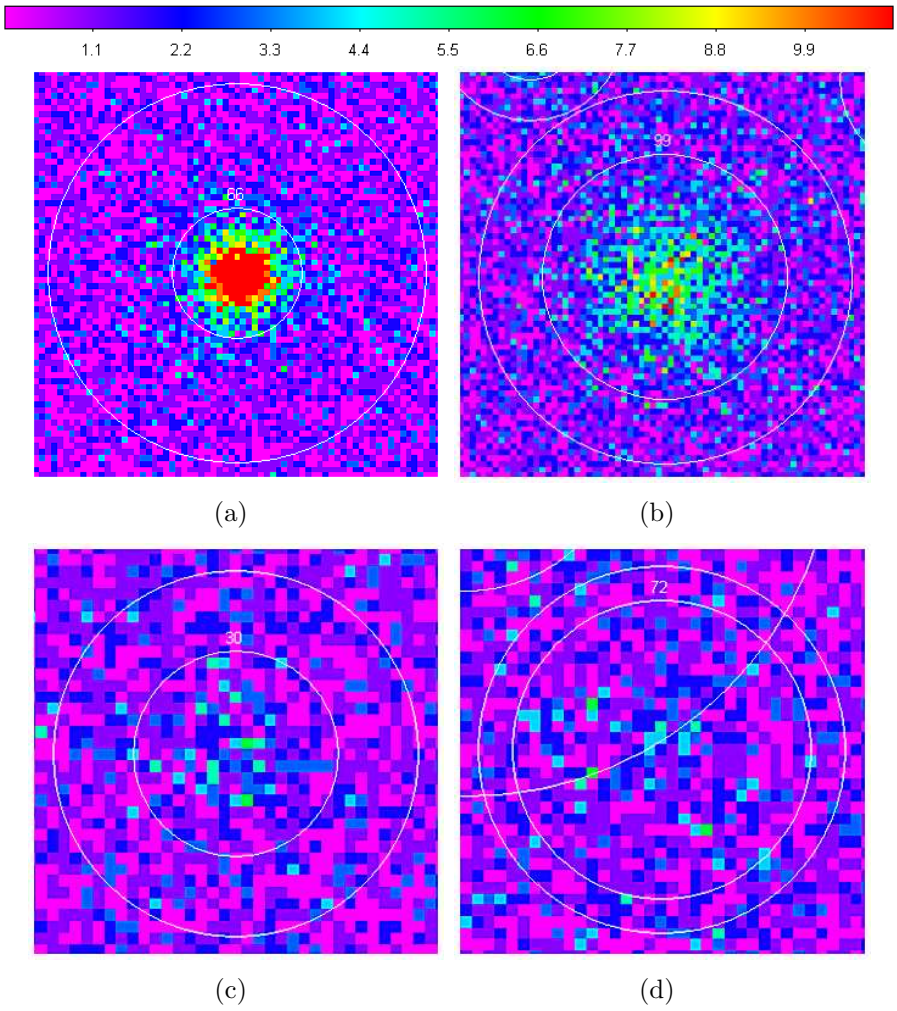

Figure 3.5: Images of 4 example source candidates. The two *left* panels are simulated point sources, whilst the *right* panels are extended sources. Colour scale is in units of counts.

If $\Delta C > 0$ then a source may be extended. Since C_β is a subset of $C_{\rm PSF}$ in XIS, $C_{\rm x}$ is approximately χ^2 distributed with 2 degrees of freedom (see Appendix A.4). Similarly, a value can also be placed on the significance of existence by comparing the best-fit model with the background model:

$$C_{\rm s} = C_{\rm Bkg} - C_{\rm best} \tag{3.8}$$

The use of ΔC to judge source existence and extent is inadequate for this research. It does not impose a punishment for the number of free parameters. Therefore, the exposed β-model tends to give a higher likelihood than the exposed PSF model due do its superiority in matching noisy data.

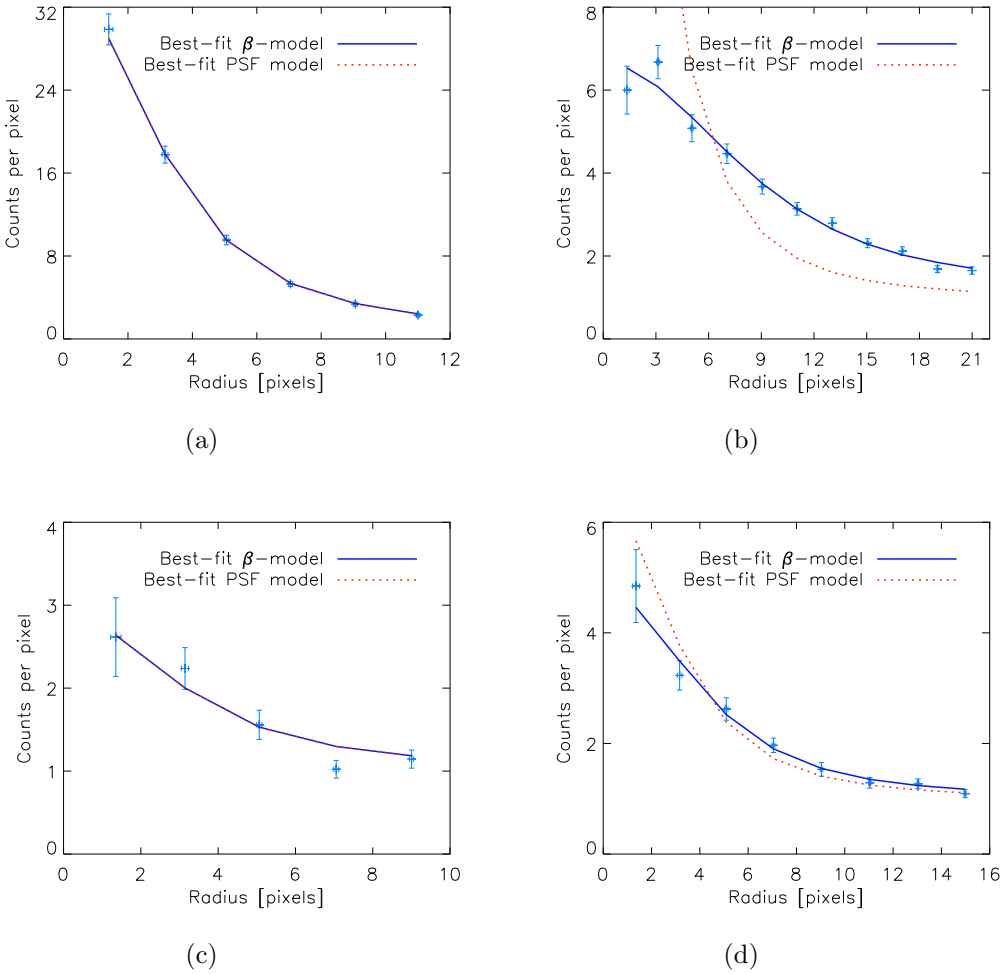

Figure 3.6: Radial profiles of the 4 example source candidates shown in Figure 3.5. The solid blue line shows the best-fit exposed β-model, whilst the red dotted line shows the exposed PSF model. Each radial profile is centred on the location of the best-fit exposed β-model. The lower 2 sources are fainter, ergo they have fewer counts per pixel in each annulus.

The literature includes several statistical 'information criteria' that have been derived for the purpose of punishing a model for the number of free parameters. A simple measure of the goodness of fit can be provided by the Akaike Information Criterion (AIC) (Akaike 1981):

$$\mathrm{AIC} = -2 \ln \mathcal{L}_{\max} + 2p \tag{3.9}$$

where $\mathcal{L}_{\max}$ is the maximum likelihood of a model fitted with p free parameters. This model provides a fixed punishment for the exposed β-model, reducing all values of C_{x} by 4. A sample-size-dependent punishment can be applied by using the Bayesian Information

Criterion (BIC) (Schwarz 1978):

$$\mathrm{BIC} = -2 \ln \mathcal{L}_{\max} + p \ln n \tag{3.10}$$

where n is the number of data points (pixels) included in the model. BIC is an approximation to the Bayes factor, discussed next.

3.2.4 Extent from Marginal Likelihood

An alternative to comparing the maximum likelihood models is comparing how effective models are over the whole parameter space. This can be done using a Bayesian method of conditional probabilities. Bayes' theorem states that the posterior probability of a model given the data

$$P(m|d) = \frac{P(d|m)P(m)}{P(d)} \tag{3.11}$$

where $P(d|m)$ is the probability of the data given the model. When comparing two models m_1 and m_2, one can calculate the Bayes factor

$$K = \frac{P(d|m_1)}{P(d|m_2)} = \frac{\int P(\theta_1|m_1)P(d|\theta_1, m_1)d\theta_1}{\int P(\theta_2|m_2)P(d|\theta_2, m_2)d\theta_2} \tag{3.12}$$

where θ_1 and θ_2 are the parameter vectors of the respective models, and $P(\theta_1|m_1)$ and $P(\theta_2|m_1)$ are the prior probabilities. $P(d|m_1)$ and $P(d|m_2)$ are known as marginal likelihoods. If $K > 1$ then m_1 is more strongly supported by the data. Integrating over the entire parameter space naturally punishes more complex models, as a greater number of 'unlikely' regions are included. Prior probabilities allow knowledge about the distribution of parameter θ to influence the marginal likelihood.

Ideally one would perform a detailed integral over all 5 parameters of the exposed β-model, and compare this to one performed over the 3 parameter exposed PSF model. The ratio of the marginal likelihoods from these two models give a statistic for the source extent. However, this approach needs to be reduced in scale to process the large quantity

of sources required for this work.

Consequently, XIS uses the best-fit values of x and y to reduce the size of the parameter space and calculates C over a sparse grid of $\log N$, $\log r_c$ and β. For the latter two parameters the full range of the parameter space is used, defined as $\Delta \log r_c$ and $\Delta\beta$, respectively. $\log N$ is followed out to 3σ, defining $\Delta \log N$, to capture the peak of the probability density in this parameter. The best-fit parameters are placed at the centre of the grid, with the other points spaced evenly in the appropriate domain. Imposing a flat prior across each point of the grid, we find the integrated probability of the exposed β-model over the entire (N, r_c, β) space to obtain the marginal likelihood

$$P(d|m_\beta) = \iiint e^{-C_\beta(N,r_c,\beta)/2} \frac{\mathrm{d}\log N}{\Delta \log N} \frac{\mathrm{d}\log r_c}{\Delta \log r_c} \frac{\mathrm{d}\beta}{\Delta\beta} \tag{3.13}$$

This is repeated for the exposed PSF model (using only the N dimension). The extent statistic is then defined as ratio of the marginal likelihood of the exposed β-model to the exposed PSF model:

$$B_\mathrm{x} = \frac{P(d|m_\beta)}{P(d|m_\mathrm{PSF})} \tag{3.14}$$

As with the C statistic, the model which appears to be a better representation of the data is used compute the significance of existence statistic:

$$B_\mathrm{s} = \frac{P(d|m_\mathrm{best})}{e^{-C_\mathrm{Bkg}/2}} \tag{3.15}$$

This value can become higher than logarithmically representable by a computer. In such cases it is fixed at $\log B = 1000$. Calculations are performed in units of minimum C_β for the particular source to make sure that all significant likelihood contributions are computationally representable. Another advantage of this method is that it is not entirely dependent on good fits to the data. Use of a large region of the parameter space means that fitting errors have a less significant effect on the measurements of existence and extent. A more thorough approach could involve an iterative process such as Markov

chain Monte Carlo to sample the parameter space in more detail.

Other than the choice of integration space, no prior is imposed any parameter during the research that involves IXO-09. One could increase the weight of models with low r_c and high β due to the large fraction of sources which are point-like. However, the respective weights of different source types was uncertain until late in the research. The ratio of the number of these sources is also a function of flux (see Section 2.3.5). Such a prior is experimented with during the IXO-10 calibration discussed later.

The value of B_{x} for which a source could be reliably classified as extended is calibrated in a Monte Carlo fashion using XIS simulations. This procedure is covered in the next section.

3.3 Classifying Sources

To determine the effectiveness of the source detection and measurement procedures, the source candidates must be linked with a simulated source at approximately the same location. This is also allows the detections within a simulation to be attributed to sources with certain properties. Described below is the method by which identified candidates are correlated with simulated sources and the classifications that are used to sort them. With the method in place, numerous simulations are used to assess the statistical techniques available and identify significance thresholds to classify the source candidates during general use.

3.3.1 Matching Detections with Simulations

A significance of existence threshold is used to decide if a source candidate is a detected source. Sources with an existence statistic greater than the chosen threshold are kept for the matching stage, whilst the rest as classified as false sources. During source matching, those for which the extent statistic exceeds the significance of extent threshold are classified as extended sources, whist the rest are classified as point sources.

Positions of each of the detected extended sources are compared with those of the clusters. The closest cluster within a distance equal to twice the PSF FWHM is used as the match. If a match is found, that cluster is marked as detected and removed from those available to detect, otherwise that extended source is marked as a spurious detection. Once this process is complete, we label any cluster not matched with a detected extended source as undetected. The above process is repeated for the matching of detected point sources with both simulated galaxies and AGN, using the PSF FWHM as the matching length. This results in source catalogues for the following 10 categories:

- Detected clusters
- Detected galaxies
- Detected AGN
- Undetected clusters
- Undetected galaxies
- Undetected AGN
- False extended sources
- False point sources
- Spurious extended sources
- Spurious point sources

To reiterate, false sources are those which do not exceed the existence threshold, whilst spurious sources exceed the threshold but do not match with a simulated source. Detected galaxies and AGN are sometimes grouped into detected point sources for convenience. Undetected sources which do not significantly cross onto the exposed region of the detector are not included in the catalogues. To check which sources this applies to, the PSF FWHM

is used as the radius of galaxies and AGN, with an additional radius of r_c added to check clusters.

At the completion of the source correlation process the catalogues are output as FITS tables with corresponding DS9 region files. These tables include the properties listed in Table D.4 (see Appendix D). Cluster, galaxy and AGN tables included the data from Table D.1, Table D.2 and Table D.3, respectively.

3.3.2 Calibrating Source Classifications

The source detection and extension statistics provide information on which of the three models (background, PSF and β) best represents each source based on the analysis method and the quality of the data. Given the uncertainties caused by the amount of noise in an image, it can be more effective to confirm that a source belongs in a class only if it is many times more likely than the alternatives. Another option is to allow a certain number of false classifications to take place in a given field. This leads to thresholds being established which divide up the source categories. In this work the decision of where to place a threshold is determined by using simulations, as described below.

3.3.2.1 IXO-09 Calibrations

Source identification calibration is performed for IXO-09 in preparation for the survey bias study. To illustrate the large scale effectiveness of the source identification process the full extent of the secondary sky field is utilised. This contains 51225 clusters with $(0.02 \leq M_{500} \leq 3.41) \times 10^{14}$ $M_\odot$ within a comoving volume of 0.456 Gpc^3. 3413 of these clusters are at $z < 0.5$. Simulated pointings are configured to maximise the number of XIS source extraction fields[1] that can cover the sky field area with no overlap. The separation between each pointing is set by the source extraction field to make simulation of the same object twice unlikely. A hexagon grid is used to obtain a larger number of pointings than a square grid. This allows for 180 pointings with IXO-09, referred to as a run, with a

[1]The region within which XIS checks for clusters that would appear within the field of view.

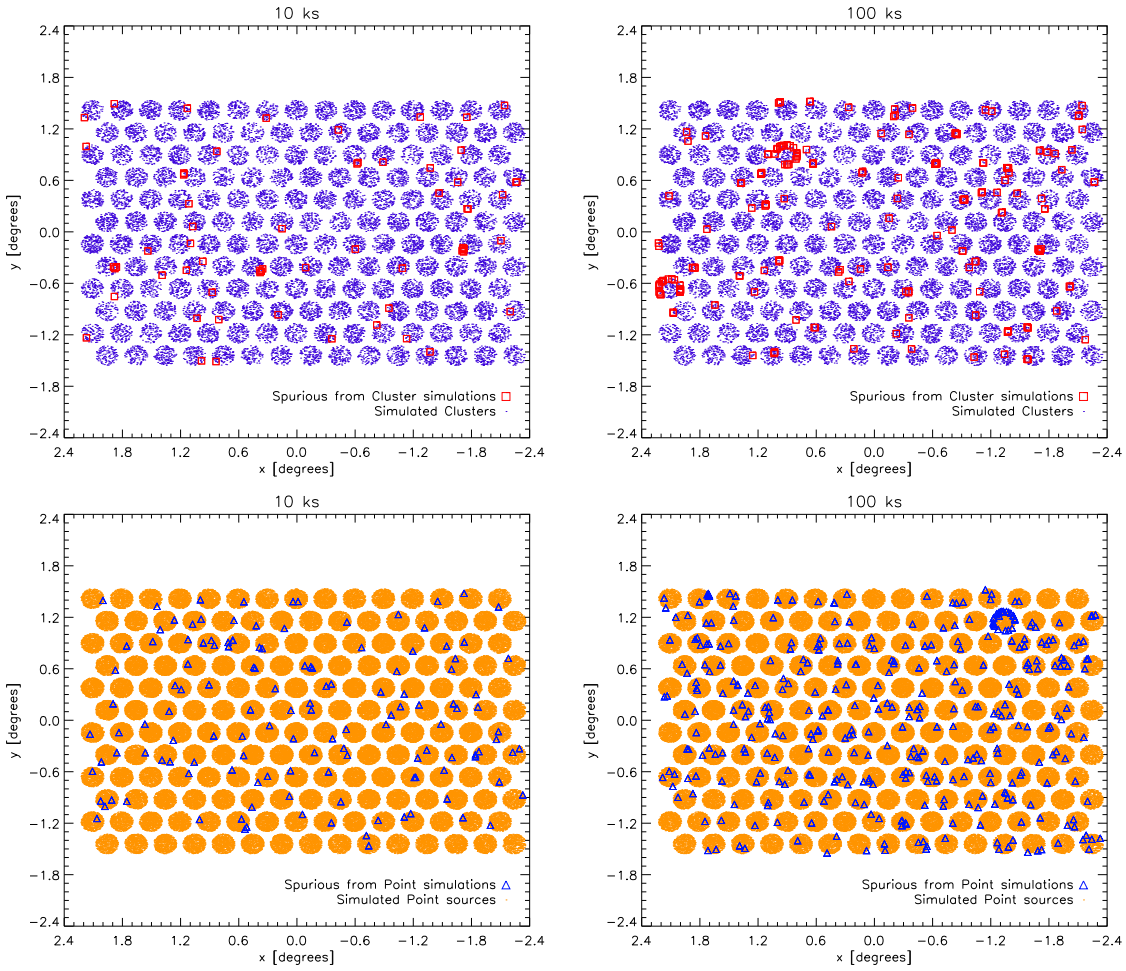

Figure 3.7: Positions of spurious detections in the 10 ks and 100 ks IXO-09 calibration simulations. Blue and orange dots are simulated clusters and simulated point sources, respectively. Red squares and blue triangles display detections which do not match up with a simulated source. *Top row:* Cluster only simulations. *Bottom row:* Point source only simulations.

total exposed area of 7.70 degree^2 ($\sim 51\%$ of the sky field area) containing 26103 clusters.

A run containing only clusters and another run containing only galaxies and AGN are generated, with the B_s and B_x thresholds disabled. This ensures that clusters can only be matched with clusters and point sources only with point sources. These runs are performed for 4 different exposure times: 10 ks, 20 ks, 50 ks and 100 ks; to assess how exposure affects the classifications. Since no B thresholds have been set, all detected source candidates (from wavelet decomposition) that have not been matched to a simulated source are classed as spurious sources.

Figure 3.7 gives the positions of spurious detections from four of the runs. As no

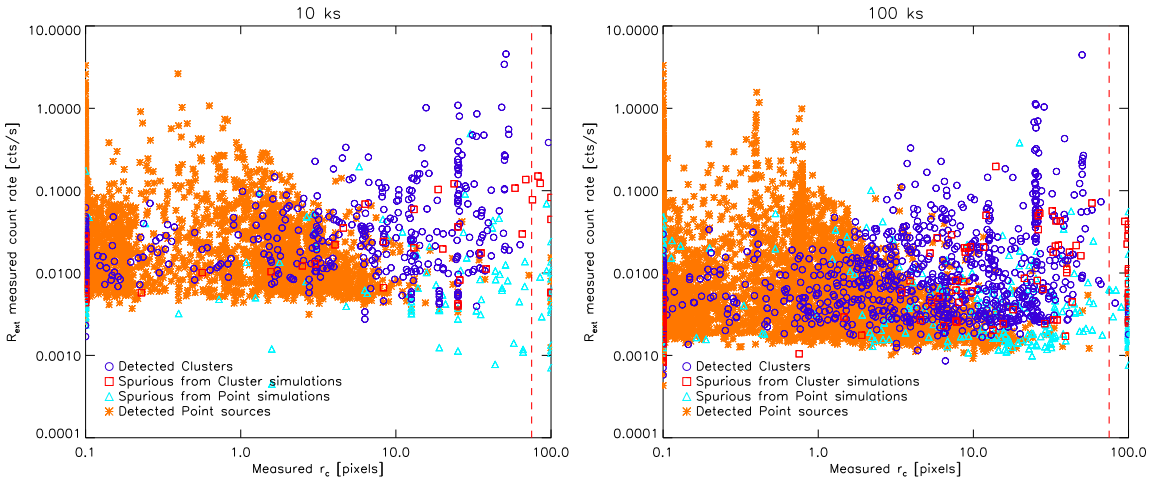

Figure 3.8: Best-fit count rates (within the extraction radius) against best-fit r_c detections in the 10 ks and 100 ks IXO-09 calibration simulations. Dark blue circles show the detected sources from the cluster-only simulations which match with simulated clusters, while red squares show those that do not. Orange stars and light blue triangles show the detected sources from the point source-only simulations which do and do not match with simulated sources, respectively. The red dashed line gives the best-fit r_c cut, above which sources are ignored.

existence statistic threshold has been set, these spurious detections are source candidates which do not match up with simulated source positions. Several pointings suffer from a clear surplus of spurious detections around the field of view edge. In these cases the filter used to remove edge detections proves ineffective, possibly due to a low mean background estimate. To remove the majority of these detections, all sources (from all catalogues) are ignored if they are more than $R_{\rm FoV} - 32$ pixels from the the pointing centre. This reduces the included area in each run to 6.77 degree^2.

The calibration simulations also show that the majority of sources with best-fit r_c near the fitting limit of 100 pixels are spurious, as shown in Figure 3.8. To purge this spurious population, all sources with best-fit $r_c \geq 75$ pixels are removed. This removes $\sim 20\%$ of the spurious detections and $< 1\%$ of the true cluster detections. For reference, the highest simulated r_c present in the simulations is 42 pixels.

The distributions of the existence and extent statistics for the BIC and marginal likelihood statistics can be seen in Figure 3.9. Both statistics produce a wide distribution of existence statistics, with point sources densely populating the low extent side of the

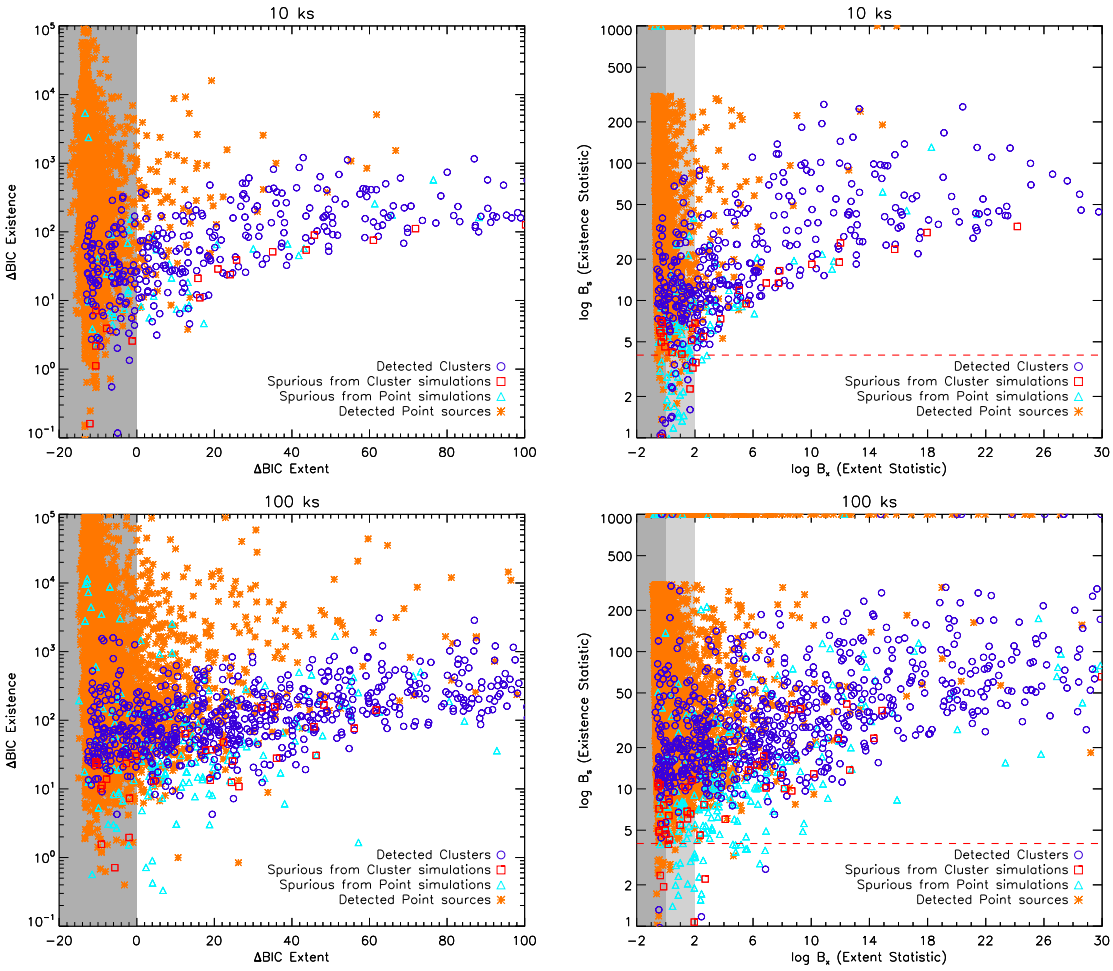

Figure 3.9: Results for different types of existence and extent statistics from 10 ks and 100 ks IXO-09 calibration simulations, with extent scales given as both linear and log. *Top row:* BICs. *Bottom row:* Marginal likelihood. *Left column:* 10 ks. *Right column*: 100 ks. Dark blue circles show the detected sources from the cluster-only simulations which match with simulated clusters, while red squares show those that do not. Orange stars and light blue triangles show the detected sources from the point source-only simulations which do and do not match with simulated sources, respectively. The red dashed line gives the $B_{\rm s}$ threshold. Dark shading covers the region where the exposed PSF model is more likely than the exposed β-model, while light shading covers the region below the chosen $B_{\rm x}$ threshold.

plot as expected. Spurious detections constitute $< 3\%$ of the total detections. They populate the entire parameter space, but are more concentrated at low existence values. From Figure 3.9, neither statistic presents clear locations for thresholds to be defined.

To obtain a clearer picture of how different types of detections are distributed in existence, we examine the cumulative number of sources as a function of existence statistic. These are plotted as the number of sources in each classification as a fraction of the total number in that classification. The results for 10 ks are presented in Figure 3.10. The

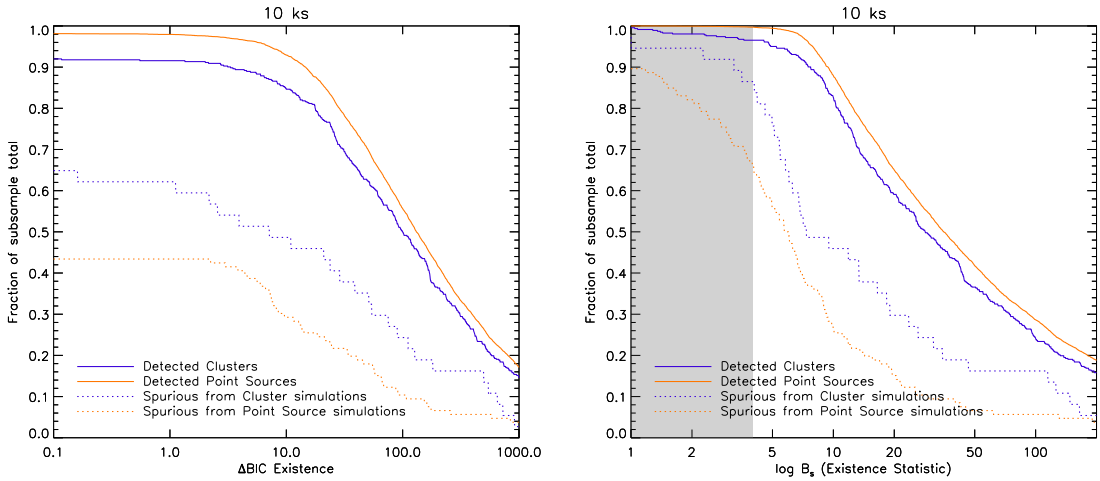

Figure 3.10: Cumulative number of sources as a fraction of the total in that classification, as a function of the existence statistic, for the 10 ks IXO-09 simulations. Left and right panels show BIC and marginal likelihood statistics, respectively. Blue and orange represent the data from cluster and point source simulations, respectively. Shading covers the region below the chosen B_s threshold. Note that the fraction for ΔBIC does not reach unity on the plot due to presence of negative values.

existence axis is given in log-space for clarity.

Because it is largely independent of the number of sources within a simulation[1], existence and extent statistics are judged in terms of a fraction of the total number of that type. The fraction of spurious sources less than or equal to a given threshold is referred to as the spurious source rejection rate, and the fraction of true sources greater than the threshold is referred to as the true source acceptance rate. For both BIC existence and $\log B_s$, values below zero should be interpreted as background noise.

Due to the noise in an image, it is inevitable that there is a trade-off between removing some of the spurious detections keeping some of the true detections. For the BIC, an existence threshold of zero reduces the detection fractions of clusters and point sources by 8% and 2%, respectively, while removing half of the spurious detections. As the threshold is increased, the spurious source rejection rate drops by a similar amount to the true source acceptance rate, with no obvious location for a threshold. Such a trend could come about if the spurious detections are the result of source distruption and confusion with other sources, which would produce candidate data inconsistent with the background.

[1] Although not independent of the properties of those sources.

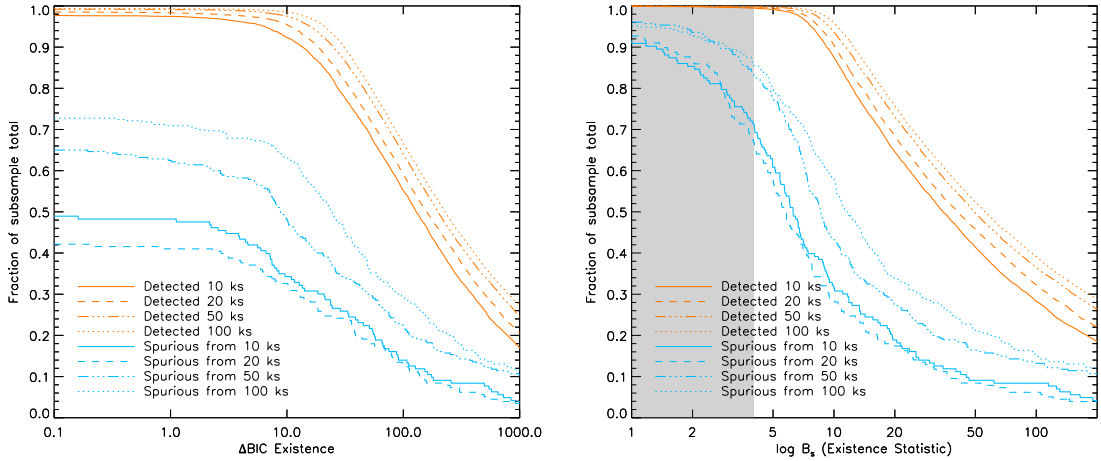

Figure 3.11: As Figure 3.10 but for the different exposure times. For clarity, sources have been re-binned into just two categories: all true detected sources and all spurious detections, shown by orange and light blue lines, respectively.

To assess the effect of source confusion on the number of spurious sources, we count the number of spurious sources that are within a PSF FWHM of any simulated point sources or have a contaminating source within their extraction radius. More than half of the spurious sources satisfy these conditions, supporting the idea that these are more than just background fluctuations. This is likely due to imperfections in the wavelet decomposition and scale matching processes. Also, visual inspection of the images shows many spurious detections to be at the location of large Poisson fluctuations near the outskirts of a cluster. This suggests that more calibration of the initial source detection process is required.

The $\log B_{\rm s} > 0$ result is less effective at removing spurious detections, removing only 4%, but with a true source acceptance rate of $> 99.9\%$. However, the spurious source rejection rate from point source simulations climbs to 53% when the true point source acceptance rate drops to 99% at $\log B_{\rm s} \approx 6$. Similar trends exist in the cluster simulations, but the values of $B_{\rm s}$ are generally higher for spurious sources in the cluster simulations.

In Figure 3.11 the aforementioned fractions (regrouped into true and spurious detections) are shown for different exposure times. Unfortunately, the spurious source rejection rate at high existence thresholds decreases with exposure time. Most affected are the BIC

existence statistics of the spurious detections.

To minimise the damage to the true population while maximising the spurious source rejection rate, a sensible threshold would be in the region $0 < \log B_{\rm s} < 7$. We select a threshold of of $\log B_{\rm s} > 4$, which occurs before the rapid decline in cluster detections. No attempt is made to scale the threshold with exposure time. This gives a true cluster acceptance rate of 97% at 10 ks and 99% at 100 ks. Note that a scale-dependent detection threshold of between 4.5σ and 7σ has already affected the data at the wavelet decomposition stage.

A threshold must also be established for the extent statistic, for which higher values identify extended sources and low values indicate point sources. As the majority of sources being compared by this statistic are true sources, in general they should conform to models better than those judged with the existence statistic. Given angular resolution limits, one can expect some distant clusters to be indistinguishable from point sources.

Following the method used for the existence threshold, the cumulative fraction of true detected clusters is calculated as a function of the extent statistic and compared to that of point sources. These are shown for all exposure times in Figure 3.12. The fraction of point sources less than or equal to a given threshold is referred to as the point source rejection rate, and the fraction of clusters above the threshold is referred to as the cluster acceptance rate. The ΔBIC extent and $\log B_{\rm x}$ thresholds have similar behaviour. They produce a rapid increase in the point source rejection rate as they increase to zero, along with an approximately linear drop in the cluster acceptance rate. Further increase of the thresholds continues to reduce the cluster acceptance rate with approximately the same gradient, but becomes exponentially less effective at rejecting point sources.

At 10 ks, both extent statistics have similar cluster acceptance rates for any particular point source rejection rate, as shown in Table 3.2. Increasing the exposure time raises the overall values of both extent statistics and for both detected source classifications, thereby causing more point sources to be identified as extended at a particular threshold. For positive values, $\log B_{\rm x}$ thresholds give a cluster fraction $\lesssim 1\%$ more than ΔBIC for

Table 3.2: IXO-09 cluster acceptance rate for a $B_{\rm x}$ threshold that gives a certain point source rejection rate at 10 ks, shown in the leftmost column. Cluster acceptance rates are shown for all four exposure times. Columns $2-5$ contain the ΔBIC extent results, whilst columns $6-9$ contain those for $B_{\rm x}$. 10 ks point source rejection rates are relative to the respective extent statistics.

	Cluster acceptance rate (%)							
	BIC extent				$B_{\rm x}$			
	Exposure time (ks)							
Point src. rej. rate (%)	10	20	50	100	10	20	50	100
99.0	71.3	74.5	77.7	83.4	69.5	70.5	75.3	81.2
98.5	75.1	77.4	81.7	86.3	76.0	76.1	81.2	85.4
98.0	77.6	80.4	84.0	88.0	78.5	79.1	83.7	86.9
97.5	79.1	82.2	85.9	89.3	80.9	81.6	85.2	88.5
97.0	81.4	83.4	87.5	90.3	84.5	83.4	86.5	89.3

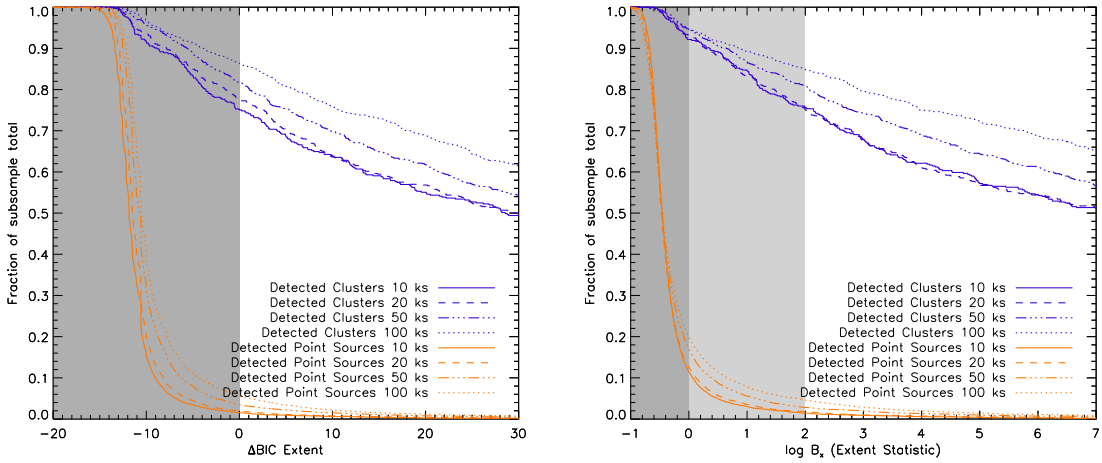

Figure 3.12: Cumulative number of sources as a fraction of the total in that classification, as a function of the extent statistic, for the all exposure times with IXO-09. Left and right panels show BIC and marginal likelihood statistics, respectively. Blue and orange represent the detected clusters and true detected point sources, respectively. Only sources that exceed the existence threshold are included. Dark shading covers the region where the exposed PSF model is more likely than the exposed β-model, while light shading covers the region below the chosen $B_{\rm x}$ threshold.

the same point source rejection rate.

The $B_{\rm x}$ statistic is chosen to classify extended sources due to slightly higher reliability than the BIC and the possibility of further improvement. An extent threshold of $\log B_{\rm x} > 2$ is adopted. This results in a 10 ks cluster acceptance rate of 75.6% for a point source rejection rate of 98.6%. As with $B_{\rm s}$, the threshold is fixed with exposure time. At 100 ks the cluster acceptance rate is 84.9% for a point source rejection rate of 95.4%.

The effectiveness of this extension statistic is impeded by blends of point sources.

This is somewhat reduced by the method of handling source contamination described in Section 3.2.1. However, this method is not always effective, especially when sources are not individually identified after wavelet decomposition and cross-scale matching. The amount of disruption one point source causes another is determined by their respective brightnesses and the size of the PSF. Knowledge of the latter can be used to demonstrate how source proximity affects $B_{\rm x}$. Removing all point sources (detected and undetected) which are within a PSF FWHM of another increases the 10 ks and 100 ks rejection rates to 98.9% and 96.4%, respectively, for $\log B_{\rm x} > 2$.

The number of spurious detections and detected point sources above both B thresholds is equal to 15% and 24% of the total number of detected clusters, respectively. Assuming ~ 3000 simulated cluster centres per degree^2 and a matching area per cluster of 2.42×10^{-5} degree^2, an estimated 7% of these spurious detections could match to a simulated cluster. Therefore $2 - 3\%$ of matched detected clusters in a simulated survey could be spurious matches. The majority of these matches would be with the large population of very faint, low mass systems. Therefore, it is sensible to limit matches to those systems that are above a certain count rate. This limiting count rate is selected after the selection function is examined in the next chapter.

Overall, this implementation of the Bayes factor method ($B_{\rm s}$ and $B_{\rm x}$) gives very little improvement in performance over a maximum likelihood approach which uses the BIC to punish a model with more free parameters. The real advantage in using $B_{\rm s}$ and $B_{\rm x}$ here comes from partial-independence from the best-fit parameters (but not the source position). The marginal likelihood technique also leaves room for improvement, as the sampling of the parameter space can be improved and the prior distribution can be changed. The latter idea is explored below.

Note that the contents of these simulations means that the effect of point sources within extended sources is not included. In ordinary XIS simulations, clusters and point sources are both present and therefore can contaminate each other. This is somewhat alleviated by the exclusion of contaminated pixels and inclusion of fitted sources in the

background map. However, in a more crowded field we can expect some faint sources to be lost under the emission of brighter ones, and greater $B_{\rm x}$ values from contaminated point sources, raising the number of spurious extended sources.

3.3.2.2 IXO-10 Calibrations

The instrument trade-off study involves IXO-10 and concentrates on 100 ks. To give results more suitable to this study, especially with the higher exposure time, the $B_{\rm s}$ and $B_{\rm x}$ threshold are re-calibrated for IXO-10 using 100 ks IXO-10 simulations. The simulation set-up is the same as in Section 3.3.2.1, however the use of the sky field is maximised after only 80 pointings with the IXO-10 field of view. This gives an exposed area of 5.65 degree^2. The same source cuts at the field of view edge are also imposed, reducing the exposed area to 4.98 degree^2. A best-fit r_c cut of 70 pixels removes $\sim 20\%$ of the spurious detections and $< 0.4\%$ of the true cluster detections.

The previous Bayes factor calculation involved a flat prior over $\log N$, $\log r_c$ and β (see Section 3.2.4). For the IXO-10 simulations we experiment with using a 'point source prior', which gives weight to the region of the parameter space occupied by point sources. The evidence for such a prior is the far greater number of point sources detected in the calibration simulations.

In the initial calibration simulations, IXO-10 obtains a detected point source to detected cluster ratio of approximately 10:1. Thus, the points of the integration grid which have the lowest r_c and highest β (i.e. most closely resemble a point source) are given a prior 10 times higher than the other points, and the entire parameter space is renormalised to unity. The point source prior is only used in the calculation of $B_{\rm x}$. As before, $B_{\rm s}$ is determined using the model which is favoured by $B_{\rm x}$ (which may have changed in light of the new prior).

The prior produces only a small change in the statistics, at most altering the second significant figure. There is no change to any of the rejection and acceptance rates. Therefore, this point source prior does not improve the effectiveness of these statistical

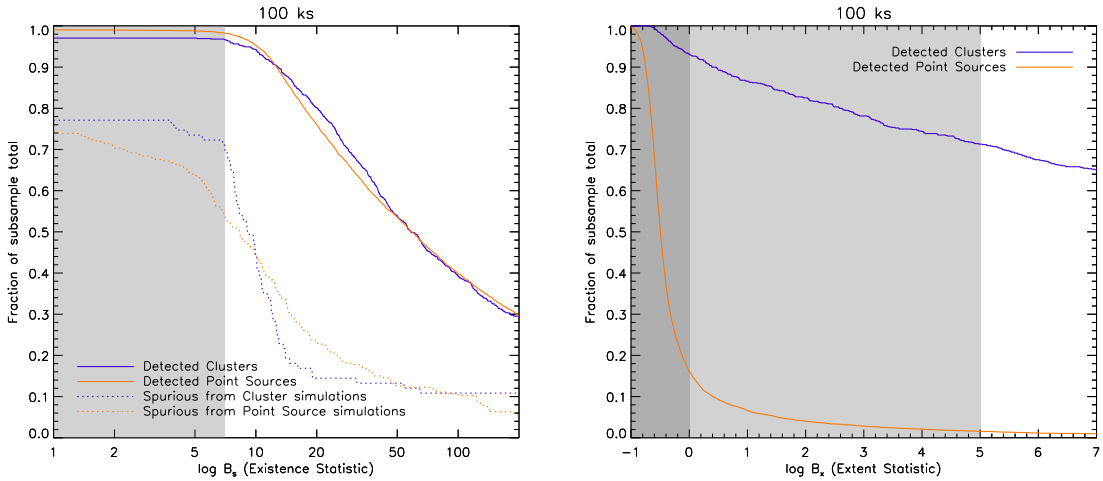

Figure 3.13: *Left:* Cumulative number of sources as a fraction of the total in that classification, as a function of the existence statistic, for 100 ks IXO-10 simulations. Blue and orange represent the data from cluster and point source simulations, respectively. Shading covers the region below the IXO-10 $B_{\rm s}$ threshold. *Right:* Cumulative number of sources as a fraction of the total in that classification, as a function of the extent statistic. Blue and orange represent the detected clusters and true detected point sources, respectively. Only sources that exceed the existence threshold are included. Dark shading covers the region where the exposed PSF model is more likely than the exposed β-model. Light shading covers the region below the IXO-10 $B_{\rm s}$ threshold.

tests.

The cumulative fraction of true detections and spurious detections from both cluster and point source simulations is shown in Figure 3.13. The $\log B_{\rm s} > 4$ threshold results in a spurious source rejection rate of 31.3% and true source acceptance rates of 97.2% and 99.2% for clusters and point sources, respectively. Following the reasoning used for the 10 ks IXO-09 simulations, the existence threshold is set at $\log B_{\rm s} > 7$, just before the true cluster acceptance rate rapidly declines. This gives a spurious source rejection rate of 42.3% for a true cluster and point source acceptance rates of 96.7% and 98.2%, respectively.

Note that the spurious source rejection rate from the cluster simulations drops rapidly in the region $7 < \log B_{\rm x} < 13$, so a higher threshold may be preferable for surveys without follow up observations.

Cumulative fractions of clusters and point sources with $B_{\rm x}$ are also shown Figure 3.13. Thresholds of $\log B_{\rm s} > 7$ and $\log B_{\rm x} > 2$ give point source rejection rate of 95.9% and a

cluster acceptance rate of 82.5%. To achieve a point source rejection rate approximately as high as the 10 ks IXO-09 simulations the extent threshold is increased to $\log B_{\mathrm{x}} > 5$. This gives a point source rejection rate of 98.4% and a cluster acceptance rate of 71.3%.

3.4 Summary

This chapter covers the subjects of X-ray source detection and the identification of extent. The methods selected for each of these subjects are geared towards detecting clusters in XIS simulations while minimising the number of spurious sources and point sources which appear as clusters.

The source detection process uses wavelet decomposition to determine significant features in an image on various spatial scales. The locations of the centres of these features are correlated between the scales to produce a list of candidate sources. Filters are applied to the list to remove common spurious sources. Another decomposition process is used to estimate the background in the image.

Each source candidate has its raw image extracted from the image based on the scale it appeared on most significantly. This is fitted with two models, representing a point source and a cluster β-model and including instrumental effects. The fitting process uses the Cash maximum likelihood statistic. The significance of the existence and the extent of a source can be tested by comparing background, point source and cluster models. Four methods for these tests are presented: ΔC, AIC, BIC and Bayesian marginal likelihood.

Detected sources are matched up with simulated sources so that the effectiveness of both the source identification procedure and simulated observatories can be evaluated. IXO-09 simulations with various exposure times are used to compare the BIC and marginal likelihood methods, and to choose thresholds to place source candidates into categories. The marginal likelihood statistic is selected for the significance tests due to marginally better performance. With a focus on the 10 ks simulations, significance of existence threshold is set as $\log B_{\mathrm{s}} > 4$, and the extent threshold is set as $\log B_{\mathrm{x}} > 2$. These are

recalibrated to $\log B_{\rm s} > 7$ and $\log B_{\rm x} > 5$ for 100 ks IXO-10 simulations.

CHAPTER 4

Cluster Surveys

With methods in place for both the simulation of X-ray images and their subsequent analysis, XIS is used to explore the topic of cluster surveys. The focus of this work is how IXO would perform in cluster studies. XIS is designed to allow the large scale performance of IXO to be assessed by the generation of simulated surveys. As previously mentioned, these surveys can be subject to biases due to the way in which the cluster population is sampled as a result of the survey selection function.

The main advantage of a simulated survey is that the underlying population is entirely known. This allows one to uncover how much bias is present in a simulated survey and to use this to predict the amount of bias that could be expected in real surveys. The origins of this bias can be better understood by generating an assumed selection function, which gives the probabilities of detecting clusters with particular properties. By modelling how a hypothetical cluster population would appear when subject to a selection function, the distribution of properties for the whole underlying population can be estimated. How close this comes to resembling the true cluster population depends on the assumed selection function and how it is applied.

In this chapter, XIS is used to produce IXO-09 simulations which incorporate the main

features of the X-ray source populations, instrumental effects, noise and data analysis techniques, so that the actual selection function within the simulated observations is realistic. We can then examine the impact of different assumed selection functions on correcting the bias in the 'observed' evolution of the $L_{\rm X} - T$ relation.

First the factors that contribute to a selection function are discussed, followed by the generation of a multi-parameter assumed selection function using a subset of those factors. Next, several simulated surveys are created, each of which differ in the evolution of their luminosity. The assumed selection function is then applied in different ways to examine how well it corrects the bias in observations of $L_{\rm X} - T$ evolution. Possible bias in the recovery of the cool core population is also investigated. To conclude, the trade-off between survey area and survey depth is explored.

Throughout this research the standard XIS cosmological parameters are adopted: $H_0 = 70.4$ km s^{-1} Mpc^{-1}, $\Omega_m = 0.272$ and $\Omega_\Lambda = 0.728$ (see Section 2.1.2). Thresholds for the significance of source existence and extent are those calibrated for IXO-09 in Section 3.3.2.1.

4.1 Selection Function

One focus of this study is to see how the sophistication of a cluster survey's assumed selection function affects its ability to accurately recover evolutionary properties. To do this an assumed selection function with several dimensions is created, which can then be reduced in sophistication as necessary. The methodology behind the production of the assumed selection function is covered in this section. Also demonstrated is what impact such a selection function would have on the appearance of the $L_{\rm X} - T$ relation if we assume that it is a full representation of the survey selection function.

4.1.1 Selection Criteria

The ability to detect a cluster is dependent on a wide range of factors relating to the cluster, nearby sources, the observatory and the observation. This chapter focuses on the cluster properties that affect detection, as these can lead to biases in the observed population.

When considering what cluster properties affect its detectability, the most obvious property is the observed flux, which is determined by many properties including $L_{\rm X}$, T and z (which all have trends with M). Many X-ray surveys have attempted to account for the effect of flux on a cluster sample in the form of a flux cut, but rarely consider how detections are reduced as a function of flux and the distribution of cluster surface brightness. When placed high enough, a flux cut allows for the naive assumption that a survey is statistically complete, i.e. the distributions of the relevant cluster parameters are well characterised by the distribution of the data. However, due to scatter, the low flux samples within a scaling relation are biased upwards by over-luminous systems which escape the cut. This affects the low temperature systems at low redshift, and with increasing redshift this bias afflicts higher temperature systems due to the decreasing flux for a certain $L_{\rm X}$. Therefore, the cut must be accounted for in any analysis which would be affected by this bias.

By identifying how the detection probability changes with flux, all of the detected systems can be included in an analysis but with an appropriate weighting. Due to the errors present in spectral models, it is often more convenient to trace the detection probability as a function of observed flux as a count rate, rather than erg cm^{-2} s^{-1}.

It is more appropriate to expand the detection criteria to include the entire surface brightness parameter space. When represented by a β-model, the core radius of a cluster would affect its chance of being detected. A larger r_c means that the flux from a cluster is spread over a larger region on the sky, and it becomes harder to separate from the background as a result. This aspect of the assumed selection function was explored by

Pacaud et al. (2007).

Another parameter of cluster shape that may significantly influence cluster selection is the slope of the surface brightness profile, β. A more shallow slope would have a similar affect on the cluster flux distribution as a larger core radius. It is possible that the ellipticity and rotation angle also factor into detectability, especially when considering observatories with an asymmetric PSF.

The cuspiness of cluster profiles tends to be higher for a sample of cool core systems, possibly creating another selection effect when r_c is not accounted for. Other morphological features could affect detection, such as disruption of the cluster gas due to merging, or cavities from AGN activity.

Contamination from galaxies, AGN or other clusters would affect our ability to detect a cluster. The amount of contamination increases with the number of sources in a field of fixed size. Therefore, there is a relationship between the total $\log N - \log S$ and the selection function. For example, in a uniform distribution of sources, a larger cluster is likely to have more sources projected on its surface brightness profile than a smaller one. However, more massive clusters tend to be more luminous, reducing the impact of any contamination.

Such contamination effects would be subject to cosmological variance. Even with a thorough understanding of the entire source population, it may only be feasible to correctly model contamination effects on a large survey. Other spatially-dependent selection factors are the local XRB and Galactic absorption, which limit the observable flux but change over large spatial scales. A survey which crosses the Galactic plane would suffer a significant variation in the incident flux.

Local factors affecting cluster selection relate to the observatory and the observation itself. The mirror PSF broadens the surface brightness profiles and increases the chance of significant point source contamination. Increased effective area allows for fainter systems to be detected amongst the background noise, but this can be countered by an increased particle background rate. Increasing the exposure time of an observation decreases the

effect of noise. Vignetting means that outer regions of the detector have a reduced effective area, and certain areas of the detector may be less efficient.

Many of these observational effects are accounted for when measuring cluster properties, as covered in Chapter 3. While they do affect the cluster detection rates, their biasing effects are folded into how they affect the observation of surface brightness profiles. This means that an assumed selection function is valid only for a particular observatory with a particular observation configuration. Therefore, each survey requires its own assumed selection function for its results to be interpreted correctly.

4.1.2 Mapping the Selection Function

To investigate the IXO cluster selection function and associated biases we concentrate on a hypothetical IXO-09 WFI survey which uses 10 ks exposures. 10 ks is a reasonable exposure time for XMM-Newton pointings when conducting a large survey, as it gathers sufficient counts to identify sources and allows a large number of pointings to be conducted in the allocated time. With IXO this exposure time will produce images that rival the more deep XMM-Newton observations, allowing the group regime of the $L_{\rm X} - T$ relation to be probed.

XIS simulations effectively apply a realistic selection function to the data. When analysing simulated results one has to assume a selection function to correct for biases. As mentioned above, many factors enter into the selection function. Producing a 'map' of the assumed cluster selection function in sufficient detail requires a large number of simulations. Each dimension needs to be sampled across several points, and the accuracy at each point is limited by the number of clusters present. Because the time scale of such an endeavour is proportional to the power of the number of equally sampled dimensions, the assumed selection function is limited to the three surface brightness properties we consider to be the most important: $0.5-2$ keV X-ray flux, r_c and β. This is referred to as the Surface Brightness Selection Function (SBSF). So that this assumed selection function is valid for all redshifts, temperatures and metallicities, the flux dimension is assessed as

a soft X-ray count rate $S_{\rm SX}$ (hereafter S), which more directly affects detectability.

The effect of exposure time t is also evaluated, giving a fourth dimension to the SBSF. To reduce the computation time required, different exposure times are only explored with a subset of the other SBSF parameters.

To determine the selection function f, we perform multiple simulations of clusters with properties corresponding to each point in a (S, r_c, β) parameter space, rather than drawing assorted clusters from the cosmological simulation. These clusters have symmetric β-models. Clusters are evenly spaced on each image, with a randomly positioned distribution of point sources drawn from the galaxy and AGN SXLFs, not correlated with the clusters. This approach has the advantage of sampling the parameter space much more rapidly, and sampling it thoroughly at several evenly spaced points. Unfortunately, cluster-cluster contamination is not represented and point source contamination does not reflect large scale structure. The influence of a more plausible AGN distribution on an important region of the SBSF is examined in Appendix A.3.

Background in these simulations is a combination of the predicted IXO particle background, the diffuse soft X-ray background and unresolved point sources. The particle background is fixed, along with all of the X-ray background below 10^{-17} erg cm^{-2} s^{-1}. Excluding Poisson noise, only unresolved point sources above 10^{-17} erg cm^{-2} s^{-1} can produce a variable contribution to the noise in the image.

The sampled values are shown in Table 4.1. The majority of the sampling is on the (S, r_c) plane, as this surface is known to be non-linear in the case of XMM-LSS (see Pacaud et al. 2006). Both of these dimensions are sampled logarithmically due to the range of parameter space and sensitivity at small values. Behaviour of the selection function with β is also expected to be non-linear. Due to the time constraints for extra sampling in this 3rd dimension a simple decimal sampling is used which covers the most common values in the $\beta - T$ relation.

Each point in the parameter space is sampled with 100 clusters. To maximise the amount of samples per simulation, images containing hexagonal grids of clusters are gen-

Table 4.1: Values used to parametrise the IXO selection function.

Count rate (cts s^{-1})	r_c (arcsec)	β
3.162×10^{-3}	0.1000	0.3[a]
5.623×10^{-3}	0.1585	0.4[b]
1.000×10^{-2}[a]	0.2512	0.5[a,b]
1.778×10^{-2}	0.3981[a]	0.6[b]
3.162×10^{-2}	0.6310	0.7[a,b]
5.623×10^{-2}	1.0000	0.8
1.000×10^{-1}[a]	1.5849[b]	
1.778×10^{-1}	2.5119	
3.162×10^{-1}	3.9811 [a,b]	
5.623×10^{-1}	6.3096	
1.000×10^{0}[a]	10.000[b]	
1.778×10^{0}	15.849	
3.162×10^{0}	25.119	
5.623×10^{0}	39.811[a]	
1.000×10^{1}[a]	63.096	
	100.000	

[a] Performed with the following exposure times (in ks): 1, 2.1544, 4.6416, 10, 21.544, 46.416, 100, 215.44, 464.16.
[b] Used to determine the amount of smoothing (see Appendix A.5).

erated. To avoid interference between each cluster, we impose a minimum spacing between cluster centres of $2r_c\sqrt{0.02^{-1/(3\beta+0.5)} - 1}$ (i.e. twice the radius at which the cluster flux drops to 2% of that at the centre) or $2.2R_{500}$, whichever is smaller. Therefore, number of clusters per image can be larger for clusters with smaller r_c or higher β. Source identification is performed on each image, and the detection probability is simply the number of clusters detected divided by the number of clusters simulated.

The IXO-09 WFI 10 ks selection function is presented in Figure 4.1. To create a more regular surface, the selection function has been smoothed onto a grid with 10 times the resolution in all 3 parameters. The smoothing method is discussed in Appendix A.5. The original 10 ks selection function is available in Appendix F.

At high r_c, increasing S and decreasing r_c raises the detection probability $f(S, r_c, \beta)$ as expected. However, at a low S, the probability begins to reduce with decreasing r_c

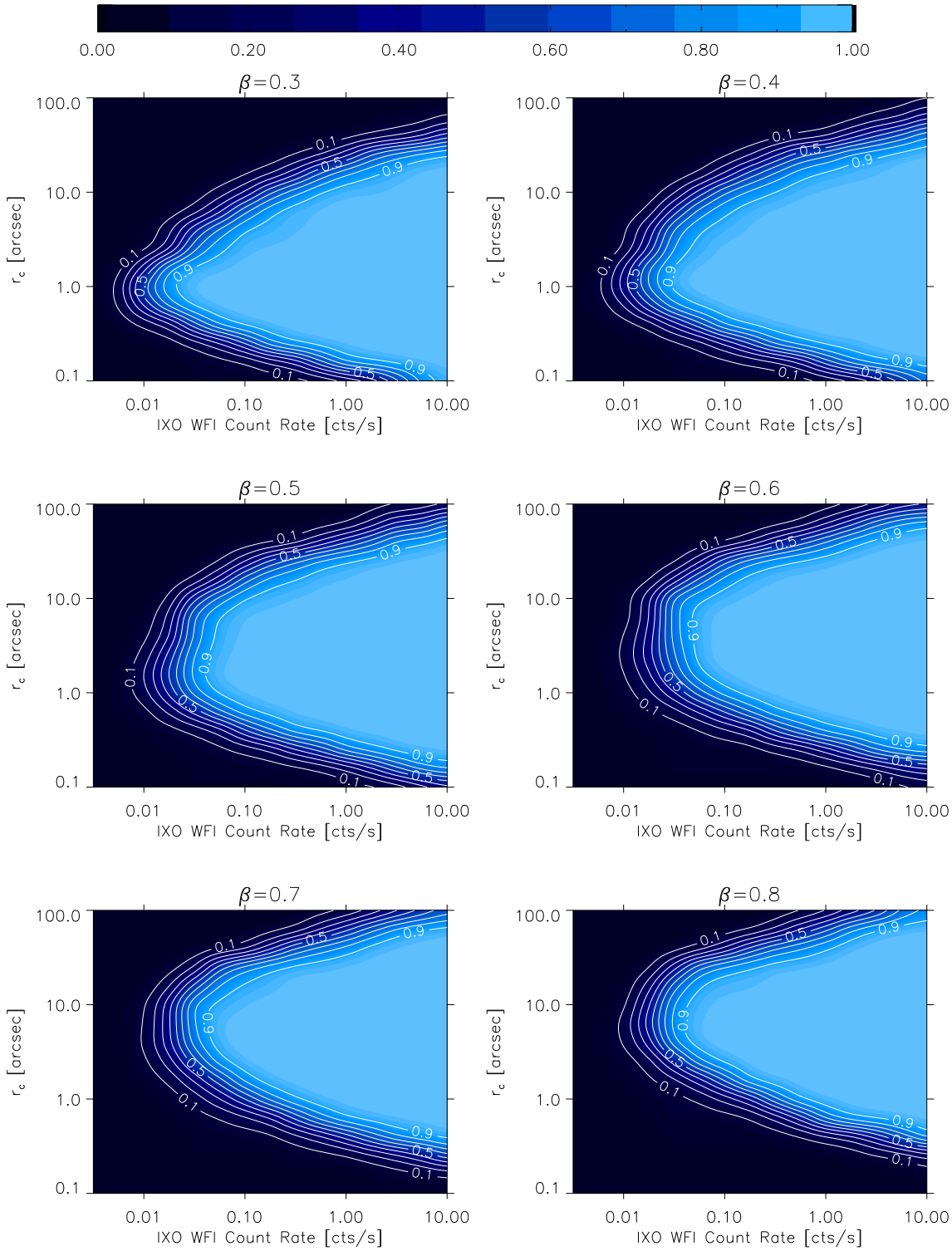

Figure 4.1: IXO-09 10 ks selection function. Lighter blue represents higher detection probability. The plots from *top-left* to *bottom-right* are cross-sections in the β dimension of the selection function, increasing from 0.3 to 0.8 in increments of 0.1.

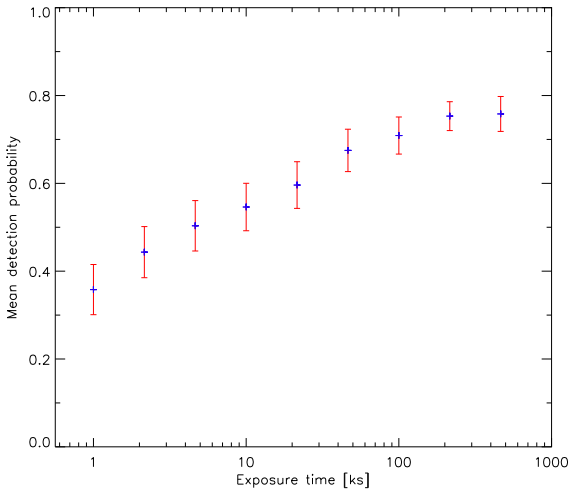

Figure 4.2: Mean cluster detection probability as a function of exposure time for IXO-09. The mean is that of all selection function regions sampled at multiple exposure times (see Table 4.1). Error bars give the standard error on the mean probability, but do not represent the full extent of the variation across $f(S, r_c, \beta)$ at each exposure time.

below a certain r_c. This turnaround r_c is ~ 2 arcsec for $\beta = 0.5$ and increases to ~ 7 arcsec by $\beta = 0.8$. This feature is likely the result of difficulty distinguishing between point sources and extended sources which have small core radii and sharp β profiles. The problem becomes significant at scales similar to the IXO PSF, which has a FWHM of 5 arcsec. The PSF causes the difference in size between the image of a point source and that of a cluster of a particular size to be a fraction of what it would be if just limited by the pixel size. Noise in the data then becomes very significant for small sources. The smaller the region containing the majority of the cluster emission, the greater the number of counts required to distinguish it from a point source, producing the trend seen at low r_c in Figure 4.1.

In general, lower r_c systems are more detectable when they have lower β. The effect of increasing r_c on the number of cluster detections becomes less prominent at higher values of β, highlighting the importance of both of these parameters of shape in cluster selection.

Note that the lowest sampled r_c of 0.1 arcsec is equivalent to a physical size of 862 pc at $z = 1.64$, where the angular diameter distance is at its maximum. Therefore, it is realistic to assume that such systems with such a small r_c do no exist (cf. Section 2.2.4.3).

A SBSF with a reduced parameter space is also generated for a range of exposure times t to explore the effect of exposure. The range sampled is $1 \leq t < 500$ ks. The parameters used in this selection function are labelled in Table 4.1. How the mean detection probability changes with exposure time is illustrated by Figure 4.2. Increasing the exposure time from 1 to 10 ks produces a gain of $\sim 20\%$, while an increase to 200 ks is required to raise the probability by $\sim 40\%$. Further detections are limited by the range sampled in S, with 100% detections for some of the $S = 0.01$ cts s^{-1} samples.

The change in each point of $f(S, r_c, \beta)$ with exposure time is non-linear and different at each point in the parameter space. With the limited resolution in each dimension, no obvious way can be seen to rescale the 10 ks selection function analytically. Thus, an interpolation-based approach is used.

The following method is used to approximate a smoothed 100 ks function. At each point sampled at 100 ks, the value of $f(S, r_c, \beta, 100\text{ ks}) - f(S, r_c, \beta, 10\text{ ks})$ is calculated. This 'probability increase' is interpolated onto a grid with the same resolution as the full 10 ks selection function. For consistency, this grid is smoothed with the same parameters as used on the 10 ks selection function. The probability increase grid is then added to the full $f(S, r_c, \beta$,10 ks) to give a rough estimate of a larger and more detailed form of $f(S, r_c, \beta$,100 ks), which is shown in Figure 4.3.

100% detection probabilities reach down to count rates half an order of magnitude lower than for 10 ks. However, the smoothed $f(S, r_c, \beta, 100\text{ ks})$ does not fairly represent the extreme ends of the parameter space due to the limited sampling used. The method presented above could be expanded to create a rough selection function at any of the sampled exposure times. Also, interpolation could be used to scale to any of the intervening exposure times, but with very poor accuracy at low detection probabilities.

4.1.3 Other Selection Functions

It is useful to see how correcting for bias using the SBSF compares with less thorough corrections. This gives an indication of how well existing surveys have corrected for bias,

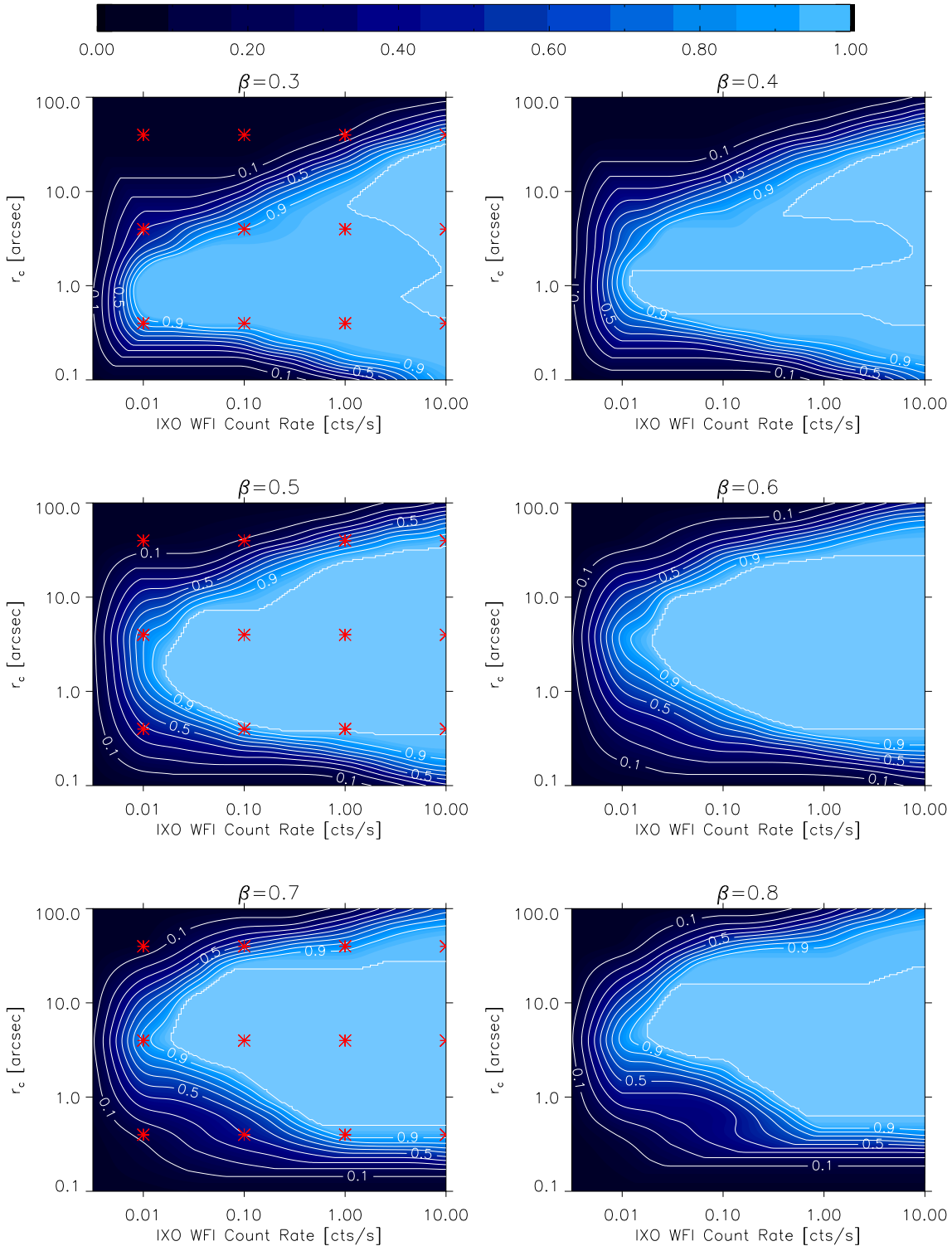

Figure 4.3: IXO-09 selection function from Figure 4.1 but scaled to 100 ks (see text). Red asterisks mark the locations which have been sampled using 100 ks simulations, and are therefore the most accurate. The irregular shape is due to the poor sampling of the selection function at 100 ks.

and demonstrates the effectiveness of the SBSF approach. The assumed selection function is investigated in the following levels of detail:

1. no selection function correction;
2. a flux cut of $S_{500} = 10^{-15}$ erg cm^{-2} s^{-1};
3. count rate, fixed physical r_c and fixed β selection of Pacaud et al. (2007), referred to as the Pacaud-style selection function;
4. count rate, r_c and β selection of the SBSF.

Choosing a flux cut directly yields an assumed selection function where $f(\geq S_{500}) = 1$ and $f(< S_{500}) = 0$, and can be converted to a count rate if necessary. The flux cut is $S_{500} \geq 10^{-15}$ erg cm^{-2} s^{-1} for both 10 ks and 100 ks. This allows us to see how effective a flux cut is when it excludes different amounts of data. For reference, the flux cut is equivalent to a count rate $S \approx 0.008$ cts s^{-1} for a $T = 1$ keV system at $z = 0.25$. The Pacaud-style selection function can be recovered from the SBSF by using interpolation. The exact procedure used to produce the different assumed selection functions is covered during their application later in this chapter.

4.1.4 Impact of Selection on $L_{\rm X} - T$

The assumed selection function can be used the demonstrate the way in which bias afflicts the observed $L_{\rm X} - T$ relation at different redshifts in the absence of any correction, *under the naive assumption that the assumed selection function represents the true survey selection function.* This involves creating a hypothetical distribution of luminosity for each temperature in an $L_{\rm X} - T$ relation, and then modifying it with the selection function to determine the most probable $L_{\rm X}$ for detections at each T. With the exception of the assumed selection function itself, no simulations are required (and no corrections are being applied). Note that this method does not include a T distribution for the clusters, so cannot be used to correct the $L_{\rm X} - T$ relation for a sample of clusters.

When applying the assumed selection function to the $L_{\rm X} - T$ relation it is more useful to state it in the form $f(L_{\rm X}, T, z, r_c, \beta)$, rather than $f(S, r_c, \beta)$. This allows the creation of a likelihood model for a cluster originating from a particular $L_{\rm X} - T$ relation. The selection function can also be reduced to $f(L_{\rm X}, T, z)$ by integrating over r_c and β using their respective scaling relations. This form can be directly applied to a model of the $L_{\rm X} - T$ relation, permitting us to predict the effect of selection bias.

Computing the assumed selection function $f(L_{\rm X}, T, z, r_c, \beta)$ from $f(S, r_c, \beta)$ is relatively straightforward. The count rate observed by IXO is calculated at each point in the ($L_{\rm X}$,T,z) parameter space. Conversion of flux to count rate assumes the standard XIS cluster model. We then interpolate in the S dimension of $f(S, r_c, \beta)$ to find the detection probability for each position in $f(L_{\rm X}, T, z, r_c, \beta)$. To demonstrate the effect of no selection function one sets $f(L_{\rm X}, T, z, r_c, \beta) = 1$.

To estimate the SBSF for $f(L_{\rm X}, T, z)$ we need to integrate over the scaling relations. For each temperature and redshift, a logarithmic grid of $10^{-5} \leq \log r_{cf} \leq 10^{0}$ is created. The $M_{500} - T$ and $r_{cf} - T$ relations are used to create a distribution of r_c and determine probability of each occurring for a given T and z. This probability array is then sampled to predict the probability of occurrence of each r_c on the selection function grid. Similarly, the probability of each selection function β is calculated for each T and z using the $\beta - T$ relation. When interpolating in the S dimension of $f(S, r_c, \beta)$, the whole of the r_c and β dimensions are also integrated over. This scales each detection probability with the probability of that point in the grid occurring for that particular T and z. The resulting detection probabilities form our $f(L_{\rm X}, T, z)$ for the SBSF.

To predict the bias in the $L_{\rm X} - T$ relation we use the same approach as Pacaud et al. (2007). Consider the luminosity distribution of sources at a particular T and z. Assume that these luminosities can be modelled by a log normal Probability Density Function (PDF), which is referred to as the true distribution:

$$\frac{{\rm d}P_{\rm true}(L_{\rm X}|T,z)}{{\rm d}\log L_{\rm X}} = \frac{1}{\sqrt{2\pi}\sigma_{\log L_{\rm X}}} \exp\left[-\frac{\log(L_{\rm X}/\overline{L_{\rm X}})^2}{2\sigma^2_{\log L_{\rm X}}}\right] \tag{4.1}$$

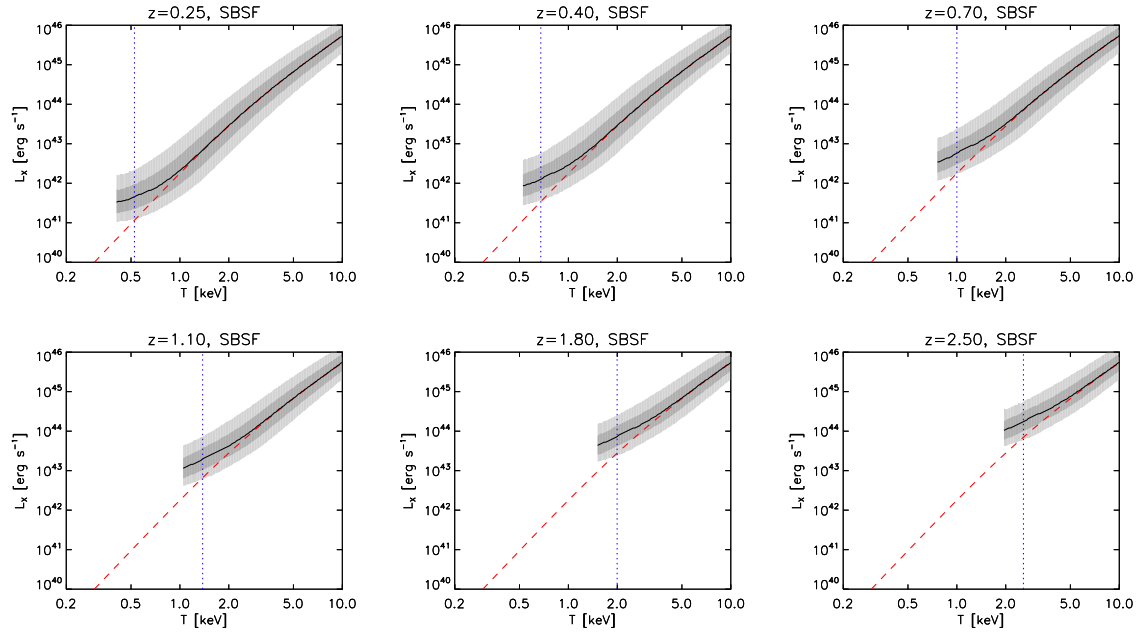

Figure 4.4: The mean of the modelled $L_{\rm X} - T$ relation used in XIS simulations (dashed line) with the maximum of the detections PDF (solid line) for each temperature, at $z = 0.25, 0.4, 0.7, 1.1, 1.8$ and 2.5, assuming the SBSF. The light and dark regions show, for each temperature, the luminosity interval that contains respectively 95.5 and 68.3% of the expected detections. The dotted lines show the temperature for which the detection probability (integrated over $L_{\rm X}$) falls to 10%. The shaded regions showing expected detections is cut where the integrated detection probability falls to 2%.

The mean of this normal distribution $\overline{L_{\rm X}}(T,z)$ and standard deviation $\sigma_{\log L_{\rm X}|T}$ are taken from our $L_{500} - T$ scaling relation (see Table 2.1). Both $\overline{L_{\rm X}}(T,z)$ and $\sigma_{\log L_{\rm X}|T}$ are assumed to be non-evolving with redshift.

A PDF for the detections in $(L_{\rm X}, T, z)$ space is found by normalising the true PDF model and folding in the selection function:

$$\frac{{\rm d}P_{\rm det}(L_{\rm X}|T,z)}{{\rm d}\log L_{\rm X}} = P_0(T,z) \times \frac{{\rm d}P_{\rm true}(L_{\rm X}|T,z)}{{\rm d}\log L_{\rm X}} \times f(L_{\rm X},T,z) \tag{4.2}$$

where

$$P_0(T,z) = \left(\int \frac{{\rm d}P_{\rm true}(L_{\rm X}|T,z)}{{\rm d}\log L_{\rm X}} {\rm d}(\log L_{\rm X}) \right)^{-1} \tag{4.3}$$

The results for 4 redshifts are shown in Figure 4.4. These plots show how large the $L_{\rm X} - T$ bias would be if the assumed SBSF represented all of the selection effects. The selection function renders under-luminous cool clusters undetectable by IXO, as shown for XMM-

Newton by Pacaud et al. (2007). The SBSF predicts a bias toward high luminosities when observing clusters of low temperatures. At $z < 0.25$ IXO is able to detect the low luminosity galaxy groups, which results in minimal bias above 0.7 keV. By $z = 0.7$ the bias in the group regime is significant, and less than 10% of the systems below 1 keV are recovered. At $z > 1$ the bias starts to become significant in the cluster regime, affecting systems with $T < 4$ keV by $z = 2.5$. In a cluster sample covering a range of redshifts, combinations of the slope bias at each redshift would result in an overestimation of the normalisation of the $L_{\rm X} - T$ relation.

Since a survey would contain clusters at a variety of redshifts, the actual amount of bias in the $L_{\rm X} - T$ relation can only be found be integrating over each redshift. This requires information about the distribution of clusters with redshift and temperature. We explore this further in the next section.

The prediction method shown here can be used explore how bias would affect the $L_{\rm X} - T$ relation in a universe where other types of assumed selection functions are the true selection function. Therefore, it can be used to find out how much correction to expect from other assumed selection functions, relative to the SBSF.

The Pacaud-style selection function is included to evaluate the effectiveness of this approach. This is a simplification of the SBSF. To replicate the method of Pacaud et al. (2007), each cluster is assumed to have a fixed physical $r_c = 180$ kpc and $\beta = 0.67$.[1] For every redshift, the angular size of r_c is calculated. Interpolation on $f(S, r_c, \beta)$ is then used to obtain $f(L_{\rm X}, T, z)$, which is referred to as the Pacaud-style selection function.

Presented in Figure 4.5 is predicted bias in $L_{\rm X} - T$ at $z = 0.25, 1.1$ and 2.5 using the Pacaud-style selection function as the true survey selection function. As before, these plots show the shape of the bias if this assumed selection function is a full representation of the survey selection function. Our Pacaud-style selection function predicts a much larger bias than the SBSF at low redshift. Most of the group regime suffers from bias by $z = 0.25$, and the mean of the $L_{\rm X} - T$ relation is $\sim 2\sigma$ from that of the SBSF. The

[1] $\beta = 2/3$ is common in cluster modelling.

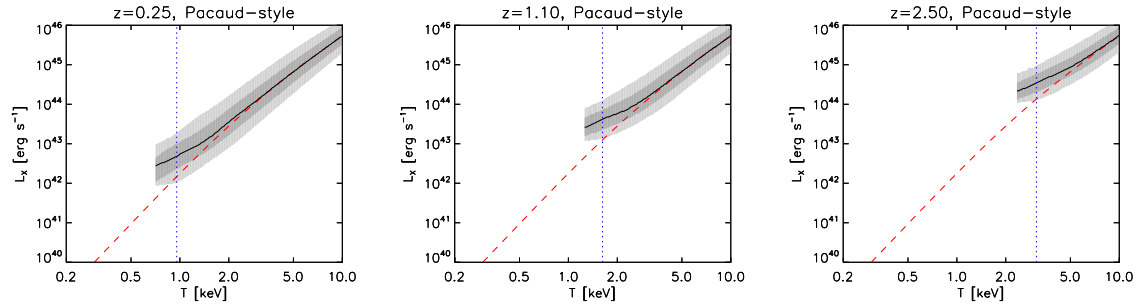

Figure 4.5: As Figure 4.4 but assuming a Pacaud-style selection function for the true survey selection function *(From left to right)* $z = 0.25, 1.1$ and 2.5.

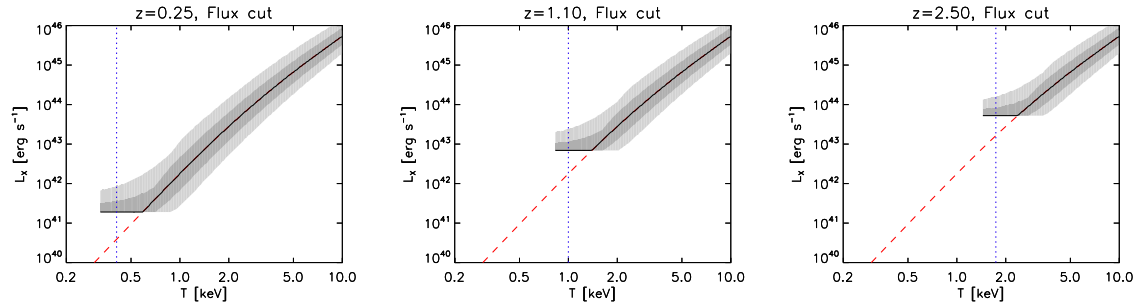

Figure 4.6: As Figure 4.5 but assuming flux cut selection for the true survey selection function.

discrepancy between the Pacaud-style selection function and the SBSF has reduced to 1σ by $z = 1.1$. Therefore, during the recovery of $L_{\rm X} - T$ evolution the Pacaud-style selection function should over-correct at low redshifts, relative to the SBSF.

We also produce a flux cut model as such an approach is common practise in X-ray surveys. This assumed selection function can be created without simulations as no instrumental effects are included. Our flux cut selection function assumes a 100% detection rate at $S \geq 10^{-15}$ erg cm^{-2} s^{-1}. This is effectively a selection function with $f(S, r_c, \beta) = 0$ below a T and z dependent count rate, and $f(S, r_c, \beta) = 1$ elsewhere. Therefore, it can be replicated by setting $f(L_{\rm X}, T, z) = 1$ if its equivalent $S \geq 10^{-15}$ erg cm^{-2} s^{-1}, otherwise $f(L_{\rm X}, T, z) = 0$.

The predicted bias in $L_{\rm X} - T$ with the flux cut representing the true selection function is shown in Figure 4.6. The flux cut model causes the mean of the $L_{\rm X} - T$ relation to suddenly change to a flat gradient. This occurs at a lower T than the SBSF, with the

mean deviating by 2σ. However, this difference reduces to 1σ by the 2% detection limit. The situation remains constant with redshift. Since the flux cut predicts less bias than the SBSF, it is expected to under-correct relative to the SBSF when used to recover the $L_{\rm X} - T$ evolution.

4.2 Survey Bias

Now that a well-defined assumed selection function has been established for the IXO-09 observatory configuration it can be applied to simulated surveys generated by XIS. These surveys use the Millennium simulation and empirical cluster scaling relations as established in Section 2.2, so contain a source population that is well motivated by both theory and observation. Use of the normal simulation process imposes a pseudo-realistic selection function on the data.

This study demonstrates the bias present in the 'observed' evolution of the $L_{\rm X} - T$ relation from the detected cluster sample, caused by the survey selection function. Attempts are made to correct for the bias using the SBSF and other assumed selection functions to judge their effectiveness. The sensitivity of the bias correction to the assumptions made about the $L_{\rm X} - T$ relation is also probed. The section concludes with an investigation into the recovered fraction of CC clusters when the evolving cool core model (see Section 2.2.4.4) is utilised in simulations.

4.2.1 Simulated Scenarios

The simulations within this section are performed using the primary sky field. Therefore, the cluster field is from a lightcone that passes through the Millennium simulation with a different vector to the one used in the calibration simulations. 180 pointings are generated in a hexagonal grid, creating a wide-angle survey with a total useful area[1] of 6.77 degree^2. The exposure time for each pointing is 10 ks to conform with the primary SBSF, resulting

[1]The outermost 32 pixels of the field of view are ignored as done in the calibration.

in a total survey time of 1.8 Ms. This is referred to as a survey simulation. The source identification process is used to catalogue the sources detected in the survey. Since there is no spectral information available in the simulations, recovered cluster properties z, T and L_{500} are the exact values that went into the simulation. The total number of clusters present in the survey area is 23251.

This survey simulation is performed several times to cover the following evolution scenarios for the $L_{\rm X} - T$ relation:

(i) no evolution (hereafter NE),

(ii) self-similar evolution with respect to the background density of the Universe (hereafter BD), $L_{\rm X} \propto (1+z)^{1.5}$,

(iii) self-similar evolution with respect to the critical density of the Universe (hereafter CD), $L_{\rm X} \propto H(z)$,

(iv) similarity linked to the threshold for radiative cooling (hereafter TC), $L_{\rm X} \propto H(z)^{-3} t(z)^{-2}$.

The origin of these relations was discussed in Section 1.3.7. The self-similar models represent a continuous rise in the mean luminosity with redshift. Contrastingly, the TC model has the mean luminosity increasing until $z \approx 0.5$ and then decreasing, bringing $L_{\rm X}$ below the local value at $z \approx 1.2$. Recovering the $L_{\rm X} - T$ evolution from the detected cluster sample reveals how that particular scenario would appear to the naive observer, when no selection function correction is applied. With an assumed selection function implemented in the recovery of the evolution, one can see if the true scenario can be recovered or if the best-fit model has the appearance of one of the other scenarios.

To see how exposure time influences survey bias, each of the survey simulations are also repeated with an exposure time of 100 ks for each pointing, equivalent to an 18 Ms survey. Such a large amount of allocated exposure time is unrealistic, but the intention here is to examine the effect of directly scaling up the exposure time over the same survey

Table 4.2: The number of clusters detected in each of the simulated surveys.

	$L_X - T$ evolution scenario			
Exposure time (ks)	NE	BD	CD	TC
10	340	563	436	352
100	758	1279	982	795

area (increasing the volume sampled). All of these simulations use the standard $r_{cf} - T$ relation.

Due to the the matching length and the number of false extended detections expected in 10 ks and 100 ks survey, 3% and 6% of the total number of clusters, respectively, may be due to chance matches of these spurious detections with faint simulated clusters (see Section 3.3.2.1). To minimise the number of these occurances, detected clusters are treated as undetected if they are below a minimum S_{500} count rate. Since the 10 ks SBSF has detection probabilities of $\sim 1\%$ at its lower limit of $S = 3.16 \times 10^{-3}$ cts s^{-1}, this lower limit is 10^{-3} cts s^{-1} for 10 ks surveys. It is reduced to 3.16×10^{-4} cts s^{-1} for the 100 ks surveys. The final number of clusters detected from each survey simulation is shown in Table 4.2.

The distribution of the detections in each 10 ks and 100 ks survey are presented in Figure 4.7 and Figure 4.8, respectively. At $T > 2.5$ keV both NE surveys are 85% complete. The smallest and largest $T \leq 1$ keV samples in the 10 ks surveys are 67 and 135 detected systems from the NE and BD surveys, respectively. These samples increase to 266 and 498 in the 100 ks surveys. For $z > 1.5$, the smallest and largest samples detected in the 10 ks surveys are in the TC and BD surveys, with 8 and 38 systems, respectively. Their 100 ks equivalents yield 26 and 146 systems. The 100 ks BD survey produces detections at the lowest temperatures and at the highest redshifts within the cluster sky field.

The sky field only contains 2 clusters above 5 keV, and neither of these are present in the simulated surveys. From the XIS cosmology adjustment of the MS mass function, we can expect ~ 1 cluster with $T > 5$ keV in survey of this size. Assuming this cluster is at

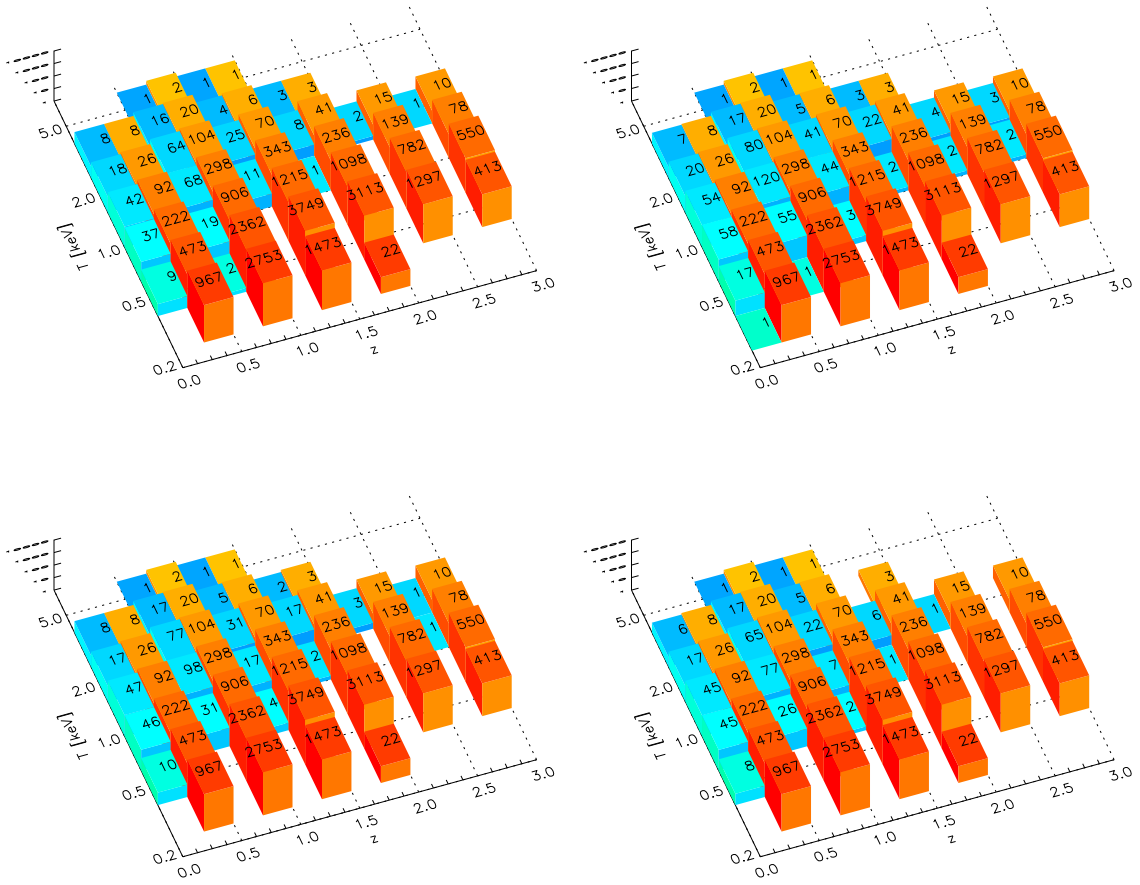

Figure 4.7: Number of detected clusters (blue) and total clusters (orange) as a function of temperature and redshift for a 10 ks exposure survey covering 6.77 degree^2 with IXO-09, repeated with the following different $L_X - T$ evolution models *(from top-left to bottom-right):* no evolution, self-similar with respect to the background density of the Universe, self-similar with respect to the critical density, similarity linked to the cooling threshold. Uses 7 temperature and 6 redshift bins of equal size from $-0.6 < \log T \leq 0.8$ and $0 < z \leq 3$, respectively. The number axis is on a log scale in the range $0 \leq \log N \leq 4$.

$z < 1$, it is expected to have $S > 0.66$ cts s^{-1}, $r_c > 9.1$ arcsec and $\beta > 0.61$, giving it a minimum detection probability of $> 99\%$.

The detections from the 10 ks and 100 ks NE surveys with respect to the the $L_X - T$ relation are shown in Figure 4.9, in which the $L_X - T$ model is valid at all redshifts. The majority of detections are at high L_X and low z as one would expect, and there is a clear bias away from the simulated $L_X - T$ relation at low temperatures. This slope bias is less for the 100 ks than the 10 ks due to the recovery of more of the low luminosity systems at a given T.

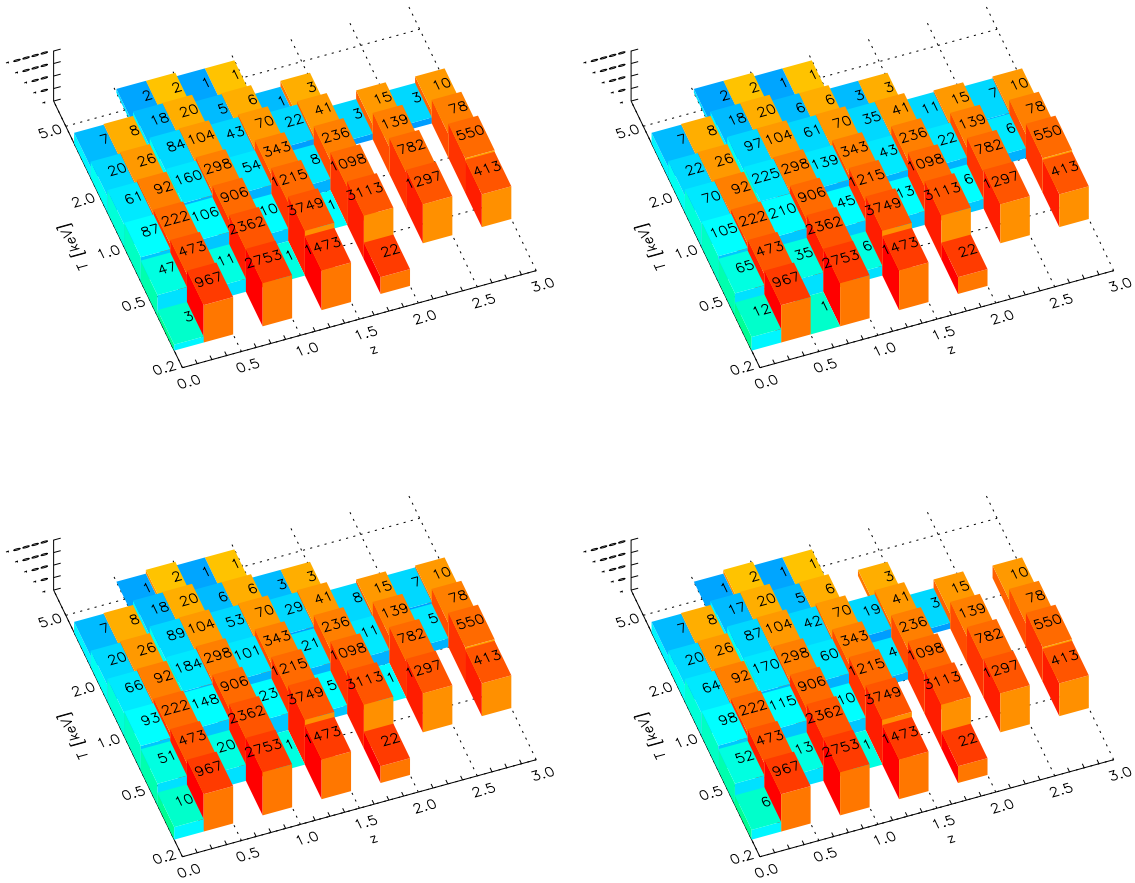

Figure 4.8: As Figure 4.7 but for 100 ks exposure surveys. The 100 ks BD survey also includes 6 detections at $3 < z < 3.11$ with the following temperatures (keV): 0.85, 1.03, 1.04, 1.08, 1.59, 2.08.

The slope bias appears to dominate over any normalisation bias on $L_X - T$ relation, despite the large redshift range covered. This is likely due to the small size of the survey and the resulting absence of $T > 5$ keV clusters. The normalisation of $L_X - T$ is also biased high by more luminous systems being detected over a greater volume, but this is also insignificant compared to the slope bias. Additionally, the lack of high T systems means that the shallow end of the $L_X - T$ relation is poorly represented (c.f. Figure 2.20, Section 2.2.8). Since the biasing effect of scatter is reduced for shallower slopes, a wider survey with the same exposure time per pointing would detect more high T systems and would have a less biased slope. $T > 5$ keV systems would also bias the slope less due to the high fraction of them detected at a given T.

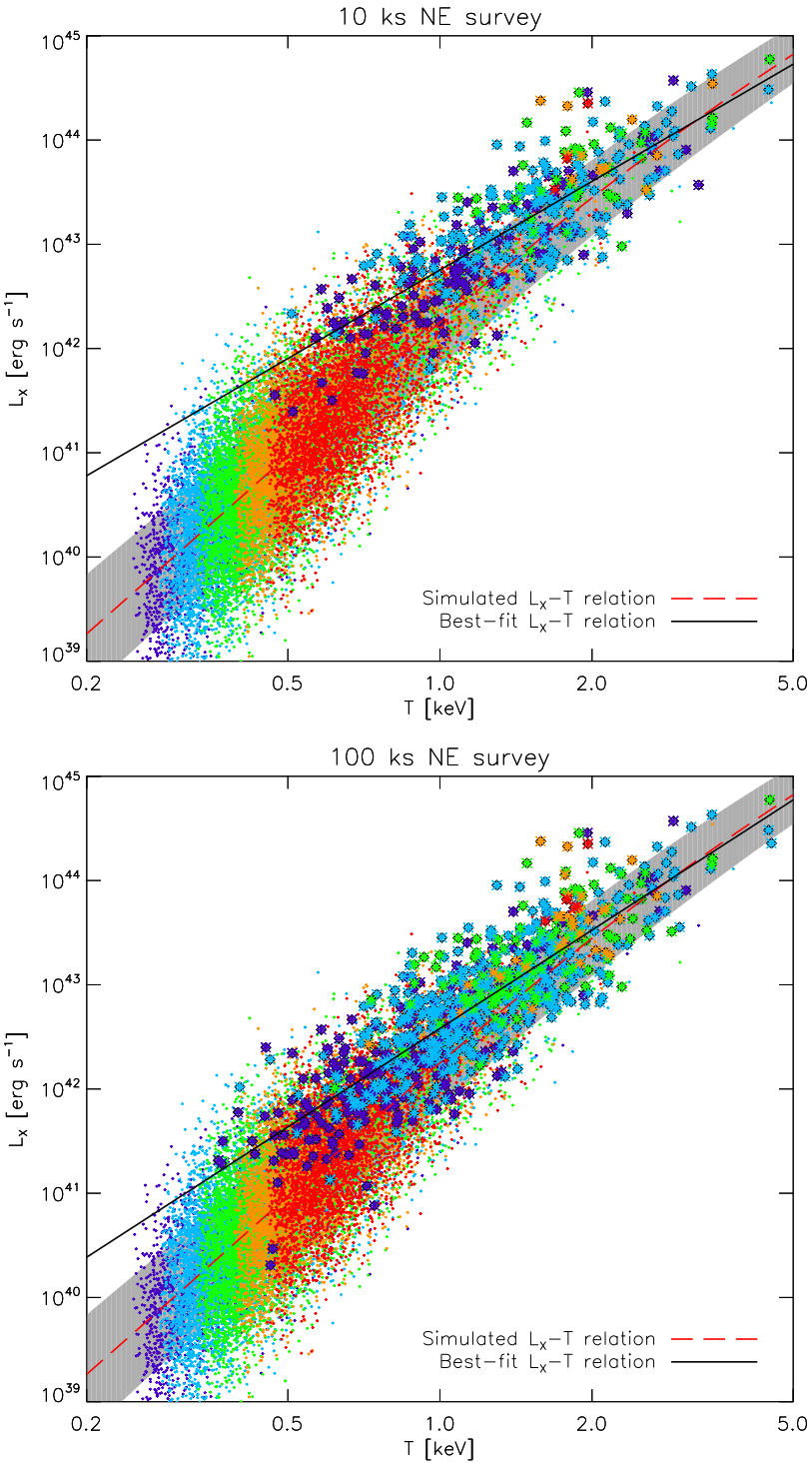

Figure 4.9: *Top:* Bias in the simulated non-evolving $L_{\rm X}-T$ relation from the 10 ks survey. The diamonds show the detected clusters, whilst dots represent undetected clusters. Symbol colours represent the following sequential redshift ranges: $z \leq 0.5$ dark blue, $z \leq 1$ light blue, $z \leq 1.5$ green, $z \leq 2$ orange, $z \leq 3$ red. The red long dashed line shows the mean of the input $L_{\rm X}-T$ relation. A power law fit to the detected clusters (black solid line) used to illustrate bias caused by detection of only the brightest low T systems. The shaded region shows the 1σ standard deviation of the simulated scatter. *Bottom:* As above, but from the 100 ks survey.

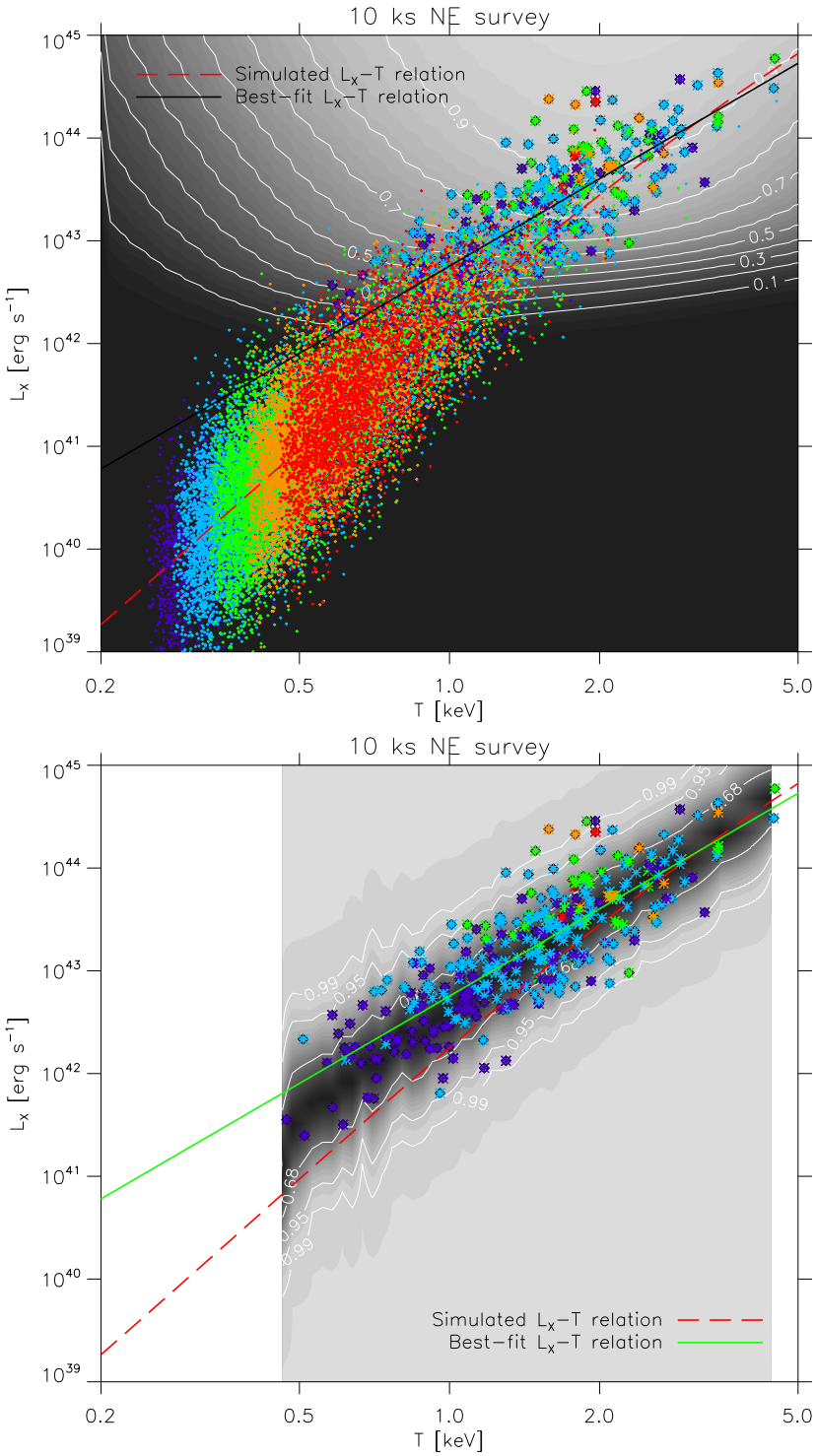

Figure 4.10: *Top:* As Figure 4.9 but with the selection function at $z = 0.55$ shown for comparison with the cluster detections. This selection function is marginalised over r_c and β using the method described in Section 4.1.4. The shaded region indicating the simulated scatter has been omitted for clarity. *Bottom:* Detected clusters overlaid on the predicted distribution of clusters at a given T (shaded region), shown in units of Gaussian σ. This prediction is based on the method from in Section 4.1.4 using the selection function above, but multiplied by (T, z) distribution of simulated clusters and integrated over z in bins. The shaded region has been truncated where the predicted number of detections is < 1.

In Figure 4.10 we compare the $L_{\rm X}-T$ results with interpretations of the assumed selection function. The upper plot shows the detection probabilities of the SBSF at the peak of the detected cluster z distribution, integrating over r_c and β following the method in Section 4.1.4. The lower plot includes an advancement on the $L_{\rm X}-T$ bias prediction shown in Figure 4.4. Instead of showing the expected $L_{\rm X}$ distribution $\mathrm{d}P_{\rm det}(L_{\rm X}|T,z)/\mathrm{d}\log L_{\rm X}$ for a particular z, the distribution is multiplied by the number of simulated clusters as a function of T and z (i.e. the orange bars from Figure 4.7, but with much finer bins). This probability function is then integrated over the $0<z\leq 3$ range and used to calculate the expected distribution of clusters at each T.

In general, the locations of the detected clusters agree well with the assumed selection function. The expected slope bias is more significant than the expected normalisation bias, as seen in the survey data. However, the $L_{\rm X}$ distribution of detected clusters with $T\lesssim 1$ keV suggests that the SBSF underestimates the amount of bias for these systems, with very few clusters lying more than 1σ below the mean. Note that statistics are poor at $T\ll 1$ keV.

4.2.2 Recovering the Evolution of $L_{\rm X}-T$

Here the simulated survey is used to demonstrate how bias effects the recovery of the evolution of the $L_{\rm X}-T$ relation, and how well different assumed selection functions correct for it. The effect of evolution of the $L_{\rm X}-T$ relation can be illustrated by dividing the observed luminosity of a cluster with that expected from its temperature at $z=0$ (i.e. from the local $L_{\rm X}-T$ relation), giving an $L_{\rm X}-T$ enhancement factor $F(z)$. We can show how selection bias influences the recovery of the $L_{\rm X}-T$ evolution by comparing the enhancement factor calculated from detected clusters with that from all of the clusters present in a simulation.

The method used to predict the bias in $L_{\rm X}-T$ (see Section 4.1.4) can be extended to correct for the bias in the evolution of $L_{\rm X}-T$, following the approach of Pacaud et al. (2007). A likelihood is calculated for each cluster within a hypothetical true $L_{\rm X}-T$

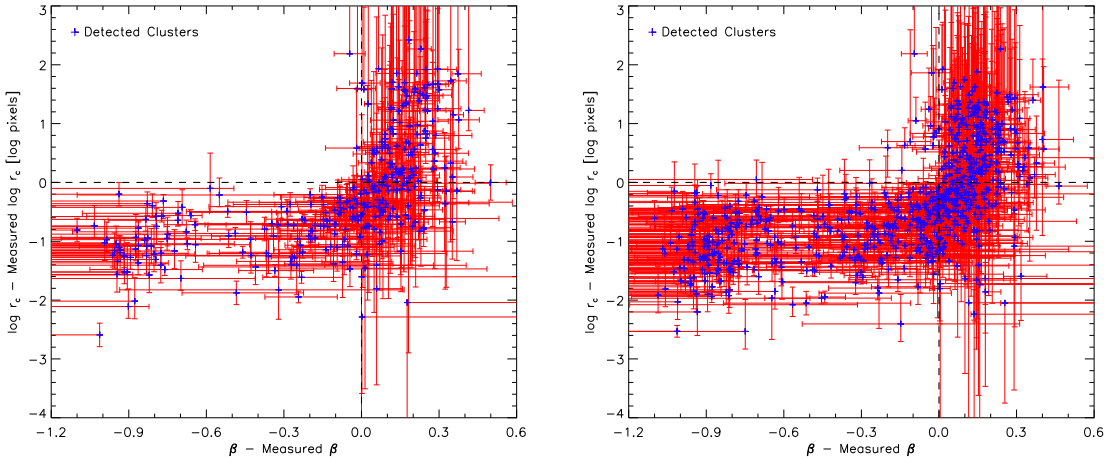

Figure 4.11: *Left:* The difference between simulated and best-fit $\log r_c$ against difference between simulated and best-fit β in the 10 ks no evolution survey. *Right:* As left, but from the 100 ks survey.

distribution (see Equation 4.1) with mean $\overline{L_{\rm X}}(T,z)$. An evolution enhancement factor $F(z)$ is assumed, thus $\overline{L_{\rm X}}(T,z) = L(T,z=0) \times F(z)$. In this study it is assumed that the local $L_{\rm X} - T$ relation is known. With individual cluster data now available, r_c and β can be kept as as separate dimensions in the calculation, resulting in the following modifications of Equation 4.2 and Equation 4.3:

$$\frac{{\rm d}P_{\rm det}(L_{\rm X}|T,z,r_c,\beta)}{{\rm d}\log L_{\rm X}} = P_0(T,z,r_c,\beta) \times \frac{{\rm d}P_{\rm true}(L_{\rm X}|T,z)}{{\rm d}\log L_{\rm X}} \times f(L_{\rm X},T,z,r_c,\beta) \qquad (4.4)$$

where

$$P_0(T,z,r_c,\beta) = \left(\int \left[\frac{{\rm d}P_{\rm true}(L_{\rm X}|T,z)}{{\rm d}\log L_{\rm X}} \times f(L_{\rm X},T,z,r_c,\beta) \right] {\rm d}(\log L_{\rm X}) \right)^{-1} \qquad (4.5)$$

The likelihood $\mathcal{L}$ of an observed cluster C is computed with a model of $F(z)$. Ideally one would use the true cluster properties to determine its detection probability. Realistically, the best-fit parameters for each cluster would have to be used. This leads to inaccuracies in the correction. An example of the amount of discrepancy in a sample is shown in Figure 4.11, which gives the difference between the simulated and measured $\log r_c$ and β in an NE simulation. The effect of inaccuracies can be minimised by marginalising over

the best-fit parameters.

Due to the lack of spectral information in these simulations, all clusters are corrected using their true $L_{\rm X}$, T and z. To see how the limitation of using surface brightness fits affects the correction, we try both the true r_c and β and the best-fit r_c and β. The latter correction is integrated over the entire $\log r_c$ and β space. In this case, the likelihood for a given $F(z)$ is

$$\mathcal{L}(F|C) = \iint_0^\infty \left[\frac{\mathrm{d}P_{\rm det}(L_{\rm X}|T,z,r_c,\beta)}{\mathrm{d}\log L_{\rm X}}\right] \times P_C(r_c,\beta)\mathrm{d}r_c\mathrm{d}\beta \tag{4.6}$$

where $P_C(r_c,\beta)$ is the PDF for both r_c and β, based on the errors in both parameters. A best fit model for $F(z)$ is found by maximising the likelihood for the entire cluster sample. This is the product of the detection probability of each cluster for the given $L_{\rm X}-T$ model:

$$\mathcal{L}(F) = \prod_{i=0}^{N} \mathcal{L}(F|C_i) \tag{4.7}$$

Since the product of a large sample of detection probabilities is too small to be represented on a computer, the fits are computed by minimising $-\ln\mathcal{L}$.

$f(L_{\rm X},T,z,r_c,\beta)$ is recovered from $f(S,r_c,\beta)$ as discussed earlier. When predicting the bias in the $L_{\rm X}-T$ relation each redshift can be dealt with individually and there is no fitting to perform. This is no longer the case. Computer limitations restrict our resolution when dealing with a parameter space with a large number of dimensions. For our $F(z)$ fits, $f(L_{\rm X},T,z,r_c,\beta)$ has dimensions of size $(86,181,9,31,26)$, respectively. The first two dimensions have ranges of $38 \leq \log L \leq 47$ erg s^{-1} and $-0.7 \leq \log(T \text{ keV}) \leq 1$. Our z dimension consists of the following 9 values: $0.25, 0.4, 0.55, 0.7, 0.8, 0.95, 1.1, 1.8, 2.5$. The final bin samples the far end of the z distribution, while the rest have been selected to contain similar numbers of detected clusters in each bin. The final two dimensions use the full range and every other value of r_c and β from the smoothed SBSF (which has 10 times the resolution of the original).

The consequence of using other assumed selection functions is also of interest. A

Pacaud-style correction is implemented using the SBSF by assuming each cluster has $\beta = 0.67$ and an angular size equivalent to a physical $r_c = 180$ kpc.

A flux cut selection function for $f(L_{\rm X}, T, z)$ is produced as before. This correction effectively excludes clusters from the likelihood calculation if they lie below the cut. Therefore, by using the $S_{500} \geq 10^{-15}$ erg cm^{-2} s^{-1} on both the 10 ks and 100 ks surveys we can illustrate the effect of removing more of the low flux systems in the 100 ks case. Since there is no change with r_c or β, $f(L_{\rm X}, T, z)$ directly gives $f(L_{\rm X}, T, z, r_c, \beta)$.

To fit the detected cluster data we require a non-monotonic model that can represent the different forms of evolution. Ideally this would be the same model as used for the simulations: $(1+z)^u E(z)^v \tau(z)^w$. However, this is a computational expensive model and suffers from considerable degeneracy. To compromise we follow Pacaud et al. (2007) and use a less degenerate two-parameter model of the form $F(z) = (1+z)^u E(z)^v$ (effectively setting $w = 0$). As this is a subset of our previous model, it is still capable of accurately representing the first 3 evolutionary models, and can closely resemble the cooling threshold model.[1] Unfortunately, given the imperfect nature of the correction to each data point, the degeneracy in this model may still prevent the recovered u and v from exactly matching those input into the simulations.

1σ errors on our fitted parameters are estimated by associating a change in $-2 \ln \mathcal{L}(F)$ with a χ^2 distribution, analogous to the method used when fitting surface brightness profiles. Wilks' theorem states that this association is asymptotically valid in the limit of large samples.

4.2.3 Bias in the Evolution of $L_{\rm X} - T$

Likelihood fits to $F(z)$ are obtained using no selection function correction, correction for a Pacaud-style selection function and correction for a SBSF, all using the true cluster properties. The SBSF $F(z)$ fit is repeated using the best-fit r_c and β of each cluster. 100 ks surveys use the extrapolated 100 ks SBSF rather than the smoothed 10 ks SBSF.

[1] Evolution of $u = 1.57$, $v = -1.95$ is very similar to $v = -3$, $w = -2$ at $z < 2$.

Table 4.3: Results of fits to the $L_X - T$ enhancement factor $F(z)$ for each survey evolution model, exposure time and selection function correction. $F(z) = (1+z)^u E(z)^v$. Surveys have the following $L_X - T$ evolution models: NE, BD, CD and TC. Fitting parameters are limited to the range between $-6 \leq u \leq 6$.

Survey		No correction	Flux cut	Pacaud-style	SBSF	SBSF with fits
NE 10 ks	u	2.80 ± 0.13	2.28 ± 0.15	-2.91 ± 0.20	1.45 ± 0.17	-0.45 ± 0.21
	v	-2.21 ± 0.17	-1.91 ± 0.20	$2.99^{+0.26}_{-0.27}$	-1.91 ± 0.23	$-0.07^{+0.28}_{-0.29}$
NE 100 ks	u	2.45 ± 0.09	$0.21^{+0.13}_{-0.12}$	-2.34 ± 0.10	0.84 ± 0.10	$-0.13^{+0.11}_{-0.10}$
	v	-2.03 ± 0.12	$0.16^{+0.15}_{-0.18}$	2.68 ± 0.13	-0.77 ± 0.13	$0.27^{+0.14}_{-0.13}$
BD 10 ks	u	4.09 ± 0.10	3.39 ± 0.11	-0.47 ± 0.13	2.21 ± 0.12	0.28 ± 0.14
	v	-2.12 ± 0.12	-1.44 ± 0.13	2.03 ± 0.17	-0.72 ± 0.15	1.32 ± 0.17
BD 100 ks	u	$3.76^{+0.06}_{-0.07}$	2.63 ± 0.08	0.14 ± 0.07	2.47 ± 0.07	1.88 ± 0.07
	v	-1.90 ± 0.08	-1.12 ± 0.10	$1.39^{+0.08}_{-0.09}$	-0.96 ± 0.09	-0.37 ± 0.09
CD 10 ks	u	$2.61^{+0.11}_{-0.12}$	1.87 ± 0.13	-3.08 ± 0.16	0.82 ± 0.14	-1.44 ± 0.16
	v	-0.99 ± 0.15	-0.31 ± 0.16	$4.41^{+0.20}_{-0.21}$	0.17 ± 0.18	2.59 ± 0.21
CD 100 ks	u	2.62 ± 0.08	0.82 ± 0.10	-1.49 ± 0.08	$1.16^{+0.08}_{-0.09}$	0.48 ± 0.09
	v	-1.30 ± 0.09	$0.34^{+0.12}_{-0.13}$	2.55 ± 0.10	$-0.18^{+0.09}_{-0.11}$	0.49 ± 0.11
TC 10 ks	u	4.00 ± 0.14	$3.45^{+0.15}_{-0.16}$	-0.99 ± 0.20	$3.00^{+0.17}_{-0.18}$	-0.10 ± 0.21
	v	-3.49 ± 0.19	-3.12 ± 0.21	0.82 ± 0.27	-3.57 ± 0.24	$-0.07^{+0.28}_{-0.29}$
TC 100 ks	u	4.67 ± 0.09	2.49 ± 0.13	-0.59 ± 0.10	3.09 ± 0.10	2.23 ± 0.11
	v	-4.85 ± 0.12	-2.73 ± 0.17	0.49 ± 0.13	-3.63 ± 0.13	-2.72 ± 0.14

The best-fit parameters are given in Table 4.3.

It is useful to quantify how well the best-fit $F(z)$ models agree with different evolutionary models. This is achieved by identifying the change in $-2 \ln \mathcal{L}(F)$ between each best-fit $F(z)$ and the four models which represent the four evolutionary models used for the simulations (i.e. applications of $(1+z)^u E(z)^v \tau(z)^w$). The change in $-2 \ln \mathcal{L}(F)$ is presented in terms of Gaussian standard deviations in Table 4.4.

4.2.3.1 No Selection Function Correction

Results from the 10 ks simulations using the four different evolution models (red long dashed line) are presented in Figure 4.12. Without any correction for the selection function (light blue solid line), the luminosity evolution is overestimated across all redshifts as expected from selection bias. This overestimate gives the appearance of very strong positive evolution in the low redshift Universe, caused by the detection of only the most luminous $T < 1$ keV systems. The NE and TC surveys show very minor negative evolution at $z > 1$, while positive evolution appears to continue in the BD and CD surveys. For

Table 4.4: How well the $L_X - T$ enhancement factor fits can be identified with the different evolutionary models. For each simulated survey given in the first column, we calculate the probability that the fit in each column is drawn from the test evolution models in each row. Test models are the same as those used in the simulated surveys: no evolution (NE), self-similar with respect to the background density (BD), self-similar with respect to the critical density (CD) and similarity linked to the threshold for radiative cooling (TC). This assumes the difference in $-2 \ln \mathcal{L}(F)$ is χ^2 distributed. The results are represented as σ of a Gaussian distribution. Values of 10σ and above are omitted for clarity.

Survey	Model	σ				
		No correction	Flux cut	Pacaud-style	SBSF	SBSF with fits
NE 10 ks	NE			5.68	1.24	3.46
	BD	4.94	6.89			
	CD	5.62	2.80		6.68	
	TC		6.80	7.64	0.64	5.04
NE 100 ks	NE		3.54	5.56	3.72	0.77
	BD					
	CD	5.87	5.35			
	TC		1.65		2.92	3.47
BD 10 ks	NE					
	BD			5.00	1.83	2.36
	CD			3.69		5.57
	TC					
BD 100 ks	NE					
	BD		4.71	5.79	4.61	1.47
	CD					
	TC					
CD 10 ks	NE			4.84		5.15
	BD	4.55	1.14		5.89	
	CD			5.64	1.78	2.25
	TC			6.42		5.46
CD 100 ks	NE					
	BD	3.29	6.32			
	CD		4.58	5.26	4.47	1.31
	TC					
TC 10 ks	NE			2.70	4.29	0.66
	BD	3.38	4.04			
	CD		5.56		4.14	6.64
	TC			4.66	1.86	2.39
TC 100 ks	NE		6.39	3.01	7.64	4.45
	BD					
	CD		4.74			
	TC		3.57	6.03	3.87	0.72

each 10 ks survey except BD there is weak agreement between the recovered evolution with no correction and the BD model.

We present the results for the 100 ks simulations in Figure 4.13, along with Table 4.3. The increased exposure reduces the overall amount of bias in each survey, as can be

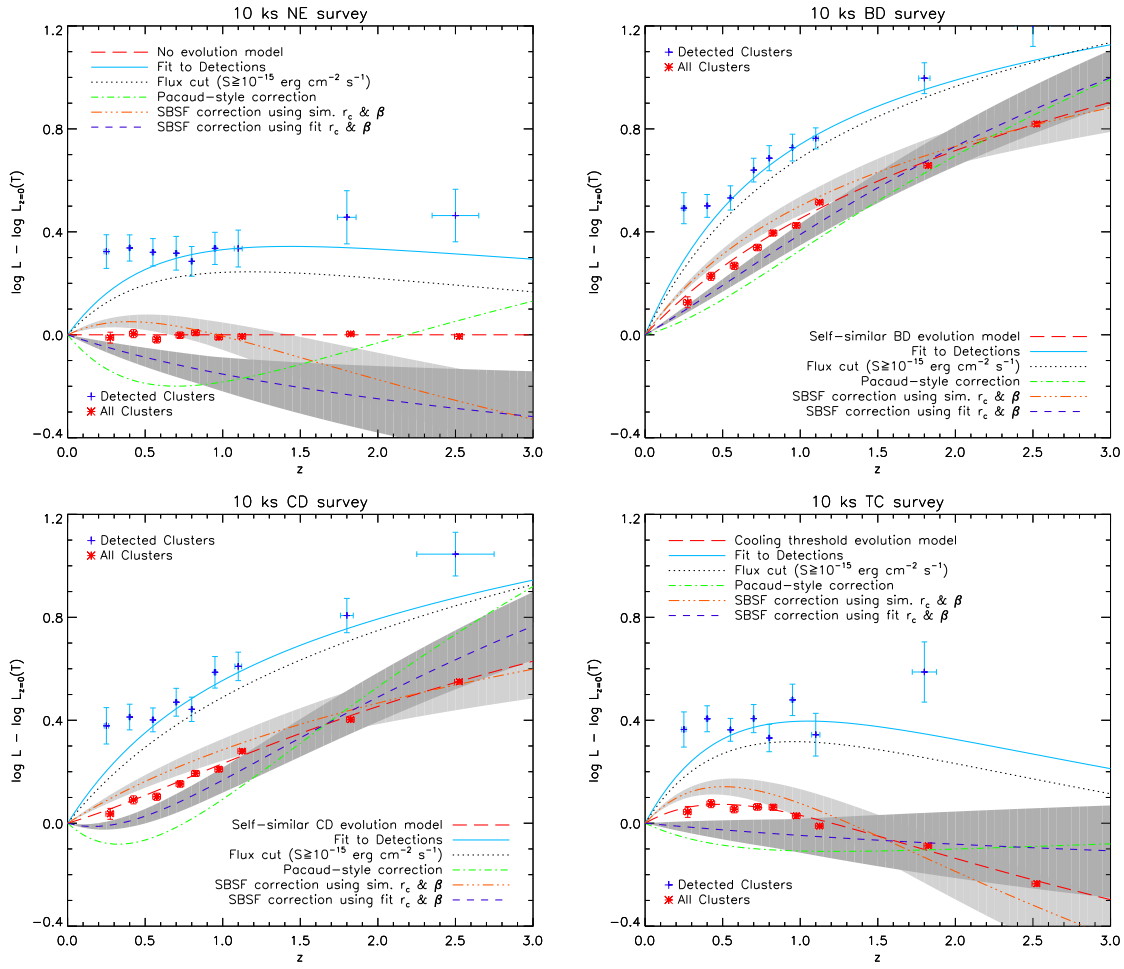

Figure 4.12: Bias in the simulated $L_{\rm X}-T$ enhancement factor for a 10 ks exposure IXO-09 survey covering 6.77 degree^2, repeated with the following different evolution models *(from top-left to bottom-right):* no evolution, self-similar with respect to the background density, self-similar with respect to the critical density, similarity linked to the cooling threshold. Blue points represent the mean enhancement factor of the detected clusters within a redshift bin, whilst the orange points include all of the simulated clusters. z bins are centred at 0.25, 0.4, 0.55, 0.7, 0.8, 0.95, 1.1, 1.8, and 2.5, with equidistant widths. The red long dashed line shows the evolution model, whilst the light blue solid line is the $F(z)$ model fit to the detected cluster data. Black dotted and green dot-dash lines are the flux cut and Pacaud-style corrected fits, respectively, applied using the true cluster properties. Orange dot-dash and dark blue short dashed lines show the SBSF corrected fits applied using the true and best-fit cluster properties, respectively.

expected from the increased detection probabilities. However, the bias is still significant enough to cause each uncorrected $F(z)$ fit to return a result inconsistent with the true evolution.

4.2.3.2 Flux Cut Correction

When dealing with the 10 ks surveys, the $S_{500} \geq 10^{-15}$ erg cm^{-2} s^{-1} flux cut is very similar to the faintest detection as only $3-5$ clusters lie below it. Therefore, it is similar to assuming that all clusters up to the cut can be observed because a system has been detected at that flux. Applying the flux cut correction to the $F(z)$ fit (black dotted line) slightly reduces the bias for all 10 ks surveys, but they continue to produce misleading results. Agreement with the true evolution is negligible in all cases.

The flux cut performs better at 100 ks than at 10 ks due to the availability of a more thorough sample of the clusters above the cut. $126-153$ clusters have now be excluded by the cut. With the remaining clusters, all 100 ks surveys except NE have $F(z)$ fits that are closer to the true evolution than the 3 alternative models. However, the overall agreement is still $> 3\sigma$ from the true evolution for all surveys. Systems that scatter higher than the mean luminosity and lie above the cut are given equal weight in the analysis and consequently create a bias. The flux cut could be moved higher to remove more of the bias, but this comes at the expense having less data and therefore more noise in the fit.

4.2.3.3 Pacaud-style Correction

A considerably different situation emerges when the Pacaud-style correction (green dot-dash line) is used. The low redshift systems are over-corrected as indicated in Section 4.1.4. A large portion of the low z systems have low T, and generally have $\beta < 0.6$ due to the $\beta - T$ relation. This means that if one assumes a selection function with β fixed at 0.67 the detection probability of the systems is often underestimated (see Figure 4.1, Section 4.1.2). This underestimation is somewhat reduced by assuming all systems have a physical r_c of 180 kpc, as this is an overestimation for all but $1-2$ systems, generally moving them to a higher probability region of the selection function. However, it is still a significant problem.

Since low T, low z systems are assigned a low detection probability, the assumed distribution of detections $\mathrm{d}P_{\mathrm{det}}(L_{\mathrm{X}}|T, z, r_c, \beta)/\mathrm{d}\log L_{\mathrm{X}}$ is biased higher than in the simulated

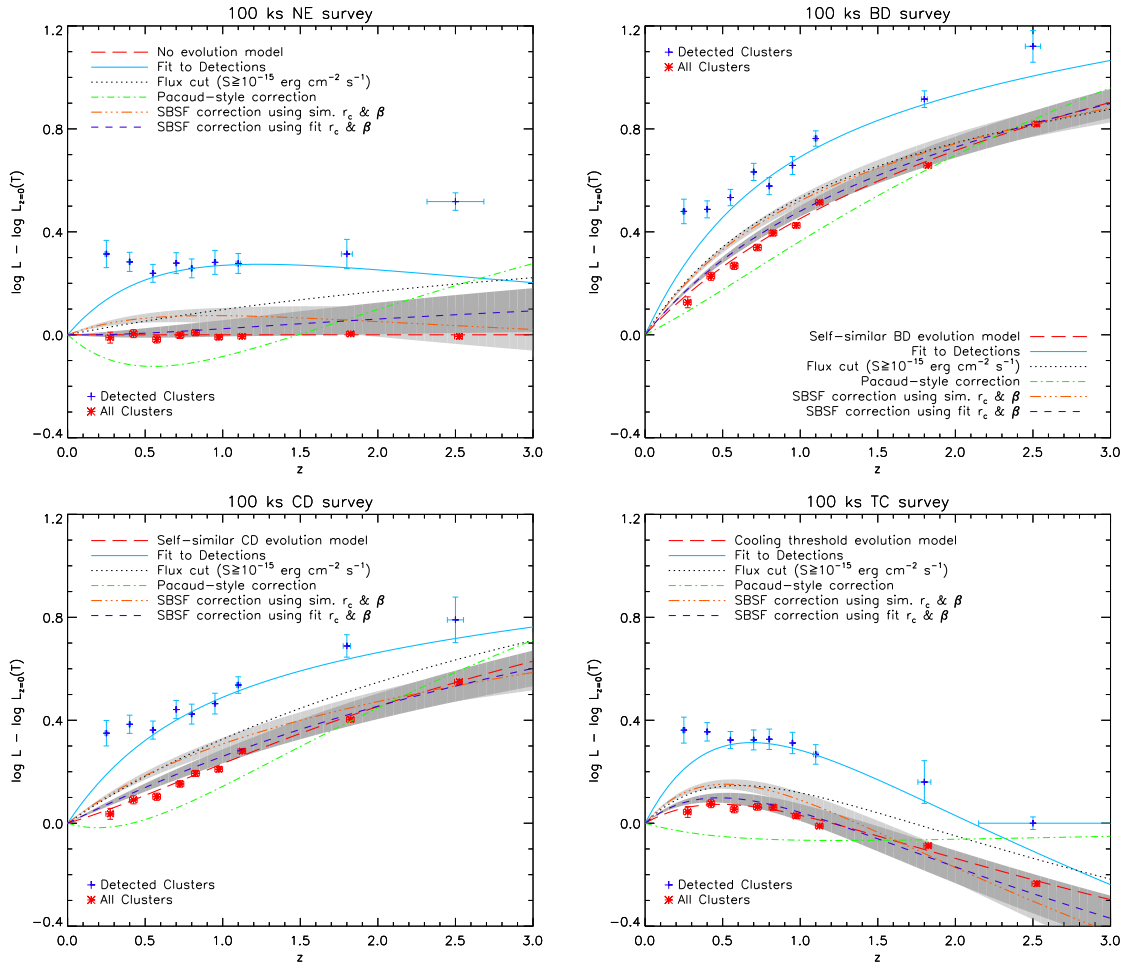

Figure 4.13: As Figure 4.12, but from the 100 ks exposure IXO-09 survey simulations covering 6.77 degree^2. The SBSF correction uses the estimated 100 ks SBSF.

surveys. The best-fit $F(z)$ model has negative luminosity evolution at low z to align the expected $L_{\rm X} - T$ relation with that found in the survey.

The over-correction causes all 10 ks surveys except BD to show negative luminosity evolution until at least $z = 0.3$. Unsurprisingly, this results in poor agreement with the true evolution. At medium redshifts the fit becomes closer to the true model due to the lack of low temperature (and therefore low β) detections. However, it is unable to follow the true model at these redshifts because it is limited by the flexibility of the $F(z)$ model.

For the 100 ks surveys, the low z over-correction of the Pacaud-style assumed selection function still hinders the evolution recovery in all cases.

4.2.3.4 SBSF Correction

Using the SBSF (orange triple-dot-dash line) for the 10 ks surveys considerably improves $L_{\rm X} - T$ recovery all cases, bringing $F(z)$ to within 2σ of the true evolution. There is a slight under-correction at $z < 1$, but close agreement with the true form of the evolution of all 10 ks surveys except NE.

Applying the SBSF using the r_c and β fit PDFs (dark blue short dashed line) noticeably changes the fit for each survey. The NE survey is over-corrected at all redshifts, giving the appearance of continuous negative evolution. Over-correction only affects the low redshift regions of the other surveys, but reduces the agreement with their true models to $\sim 2 - 3\sigma$. These fits highlight the importance of correctly identifying the surface brightness properties of each cluster when correcting for bias.

When analysing the 100 ks simulations, under-correction at low z is still a problem for the correctly applied SBSF, and agreement with the true evolution has diminished to $\sim 4\sigma$ in all cases. However the 100 ks SBSF is only a rough estimate. Also, imprecisions in the 10 ks SBSF would have propagated to the 100 ks and could have become exaggerated, resulting in a less effective correction. Surprisingly, the SBSF correction applied using fits comes much closer to recovering the true evolution, giving $< 2\sigma$ agreement with the BD and CD surveys and $< 1\sigma$ agreement with the NE and TC surveys.

The under-correction at low redshift is likely related to the under-estimation of the bias at low T from the SBSF shown in Figure 4.10, Section 4.2.1, since the majority of low T systems are detected at low z. Over-correction at high redshift could be a result of poor z resolution in the selection function at high z combined with a limited sample of high z clusters. It could also come from the limited flexibility of the $F(z)$ model, which is more constrained by the more numerous cluster population at low z.

To better understand the inadequacy of the SBSF we use its current form (including the limited quality of the z dimension) to predict the number of expected detections in the NE survey. This is shown in the lower half of Table F.2, Appendix F, as a fraction of the total number of simulated clusters (hereafter completeness). The expected completeness

is significantly larger than the survey completeness at $z \leq 0.5$, except at $T > 2.5$ keV. This causes the $F(z)$ under-correction at low z. At greater redshifts the SBSF under-predicts the completeness, consistent with the high z over-correction, although the under-prediction is not significant in most (T, z) bins.

The top half of Table F.2 gives the expected completeness directly from the smoothed $f(S, r_c, \beta)$ form of the SBSF. Comparison with the lower half of the table shows that the interpolation of the selection function to the $f(L_{\rm X}, T, z, r_c, \beta)$ form does not disrupt the predictions by more than 6%, and only 2% at low z. These discrepencies are small compared to the over-prediction at $z \leq 0.5$, therefore the interpolation cannot be the main cause of the inadequacy of the SBSF.

Inaccuracies at low redshift indicate that a more thorough SBSF is required. This could involve improving the sampling of the (S, r_c, β) parameter space, both through simulating a greater number of clusters at each sampled point and by sampling a greater number of points. Another possibly is to add another dimension to SBSF. This is discussed further in Section 4.4.

The simulations presented here use 2D β-models to represent clusters. In reality clusters are more complicated. The combined shape of the core and outer regions cannot be modelled accurately with a single β-model, and irregular gas distributions can also be present. This issue becomes greater at high redshift, where the cluster population is less relaxed. Therefore, accurately correcting for the selection function of real observational data is even more complicated.

4.2.4 Scatter in $L_{\rm X} - T$

Until now, the bias correction has assumed that the local $L_{\rm X} - T$ has been correctly recovered, but this might not be the case. One aspect of the $L_{\rm X} - T$ relation that may be significant is its population scatter. The XIS $L_{500} - T$ relation includes temperature-dependent scatter, which should have an impact on the bias. More scatter at low temperatures, where detections occur less often, would lead to a higher mean $L_{\rm X}$ for the detected

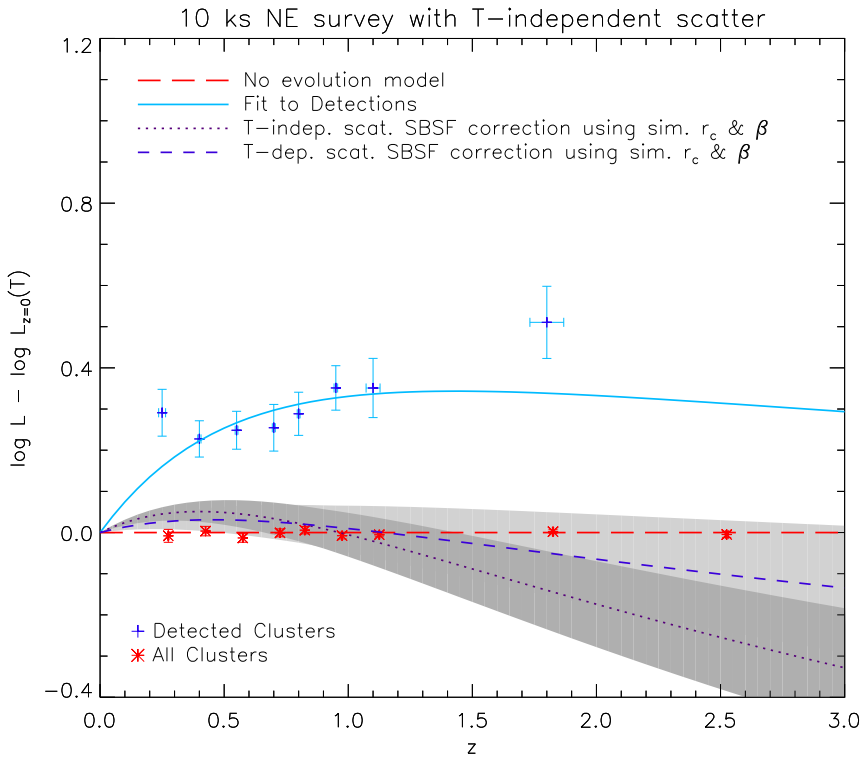

Figure 4.14: Luminosity enhancement plot for the 10 ks no evolution $L_X - T$ relation survey repeated with temperature-independent scatter in $L_X - T$. Similar to Figure 4.12, but only showing correction with the SBSF using the true cluster properties. The purple dotted line shows the $F(z)$ model fit after correcting with the SBSF assuming (correctly) that the scatter in $L_X - T$ is T-independent. The dark blue short dashed line shows how this differs if T-dependent scatter is assumed, as used previously.

clusters at a particular T. The number of detected low T systems peaks at low redshift, so bias is expected to be greater for scatter that increases with lower T, compared to that of T-independent scatter based on the standard deviation.

To better understand the effect of temperature-dependent scatter on the bias, the 10 ks NE survey simulation is repeated with $\alpha_\sigma = 0$, removing the temperature dependence, and $N_\sigma = 0.373$ (the standard deviation of the XIS $L_{500} - T$ relation fit). The results are fitted with the SBSF correction using the true cluster properties. This is done twice, first by assuming that $L_X - T$ relation has T-independent scatter, and then again with the T-dependence of the original XIS $L_X - T$ relation. These fits can be compared to see what assuming the wrong scatter for $L_X - T$ can do to the recovery of its evolution.

Results for the 10 ks survey which has constant $L_X - T$ scatter with T are given

in Figure 4.14. It can be compared with the *top-left* plot of Figure 4.12, which has temperature-dependent scatter. The T-independent scatter survey has a reduced amount of bias at low redshift, as expected from obtaining a sampled population that is closer to the mean $L_{\rm X}$.

Both SBSF fits suffer from the same low z under-correction as in the surveys discussed previously. Applying the SBSF correction with the incorrect assumption of T-dependent scatter (i.e the method used in the last section) gives a fit of $u = 0.74 \pm 0.18$ and $v = -0.93^{+0.24}_{-0.25}$ (dark blue short dashed line), which is 0.5σ for the true evolution and 0.9σ from a TC model. Switching to the T-independent scatter to a survey with T-independent scatter (purple dotted line) gives a fit of $u = 1.67 \pm 0.18$ and $v = -2.05 \pm 0.25$. This is 1.9σ from the true evolution, but gives much stronger evidence for TC evolution at 0.1σ.

The assumption of T-dependent scatter in the correction produces a likelihood model which expects more bias. This compensates for some of the under-correction of the SBSF. In a hypothetical situation where a superior assumed selection function with the true $L_{\rm X} - T$ model for this survey recovers the true evolution, we can expect the use of a T-dependent $L_{\rm X} - T$ model to produce a slight over-correction at low z.

It appears that making an incorrect assumption about the temperature dependence of the scatter in the $L_{\rm X} - T$ relation leads to a small error in SBSF correction of the bias in the $L_{\rm X} - T$ evolution. However, the discrimination between the NE and TC models is sensitive to this assumption, in addition to the quality of the assumed selection function. Further complications may be present if the scatter in $L_{\rm X} - T$ is evolving. Therefore, it is important to characterise the local $L_{\rm X} - T$ thoroughly before certain evolutionary models can be ruled out.

4.2.5 Bias with Cool Cores

Another topic that can be explored with simulations is the evolution of cool core clusters. Earlier we described an optional CC model for XIS, which represented CC and NCC clusters using a shift in the normalisation of the $L_{\rm X} - T$ and $r_{cf} - T$ relations (see

Section 2.2.4.4). The number of CC systems is reduced with redshift. The increased mean $L_{\rm X}$ of CC systems means that they should be more detectable at high z. Since r_c has an effect on cluster selection, the shift in the $r_{cf} - T$ relation may also have an effect on the overall detectability of CC and NCC systems. How it would differ is unclear *a priori*, as reducing r_c increases the central surface brightness but very small r_c brings a risk of the system being identified as a point source. As with other selection effects, there is the possibility of a bias.

To investigate bias in the cool core population, the 10 ks simulations from the previous section are repeated with the evolving CC model for $L_{\rm X}-T$ and $r_{cf}-T$. Using the resulting source catalogues, the fraction of detected clusters that are CC is determined within 3 equal redshift bins centred on 0.25, 0.75, and 1.25. A small number of z bins is used to improve statistics. This detection fraction is compared with the fraction of simulated clusters that are CC. These calculations only include systems above a fixed count rate, representing the need to identify the presence of a cool core in a cluster.

Results from all 4 survey simulations using our evolving CC model are shown for high T systems in Figure 4.15 and for low T systems in Figure 4.16. There is evidence for a bias towards detecting a larger recovering a larger fraction of CC systems at $z \leq 1$. This bias is stronger in the $T \leq 1.6$ keV systems, reaching an overestimate of $\sim 20\%$. While this bias appears to remain consistent at $z > 1$, statistics are poor due to the lack of CC systems simulated at high z. Also, the bias for hot systems with $z < 0.5$ is within 1σ, so it may be the result of statistical fluctuations.

The bias is seen in all 3 redshift bins across all 4 evolutionary models. At $T > 1.6$ keV the bias is generally greater in the 2 surveys with dimmer clusters (NE and TC). In the central z bin, which is the best most thoroughly sampled, the increase in the fraction of CC systems ranges from 4% in the BD survey to 11% in the TC survey. A similar increase exists at $T \leq 1.6$ keV, with a central z bin bias of 18% in both the NE and TC surveys, and 25% in the BD and CD surveys. Poor sample size at $z > 1$ makes this $L_{\rm X}$ evolution-related effect difficult to follow to high redshift.

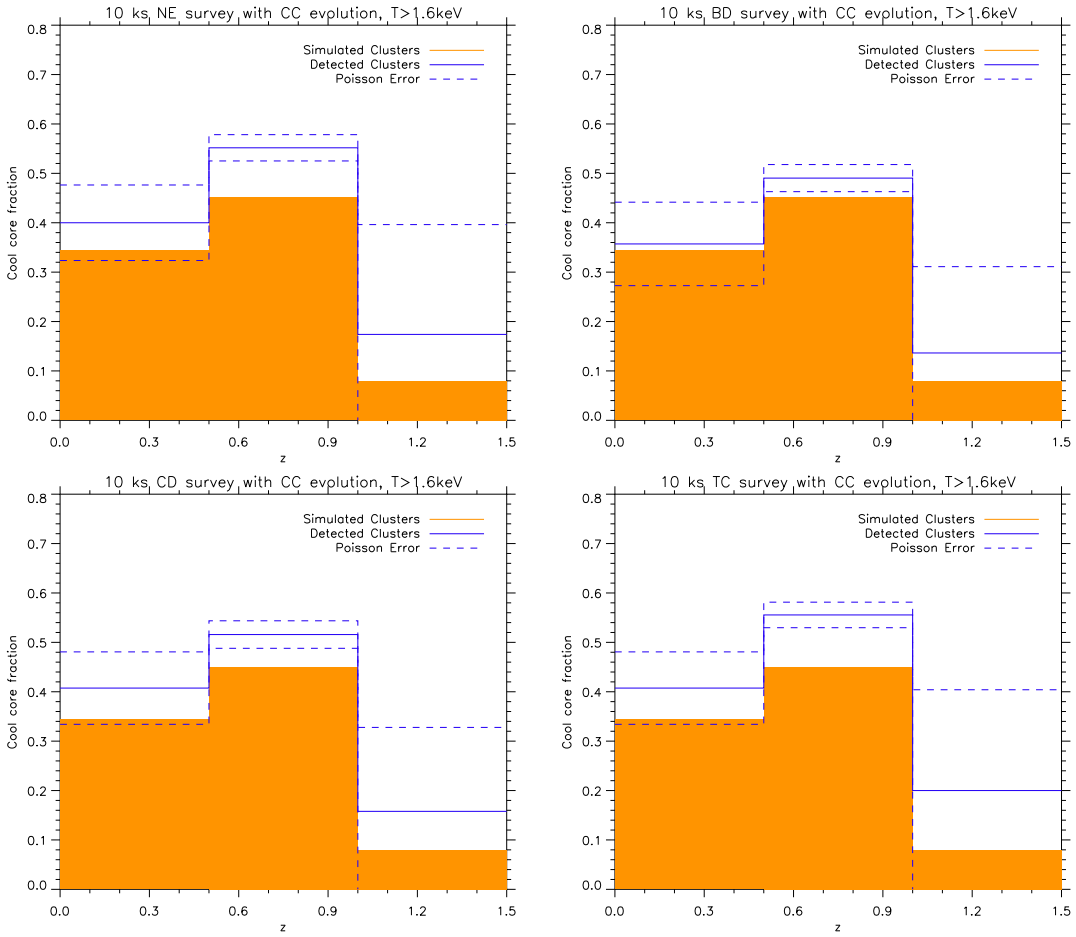

Figure 4.15: Detected fraction of cool core systems with $T > 1.6$ keV as a function of redshift in a 10 ks exposure IXO-09 survey covering 6.77 degree^2, repeated with the following different evolution models *(from top-left to bottom-right):* no evolution, self-similar with respect to the background density, self-similar with respect to the critical density, similarity linked to the cooling threshold. These surveys differ from the previous ones in that they include an evolving CC fraction. The orange bars give the number of simulated CC clusters as a fraction of the total number of simulated clusters in 3 redshift bins: $0 < z \leq 0.5$, $0.5 < z \leq 1$ and $1 < z \leq 1.5$. Blue solid lines show the number of detected CC clusters as a fraction of the total number of detected clusters. Only includes systems with > 200 counts predicted (from the count rate) within R_{500}. Therefore, this assumes that CC and NCC are perfectly discriminated with this count rate. Errors on the cool core fraction are Poissonian, based on the number of detected cool core systems.

We also repeat the 4 cool core surveys with the $L_{\rm X} - T$ relation CC shift removed, so that only the spatial distribution of the cluster brightness is affected. The bias is not significant in these simulations in any evolutionary model, even at low temperatures. Therefore, the higher luminosity of CC systems is responsible for the bias found when the full CC model is used.

The presence of a bias indicates that increased central surface brightness of CC systems

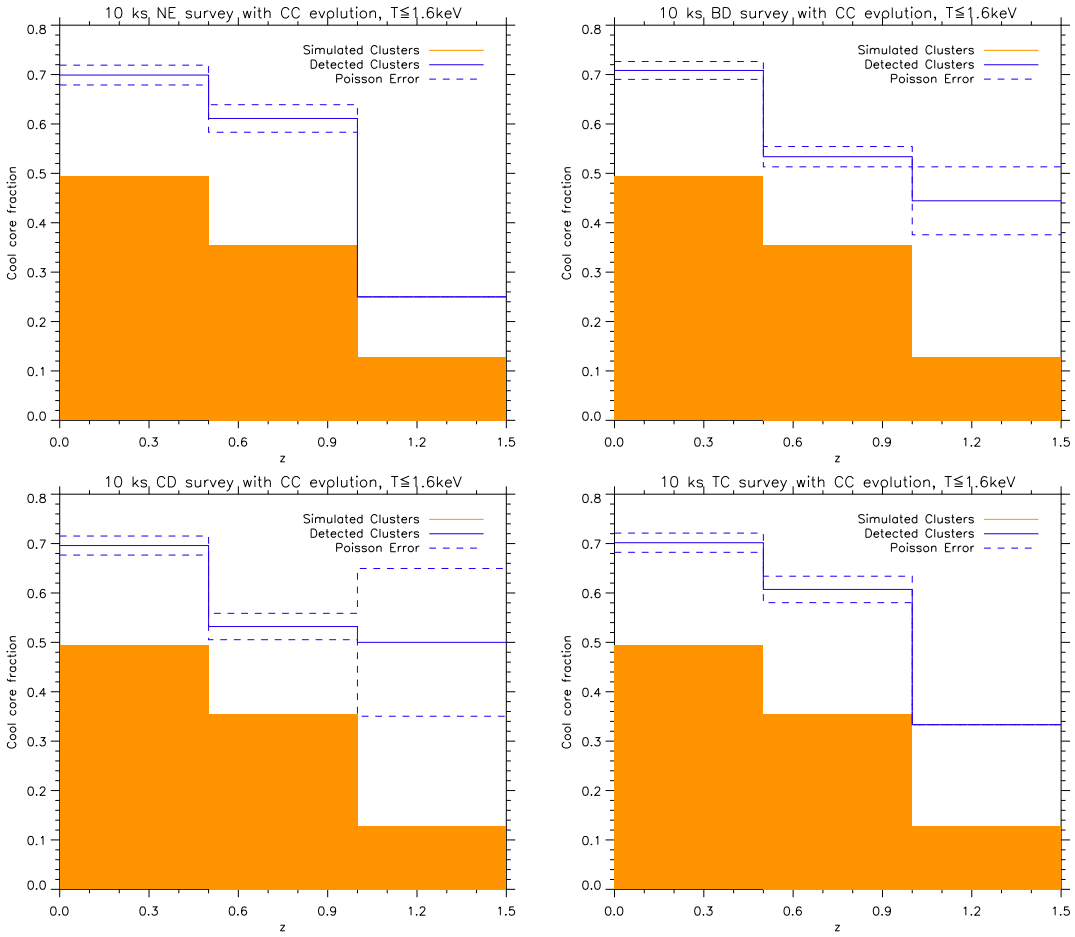

Figure 4.16: As Figure 4.15 but for systems with $T \leq 1.6$ keV.

is more significant for detectability than the point source confusion it causes. These results may go some way towards reconciling the observed drop in the fraction of CC clusters at high redshift (e.g. Santos et al. 2008) with the increase in the fraction of CCs with z for groups found XMM-Newton data by Alshino et al. (2010). In our results the detected fraction of CCs at $z > 1$ in the group regime is $3-5$ times greater than the fraction simulated. In the BD and CD surveys this fraction is 1σ consistent with that detected in the $0.5 \leq z < 1$ bin. Therefore, in the case of self-similar evolution of the $L_{\rm X} - T$ relation, the bias could make the CC fraction in the group regime appear approximately constant across the $0.5 \leq z < 1.5$ range, whilst it would not in the cluster regime. However, our results also show significant drop in the CC fraction between the $z \leq 0.5$ and the $0.5 \leq z < 1$ bins in the group regime.

It is important to note that these simulations are of 10 ks IXO images and therefore the results are not directly comparable with those of Chandra and XMM-Newton, which often have worse statistics. The high angular resolution of Chandra means that there is less confusion between systems with small core radii and AGN. Also, the sample of Alshino et al. (2010) is small, and a larger group survey would be required for significant observational evidence for the bias.

There is still the possibility that bias could be present in the identification of the cool cores within detected extended sources, and this needs to be addressed by any survey performing this kind of study. Finally, these results apply to a non-evolving $\beta - T$ relation and CC scaling relations that have been extrapolated to low temperatures, and may not hold if these assumptions are incorrect. Nevertheless, care must be taken to correctly understand the results of a study of CC evolution.

4.3 Survey Strategy

Another issue that concerns surveys is the allocation of exposure time. Surveys for a given total length of exposure can be wide-angle, covering a large area with short exposures, or deep, integrating over a small area for a long time. A mixing of the two is also an option. The strategy used influences the sample obtained. Wide-field surveys obtain a larger sample of brighter sources, while deep surveys reach lower fluxes but the number recovered is more affected by cosmic variance. The distribution of the sample will have repercussions on the science being done.

In this section a subsample of the simulated pointings from the bias study are used to explore the issue of area versus depth with respect to cluster surveys. It is approached in two ways: the ability to recover different masses as a function of redshift, and an $L_{\rm X} - T$ relation evolution analysis as conducted earlier. The former is related to the recovery of the cluster mass function, which is important for placing constraints on cosmological parameters.

4.3.1 Simulated Scenarios

This study involves a simple comparison of a simulated wide-angle survey with 3 simulated deep surveys. A larger number of deep surveys are useful because of the larger effect of cosmic variance on the number and range of clusters within a survey. For the wide-angle survey we use the 10 ks cooling threshold evolution IXO-09 survey from Section 4.2.1. This evolutionary law has been selected to provide conservative results, compared to the brighter clusters sampled by surveys with simulated self-similar evolution.

Each of the deep surveys is an 18 pointing subset of the 100 ks cooling threshold evolution survey. This gives each of them a total exposure time equal to that of the wide-angle survey (1.8 Ms). The pointings are contiguous in terms of their XIS source extraction fields and are different for each deep survey.

The 3 deep surveys contain 107, 67 and 74 cluster detections within an area of 0.68 degree^2, compared to the 352 detections in the wide-angle survey. Therefore, the recovery of more faint clusters does not compensate for the reduction in the surveyed area. This wide-angle survey is $3-5$ times as effective at generic cluster detection.

Since the same might not be true for self-similar evolution, we compare the number of clusters detected in the 10 ks BD evolution survey, 563, with the number in the 100 ks BD evolution survey, 1279 (both defined in Section 4.2.1). As the 100 ks survey should be judged on one-tenth of the area, a wide-angle survey would be, on average, 4.4 times as effective at generic cluster detection in a universe with self-similar evolution with respect to the background density. This IXO-09 wide-field survey is effective as it captures the peak of the redshift distribution.

4.3.2 Mass Sampling with Redshift

Clusters can provide constraints on cosmological parameters. This is done using the cluster mass function (e.g. see Vikhlinin et al. 2009b), which is a measure of the growth of structure in the Universe, and incorporates cosmological distance information. Recovering

Table 4.5: Number of clusters detected with $13.25 < \log M_{500} \leq 13.5$ as a fraction of the total simulated in a wide-angle survey and 3 deep surveys. The number in brackets is the actual number of detected clusters within that bin. Divided into three equal redshift bins from $0 < z \leq 2.4$. Poisson errors are assumed.

Survey	Cluster completeness (Number Det.)		
	$0 < z \leq 0.8$	$0.8 < z \leq 1.6$	$1.6 < z \leq 2.4$
Wide-angle survey	$49 \pm 5\%(85)$	$23 \pm 3\%(64)$	$13 \pm 6\%(4)$
Deep survey 1	$65 \pm 18\%(13)$	$65 \pm 14\%(22)$	$33 \pm 33\%(1)$
Deep survey 2	$75 \pm 19\%(15)$	$83 \pm 37\%(5)$	$50 \pm 35\%(2)$
Deep survey 3	$84 \pm 26\%(11)$	$59 \pm 19\%(10)$	$50 \pm 29\%(3)$

the cluster mass function is limited by the sample size and measurements of the cluster properties. Here we briefly examine the former in the context of survey strategy.

To examine the effectiveness of the different survey strategies at sampling cluster masses, the number of detected and total simulated clusters are counted in bins of mass and redshift, as shown in Figure 4.17. At $z < 1.6$, the wide-angle survey produces a considerably higher number of detections above a mass of $10^{13}\ h^{-1}\ \mathrm{M}_{\odot}$. In the other regions the difference between the survey sample size is similar to the counting errors.

Also relevant in determining the evolution of the cluster mass function is the completeness as function of redshift. For this test, completeness is the number of clusters detected as a fraction of the number simulated as a function of mass and redshift. To get an indication the difference in completeness between the survey strategies as a function of redshift, we focus on the $13.25 < \log M_{500} \leq 13.5$ bin and half the number of redshift bins for better statistics in the number of detections. The completeness in each survey is given in Table 4.5. Deep surveys provide higher completeness at all redshifts, as expected from the longer integration time, but have much poorer statistics. These errors are compounded by sample variance from large scale structure. The difference between the bins in the deep surveys is often greater than the statistical error, which highlights the impact of cosmic variance.

Given these sampling uncertainties and the number of high mass clusters detected, an IXO wide-angle survey with a well defined selection function may prove to be a better way to determine the mass function at $M_{500} \gtrsim 10^{13}\ h^{-1}\ \mathrm{M}_{\odot}$ than using a smaller number

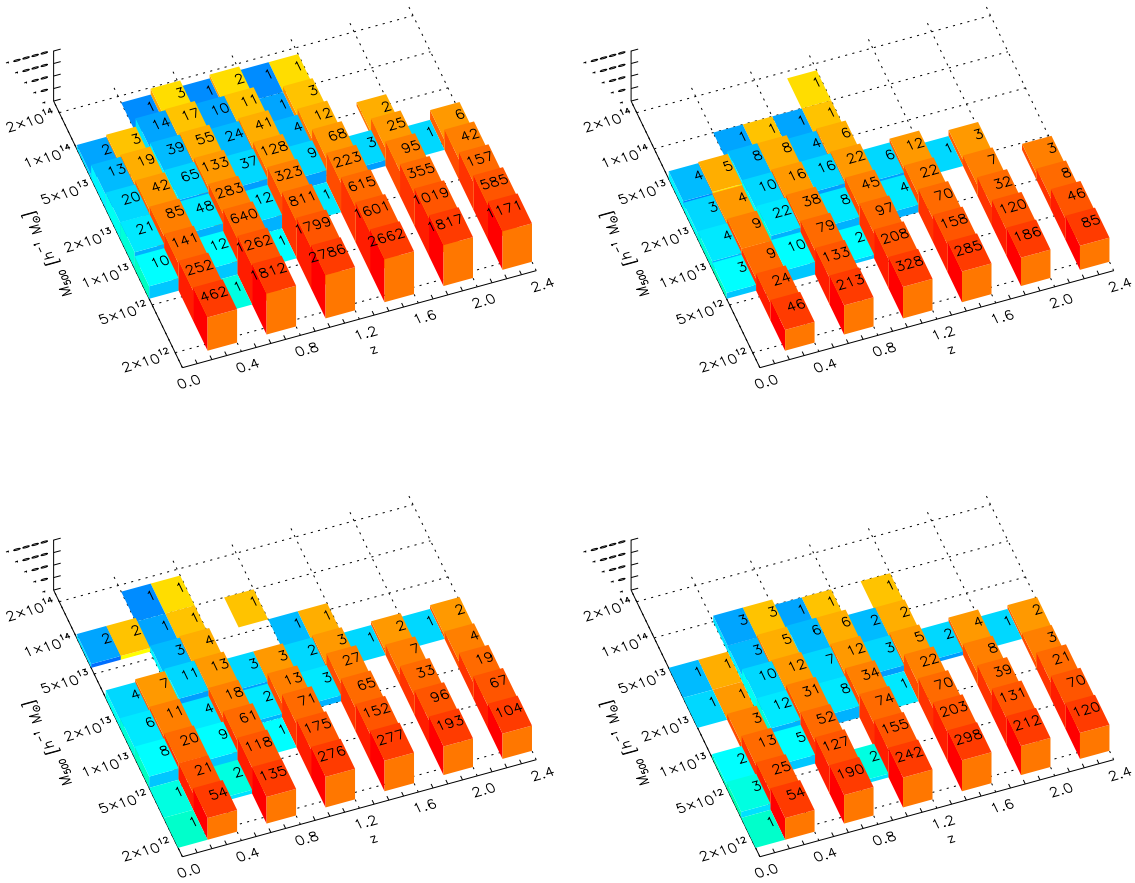

Figure 4.17: Number of detected clusters (blue) and total clusters (orange) as a function of mass and redshift in a wide-angle survey *(top-left)* and 3 deep surveys. Uses 8 mass and 6 redshift bins of equal size from $12.25 < \log M_{500} \leq 14.25$ and $0 < z \leq 2.4$, respectively. Labels indicate the number in each bin.

of deeper pointings. High mass clusters are especially important for studying cosmology as cosmological effects are more prominent at this end of the mass function.

This would need to be repeated with self-similar $L_{\rm X} - T$ evolution to see if the situation is consistent independent of the evolution. Note that this analysis does not include the errors inherent to measuring cluster mass, which become increasingly significant for the dimmer and less virialised sources at both lower mass and higher redshift.

Table 4.6: As Table 4.4 (Section 4.2.3), but comparing the 10 ks survey with similarity linked to the cooling threshold (wide-angle) survey to 3 deep surveys with 100 ks pointings and equivalent total exposure time.

Survey	Model	σ		
		No sel. fn.	SBSF	SBSF with fits
Wide-angle survey	NE		4.29	0.66
(TC 10 ks)	BD	3.38		
	CD		4.14	6.64
	TC		1.86	2.39
Deep survey 1	NE	6.41	2.21	1.33
	BD	4.86	7.91	
	CD	3.62	4.15	4.41
	TC	5.08	0.82	0.37
Deep survey 2	NE	5.78	2.18	1.05
	BD	1.12	3.20	3.99
	CD	2.87	0.87	0.98
	TC	4.83	1.46	0.75
Deep survey 3	NE	4.92	1.68	0.96
	BD	4.52	6.90	7.39
	CD	2.80	3.51	3.88
	TC	3.95	0.58	0.30

4.3.3 $L_{\rm X} - T$ Evolution

Here the ability to recover the evolution of an $L_{\rm X}-T$ relation that is linked to the threshold for radiative cooling ($L_{\rm X} \propto H(z)^{-3}t(z)^{-2}$) with small, deep surveys is compared with that of the wide-angle field survey used earlier. The deep surveys are analysed with the same method as in Section 4.2.2, but omitting the Flux cut and Pacaud-style corrections. The best-fit parameters are available in Appendix G, Table G.1. Deviations of each $F(z)$ from the different test evolution models are presented in Table 4.6, within which the previous results for the 10 ks cooling threshold survey are reiterated.

The enhancement factors of the clusters in the 4 surveys and their best-fit $F(z)$ models are shown in Figure 4.18. Cosmic variance and population scatter in the simulated $L_{\rm X}$ causes the total simulated cluster sample in a deep survey to have greater scatter around true evolution model than in the wide-angle survey. The amount of bias in the luminosity enhancement factor also varies significantly between the different deep surveys, partially due to the low number of detections. Despite these drawbacks, deep surveys 1 and 3

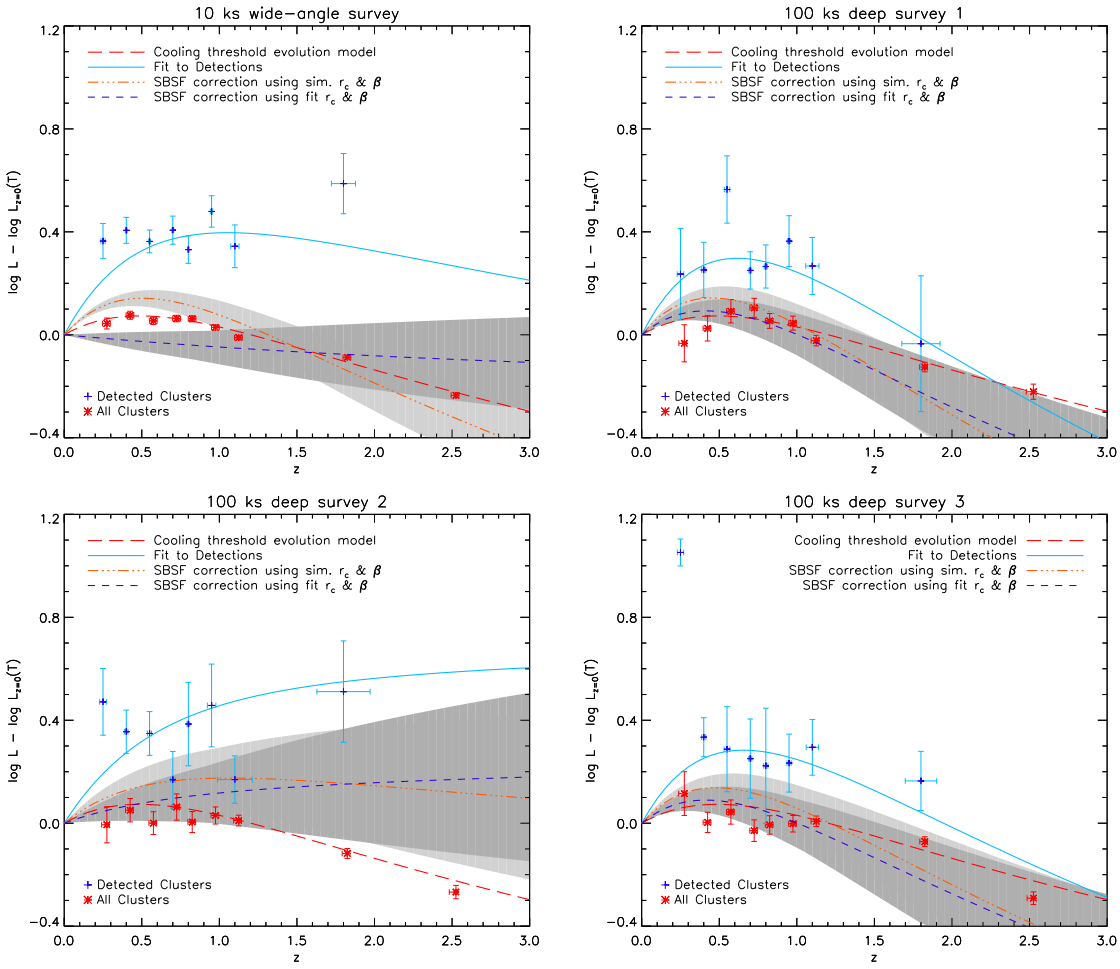

Figure 4.18: Bias in the simulated $L_{\rm X}-T$ enhancement factor with simulated cooling threshold evolution, for a 180 pointings 10 ks IXO-09 wide-angle survey *(top-left)* and three 18 pointing 100 ks deep surveys. Data points and lines as Figure 4.12.

allow the correct evolution to be constrained to $< 1\sigma$ with either method of applying the SBSF. This is more successful than the $1.8-2.4\sigma$ constraints obtained from the wide-angle survey. Unfortunately less success is had with deep survey 2, which supports the NE, BD and TC models within $\sim 2\sigma$. Therefore, results from surveys conducted over a small area should be treated with caution, even with the collecting power of a deep IXO observation.

The reason for the effectiveness of the deep surveys is better understood by looking at where the detections lie relative to the $L_{\rm X}-T$ relation, as shown in Figure 4.19. Deep surveys obtain a more complete sample at both lower T and higher z (cf. Figure 4.17),

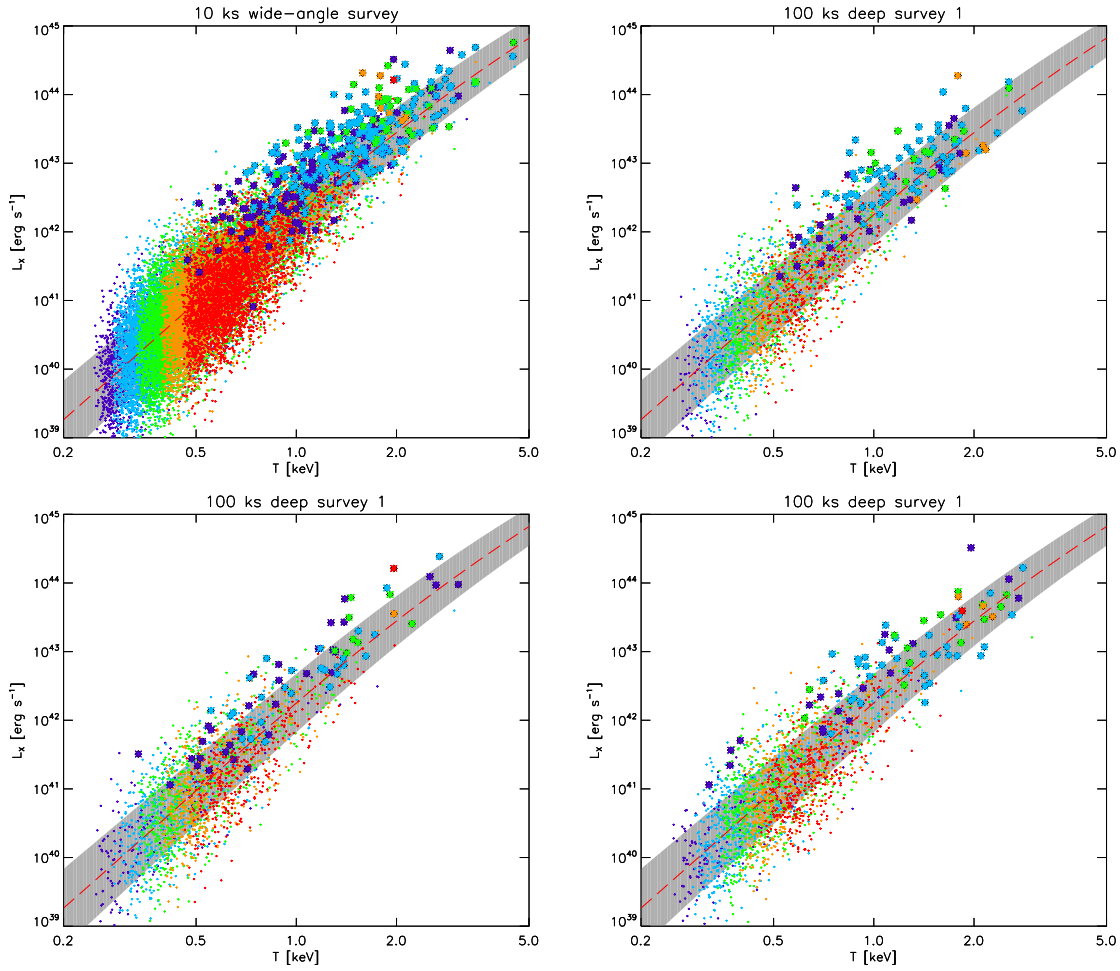

Figure 4.19: $L_{\rm X} - T$ relation for the four surveys in Figure 4.18. Large points show the detected clusters, whilst dots represent undetected clusters. Symbol colours represent the following sequential redshift ranges: $z \leq 0.5$ dark blue, $z \leq 1$ light blue, $z \leq 1.5$ green, $z \leq 2$ orange, $z \leq 3$ red. The red long dashed line shows the $z = 0$ XIS $L_{\rm X} - T$ relation. Note that the $\log \overline{L_{\rm X}}(T, z))$ rises to $\log L(T, z = 0) + 0.1$ at $z = 0.5$ and then drops, returning to $\log L(T, z = 0)$ at $z = 1.2$ and continuing down to $\log L(T, z = 0) - 0.3$ at $z = 3$.

which compensates for the smaller sample size. The deep surveys are $70 - 83\%$ complete at $T > 2$ keV, while the wide-angle survey is only 55% complete. This completeness means that inaccuracies in SBSF correction are less of an issue, and better measurements of surface brightness properties allow the correction to be applied more accurately.

These results indicate that a deep survey gives better constraints on the evolution of the $L_{\rm X} - T$ relation, but cosmic variance means there is a risk of collecting a sample that is a poor representation of the Universe. This is especially true at the lowest and highest redshifts, where the sample size is smallest. It should be noted that this study only uses

a single wide-angle survey and evolution model, so is not conclusive. A larger selection of surveys and a more effective bias correction should be developed to determine which strategy is generally a better choice for studying $L_{\rm X} - T$ evolution.

4.4 Summary

In this chapter the topic of cluster surveys has been investigated with a focus on the assumed selection function and the evolution of the $L_{\rm X} - T$ relation. Survey strategy relating to the trade-off between survey area and survey depth has also been explored.

We have mapped out the 10 ks IXO-09 WFI cluster selection function over $f(S, r_c, \beta)$, sampled within the limit of available resources. This is smoothed to a higher resolution. We use the selection function to predict the bias expected in the $L_{\rm X} - T$ relation. This bias is substantial in the group regime at $z \sim 1$. At $z = 2.3$ this bias affects the cluster regime and systems below 2 keV are rarely detected. The selection function is investigated at multiple exposure times using lower resolution samples. The 100 ks data have been used to rescale the 10 ks smoothed function, creating a rough estimate of the full form at 100 ks but with some irregularity. A more detailed sampling is required to correct this.

Simulated IXO-09 surveys covering 6.77 degree^2 have been produced using 4 different evolutionary models and with exposure times of 10 ks and 100 ks per pointing. Results from each of these surveys included bias in the $L_{\rm X} - T$ relation because of the survey selection function, even with the high throughput of IXO. Fits to the systems detected in these surveys demonstrated that uncorrected bias in the $L_{\rm X} - T$ relation leads to incorrect conclusions about its evolution.

The bias must be corrected for using an assumed selection function. Fundamentally, this correction should account for surface brightness parameters of flux, core radius and β, along with exposure time. An assumed selection function of this nature can discriminate between the most of the evolution models tested here so long as good fits are obtained to all of the relevant cluster properties. Unfortunately, the surface brightness fits to the

IXO simulations require improvement before corrections of this quality can be performed on real data.

Improved sampling of the SBSF may be necessary to improve the agreement between the recovered evolution and the true evolution. Adding more selection function parameters may yet improve the correction. This could take the form of shape-related parameters such as ellipticity, or be some measure of contamination/obscuration between sources, perhaps taking into account the large scale structure.

A survey has also been simulated with no temperature-dependence in the $L_{\rm X} - T$ relation, and then analysed with the assumption that such dependence exists. This affected the ability to recover the true evolution to the order of $\sim 1\sigma$, compared to using the more appropriate analysis. Therefore, it is important to characterise the local $L_{\rm X} - T$ relation as thoroughly as possible before making judgements about the evolution.

Pacaud et al. (2007) also comment on the sensitivity to the local $L_{\rm X} - T$ relation. The bias-corrected, observed $L_{\rm X} - T$ relation recovered from their preliminary results favoured the self-similar model (with respect to critical density), but did not exclude the case of no evolution. The simulated 10 ks IXO surveys recover a much larger sample than XMM-LSS over a similar area (see Table 1.1, Section 1.4.5).

If the behaviour of the Pacaud-style bias correction in this work was similar for Pacaud et al. (2007), it would mean their low redshift systems had been over corrected. This would further detract from the no evolution scenario. However, the methods are not directly comparable as Pacaud et al. (2007) used a different source identification procedure, including using a fixed β for all surface brightness fits (see Pacaud et al. 2006). This would increase the best-fit r_c of each cluster compared to using a free β, so it would be associated with a part of the selection function parameter space that better represents its true detection probability. The assumed selection function should represent the method used to analyse the observational data.

Also, the IXO detections include a larger proportion of low temperature systems than

XMM-LSS[1], which are the greatest source of over-correction. Therefore, the Pacaud-style correction would work better on XMM-LSS data than in it does in this work.

The detected ratio of cool core to non-cool core clusters is followed out to $z = 1.5$ in a set of 10 ks IXO-09 surveys with two different CC models. There is evidence for a bias whereby a higher fraction of CC systems is detected than is actually present. This bias is more significant for the low temperature systems, and causes the CC fraction to be seriously overestimated at high z. This means that studies of the evolution of CC clusters also need to understand their selection function in order to correctly interpret their results.

For the issue of survey area versus depth, a wide-angle 10 ks exposure IXO-09 survey is compared with 3 subsets from the equivalent 100 ks survey with the same total exposure time. In the case of TC evolution, a wide-angle survey produces a greater sample of $N(M, z)$ than a deep survey and over approximately the same parameter range. With less impact from cosmic variance, the wide-angle is given preference for sampling $N(M, z)$ so long as a selection function is used to account for lower completeness with redshift.

A different situation emerges from fits to the $L_{\rm X} - T$ evolution for the two different survey strategies. Completeness from a deep survey reducing the low T and high z bias seems to be more important than having the larger sample size of a wide-angle survey when attempting to recover TC evolution, but risks irregular results at high z due to cosmic variance. It is clear that more study is required in this area, with a variety of different simulated scenarios, before a particular survey strategy can be recommended for particular science goals.

The main finding are summarised as follows:

- The selection function of IXO surveys causes a bias in the recovered $L_{\rm X} - T$ relation and its evolution if no correction is applied. This is true for large surveys using 10 ks and 100 ks pointings, but worse with 10 ks.

[1] 10% of the XMM-LSS detections have $T < 1$, and 52% have $T < 2$. The respective values for the 10 ks IXO surveys are $20 - 24\%$ and $79 - 85\%$.

- Failure to correct adequately correct for this bias leads to erroneous conclusions about the most appropriate evolutionary law. Bias from inadequate corrections is more serious in shallower surveys.

- A flux cut can be used to remove some of the biased data, but increases the noise in the fit.

- Effectiveness of the selection function correction depends on many factors, including:

  - All three of the sampled β-model parameters: count rate, core radius, β. Assuming a fixed β of the canonical cluster value of 2/3 causes an over-correction at low temperatures and low redshift.

  - The quality of measurements of the surface brightness properties of the detected clusters.

  - Characterisation of the local $L_{\rm X}-T$ relation and its scatter, which have already been biased.

- There is a significant drop in the detection probability for clusters with both very large and very small r_c. The former is due to the reduction in surface brightness, while the latter is caused by cuspy clusters being identified as point sources.

- Incorrect conclusions about $L_{\rm X}-T$ evolution are drawn from a 10 ks exposure IXO-09 survey covering 6.77 degree^2 unless the bias is corrected for using a correctly applied SBSF.

- There is evidence for a bias high recovered ratio of cool core to non-cool core systems out to $z = 1.5$ in a 10 ks exposure IXO-09 survey covering 6.77 degree^2. This bias is greater for lower temperature systems. This result applies to any of the assumed $L_{\rm X}-T$ evolution models.

- In a universe where $L_{\rm X}-T$ evolution is linked to the cooling threshold and ignoring mass measurement issues, there is evidence that a wide-angle IXO survey is likely

to be more effective than an time-equivalent deep survey for studying the mass function. The reverse seems to be the case for recovering the evolution of $L_{\rm X} - T$. However, selection function correction is crucial for wide-angle surveys.

CHAPTER 5

Instrument Trade-off

When designing a new observatory choices have to be made about the quality of the components. For a space-borne observatory, such as IXO, the limitations on these choices come from their expense, weight and technical feasibility. The components need to give the observatory the ability to achieve its science goals, so these have to be well defined. Science goals for IXO and the technical requirements to carry them out are defined in Appendix B.2. While development of the observatory is aimed towards meeting these technical requirements there may be a need to scale them back. New advances in science may also give compelling reasons to push the observatory capabilities further.

In this short chapter we explore the effects of changing two instrument-related properties, the PSF and the particle background rate, on the ability to detect X-ray sources with the IXO-10 WFI. The intent is to get a general idea about how changing the current design would impact the overall imaging performance of IXO.

5.1 Angular Resolution (PSF)

The point spread function has always been an important factor in X-ray astronomy. Reducing the size of the point spread function has allowed more point sources to be resolved from the X-ray background, and has enabled the study of both spatial and spectral features within the cores of clusters. The current target for IXO is an on-axis PSF width of 5 arcsec FWHM, similar to that of the XMM-Newton telescopes. Here we experiment with 5 different PSF widths of 1, 3, 5, 7 and 9 arcsec. A 1 arcsec PSF approaches the fine resolution achieved by the Chandra mirrors. No off-axis model is available for IXO at this time, so the on-axis width is used over the whole field.

The effect of changing the PSF is evaluated using four methods, with a focus on cluster detection. Each of these methods has previously been used in this work: cumulative $\log N - \log S$ of the sources, cluster detections as a function of mass and redshift $N(M, z)$, the $L_{\rm X} - T$ relation and the evolution of the $L_{\rm X} - T$ relation. The final method is only conducted on the 9 arcsec PSF survey.

5.1.1 Simulations

A large sample is important for this study to maximise the discrimination between the different test cases. To obtain a large sample of images, XIS is used to produce a simulated survey containing 80 pointings each with an exposure time of 100 ks. The survey uses the primary sky field and covers a total area of 4.98 degree^2 after ignoring the outer 32 pixels of each pointing. This area contains 16902 clusters, 48838 galaxies and 52792 AGN.[1] The survey is repeated for the 5 different PSF FWHM being tested, with no evolution of the $L_{\rm X} - T$ relation. These surveys are used for the $\log N - \log S$, $N(M, z)$ and $L_{\rm X} - T$ relation analyses. A further set of surveys with 5 arcsec and 9 arcsec PSF sizes are produced with both self-similar evolution with respect to the background density of the Universe (BD) and similarity linked to the threshold for radiative cooling (TC). These

[1]Note that point sources are only generated down to the 10^{-17} erg cm^{-2} s^{-1} limit.

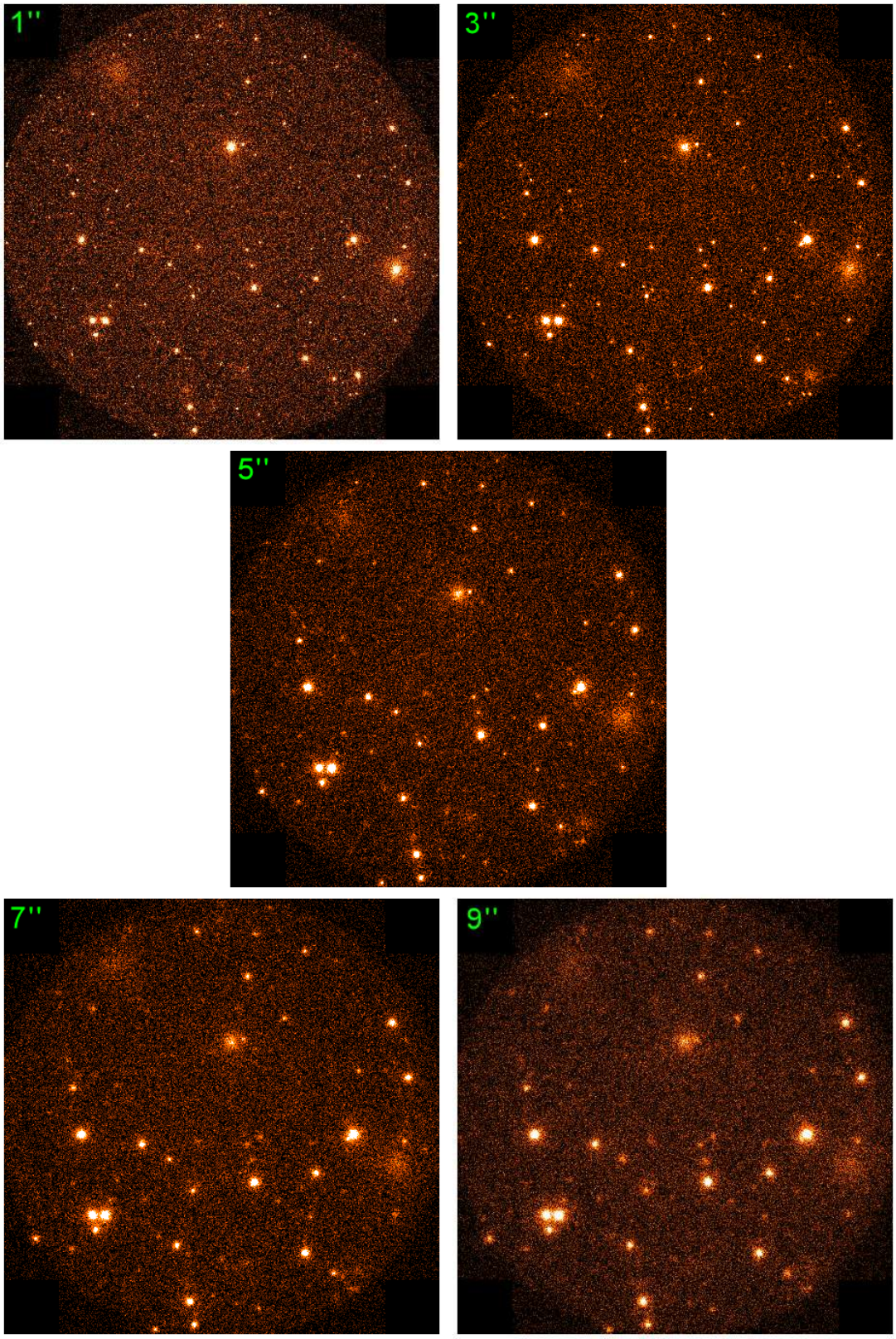

Figure 5.1: 100 ks, $0.5-2$ keV IXO-10 images covering the same area but with 5 different PSF FWHM. *From top-left to bottom right:* 1, 3, 5, 7 and 9 arcsec. These images are from the simulations with no evolution in the $L_{\rm X}-T$ relation. Each image is scaled separately with a 99.5% linear scale.

two models represent the extremes of the high redshift detectability from the models used in Section 4.2.1.

An example of a pointing simulated with each of these PSF sizes is given in Figure 5.1. Increasing the PSF width smooths out bright centres, merges counts from different sources and causes faint sources to become lost in the noise.

Source identification is performed on each image to produce catalogues of detections for each source type. Significance thresholds are those calibrated for IXO-10 in Section 3.3.2.2. Note that these threshold have been calibrated to reject point sources from the cluster catalogues, so some point source detections may be clusters that lie below the $B_{\rm x}$ threshold. Based on the cluster acceptance rate, the number of clusters below the threshold is expected to be $\sim 40\%$ of the number of cluster detections. Assuming 95000 unmatched point sources in an area of 5 degree^2, and a matching length equal to the PSF FWHM, there is an 11% probability of a false point source detection matching to a true point source with a 5 arcsec PSF.

5.1.2 Source $\log N - \log S$

The cumulative $\log N - \log S$ for clusters, galaxies and AGN for each PSF test case are given separately within Figure 5.2. All of the simulated surveys (blue lines) perform better at cluster detection than the COSMOS (crosses), which covers 2.1 degree^2 with 1.4 Ms of XMM-Newton observations. This is an average of 667 ks degree^{-2}, 42% of the coverage of this IXO survey, so superior perfomance at 5 arcsec is not suprising.

A 5 arcsec PSF gives a maximum of $\sim$ 90 cluster detections per degree^2. Use of a 1 arcsec PSF rivals the $\sim$ 1 Ms Chandra deep fields, with cluster detections of $\sim$ 130 degree^{-2} and a minimum flux $S_{\rm X} \approx 2 \times 10^{-16}$ erg cm^{-2} s^{-1}. Increasing the size of the PSF to 9 arcsec drops the total number of cluster detections to $\sim$ 70 degree^{-2} and a minimum flux of $S_{\rm X} \approx 4 \times 10^{-16}$ erg cm^{-2} s^{-1}. This minimum does not change drastically between 9 and 3 arcsec. The variance at high $S_{\rm X}$ is not significant due to the large statistical errors.

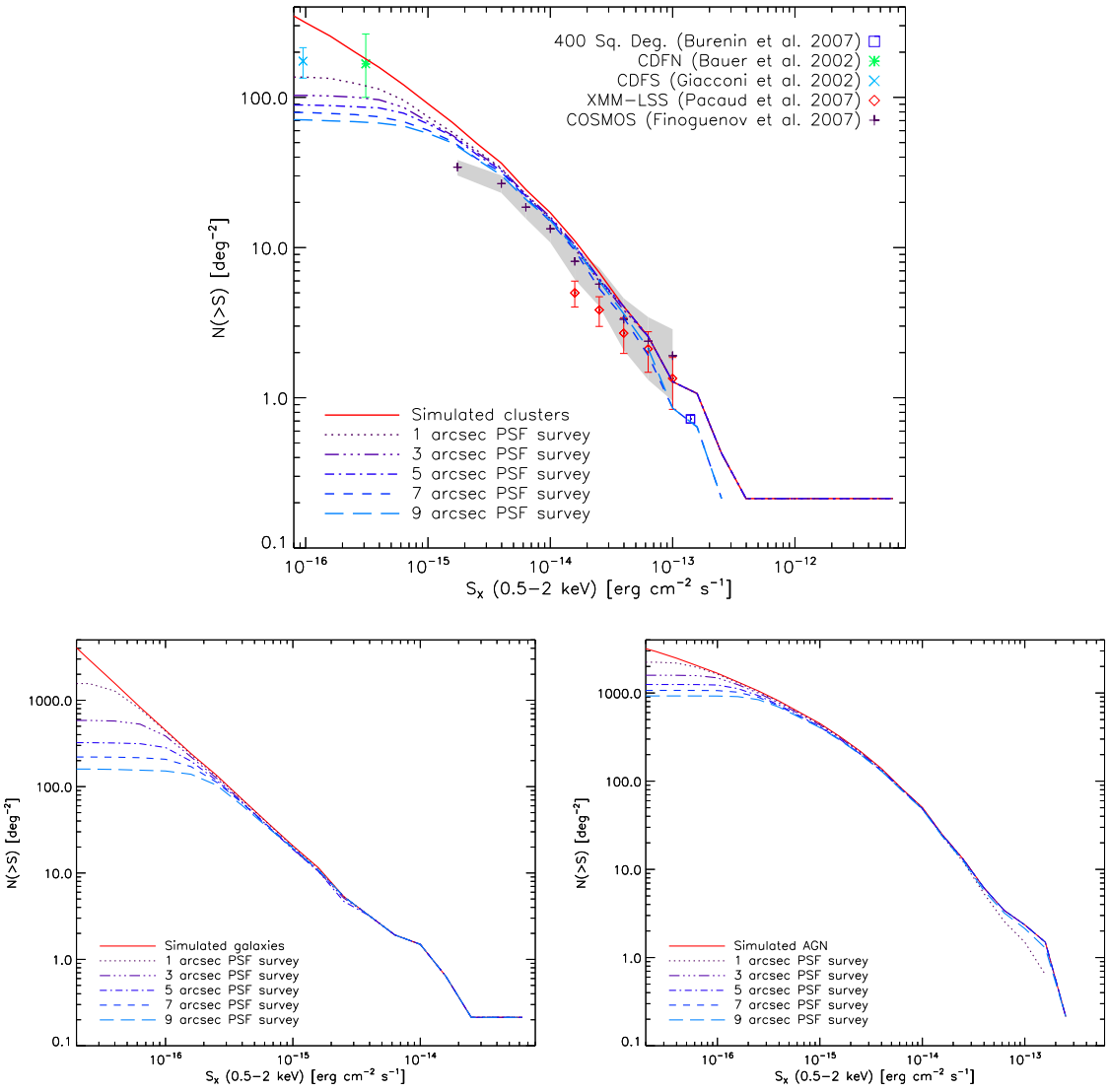

Figure 5.2: *Top:* Cumulative $\log N - \log S$ plot comparing the simulated clusters (red solid line) in an 80×100 ks pointing IXO-10 survey to the detected clusters with 5 different PSF FWHM indicated by blue lines: 1 (dotted), 3 (triple-dot-dashed), 5 (dot-dashed), 7 (short dashed) and 9 arcsec (long dashed). The points show the results of cluster surveys by Bauer et al. (2002); Giacconi et al. (2002); Burenin et al. (2007); Finoguenov et al. (2007); Pacaud et al. (2007). Error bars give Poissonian 1σ confidence levels for the observational data. The shaded area shows the 1σ confidence interval around the Finoguenov et al. (2007) clusters. *Bottom-left:* As above, but comparing the galaxies. *Bottom-right:* As above, but comparing the AGN.

Galaxy detection is more seriously affected than cluster and AGN detection. The number of detections increases an order of magnitude when moving from a 9 arcsec to a 1 arcsec PSF, and the limiting flux changes from $\sim 10^{-16}$ to $\sim 2 \times 10^{-17}$ erg cm^{-2} s^{-1}. AGN detection behaves in a similar fashion to that of clusters, approximately doubling from a PSF width change of 9 arcsec to 1 arcsec. This change reduces the limiting flux from $\sim 1.3 \times 10^{-16}$ to 4×10^{-17} erg cm^{-2} s^{-1}. The galaxy $\log N - \log S$ is affected more significantly than that of the AGN due to the much steeper rise in the number of sources with decreasing flux.

It should be noted that the unresolved point source flux limit of 10^{-17} erg cm^{-2} s^{-1} used in the simulations becomes less valid for smaller PSF sizes, as more counts will be present in the central pixel of a source. Repeating the calculation from Section 2.4.10 using IXO-10 with a 1 arcsec PSF and a Poisson error based on 100 ks of exposure time gives a flux limit of 3×10^{-18} erg cm^{-2} s^{-1}. The detections in these surveys do not reach 10^{-17} erg cm^{-2} s^{-1}, which suggests that no objects have been excluded that would otherwise have been detected. However, the point source population below this limit is used to increase the flat X-ray background. Therefore, the background in the 1 arcsec and 3 arcsec surveys has been overestimated. This would affect the number of detected sources, so the results for these surveys are lower limits.

Also note that the recipe for cluster-point source position correlation does not include sufficient numbers of point sources near the centres of clusters. A more appropriate distribution is likely to reduce the number of detections of all source types, especially in surveys with poor angular resolution, due to confusion.

5.1.3 Mass Sampling with Redshift

A histogram of the mass and redshift distribution of detected clusters is constructed for each PSF survey, mirroring the approach in Section 4.3.2. This is presented in Figure 5.3. Changing the width of the PSF does not significantly change the distribution of the clusters with M_{500} and z, only the overall normalisation. However, decreasing the width

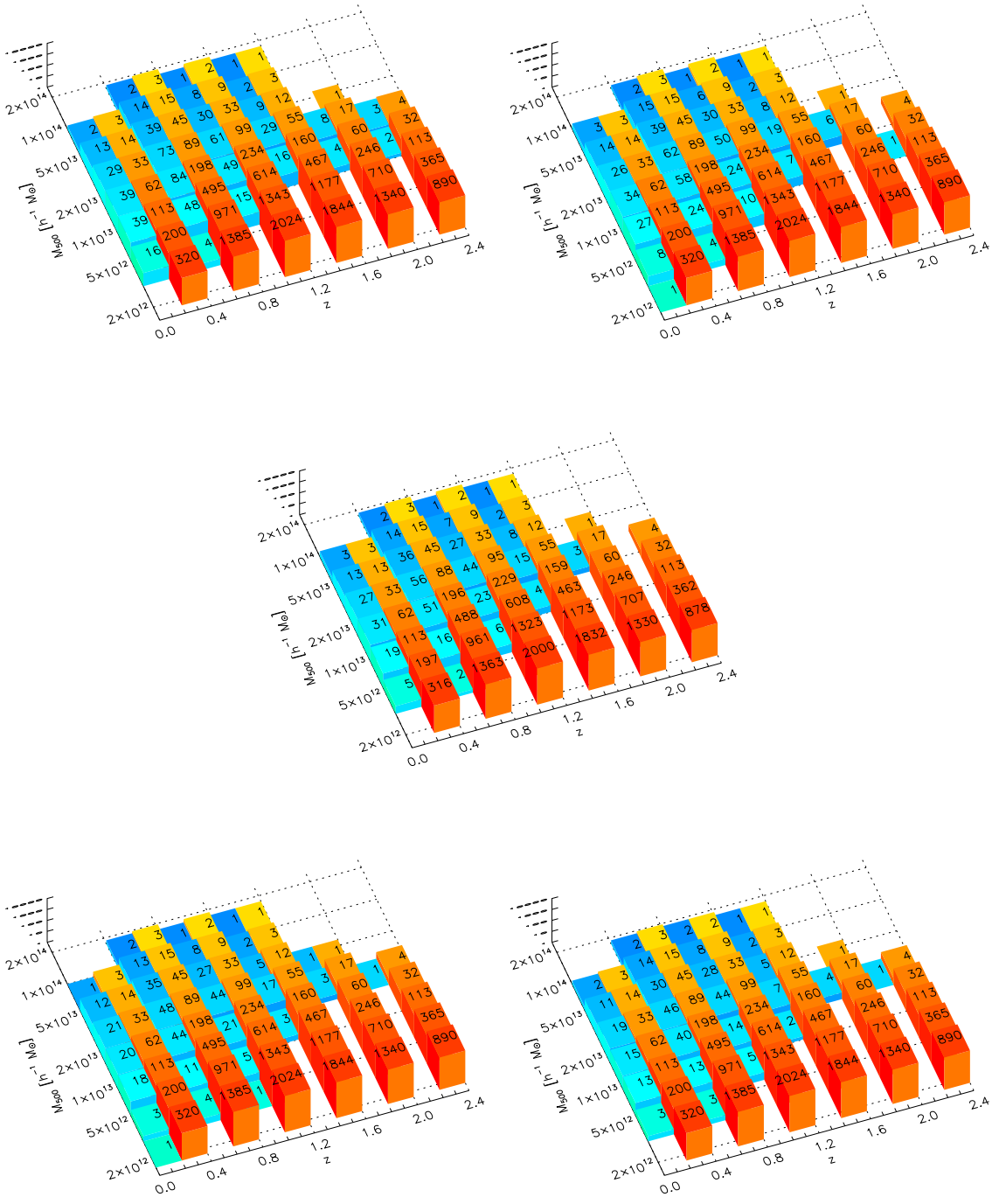

Figure 5.3: Number of detected clusters (blue) and total clusters (orange) as a function of mass and redshift in an 80×100 ks pointing IXO-10 survey, with 5 different PSF FWHM. *From top-left to bottom right:* 1, 3, 5, 7 and 9 arcsec.

to < 5 arcsec reveals significantly more $M < 10^{-13}\ h^{-1}\ \mathrm{M}_{\odot}$ systems and high z. Allowing for counting noise, high masses remain consistently sampled.

5.1.4 $L_{\mathrm{X}} - T$ Relation

The $L_{\mathrm{X}} - T$ relation for the different PSF surveys is given in Appendix H, Figure H.1. Power law fits to the detected clusters give the following slopes for the five PSF widths from $1-9$ arcsec: 3.35 ± 0.07, 3.16 ± 0.08, 3.24 ± 0.08, 3.13 ± 0.08 and 3.13 ± 0.09. Therefore, the change in slope between 5 arcsec and either extreme has significance of $< 2\sigma$. However, as the original slope is 4 this change is negligible compared to the amount of bias present.

5.1.5 $L_{\mathrm{X}} - T$ Evolution

Unlike the previous three analyses, the ability to recover the evolution of the $L_{\mathrm{X}} - T$ relation is assessed with 5 arcsec and 9 arcsec PSF surveys performed with the SB and TC evolution models. To perform the recovery we require selection functions appropriate to both IXO-10 100 ks images and these two PSF sizes. Two SBSFs are obtained using sparse sampling and interpolation from the IXO-09 10 ks SBSF following the method used for the IXO-09 100 ks SBSF in Section 4.1.2. In addition, count rates of 10^{-2}, 3.162×10^{-2} and 10^{-1} cts s^{-1} are sampled at $\beta = 0.3$ and 0.5 with $r_c = 1$ arcsec. This increases the accuracy of the selection function in the region where it changes rapidly and where a large number of detected systems lie. Samples of the resulting smoothed SBSFs are given in Appendix H.

Enhancement factor $F(z)$ fits are performed on the 4 surveys using the $f(L_{\mathrm{X}}, T, z, r_c, \beta)$ form of the appropriate SBSF, following the method in Section 4.2.2. The results are shown in Figure 5.4 and Table 5.1, along with Table H.1, Appendix H.

With no correction, increasing the PSF size from 5 to 9 arcsec causes a general increase in the enhancement factor in most bins at $z < 1.2$, but within 1σ in the BD surveys. The best-fit $F(z)$ model (solid blue line) fails to recover the true evolution in all cases.

Applying the SBSF correction using the true r_c and β (orange triple-dot-dash line)

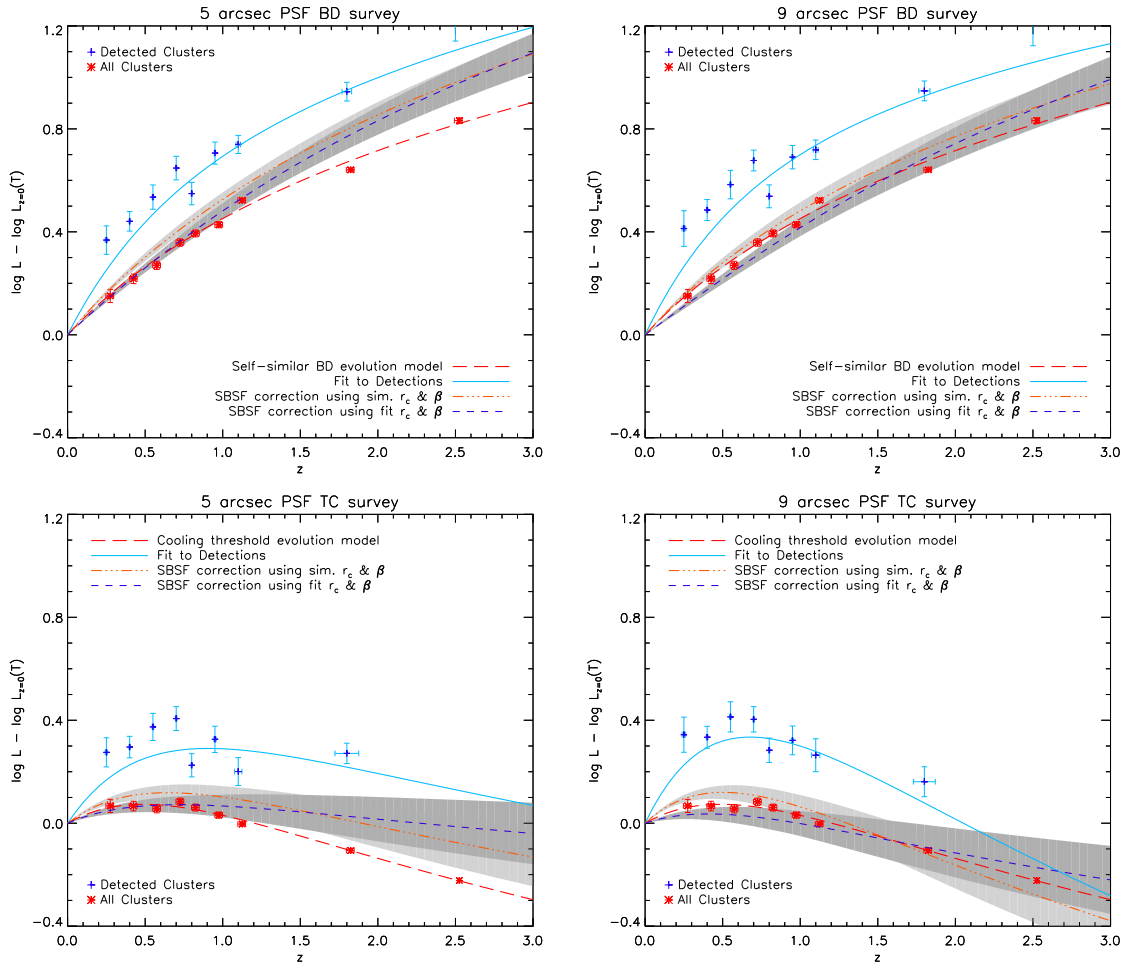

Figure 5.4: Bias in the simulated $L_X - T$ enhancement factor for an 80×100 ks pointing IXO-10 survey with PSF widths of 5 arcsec (*left*) and 9 arcsec (*right*) FWHM. *Top-row:* $L_X - T$ evolution that is self-similar with respect to the background density. *Bottom-row:* $L_X - T$ evolution with similarity linked to the cooling threshold. Data points and lines as defined in Figure 4.12, Section 4.2.2.

causes the $F(z)$ fit to favour the true model in all 4 surveys, although to only 4σ in the 5 arcsec BD survey. Unexpectedly, the 9 arcsec surveys fits are in better overall agreement to the true evolution than their superior resolution counterparts, both recovering the correct evolution at 1σ. This is likely due to the low quality of the SBSF, which has been adapted from that for a different instrument and exposure time. A thorough exposure time for the two configurations used here may yield different results.

Using the r_c and β fit PDFs to perform the correction (dark blue short dashed line) improves the agreement to the true evolution in all cases except 9 arcsec BD, where there is an over-correction at low redshift. This improvement is similar to what happened for

Table 5.1: Identifying the $L_X - T$ enhancement factor fits with different PSF widths. As Table 4.4, Section 4.2.2, but for the $L_X - T$ enhancement factor fits in Figure 5.4.

Survey	Model	σ		
		No correction	SBSF	SBSF with fits
BD 5 arcsec	NE			
	BD		4.01	2.05
	CD			
	TC			
BD 9 arcsec	NE			
	BD		1.00	1.46
	CD			8.04
	TC			
TC 5 arcsec	NE		4.83	2.54
	BD	6.81		
	CD	6.94	4.64	5.38
	TC		2.27	0.90
TC 9 arcsec	NE		3.86	0.74
	BD	6.96		
	CD	8.08	5.92	7.14
	TC		1.21	0.86

the IXO-09 100 ks simulations, where the small amount of extra bias correction from this method makes up for shortcomings in the SBSF. Using this method also moves the fits to a less accurate mix of u and v (e.g. u is no longer the dominant parameter in the BD survey fit), and inaccuracy gets worse with a broader PSF (see Table H.1). This may affect more precise studies of evolution, but does not affect the general agreement with the true evolution model.

5.2 Particle Background

Particle background is a very different issue to the PSF for the design of an observatory. Instead of improving the performance of the equipment, it must be protected from the environment it is operating in. The topic of particle background has been covered in Section 2.4.8. Aspects of this include cosmic rays and solar activity. XIS simulations contain a constant particle background rate of 2.39×10^{-6} cts s^{-1} arcsec^{-2}, which assumes no flare activity.

Due to the uncertainty of the IXO particle background, two simple test cases are compared to the default configuration in XIS: no particle background and a rate of 4.78×10^{-6} cts s^{-1} arcsec^{-2} (double particle background). These cases should indicate how important particle background will be to IXO images. Note that the normal particle background in IXO-10 simulations constitutes approximately a quarter of the total background counts within the field of view.[1]

The simulations are generated in a similar way to those in Section 5.1.1, but with the PSF fixed at the usual 5 arcsec FWHM and the particle background rate changed instead. Only simulations with no evolution in the $L_{\rm X} - T$ relation are generated. An example of a pointing that has been simulated with the three different particle background rates is available in Appendix H, Figure H.3. The effect of extra particle noise is visually insignificant compared to the X-ray background.

Cumulative $\log N - \log S$, $N(M_{500}, z)$ and $L_{\rm X} - T$ relation for the three different particle background rates are shown in Appendix H, Figures H.4, H.5 and H.6, respectively. Changing the particle background appears to have only a small effect on the number of detections. Number differences between the two extreme cases are $\sim 5\%$, $\sim 15\%$ and $\sim 10\%$ for clusters, galaxies and AGN, respectively. The difference in the number of cluster detections at high $S_{\rm X}$ is not significant compared to the statistical errors. Overall, altering the particle background has minimal effect on $N(M, z)$ and does not change the bias of the $L_{\rm X} - T$ relation.

5.3 Summary

In this chapter we have experimented with changing the angular resolution and particle background level of IXO. A reduction in angular resolution leads to great loss of the number of X-ray galaxies detected, with losses of $> 30\%$ per 2 arcsec. However, it is not such a significant problem for clusters and AGN studies, which lose $\sim 10\%$ of their number

[1] The total X-ray count rate before vignetting is 7.57×10^{-6} cts s^{-1} pixel^{-1}, while the particle background rate is 2.54×10^{-6} cts s^{-1} pixel^{-1}.

counts per 2 arcsec of broadening. For clusters, gains from better angular resolution are roughly evenly distributed in mass and redshift unless the PSF is < 5 arcsec FWHM. There is no substaintial change in the bias of the $L_{\rm X} - T$ relation with the PSF width. This also appears to be true for the evolution of $L_{\rm X}$, wherein the inaccuracy in correcting for cluster selection dominates over any inaccuracy that results from switching from a 5 arcsec to a 9 arcsec PSF.

It should be noted that angular resolution affects the quality of other measurements that are important for cluster science. These include surface brightness fitting, spatially-resolved spectral measurements, and studies of cool cores and other morphological features such as cavities.

Large changes made to the regular particle background rate are negligible compared to X-ray photon noise. This is good news for IXO preparation due to the uncertainties of operating at the L2 point.

CHAPTER 6

Overview and Conclusions

This thesis explores the issues with X-ray cluster surveys with a focus on the imaging capabilities of the proposed International X-ray Observatory. Analysis is performed with an X-ray image simulator and source identification software produced as part of this work. The survey issues examined are bias in detected samples and the trade-off between survey area and depth. These affect our ability to measure the $L_{\rm X} - T$ relation and its evolution, which has serious consequences for their use in understanding the baryon physics involved in the formation of cosmic structure. We also investigate the impact of two properties of the IXO instrument: its particle background and PSF.

6.1 Cluster Surveys

The issue of observational bias has been acknowledged in astronomy for many years. However, it has been treated crudely for most X-ray surveys. In this thesis I present a more sophisticated analysis. The main results presented in Chapter 4 highlighted how important bias is for recovering the true $L_{\rm X} - T$ relation, and how it evolves.

Wide-angle surveys are a good way to collect large samples of clusters, but they suffer

from serious selection bias. This can lead to very misleading conclusions about $L_{\rm X} - T$ evolution.

In the past, surveys have used flux cuts to achieve a complete sample. Applying a flux cut to the data removes some, but not all, of the bias. Moreover, this comes at the cost of excising many clusters, most of which are low temperature systems where the effects of baryon physics are more distinct.

From the surface brightness selection function employed in this work it is clear that actual survey selection functions are more than just a function of flux. The core size and asymptotic slope of the cluster surface brightness must also be accounted for. We demonstrate that correcting for bias with anything less sophisticated than this will result in erroneous conclusions about the $L_{\rm X} - T$ relation and its evolution.

Even with the sophistication of the surface brightness selection function, it is shown to be insufficient to fully recover an unbiased estimate of $L_{\rm X} - T$ evolution. In practice correctly applying a suitable assumed selection function is made more difficult for three factors:

- Real clusters are not simple β-models, they can have complex morphology.
- Good measurements of cluster properties need to be made to apply the appropriate selection function correction.
- The assumed distribution of the underlying population is based on measurements of the local $L_{\rm X} - T$ relation, which is itself biased.

In the end the only way to sufficiently improve accuracy may be to use deep surveys to negate some of the bias. Deep surveys also detect more low temperature groups, which are required for a better understanding of the non-gravitational processes taking place.

Wide-angle surveys are useful in other areas of cluster science. They surveys catch more clusters than deep ones, especially at high mass, and are less affected by cosmic variance. This means that, with adequate correction for the selection function, wide-angle surveys are more suitable for probing the cluster mass function for the purpose

of placing constraints on cosmology. With IXO, wide-angle surveys are even capable of detecting high redshift clusters.

6.2 IXO

While the surveys trialled here have involved very long total exposure times, they give some useful indications as to the expected performance of IXO. It should provide samples of the first forming clusters at $z > 2$, as well as samples of groups at $z > 1$. If the 5 arcsec goal for the PSF is scaled back to 7, or even 9 arcsec, the ability to recover these systems is not fatally compromised. However, such a change would make measurements of clusters less accurate.

The capabilities of IXO will no doubt lead to some substantial advances in the knowledge of clusters. But, as our study has shown, great care must still be taken to quantify the biases introduced by survey selection effects.

6.3 Future Work

6.3.1 XIS

The are many possibilities for improving the quality of XIS simulations and advancing its features:

- Improving cluster modelling by using double β-models, including a more detailed cool core distribution, having a metallicity-redshift relation, and creating irregular systems.

- Creation of flux cubes - images which contain spectral information. More energy dependence in instrument properties such as vignetting.

- More sophisticated source fitting, making more use of the wavelet information and allowing more free parameters for good data. Simultaneous fitting of two sources

could also be explored.

- Development of the Bayesian method of source identification, including more experimentation with prior probability distributions.

The reliability of the source identification process could be improved by mixing point and extended sources during the calibration process. Care must be taken to avoid mismatching the detected sources with those simulated. The increased number of sources would increase the chance of confusion between them, raising the extent statistics in general. The extend threshold would be raised to compensate, resulting in a reduced number of cluster identifications. The confusion problem would also become worse if a more realistic distribution of point sources is used. Optimising the modelling process is important to keep the number of cluster detections high.

6.3.2 Cluster Selection Function

Modelling of the assumed selection function could be improved in a number of ways. The most obvious is more sampling of the parameters of the SBSF. Other areas that could be explored include:

- ellipticity,
- point source population density,
- use of realistic clusters drawn from cosmological simulations,
- off-axis position (both vignetting and PSF).

However, extra detail in the assumed selection function will not help if it is not applied correctly and to an adequately modelled distribution. With such a rich amount of material available with which to construct models, there is no reason not to attempt a thorough correction of the cluster datasets for both the current and next generation of X-ray telescopes.

Appendices

APPENDIX A

Methods and Derivations

A.1 Lightcone Construction

The following method is based off that of Kitzbichler & White (2007) and is applied to the MS snapshots, which are cubes of length 500 h^{-1} Mpc.

Consider a Cartesian coordinate system originating at the corner of a comoving cube with axes aligned along the sides of the cube. This cube is at the corner of a continuous 3D grid of identical cubes. The direction of the line of sight is defined by the length of the cube, L, and two integers with no common factor, m and n. A line of sight of sight from the origin which passes through the coordinates (L/m,L/n,L) in the cube grid would reach a location equivalent to the origin at the point (nL,mL,L) (hereafter the repeat point). This is illustrated in Figure A.1. By defining the observation field as a near-pyramid enclosed by the four points $((n \pm 0.5/m), (m \pm 0.5/n), nmL)$, no part of the cube is contained within the lightcone more than once before the repeat point. The result

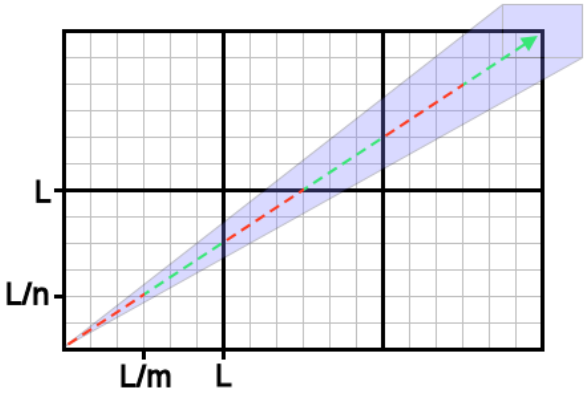

Figure A.1: The geometry of a Kitzbichler & White (2007) lightcone shown in 2D. Black lines show the sides of an assembly of comoving cubes with length L, each divided into a 6×6 grid. The dashed line shows the progress of the centre of a reverse lightcone with $m = 2$ and $n = 3$. Alternating red and green lines represent the passage of the lightcone through each cube in the 3rd dimension. For every L traversed in the third dimension, $L/2$ and $L/3$ are traversed in the other two dimensions. The blue-grey shading represents the area covered by the field within the lightcone.

is a field of size $1/m^2n \times 1/n^2m$ square radians with a repeat point at

$$D_{\rm rep} = \sqrt{(n^2 + m^2 + m^2n^2)L} \tag{A.1}$$

Therefore, $m = 2$ and $n = 3$ creates a lightcone of 4.77×3.18 deg^2 which duplicates at $z = 1.80$. Using $m = 3$ and $n = 4$ produces a much narrower lightcone of 1.59×1.19 deg^2, but with no repeat until $z = 8.10$.

A number of different lightcones can be created from the same N-body simulated volume by starting from different corners or other points within that volume. To prevent large scale structure from being replicated, the direction and position of the lightcone are changed at the repeat point. This disassociation is assisted by the change in the position of halos with cosmic evolution. It should be noted that even though a region is not reused until the repeat point, the transition back to the beginning of a cube at every $[(L/m)^2 + (L/n)^2 + L^2]^{-1/2}$ creates a discontinuity in the large scale structure being observed.

To generate a lightcone in XIS, the line of sight through the simulation volume is

defined by the unit vector

$$\boldsymbol{u}_3 = \frac{(n, m, mn)}{\sqrt{n^2 + m^2 + m^2 n^2}} \tag{A.2}$$

This forms one axis of a right-handed Cartesian coordinate system along with a unit vector $\boldsymbol{u}_1$ which is perpendicular to both $\boldsymbol{u}_3$ and the unit vector for the direction related to the smaller of m and n, and a unit vector $\boldsymbol{u}_2$ which is perpendicular to the other two. A backwards light cone is constructed along this vector in 37 stages, one for each snapshot, starting with the $z = 0$ snapshot. First, all halos within the pyramid volume are extracted by calculating their angular deviation from the line of sight vector:

$$\tan\alpha = \frac{\boldsymbol{x}\cdot\boldsymbol{u}_1}{\boldsymbol{x}\cdot\boldsymbol{u}_3},$$
$$\tan\delta = \frac{\boldsymbol{x}\cdot\boldsymbol{u}_2}{\boldsymbol{x}\cdot\boldsymbol{u}_3}$$

where $\boldsymbol{x}$ is the 3D position of the halo. Defining the field size as $\Delta\alpha \times \Delta\delta$, where $\Delta\alpha = 1/m^2 n$ and $\Delta\delta = 1/n^2 m$, those halos within the pyramid volume meet the conditions

$$|\tan\alpha| \leq \tan\Delta\alpha/2, \tag{A.3}$$

$$|\tan\delta| \leq \tan\Delta\delta/2 \tag{A.4}$$

Each snapshot is assigned a comoving distance range corresponding to its redshift, with the boundaries equidistant between each snapshot. For snapshot s centred at comoving distance D_s, the volume is truncated to contain only those halos in the range $(D_s + D_{s-1})/2 < D \leq (D_s + D_{s+1})/2$ (with $D_{s-1} = 0$ at $z = 0$), creating a lightcone 'slice'. This gives each snapshot a representative contribution to the properties of the total field, reproducing an evolving Universe within the constraints of the time resolution of the MS. The boundary of the final slice puts the maximum redshift of the lightcone at $z = 3.18$. Note that one can only extract a lightcone in this way, identical to that used for Euclidean geometry, if the region being sampled is measured in comoving coordinates and is within a flat universe.

To allow the process defined above to continue unaffected upon reaching a cube boundary, Kitzbichler & White (2007) generated a periodically replicated grid of simulated cubes and keep only those which intersect their lightcone. For XIS this approach is followed but further optimised for memory usage by dividing the cubes into 8 sub-cubes and keeping only those which are required to cover the present lightcone slice.

When a repeat point is reached, all following snapshots are rotated by $\pi/2$ around the an axis passing through the centre of the cube and parallel to one side. This rotation is different after each repeat point. Due to the non-negligible size of a slice, if a rotation occurs while the slice is near the centre of the cube it causes part of the region from the previous slice to be reused. To negate this problem, the whole grid is translated to place the slice back at a cube origin.

A problem that arises from the use of absolute distance boundaries for the contribution from each snapshot is the duplication or loss of some halos due to movement over the boundary in the intervening time. Kitzbichler & White (2007) confronted this problem by linearly interpolating the positions of halos close to the boundary between z_{i+1} and z_i. By estimating their position relative to the redshift corresponding to the boundary, they were assigned properties based on which side of the boundary they fell on.

The boundary transition problem here is not as significant as for the galaxies processed by Kitzbichler & White (2007) due to the considerably smaller number of halos above the mass cut of the XIS lightcone. However, to improve accuracy the problem is solved in a similar way. Each halo has an Identification (ID) number and a Descendant Identification (DID) number. To find duplicate halos, the DID of each halo in the current slice is compared with the ID of the previous (lower redshift) slice. The mean D is found for each set of merging halos and the corresponding $\overline{D}$ is calculated between a set and its descendant halo. If $\overline{D} \leq (D_s + D_{s-1})/2$ then the merging halos are removed and the descendant halo is kept, but with $\overline{D}$. Otherwise, only the halo closest to the descendant is removed and all other halo positions are interpolated towards each other. In both cases, the descendant halo is given a distance-interpolated M_{200} between its original and that

of the sum of the component halos. This estimates the accretion of halos below the mass cut.

To locate the 'elusive' halos, all halos within a snapshot that satisfy the conditions in Equation A.4 and lay within the first quarter of the following slice are stored. When processing the next snapshot, the IDs of halos in the current slice are compared with the DIDs of the stored halos. If the progenitors of a stored halo are not found, they are searched for in the region covered by the previous slice. If a match is found then the halos involved are merged using the same method as for the duplicates, but with reversed boundary conditions.

When the lightcone has been constructed from all 37 snapshots, the angular coordinates of each halo on the simulated sky are calculated in units of arcsec. The lightcone is centred on arbitrary coordinates defined as Right Ascension (RA) and Declination (Dec):

$$\mathrm{RA} = (6.48 \times 10^5)\alpha/\pi,$$
$$\mathrm{Dec} = (6.48 \times 10^5)\delta/\pi$$

For efficiency, M_{500} estimates and the mass function correction are conducted after the lightcone is complete. The output of the lightcone construction process is a halo catalogue with RA, Dec, D, z, M_{200} and M_{500}, referred to as the cluster sky field.

This work uses the lightcone shape parameters $m = 2$ and $n = 3$. These parameters create a large, contiguous area for use in surveys, containing a sufficiently large cluster sample within a single lightcone. The repeat point at $z = 1.80$ is distant enough to not disrupt the bulk of the surveyed population, and no other repeat points occur within the selected MS snapshots. Also, the cube edge discontinuities are less common than for the $m = 3$, $n = 4$ lightcone. The simulated volume contained within the lightcone is 0.037% of the Universe out to $z = 3.18$.

A.2 Surface Brightness Profile

A rotated two-dimensional surface brightness profile can be generated analytically by calculating an effective radius for each position. Consider a 2D Cartesian coordinate system (x, y) with its origin at the centre of the cluster (x_0, y_0). Defining

$$\Delta x = x - x_0$$

$$\Delta y = y - y_0$$

The radial distance from the centre of the cluster is then given by

$$r = \sqrt{(\Delta x)^2 + (\Delta y)^2}$$

Defining a rotation angle θ in radians, the effective angle of each position in the cluster becomes

$$\Theta = \arctan\left(\frac{\Delta y}{\Delta x}\right) + \theta$$

This gives the contribution of each radial position to the effective radius on the x-axis and y-axis, respectively, as

$$r'_x = r\cos\Theta$$

$$r'_y = r\sin\Theta$$

The total effective radius is then

$$r' = \sqrt{r'^2_x + r'^2_y}$$

$$r' = \sqrt{(r\cos\Theta)^2 + (r\sin\Theta)^2}$$

To maintain the area A of a surface brightness profile of radius R when transforming it into an ellipse, the semi-minor to semi-major axis ratio η can be substituted into the into the formula for the area of an ellipse:

$$\eta = \frac{b}{a}$$
$$A = \pi R^2 = \pi ab$$
$$R^2 = b^2\eta$$

It then follows that the change in each axis size,

$$\frac{b}{R} = \eta^{-0.5}$$
$$\frac{a}{R} = \eta^{0.5}$$

Therefore the effective radius as a function of rotation angle and axis ratio is

$$r' = \sqrt{(r\eta^{0.5}\cos\Theta)^2 + (r\eta^{-0.5}\sin\Theta)^2} \tag{A.5}$$

which can then be applied to the 1D surface brightness β-model

$$S(r) = S_0\left[1 + \left(\frac{r'(r)}{r_c}\right)^2\right]^{0.5-3\beta}$$

A.3 Cluster-AGN Cross-correlation

The cluster-AGN position cross-correlation function in XIS is based on the $\xi_{\rm CA}(s)$ power law from Cappelluti et al. (2007), but with a linear decrease to zero below their minimum considered value of $s = 2.5$ Mpc (see Section 2.3.2). This avoids the centre of cluster, concentrating AGN at a radius of ~ 4 arcmin from the bulk of the cluster population. On an individual cluster basis, this would act to avoid 'contamination' of the cluster core emission. However, with $150 - 300$ clusters present in a 9 arcmin diameter pointing

extraction field, the correlation is 'washed out'. Its overall effect is to concentrate AGN in fields with more clusters.

More relevant is the analysis of 148 Chandra-imaged clusters by Gilmour et al. (2009), which showed a mean excess of 1.46 ± 0.32 point sources, and all within the central 1 Mpc. This was compared to an excess of 0.47 ± 0.61 in the blank fields. Over half of the sources were likely to be AGN, but only 12 clusters had a central source. This highlights an inaccuracy in the prescription for point source placement in XIS.

Another source of inaccuracy comes from the limited redshift size of the elements in the AGN position matrix. While the element size of $z = 0.2$ is appropriate for the z dimension of the AGN flux function $N(S_{\rm SX}, z, n_H)$, it is not sufficient for integrating the 3D correlation around each cluster.

Point sources can affect extended source detection several ways. Detections are reduced when a point source completely obscures a cluster and is either successfully identified as point-like or is mis-identified as extended but is too far from the centre of the simulated cluster for a false match. Detections are increased when either a nearby point source (detected or not) increases the extent statistic of a cluster that would otherwise not have been identified as extended, or when a point source that is identified as extended is at the centre of a cluster image (causing a false match) that would otherwise be undetected. It is unclear *a priori* which of these effects would dominate in a simulated IXO survey.

A simple model point source position distribution with a higher density of central point sources is created to see how it would affect the selection function. The model is based on a pessimistic application of the Gilmour et al. (2009) results, geared towards group-scale systems. A mean excess of 1 AGN is placed within a $\ll 1$ Mpc radius of a cluster and a further mean excess of 0.5 AGN at the centre of each cluster. Due to the simple, z-independent design of the selection function mapping, for this method each cluster is assumed to be at $z = 0.5$, near the peak of the number of low-flux detections in the 10 ks NE survey from Section 4.2. The excess radius projected on the image is set

Table A.1: Change in the SBSF with the increased central AGN density model. Each element of the table shows the new detection probability minus the original detection probability for each S, r_c and β.

r_c (arcsec)	$\beta = 0.3$ $\log S$ -1.75	-1.25	$\beta = 0.5$ $\log S$ -1.75	-1.25	$\beta = 0.7$ $\log S$ -1.75	-1.25
0.63	-0.01 ± 0.13	0.00 ± 0.14	-0.04 ± 0.05	-0.01 ± 0.13	0.03 ± 0.02	0.00 ± 0.03
2.51	0.00 ± 0.05	0.05 ± 0.13	-0.04 ± 0.09	0.00 ± 0.14	-0.08 ± 0.06	0.03 ± 0.14

NOTE. - S is in units of cts s^{-1}.

as 27 arcsec, equivalent to 165 kpc at $z = 0.5$, rescaled from a sphere of excess radius 200 kpc. This is more sufficient to provide excess AGN close to low mass clusters. The angular size of the map of the excess radii is 2 arcsec.

The selection function $f(S, r_c, \beta)$ follows the basic set-up described in Section 4.1.2. However, it is only sampled over the following grid of $2 \times 2 \times 3$ points: $S = 1.778 \times 10^{-2}$ and 5.623×10^{-2} cts s^{-1}; $r_c = 0.6310$ and 2.5119 arcsec; $\beta = 0.3$, 0.5 and 0.7. These points cover a region contained within the bulk of the clusters detected by IXO-09, and either on or near steep gradients in the IXO-09 SBSF. They are for use in a direct comparison with the original SBSF.

When 100 clusters are simulated for the selection function, 100 of the AGN generated for the simulation are randomly selected and placed within the excess radii of those systems. An additional 50 AGN are randomly selected and positioned at cluster centres, to within the accuracy of the excess radii map. Galaxies are positioned entirely randomly in each field.

The results for the new selection function samples compared to those of the original SBSF are shown in Table A.1. For the majority of the sample points, the change in the detection probability is within the errors resulting from the sample size. The exceptions occur at $S = 1.778 \times 10^{-2}$ cts s^{-1}, $\beta = 0.7$ for both core radii. Increased central AGN density appears to have increased the detections of the more cuspy systems, and decreased the detections of wider cores. The change in behaviour between these two similar core radii is surprising, but note that both of these differences are not much greater than 1σ.

If change at $f(1.778\times10^{-2}, 0.63, 0.7)$ is a real effect, it is probably caused by the extent statistics of these cuspy systems being enhanced by contaminating AGN. For $f(1.778 \times 10^{-2}, 2.51, 0.7)$ the decreased central surface brightness may have allowed some of the contaminating AGN to become the dominant source. Extrapolating this effect to the study in Section 4.2, one would expect a small decrease in the clusters statistics at low redshift, and an increase at $1 \lesssim z \lesssim 2$ where the general angular size of clusters is smaller. These speculations are based on poor statistics, and more sampling is required of both selection functions to draw confident conclusions.

Overall, repeating the research performed here with a more plausible point source placement is not expected to alter the conclusions. The change in the selection function is smaller than the inaccuracy of the SBSF at low redshift. However, since there is evidence that point source placement has an effect, it should be considered when trying to accurately determine the selection function of a survey in order to optimise the results.

A.4 Cash Statistic

The Cash statistic (Cash 1979) is based on the probability that a model m could produce a dataset d with bins (pixels) indexed by i. Consider a Poisson distribution:

$$P(k, \lambda) = \frac{\lambda^k e^{-\lambda}}{k!} \tag{A.6}$$

where P is the probability of k counts occurring when λ counts are expected. The probability of a particular dataset occurring is the product of the probability of the expected

data being present in each pixel:

$$\begin{aligned} P &= \prod_{i=1}^{N} \frac{m_i^{d_i} e^{-m_i}}{d_i!} \\ \mathcal{L} = \ln P &= \sum_{i=1}^{N} \ln \left(\frac{m_i^{d_i} e^{-m_i}}{d_i!} \right) \\ &= \sum_{i=1}^{N} (d_i \ln m_i - m_i \ln e - \ln d_i!) \\ &= \sum_{i=1}^{N} (d_i \ln m_i - m_i - \ln d_i!) \end{aligned}$$

The Cash (C) statistic is then defined as

$$C = -2 \ln P = -2 \sum_{i=1}^{N} (d_i \ln m_i - m_i - \ln d_i!) \tag{A.7}$$

The maximum likelihood value of C is when it is at its minimum. Two values of the C statistic can be compared using Wilks theorem:

$$-2 \log \frac{\max \mathcal{L}(\theta)_{\theta \in \Theta_0}}{\max \mathcal{L}(\theta)_{\theta \in \Theta}} \approx \chi^2 \tag{A.8}$$

where θ is a parameter in the space Θ, and Θ_0 is a subspace of Θ. This allows the difference between a minimum value of C found by varying parameters $\theta_1, \ldots, \theta_p$ and one found from a subset of p to form a meaningful statistic:

$$\Delta C = C_{\min, p-q} - C_{\min, p} \tag{A.9}$$

which is χ^2 distributed with q degrees of freedom (Cash 1979). ΔC can be used to generate confidence intervals for a $C_{\min}$ fit or to compare models of different complexity.

A.5 Selection Function Smoothing

The selection function is smoothed onto a grid with 10 times the resolution in all 3 parameters. The smoothed detection probability,

$$P_{\mathrm{det},ijk} = \frac{\sum_{IJK}(e^{-d_{ijkIJK}} P_{\mathrm{det},IJK})}{\sum_{IJK}(e^{-d_{ijkIJK}})} \tag{A.10}$$

where

$$d_{ijkIJK} = \frac{(\Delta S_{iI})^2 + (\Delta r_{c,jJ})^2 + (\Delta \beta_{kK})^2}{\sigma^2} \tag{A.11}$$

where

$$\Delta S_{iI} = \log S_i - \log S_I \tag{A.12}$$

$$\Delta r_{c,jJ} = 1.25(\log r_{c,j} - \log r_{c,J}) \tag{A.13}$$

$$\Delta \beta_{kK} = 2.5(\beta_k - \beta_K) \tag{A.14}$$

where S_I is the count rate at position I on the original selection function grid, S_i is the count rate at position i on the high resolution grid, and σ is the smoothing scale. Scaling applied to the r_c and β smoothing is to make the effective distance between grid points is the same as for S.

To limit the disruption to the accuracy of the selection function, the following method is used: The flux at which the P_{det} climbed to 99% is identified for several values of r_c and β (see Table A.5). For each point, the distance to the nearest point in the $S - r_c$ plane at which P_{det} drops to 2% is then recorded. An iterative process is used to smooth the selection function in reducing steps of 0.1 σ until the distance is within 15% of its original value, which occurs at $\sigma = 2.1$.

Due to noise remaining at the outskirts of the selection function which have low probability, all regions where $P < 2\%$ are set to $P = 0\%$ (after smoothing).

APPENDIX B

IXO

B.1 Instrument Requirements

Table B.1: Instrument requirements to accomplish the main science goals of IXO, as reported for the US Decadal Survey (Astro2010) in Bookbinder (2010).

Instrument		Bandpass	PSF (HPD)[a]	FoV[b]	Energy Resolution	Science Driver
		keV	arcsec	arcmin	eV @ keV	
XMS	Core	0.3-12	5	2×2	2.5 @ 6	Gal. Clusters
	Outer			5×5	10 @ 6	
WFI/HXI	WFI	0.1-15	5	18 diameter	150 @ 6	SMBH Survey
	HXI	10-40	30	8×8	1000 @ 30	SMBH Spin
XGS		0.3-1.0	5	N/A	$E/\Delta E = 3000$	Cosmic Web
HTRS		0.3-1.0	N/A	N/A	150 @ 6	NS EoS
XPOL		2.0-10.0	6	2.5×2.5	1200 @ 6	SMBH Spin

[a] Point spread function half power diameter.

[b] Field of view.

B.2 Science Requirements

Table B.2: Instrument requirements to accomplish the main science goals of IXO, as reported for the US Decadal Survey (Astro2010) in Bookbinder (2010).

	Target Information				Observation Requirement			
Science Topic	Typical Target	# of Ptgs[a]	Src Size	Typical Flux	Analysis	S/N required	Obs Time	Abs Ast[b]
			arcmin	erg/cm^2/s			Msec	arc-sec
Strong Gravity	MCG-6-30-15	20	point	5×10^{-11}	spectra	10	8	N/A
SMBH Spin Survey	NGC 4051	200	point	10^{-12}	spectra	5-10/bin	10	N/A
	MCG-6-30-15	10	point	5×10^{-11}	polari-sation	**1% MDP**	10	N/A
Neutron Star EoS	4U1636-536	15	point	10^{-4}	spectra	20/bin	5.5	N/A
Growth of SMBH	CDF-S	38	point	3×10^{-17}	imaging spectra	5 at flux limit	10	**1**
Clusters / Feedback	z=0.1-2 cluster	250	2-18	10^{-13}	imaging spectra	50 at flux limit	14	N/A
Cosmology	z=1-2 cluster	1000	3	5×10^{-14}	image, spectra	2000 cts/obj	15	10
Cosmic Web of Baryons	QSO B1 426 +428	30	point	10^{-11}	spectra	12/bin	15	N/A

Observation Requirement									Instrum
FoV[c]	Band-pass	PSF HPD[d]	Mirror Effective Area Rqmt (m^2)			Energy Res Rqmt		Rel Timing	Primary (Second)
arcmin	KeV	arcsec	1.25 keV	6 keV	30 keV	FWHM(eV) @ E (keV)		μsec	
N/A	1-40	N/A	1.5	**0.65**	0.015	2.5	6	N/A	XMS (WFI/HXI)
N/A	**1-40**	N/A	1	0.65	**0.015**	**1000**	**30**	N/A	WFI/HXI (XMS)
N/A	2-10	N/A	2.5	0.5	N/A	1200	6	N/A	XPOL
N/A	0.3-10	N/A	3	0.6	N/A	**150**	**0.3-6**	**10**	HTRS
18 dia	0.3-2	**5**	**3**	0.65	0.015	150	1	N/A	WFI/HXI (XMS)
2 × 2	0.3-40	**5**	**3**	0.65	0.015	**2.5**	**6**	N/A	XMS (WFI/HXI)
5 × 5	0.3-7	10	1	0.1	N/A	**10**	**6**	N/A	XMS (WFI/HXI)
N/A	**0.3-1**	5	N/A	N/A	N/A	**0.1**	**0.3**	N/A	XGS (XMS)

NOTE. - Bold highlights the main drivers.

[a] Number of pointings.

[b] Absolute astrometry.

[c] Field of view.

[d] Point spread function half power diameter.

APPENDIX C

Cluster Scaling Relations

C.1 Derivation

By treating the cluster as a sphere it follows that

$$\rho \propto Mr^{-3}$$
$$r \propto M^{1/3}\rho^{-1/3} \tag{C.1}$$

where r is the radial size of the cluster, M is the cluster mass, and ρ is the total matter density. This is the first scaling relation. From the virial theorem one can state that thermal energy of the cluster has the same magnitude as the potential energy of the gravitational well, therefore

$$T \propto Mr^{-1}$$

Substitute in C.1 to get

$$T \propto M(M^{1/3}\rho^{-1/3})^{-1}$$
$$T \propto Mr^{-1} \propto M^{2/3}\rho^{1/3} \tag{C.2}$$

Assuming the gas and dark matter particles are equally gravitationally bound, we can relate the gas density to the total matter density by

$$\rho_g \propto \rho \tag{C.3}$$

The cooling time of the cluster gas is longer than its free-fall time, thus it can be assumed that the cluster is in hydrostatic equilibrium. For a spherically symmetric system, the equation of hydrostatic equilibrium is:

$$\frac{\partial P}{\partial r} = \frac{-GM_r}{r^2}\rho \tag{C.4}$$

where P is the gas pressure, and G is the Universal gravitational constant. Therefore

$$P_g \propto M_g \rho_g r^{-1}$$

Since the gas is low density, it is appropriate to use the ideal gas law

$$P = nkT \tag{C.5}$$

where n is the number density of particles, and k is Boltzman's constant. Therefore

$$P_g \propto \rho_g T$$

By equating C.4 and C.5, we get

$$\rho_g T \propto M_g \rho_g r^{-1}$$
$$T \propto M_g r^{-1}$$

By comparing with C.2, we see that

$$M_g \propto M \propto T^{3/2} \rho^{-1/2} \tag{C.6}$$

The final scaling relation can be derived from the thermal bremsstrahlung (free-free) emission of the hot gas, based on a Maxwellian distribution of electrons. Assuming the gas is ionised hydrogen, the electron density equals the ion density. Therefore, the radiated power per unit volume in free-free emission

$$e_{\mathrm{ff}} \propto n^2 T^{1/2}$$

Assuming spherical symmetry again, we integrate over the emission to get the X-ray luminosity

$$L_{\mathrm{X}} \propto \int \rho_g^2 T^{1/2} \mathrm{d}V$$
$$L_{\mathrm{X}} \propto \rho_g T^{1/2} M_g$$

Substituting in the $M_g - T$ relation gives

$$L_{\mathrm{X}} \propto T^2 \rho^{1/2} \tag{C.7}$$

C.2 Evolution

C.2.1 With respect to the mean matter density

The scale factor a relates physical coordinates to comoving coordinates in an expanding or contracting Universe:

$$x_p = x_c a \tag{C.8}$$

where x_p is a physical distance, and x_c is a comoving distance. From the first law of thermodynamics, it can be shown that for a flat Universe

$$\rho \propto a^{-3} \tag{C.9}$$

where ρ is a matter density. The scale factor is a function of time. The redshift z of an observed photon can be defined using a:

$$\frac{a(t_0)}{a(t_e)} \equiv 1 + z \tag{C.10}$$

where $a(t_0)$ the scale factor at present epoch, and $a(t_e)$ is the scale factor at the time the redshifted photon was emitted. Therefore

$$\begin{aligned} a &\propto (1+z)^{-1} \\ \rho &\propto (1+z)^3 \end{aligned} \tag{C.11}$$

Returning to our previously derived scaling relations, we can now substitute in for density:

$r \propto M^{1/3}\rho^{-1/3} \propto M^{1/3}(1+z)^{-1}$

$T \propto Mr^{-1} \propto M^{2/3}\rho^{1/3} \propto Mr^{-1}(1+z)$

$M_g \propto M \propto T^{3/2}\rho^{-1/2} \propto T^{3/2}(1+z)^{-3/2}$

$L_{\rm X} \propto T^2 \rho^{1/2} \propto T^2 (1+z)^{3/2}$

C.2.2 With respect to the critical density

The expansion of the Universe is described by the Friedmann equation

$$H(t)^2 = \frac{8\pi G}{3}\rho - \frac{kc^2}{a^2} \tag{C.12}$$

where $H(t)$ is the Hubble parameter as a function of time, G is the Universal gravitational constant, k is the curvature of the Universe, and c is the speed of light. If one assumes a flat Universe ($k = 0$) then

$$\begin{aligned} H(t)^2 &= \frac{8\pi G}{3}\rho \\ \rho &\propto H(z)^2 \end{aligned} \tag{C.13}$$

Returning to the previously derived scaling relations:

$r \propto M^{1/3} \rho^{-1/3} \propto M^{1/3} H(z)^{-2/3}$

$T \propto M r^{-1} \propto M^{2/3} \rho^{1/3} \propto M r^{-1} H(z)^{2/3}$

$M_g \propto M \propto T^{3/2} \rho^{-1/2} \propto T^{3/2} H(z)^{-1}$

$L_{\rm X} \propto T^2 \rho^{1/2} \propto T^2 H(z)$

C.3 Sample Origins

Outlined below are the details of the cluster samples used to derive the scaling relations in this research. The studies are organised alphabetically by first author. The properties used are listed by author along with a brief description of how that property is measured. CC represents the classification of cool core and non-cool core clusters. Parameter estimation performed in this research is indicated by the italic sentences.

Where the same source is present more than once in a sample, the ones with extrapolated properties are discarded, followed by discarding the ones with larger relative errors. An exception to this is the $M_{500} - T$ relation. Preference is given over the sample of Arnaud et al. (2005), which have temperatures measured to an outer radius of $0.5R_{200}$ rather than R_{500}, and preference is given to sources analysed with the 3D model of Sun et al. (2009).

A slight difference has been found between the Chandra and XMM-Newton measured temperatures, with Kotov & Vikhlinin (2005) obtaining $T_{\rm XMM} = (0.92 \pm 0.08) T_{\rm Chandra}$ with a linear fit (see also Vikhlinin et al. 2005). To optimise its accuracy while maintaining the sample size, when determining the $M_{500} - T$ relation relation this T correction is used to rescale all XMM-Newton temperature and mass data since it represents the minority of the sample.

For reference, masses are often derived by assuming hydrostatic equilibrium and spherical symmetry:

$$M(r) = -\frac{kT(r)r}{G\mu m_p}\left[\frac{d\log\rho_g(r)}{d\log r} + \frac{d\log T(r)}{d\log r}\right] \tag{C.14}$$

The constants equal -3.68×10^{13} $\mathrm{M}_{\odot}$ when a mean molecular weight of $\mu = 0.5954$ is assumed, representing primordial He abundance (Vikhlinin et al. 2006).

Arnaud et al. (2005)

XMM-Newton sample (Pointecouteau et al. 2005).

T: Spectroscopic from a single T fit to the $0.1 < r < 0.5R_{200}$, $0.3 - 2$ keV region using a MEKAL model. Free Z and n_H. R_{200} from mass fit assuming $h = 0.70$, $\Omega_m = 0.3$ and $\Omega_\Lambda = 0.7$. *Renormalised by +8% for consistency with Chandra data used for the majority of other datasets as in Kotov & Vikhlinin (2005).*

M_{500}: NFW model (Navarro et al. 1997) fit to observed mass profile (see equations C.14 and C.15), extrapolated past the observed radius (which only reached $\Delta \leq 500$ for one cluster) to R_{500}, within $0.3 - 2$ keV. See Pointecouteau et al. (2005). *Renormalised by +8% as above.*

$$M_{\mathrm{NFW}(r)} = M_{500}\frac{\ln(1+c_{500}x) - c_{500}x/(1+c_{500}x)}{\ln(1+c_{500}) - c_{500}/(1+c_{500})} \tag{C.15}$$

where c is the concentration of the halo.

Chen et al. (2007)

ROSAT sample supported by ASCA and EXOSAT data (Reiprich & Böhringer 2002).

T: Spectroscopic from a single T fit, further details depend on the origin:

Edge & Stewart (1991): In the range $r < 16 - 18$ arcsec (depending on data), $1.5 - 2$ & $2.5 - 11$ keV using a Raymond-Smith model on ASCA data. Free Z and fixed n_H from radio surveys (Dickey & Lockman 1990, hereafter DL90).

Markevitch et al. (1998): In the range $r < 10 - 20$ arcsec (depending on data), $0.1-20$ keV using a Raymond-Smith model on EXOSAT data. Free Z and free n_H.

White (2000): In the range $0.1h_{50}^{-1} < 0.4h_{50}^{-1}$ Mpc (depending on data), $0.65-9$ & $1.1 - 10$ keV (depending on detector) using a Raymond-Smith model on ASCA data. Free Z and free n_H.

Reiprich & Böhringer (2002): Preference for ASCA data. See references within.

r_{cf}: r_c from single 1D β-model fit. Original R_{500} was from Reiprich & Böhringer (2002) density model assuming $h = 0.50$, $\Omega_m = 1$ and $\Omega_\Lambda = 0$. Ω_m and Ω_Λ. This would have underestimated ρ_c by approximately a factor of 2. *Used R_{500} derived from XIS $M_{500} - T$ relation and cosmology.*

β: From β-model fit as above.

CC: Chen et al. (2007) divided their sample into pronounce cool core, small-to-moderate cool core and non-cool core systems. For this analysis their systems

are redivided into just two categories: 35 CC and 32 NCC systems, requiring a mass deposition rate of > 0.01 $M_\odot$ yr^{-1} for the former.

Helsdon & Ponman (2000)

ROSAT sample.

T**:** Spectroscopic from single T fit in the range $r < R_{\rm extraction}$ using a MEKAL model (energy range unstated). 2 sources fixed at $Z = 0.3$, others free, and fixed n_H from radio surveys (Stark et al. 1992). $R_{\rm extraction}$ based on examination of a smoothed image.

$L_{\rm X,500}$**:** Derived for $r < R_{\rm extraction}$ (energy range unstated) assuming $h = 0.50$ and converted to bolometric. *Converted to XIS cosmology. Rescaled to* $r < R_{500}$ *using best-fit* β*-model and* R_{500} *derived from XIS* $M_{500} - T$ *relation and cosmology.*

r_{cf}**:** r_c from single 2D β-model fit where constrained, 1D otherwise (energy range unstated). R_{500} *as stated above.*

β**:** From β-model fit as above.

Johnson et al. (2006)

XMM-Newton sample.

T**:** Spectroscopic from single T fit in the range $r < R_{\rm extraction}$, $0.5 - 8$ keV (ignoring instrument lines) using a MEKAL model. Fixed $Z = 0.3$ and fixed n_H at galactic value. $R_{\rm extraction}$ is optimal value from β-model fit.

r_{cf}**:** r_c from single 2D β-model fit where constrained, 1D otherwise, for $0.5 - 8$ keV. R_{500} *derived from XIS* $M_{500} - T$ *relation and cosmology.*

β**:** From β-model fit as above.

Kotov & Vikhlinin (2005)

XMM-Newton sample.

T **($M_{500} - T$ relation):** Spectroscopic from integrating a combination of $T(r)$ and $\rho^2_{\rm gas}$ in the 70 kpc $< r <$ R_{500}, $0.5 - 10$ keV region using a MEKAL model (see Vikhlinin 2006). Free Z and fixed n_H from DL90. Renormalised by +8% for comparison with Chandra data (from cross-calibration). R_{500} from density model assuming $h = 0.71$, $\Omega_m = 0.3$ and $\Omega_\Lambda = 0.7$.

T **(other relations):** Best single T fit to the integrated spectrum using a MEKAL model.

M_{500}**:** From the best-fit T and ρ profiles using equation C.14. ρ from single 1D β-model fit within $0.3 - 2$ keV.

r_{cf}**:** r_c from β-model fit as above. R_{500} as stated above.

β**:** From β-model fit as above.

Kotov & Vikhlinin (2006)

Chandra sample.

T**:** Spectroscopic from integrating a combination of $T(r)$ and $\rho^2_{\rm gas}$ in the 70 kpc $< r <$ R_{500}, $0.7 - 2$ keV region using a MEKAL model (see Vikhlinin 2006). Free Z and fixed n_H from DL90. R_{500} from density model assuming $h = 0.72$, $\Omega_m = 0.3$ and $\Omega_\Lambda = 0.7$.

M_{500}**:** From the best-fit T and ρ profiles using equation C.14, within $0.7 - 2$ keV.

Maughan et al. (2006)

Chandra and XMM-Newton sample.

T**:** Spectroscopic from single T fit in the range $r <$ $R_{\rm detection}$, $0.4 - 7$ keV using a MEKAL model. Fixed $Z = 0.3$ and n_H from DL90. $R_{\rm detection}$ from where emission detection drops to 3σ in surface brightness profile.

r_{cf}**:** r_c from single 2D β-model fit for $0.5 - 2$ keV. R_{500} *derived from XIS* $M_{500} - T$ *relation and cosmology.*

β**:** From β-model fit as above.

Maughan et al. (2008)

Chandra sample.

T**:** Spectroscopic from single T fit in the range $r < R_{500}$, $0.6 - 9$ keV, using an APEC model. Free Z and fixed n_H from DL90. R_{500} from the approach of Kravtsov et al. (2006) and the $Y_{\rm X} - M_{500}$ relation of Vikhlinin et al. (2006) assuming $h = 0.70$, $\Omega_m = 0.3$ and $\Omega_\Lambda = 0.7$.

$L_{\rm X,500}$**:** Derived for $r < R_{500}$, $0.6 - 9$ keV.

Mulchaey et al. (2003)

ROSAT sample.

T**:** Spectroscopic from single T fit in the range $r < R_{\rm extraction}$, $0.15 - 2.05$ keV using a MEKAL model. Fixed $Z = 0.3$ when it cannot be constrained, otherwise free, and fixed n_H from DL90. $R_{\rm extraction}$ from examination of surface brightness profiles. *Used those values calculated for a fixed Z due to large errors in Z.*

$L_{\rm X,500}$**:** Derived for $r < R_{\rm extraction}$, $0.15 - 2.05$ keV and converted to bolometric. *Converted to XIS cosmology. Rescaled to $r < R_{500}$ using best-fit β-model and R_{500} derived from XIS $M_{500} - T$ relation and cosmology. Hence, only those with r_c and β fits are used.*

r_{cf}**:** r_c from single 2D β-model fit where constrained, 1D otherwise, for $0.15 - 2.05$ keV. *R_{500} as stated above. Only those greater than the resolution of the detector are used.*

β**:** From β-model fit as above.

Osmond & Ponman (2004)

ROSAT sample.

T: Spectroscopic from single T fit in the range $r < R_{\rm extraction}$ using a MEKAL model (energy range unstated). Fixed $Z = 0.3$ when it cannot be constrained, otherwise free, and fixed n_H from DL90. Spectrum reliable when error on T less than fit T. $R_{\rm extraction}$ from where emission dropped to the background level. The 9 systems with cool cores were refitted with the central region removed, causing an average drop in T of 4% (well within the statistical error).

$L_{\rm X,500}$: Derived for $r < R_{500}$ (energy range unstated) assuming $h = 0.70$ and converted to bolometric. R_{500} from best-fit β-model. Used only those sources which had β-model fits, not assumed β-model values.

r_{cf}: r_c from single 2D β-model fit for $0.5 - 2$ keV. R_{500} *as stated above.*

β: From β-model fit as above.

Only those sources with measured T and more than 3 *optical galaxies were used in this research.*

Pacaud et al. (2007)

XMM-Newton sample.

T: Spectroscopic from single T fit in the range $r < R_{\rm extraction}$, $0.5 - 2$ keV using a APEC model. Fixed $Z = 0.3$ and fixed n_H from DL90. When Z was fixed at 0.1 or 0.6, T remained within 1σ of original fit.

$L_{\rm X,500}$: Derived $r < 0.5$ Mpc, $0.5 - 2$ keV, then scaled to $r < R_{500}$ and converted to bolometric. Used R_{500} from (Finoguenov et al. 2001b) $M_{500} - T$ relation scaled to ΛCDM assuming $h = 0.73$, $\Omega_m = 0.24$ and $\Omega_\Lambda = 0.76$.

Pratt et al. (2009)

XMM-Newton sample (Böhringer et al. 2007; Pratt et al. 2007).

T: Spectroscopic from single T fit in the range $r < R_{500}$, $0.3 - 10$ keV (ignoring instrument lines) using a MEKAL model. Free Z and fixed n_H from DL90

(except RXC J2014.82430). R_{500} from the $Y_{\rm X} - M_{500}$ relation of Arnaud et al. (2007) assuming $h = 0.70$, $\Omega_m = 0.3$ and $\Omega_\Lambda = 0.7$. Most clusters extracted out to $r > 0.8R_{500}$ at 3σ significance. Where required, extrapolation was performed using a power law with slope measured at large radius.

$L_{\rm X,500}$**:** Derived for $r < R_{500}$, $0.3 - 2$ keV and converted to bolometric ($0.01 -$ 100 keV).

CC: Definitions taken directly from Pratt et al. (2009).

Sun et al. (2009)

Chandra sample.

T**:** Emission weighted from integrated 3D T profile in the $0.15\ R_{500} < r < 1.6R_{500}$, 0.4 or $0.5 - 8$ keV (depending on detector chip) region in an annular cylinder with projected radii $0.15R_{500} < r < R_{500}$ along the line of sight. Used a MEKAL model with free Z and fixed n_H from a previous spectral fit to the inner region. R_{500} from 3D T and ρ profiles assuming $h = 0.73$, $\Omega_m = 0.24$ and $\Omega_\Lambda = 0.76$.

M_{500}**:** Derived from 1000 (Monte Carlo) simulated T and ρ profiles within $0.7 -$ 2 keV.

Only those sources with measured T are used in this research.

Vikhlinin et al. (2006)

Chandra sample with ROSAT support for field of view limited systems.

Same as Kotov & Vikhlinin (2006).

Table C.1: X-ray sources and their properties as used for the $M_{500}-T$ relation, including references for the original data.

Name	z	T[a] (keV)	$\log M_{500}$[b] (h^{-1} $M_\odot$)	$R_{\rm det}$[c]	Reference
3C 295	0.4600	$5.13^{+0.24}_{-0.24}$	$14.28^{+0.10}_{-0.13}$	. . .	Kotov & Vikhlinin (2006)
3C 442A	0.0263	$1.34^{+0.04}_{-0.04}$	$13.45^{+0.02}_{-0.05}$	1.07	Sun et al. (2009)
A1068	0.1375	$(5.04^{+0.12}_{-0.12})$	$(14.47^{+0.03}_{-0.03})$	1.02	Arnaud et al. (2005)
A1177	0.0316	$1.37^{+0.06}_{-0.07}$	$13.59^{+0.06}_{-0.06}$	0.76	Sun et al. (2009)
A1275	0.0637	$1.46^{+0.08}_{-0.07}$	$13.70^{+0.16}_{-0.12}$	0.90	Sun et al. (2009)
A133	0.0569	$4.14^{+0.07}_{-0.07}$	$14.36^{+0.05}_{-0.06}$	1.09	Vikhlinin et al. (2006)
A1413	0.1429	$7.38^{+0.11}_{-0.11}$	$14.74^{+0.04}_{-0.05}$	1.39	Vikhlinin et al. (2006)
A160	0.0447	$1.68^{+0.10}_{-0.10}$	$13.76^{+0.05}_{-0.07}$	1.02	Sun et al. (2009)
A1692	0.0848	$2.61^{+0.16}_{-0.24}$	$13.85^{+0.12}_{-0.10}$	1.17	Sun et al. (2009)
A1795	0.0622	$6.12^{+0.05}_{-0.05}$	$14.64^{+0.04}_{-0.04}$	1.21	Vikhlinin et al. (2006)
A1983	0.0442	$(2.35^{+0.10}_{-0.10})$	$(13.92^{+0.13}_{-0.18})$	0.57	Arnaud et al. (2005)
A1991	0.0587	$2.68^{+0.10}_{-0.08}$	$13.99^{+0.07}_{-0.07}$	1.09	Sun et al. (2009)
A2029	0.0779	$8.47^{+0.09}_{-0.09}$	$14.76^{+0.04}_{-0.04}$	1.65	Vikhlinin et al. (2006)
A2092	0.0669	$1.67^{+0.13}_{-0.12}$	$13.82^{+0.08}_{-0.09}$	0.91	Sun et al. (2009)
A2204	0.1523	$(8.92^{+0.24}_{-0.24})$	$(14.80^{+0.04}_{-0.04})$	0.90	Arnaud et al. (2005)
A2390	0.2302	$8.89^{+0.17}_{-0.17}$	$14.89^{+0.04}_{-0.05}$	1.77	Vikhlinin et al. (2006)
A2462	0.0733	$2.32^{+0.12}_{-0.10}$	$13.81^{+0.06}_{-0.06}$	1.01	Sun et al. (2009)
A2550	0.1220	$1.95^{+0.10}_{-0.10}$	$13.76^{+0.14}_{-0.06}$	1.20	Sun et al. (2009)
A2597	0.0852	$(3.96^{+0.10}_{-0.10})$	$(14.22^{+0.04}_{-0.05})$	0.83	Arnaud et al. (2005)
A2717	0.0498	$2.43^{+0.13}_{-0.12}$	$13.97^{+0.08}_{-0.06}$	1.09	Sun et al. (2009)
A383	0.1883	$4.81^{+0.12}_{-0.12}$	$14.34^{+0.04}_{-0.05}$	0.85	Vikhlinin et al. (2006)
A3880	0.0581	$2.49^{+0.14}_{-0.12}$	$14.04^{+0.13}_{-0.12}$	1.01	Sun et al. (2009)
A478	0.0881	$7.94^{+0.12}_{-0.12}$	$14.74^{+0.05}_{-0.06}$	1.50	Vikhlinin et al. (2006)
A907	0.1603	$5.96^{+0.08}_{-0.08}$	$14.52^{+0.03}_{-0.04}$	1.19	Vikhlinin et al. (2006)
AS1101	0.0564	$2.57^{+0.14}_{-0.11}$	$14.01^{+0.13}_{-0.12}$	0.85	Sun et al. (2009)
CL 0016+16	0.5400	$9.30^{+0.40}_{-0.30}$	$14.80^{+0.05}_{-0.05}$	0.84[d]	Kotov & Vikhlinin (2005)
CL 0024+17	0.3900	$3.60^{+0.20}_{-0.20}$	$14.10^{+0.02}_{-0.03}$	0.68[d]	Kotov & Vikhlinin (2005)
ESO 306-017	0.0358	$2.37^{+0.12}_{-0.14}$	$13.88^{+0.08}_{-0.06}$	0.71	Sun et al. (2009)
ESO 351-021	0.0571	$1.14^{+0.07}_{-0.04}$	$13.37^{+0.19}_{-0.14}$	1.18	Sun et al. (2009)
MACS J0159.8-0849	0.4050	$9.59^{+0.50}_{-0.50}$	$14.85^{+0.12}_{-0.17}$	. . .	Kotov & Vikhlinin (2006)
MACS J0329.6-0211	0.4500	$5.24^{+0.38}_{-0.38}$	$14.42^{+0.11}_{-0.14}$	. . .	Kotov & Vikhlinin (2006)
MACS J1423.8+2404	0.5390	$7.02^{+0.28}_{-0.28}$	$14.52^{+0.09}_{-0.11}$	. . .	Kotov & Vikhlinin (2006)
MACS J1621.3+3810	0.4610	$7.53^{+0.41}_{-0.41}$	$14.50^{+0.09}_{-0.11}$	. . .	Kotov & Vikhlinin (2006)
MKW 4	0.0200	$1.58^{+0.09}_{-0.09}$	$13.55^{+0.06}_{-0.07}$	0.91	Sun et al. (2009)
MKW 9	0.0382	$(2.62^{+0.26}_{-0.26})$	$(13.82^{+0.09}_{-0.11})$	0.60	Arnaud et al. (2005)
MS 0302.5+1717	0.4200	$4.10^{+0.80}_{-0.80}$	$14.18^{+0.11}_{-0.13}$	0.64[d]	Kotov & Vikhlinin (2005)
NGC 1550	0.0124	$1.06^{+0.02}_{-0.02}$	$13.37^{+0.04}_{-0.05}$	0.78	Sun et al. (2009)

Table C.1: Continued

Name	z	$T^{\rm a}$ (keV)	$\log M_{500}{}^{\rm b}$ (h^{-1} $M_\odot$)	$R_{\rm det}{}^{\rm c}$	Reference
NGC 4104	0.0282	$1.41^{+0.09}_{-0.06}$	$13.55^{+0.05}_{-0.05}$	0.79	Sun et al. (2009)
NGC 5098	0.0368	$0.96^{+0.04}_{-0.04}$	$13.16^{+0.06}_{-0.11}$	1.21	Sun et al. (2009)
NGC 6269	0.0348	$1.72^{+0.12}_{-0.11}$	$13.79^{+0.09}_{-0.12}$	0.79	Sun et al. (2009)
PKS 0745-191	0.1028	$(8.61^{+0.30}_{-0.30})$	$(14.74^{+0.04}_{-0.05})$	0.84	Arnaud et al. (2005)
RX J0505.3+2849	0.5100	$2.80^{+0.40}_{-0.30}$	$13.99^{+0.07}_{-0.07}$	1.54[d]	Kotov & Vikhlinin (2005)
RX J1022+3830	0.0543	$1.94^{+0.20}_{-0.14}$	$13.77^{+0.07}_{-0.08}$	0.97	Sun et al. (2009)
RX J1120.1+4318	0.6000	$5.00^{+0.30}_{-0.30}$	$14.52^{+0.10}_{-0.10}$	1.06[d]	Kotov & Vikhlinin (2005)
RX J1159+5531	0.0808	$1.84^{+0.14}_{-0.08}$	$13.78^{+0.14}_{-0.06}$	0.89	Sun et al. (2009)
RX J1334.3+5030	0.6200	$4.60^{+0.40}_{-0.30}$	$14.29^{+0.07}_{-0.05}$	1.03[d]	Kotov & Vikhlinin (2005)
RX J1347.5-1145	0.4510	$14.03^{+0.69}_{-0.69}$	$15.00^{+0.08}_{-0.10}$	. . .	Kotov & Vikhlinin (2006)
UGC 5088	0.0274	$0.81^{+0.03}_{-0.03}$	$13.03^{+0.09}_{-0.08}$	0.88	Sun et al. (2009)
UGC 842	0.0452	$1.54^{+0.14}_{-0.12}$	$13.61^{+0.17}_{-0.09}$	0.89	Sun et al. (2009)
W J1342.8+4028	0.7000	$3.10^{+0.30}_{-0.40}$	$13.96^{+0.05}_{-0.09}$	1.02[d]	Kotov & Vikhlinin (2005)

Note: Values shown include conversion to the XIS cosmology.

[a] Core corrected temperature ($r_* < r \lesssim R_{500}$, where r_* varies depending on the study the source originates from). Values in parentheses have been corrected for XMM-Newton-Chandra cross-correlation.

[b] Values in parentheses have been corrected for XMM-Newton-Chandra cross-correlation.

[c] Radius of detection or extraction of the surface brightness profile as a fraction of R_{500}. Shown as an indicator of the quality of the data.

[d] Only the radius of spectral extraction was available.

Table C.2: X-ray sources and their properties as used for the $L_{500} - T$ relation, including references for the original data.

Name	z	T[a] (keV)	$\log L_{\mathrm{X},500}$[b] (erg s^{-1})	R_{det}[c]	Reference
1E0657-56	0.2960	$11.70^{+0.40}_{-0.40}$	$45.880^{+0.003}_{-0.003}$	1.00[d]	Maughan et al. (2008)
A115	0.1970	$5.30^{+0.10}_{-0.10}$	$45.099^{+0.003}_{-0.003}$	1.00[d]	Maughan et al. (2008)
A1204	0.1710	$3.40^{+0.10}_{-0.10}$	$44.962^{+0.009}_{-0.010}$	1.00[d]	Maughan et al. (2008)
A1240	0.1590	$3.90^{+0.30}_{-0.30}$	$44.228^{+0.025}_{-0.026}$	1.00[d]	Maughan et al. (2008)
A1413	0.1430	$7.20^{+0.20}_{-0.20}$	$45.199^{+0.003}_{-0.003}$	0.90[d]	Maughan et al. (2008)
A1682	0.2340	$6.20^{+0.80}_{-0.80}$	$44.999^{+0.025}_{-0.027}$	0.70[d]	Maughan et al. (2008)
A1689	0.1830	$9.00^{+0.30}_{-0.30}$	$45.563^{+0.004}_{-0.004}$	1.00[d]	Maughan et al. (2008)
A1763	0.2230	$7.80^{+0.40}_{-0.40}$	$45.291^{+0.007}_{-0.007}$	0.95[d]	Maughan et al. (2008)
A1914	0.1710	$9.80^{+0.30}_{-0.30}$	$45.511^{+0.004}_{-0.004}$	0.81[d]	Maughan et al. (2008)
A1942	0.2240	$4.30^{+0.30}_{-0.20}$	$44.590^{+0.011}_{-0.011}$	1.00[d]	Maughan et al. (2008)
A2034	0.1130	$6.70^{+0.20}_{-0.20}$	$44.951^{+0.005}_{-0.005}$	0.81[d]	Maughan et al. (2008)
A2069	0.1160	$6.30^{+0.20}_{-0.20}$	$44.782^{+0.007}_{-0.007}$	0.74[d]	Maughan et al. (2008)
A209	0.2060	$7.10^{+0.40}_{-0.40}$	$45.244^{+0.007}_{-0.007}$	1.00[d]	Maughan et al. (2008)
A2111	0.2290	$6.80^{+0.90}_{-0.50}$	$45.029^{+0.016}_{-0.017}$	1.00[d]	Maughan et al. (2008)
A2125	0.2460	$2.60^{+0.10}_{-0.10}$	$44.230^{+0.025}_{-0.026}$	1.00[d]	Maughan et al. (2008)
A2163	0.2030	$15.50^{+0.90}_{-0.90}$	$45.942^{+0.006}_{-0.006}$	0.63[d]	Maughan et al. (2008)
A2204	0.1520	$6.80^{+0.30}_{-0.20}$	$45.578^{+0.005}_{-0.005}$	0.86[d]	Maughan et al. (2008)
A2218	0.1760	$6.80^{+0.30}_{-0.20}$	$45.116^{+0.003}_{-0.003}$	1.00[d]	Maughan et al. (2008)
A2259	0.1640	$5.60^{+0.40}_{-0.40}$	$44.927^{+0.010}_{-0.010}$	0.95[d]	Maughan et al. (2008)
A2261	0.2240	$7.20^{+0.30}_{-0.30}$	$45.424^{+0.005}_{-0.005}$	1.00[d]	Maughan et al. (2008)
A2294	0.1780	$9.00^{+0.80}_{-0.70}$	$45.163^{+0.012}_{-0.012}$	0.77[d]	Maughan et al. (2008)
A2409	0.1480	$5.50^{+0.30}_{-0.20}$	$45.023^{+0.008}_{-0.008}$	0.70[d]	Maughan et al. (2008)
A2631	0.2730	$6.50^{+0.50}_{-0.50}$	$45.253^{+0.014}_{-0.015}$	1.00[d]	Maughan et al. (2008)
A267	0.2300	$4.90^{+0.30}_{-0.30}$	$45.045^{+0.019}_{-0.020}$	1.00[d]	Maughan et al. (2008)
A383	0.1870	$3.90^{+0.10}_{-0.10}$	$44.957^{+0.009}_{-0.010}$	1.00[d]	Maughan et al. (2008)
A520	0.1990	$7.10^{+0.20}_{-0.20}$	$45.244^{+0.005}_{-0.005}$	1.00[d]	Maughan et al. (2008)
A521	0.2530	$5.10^{+0.20}_{-0.20}$	$45.143^{+0.009}_{-0.009}$	1.00[d]	Maughan et al. (2008)
A586	0.1710	$6.60^{+0.40}_{-0.30}$	$45.122^{+0.010}_{-0.010}$	0.81[d]	Maughan et al. (2008)
A665	0.1820	$7.50^{+0.20}_{-0.20}$	$45.321^{+0.004}_{-0.004}$	0.77[d]	Maughan et al. (2008)
A68	0.2550	$8.10^{+0.90}_{-0.80}$	$45.222^{+0.015}_{-0.016}$	1.00[d]	Maughan et al. (2008)
A697	0.2820	$9.00^{+0.60}_{-0.50}$	$45.562^{+0.007}_{-0.007}$	1.00[d]	Maughan et al. (2008)
A773	0.2170	$7.40^{+0.30}_{-0.30}$	$45.234^{+0.008}_{-0.008}$	1.00[d]	Maughan et al. (2008)
A781	0.2980	$5.60^{+0.60}_{-0.60}$	$45.034^{+0.020}_{-0.021}$	1.00[d]	Maughan et al. (2008)
A907	0.1530	$5.30^{+0.10}_{-0.10}$	$45.015^{+0.004}_{-0.004}$	1.00[d]	Maughan et al. (2008)
AS 1063	0.2520	$11.10^{+0.80}_{-0.90}$	$45.635^{+0.006}_{-0.006}$	1.00[d]	Maughan et al. (2008)
HCG 22	0.0091	$0.26^{+0.04}_{-0.04}$	$41.025^{+0.130}_{-0.130}$	0.16	Osmond & Ponman (2004)
HCG 42	0.0150	$0.75^{+0.04}_{-0.04}$	$42.065^{+0.020}_{-0.020}$	0.23	Osmond & Ponman (2004)

Table C.2: Continued

Name	z	T[a] (keV)	$\log L_{\rm X,500}$[b] (erg s^{-1})	$R_{\rm det}$[c]	Reference
HCG 48	0.0094	$2.56^{+2.40}_{-0.75}$	$(41.888^{+0.190}_{-0.130})$	(0.09)	Mulchaey et al. (2003)
HCG 57	0.0304	$1.14^{+1.93}_{-0.31}$	$(42.453^{+0.140}_{-0.270})$	(0.59)	Mulchaey et al. (2003)
HCG 62	0.0173	$1.43^{+0.08}_{-0.08}$	$43.195^{+0.040}_{-0.040}$	0.42	Osmond & Ponman (2004)
HCG 67	0.0270	$0.68^{+0.08}_{-0.08}$	$42.065^{+0.070}_{-0.070}$	0.48	Osmond & Ponman (2004)
HCG 68	0.0096	$0.58^{+0.06}_{-0.06}$	$41.765^{+0.040}_{-0.040}$	0.28	Osmond & Ponman (2004)
HCG 90	0.0084	$0.46^{+0.06}_{-0.06}$	$41.785^{+0.050}_{-0.050}$	0.27	Osmond & Ponman (2004)
HCG 97	0.0216	$0.82^{+0.06}_{-0.06}$	$42.425^{+0.050}_{-0.050}$	0.66	Osmond & Ponman (2004)
IC 1459	0.0061	$0.39^{+0.04}_{-0.04}$	$41.455^{+0.040}_{-0.040}$	0.35	Osmond & Ponman (2004)
IC 1860	0.0231	$1.26^{+0.14}_{-0.17}$	$(43.062^{+0.060}_{-0.060})$	(0.96)	Mulchaey et al. (2003)
IC 4296	0.0125	$0.85^{+0.33}_{-0.24}$	$(42.450^{+0.240}_{-0.350})$	(0.54)	Mulchaey et al. (2003)
MACS J0242.5-2132	0.3140	$4.80^{+0.20}_{-0.20}$	$45.437^{+0.011}_{-0.011}$	1.00[d]	Maughan et al. (2008)
MACS J0257.6-2209	0.3220	$7.40^{+0.60}_{-0.60}$	$45.213^{+0.013}_{-0.014}$	1.00[d]	Maughan et al. (2008)
MACS J1131.8-1955	0.3070	$8.30^{+0.70}_{-0.50}$	$45.470^{+0.010}_{-0.010}$	1.00[d]	Maughan et al. (2008)
MACS J2229.7-2755	0.3240	$4.20^{+0.30}_{-0.20}$	$45.291^{+0.013}_{-0.014}$	1.00[d]	Maughan et al. (2008)
MACS J2245.0+2637	0.3010	$5.10^{+0.30}_{-0.30}$	$45.218^{+0.013}_{-0.013}$	1.00[d]	Maughan et al. (2008)
MS 0906.5+1110	0.1800	$5.30^{+0.20}_{-0.20}$	$44.923^{+0.005}_{-0.005}$	0.95[d]	Maughan et al. (2008)
MS 1006.0+1202	0.2210	$5.90^{+0.40}_{-0.40}$	$44.862^{+0.012}_{-0.012}$	1.00[d]	Maughan et al. (2008)
MS 1008.1-1224	0.3010	$5.00^{+0.40}_{-0.40}$	$44.987^{+0.018}_{-0.018}$	1.00[d]	Maughan et al. (2008)
MS 1455.0+2232	0.2580	$4.50^{+0.10}_{-0.10}$	$45.305^{+0.004}_{-0.004}$	1.00[d]	Maughan et al. (2008)
NGC 1332	0.0054	$0.56^{+0.03}_{-0.03}$	$40.925^{+0.020}_{-0.020}$	0.07	Osmond & Ponman (2004)
NGC 1407	0.0061	$1.02^{+0.04}_{-0.04}$	$41.915^{+0.020}_{-0.020}$	0.18	Osmond & Ponman (2004)
NGC 1587	0.0129	$0.96^{+0.17}_{-0.17}$	$41.525^{+0.090}_{-0.090}$	0.14	Osmond & Ponman (2004)
NGC 2563	0.0171	$1.05^{+0.04}_{-0.04}$	$42.655^{+0.030}_{-0.030}$	0.63	Osmond & Ponman (2004)
NGC 3091	0.0128	$0.71^{+0.03}_{-0.03}$	$(41.949^{+0.030}_{-0.030})$	(0.36)	Helsdon & Ponman (2000)
NGC 315	0.0164	$0.85^{+0.07}_{-0.07}$	$(41.853^{+0.150}_{-0.150})$	(0.28)	Helsdon & Ponman (2000)
NGC 326	0.0477	$1.41^{+0.47}_{-0.24}$	$(42.982^{+0.120}_{-0.120})$	(1.93)	Mulchaey et al. (2003)
NGC 3557	0.0091	$0.24^{+0.02}_{-0.02}$	$42.105^{+0.040}_{-0.040}$	0.35	Osmond & Ponman (2004)
NGC 3607	0.0054	$0.35^{+0.04}_{-0.04}$	$41.495^{+0.050}_{-0.050}$	0.19	Osmond & Ponman (2004)
NGC 3647	0.0495	$2.21^{+0.98}_{-0.49}$	$(43.523^{+0.240}_{-0.110})$	(1.48)	Mulchaey et al. (2003)
NGC 3665	0.0087	$0.47^{+0.10}_{-0.10}$	$41.315^{+0.080}_{-0.080}$	0.19	Osmond & Ponman (2004)
NGC 383	0.0171	$1.51^{+0.06}_{-0.06}$	$43.095^{+0.010}_{-0.010}$	0.92	Osmond & Ponman (2004)
NGC 3923	0.0051	$0.52^{+0.03}_{-0.03}$	$41.065^{+0.020}_{-0.020}$	0.08	Osmond & Ponman (2004)
NGC 4065	0.0249	$1.22^{+0.08}_{-0.08}$	$42.775^{+0.050}_{-0.050}$	0.69	Osmond & Ponman (2004)
NGC 4073	0.0225	$1.52^{+0.09}_{-0.09}$	$43.475^{+0.020}_{-0.020}$	0.68	Osmond & Ponman (2004)
NGC 4104	0.0286	$1.48^{+0.24}_{-0.14}$	$(43.067^{+0.080}_{-0.060})$	(1.02)	Mulchaey et al. (2003)
NGC 4261	0.0096	$1.30^{+0.07}_{-0.07}$	$42.295^{+0.030}_{-0.030}$	0.17	Osmond & Ponman (2004)
NGC 4325	0.0252	$0.86^{+0.03}_{-0.03}$	$(43.064^{+0.030}_{-0.030})$	(0.73)	Helsdon & Ponman (2000)
NGC 4589	0.0068	$0.60^{+0.07}_{-0.07}$	$41.835^{+0.050}_{-0.050}$	0.28	Osmond & Ponman (2004)

Table C.2: Continued

Name	z	T[a] (keV)	$\log L_{\rm X,500}$[b] (erg s^{-1})	$R_{\rm det}$[c]	Reference
NGC 4636	0.0023	$0.84^{+0.02}_{-0.02}$	$41.705^{+0.020}_{-0.020}$	0.13	Osmond & Ponman (2004)
NGC 4697	0.0047	$0.32^{+0.03}_{-0.03}$	$41.295^{+0.020}_{-0.020}$	0.17	Osmond & Ponman (2004)
NGC 4761	0.0146	$1.04^{+0.02}_{-0.02}$	$(42.917^{+0.010}_{-0.010})$	(0.59)	Helsdon & Ponman (2000)
NGC 5044	0.0077	$1.21^{+0.02}_{-0.02}$	$43.085^{+0.010}_{-0.010}$	0.29	Osmond & Ponman (2004)
NGC 507	0.0170	$1.30^{+0.05}_{-0.05}$	$(43.207^{+0.030}_{-0.030})$	(1.28)	Mulchaey et al. (2003)
NGC 5129	0.0254	$0.84^{+0.06}_{-0.06}$	$42.595^{+0.040}_{-0.040}$	0.30	Osmond & Ponman (2004)
NGC 5171	0.0232	$1.25^{+0.40}_{-0.25}$	$(42.791^{+0.170}_{-0.230})$	(0.75)	Mulchaey et al. (2003)
NGC 524	0.0083	$0.56^{+0.08}_{-0.08}$	$(41.227^{+0.110}_{-0.110})$	(0.32)	Helsdon & Ponman (2000)
NGC 533	0.0178	$1.08^{+0.05}_{-0.05}$	$42.725^{+0.030}_{-0.030}$	0.64	Osmond & Ponman (2004)
NGC 5353	0.0081	$0.68^{+0.05}_{-0.05}$	$(41.578^{+0.030}_{-0.030})$	(0.25)	Helsdon & Ponman (2000)
NGC 5846	0.0070	$0.73^{+0.02}_{-0.02}$	$42.035^{+0.020}_{-0.020}$	0.20	Osmond & Ponman (2004)
NGC 6109	0.0312	$2.43^{+1.28}_{-0.53}$	$(43.448^{+0.140}_{-0.100})$	(1.25)	Mulchaey et al. (2003)
NGC 6269	0.0353	$1.92^{+0.44}_{-0.26}$	$(43.421^{+0.090}_{-0.070})$	(1.47)	Mulchaey et al. (2003)
NGC 6329	0.0274	$1.03^{+0.09}_{-0.10}$	$(42.728^{+0.090}_{-0.080})$	(1.12)	Mulchaey et al. (2003)
NGC 6338	0.0283	$1.69^{+0.16}_{-0.16}$	$(43.689^{+0.010}_{-0.010})$	(0.76)	Helsdon & Ponman (2000)
NGC 7176	0.0085	$0.53^{+0.11}_{-0.11}$	$(41.215^{+0.110}_{-0.110})$	(0.43)	Helsdon & Ponman (2000)
NGC 720	0.0054	$0.52^{+0.03}_{-0.03}$	$41.425^{+0.020}_{-0.020}$	0.16	Osmond & Ponman (2004)
NGC 741	0.0185	$1.21^{+0.09}_{-0.09}$	$42.495^{+0.060}_{-0.060}$	0.62	Osmond & Ponman (2004)
NGC 7619	0.0116	$1.05^{+0.05}_{-0.05}$	$(42.433^{+0.050}_{-0.040})$	(0.68)	Mulchaey et al. (2003)
NGC 7777	0.0229	$0.62^{+0.15}_{-0.15}$	$(41.716^{+0.200}_{-0.200})$	(0.51)	Helsdon & Ponman (2000)
RXJ 0232.2-4420	0.2840	$7.90^{+0.40}_{-0.40}$	$45.501^{+0.008}_{-0.008}$	1.00[d]	Maughan et al. (2008)
RX J0439+0520	0.2080	$3.80^{+0.20}_{-0.20}$	$44.923^{+0.020}_{-0.021}$	1.00[d]	Maughan et al. (2008)
RX J0439.0+0715	0.2300	$5.60^{+0.30}_{-0.30}$	$45.195^{+0.008}_{-0.008}$	1.00[d]	Maughan et al. (2008)
RX J1234.2+0947	0.2290	$6.70^{+2.30}_{-1.00}$	$44.825^{+0.019}_{-0.020}$	0.95[d]	Maughan et al. (2008)
RX J1504-0248	0.2150	$6.80^{+0.20}_{-0.20}$	$45.785^{+0.004}_{-0.004}$	1.00[d]	Maughan et al. (2008)
RX J1720.1+2638	0.1640	$6.10^{+0.10}_{-0.10}$	$45.295^{+0.004}_{-0.004}$	1.00[d]	Maughan et al. (2008)
RX J2011.3-5725	0.2790	$3.80^{+0.20}_{-0.20}$	$44.806^{+0.020}_{-0.021}$	1.00[d]	Maughan et al. (2008)
RX J2129.6+0005	0.2350	$5.60^{+0.30}_{-0.30}$	$45.305^{+0.011}_{-0.011}$	1.00[d]	Maughan et al. (2008)
RX J2247+0337	0.2000	$2.20^{+0.50}_{-0.40}$	$43.476^{+0.125}_{-0.176}$	1.00[d]	Maughan et al. (2008)
RXC J0003.8+0203	0.0924	$3.85^{+0.09}_{-0.09}$	$44.271^{+0.002}_{-0.002}$	0.84	Pratt et al. (2009)
RXC J0006.0-3443	0.1147	$5.03^{+0.19}_{-0.19}$	$44.613^{+0.005}_{-0.005}$	0.93	Pratt et al. (2009)
RXC J0020.7-2542	0.1410	$5.69^{+0.11}_{-0.11}$	$44.812^{+0.003}_{-0.003}$	1.07	Pratt et al. (2009)
RXC J0049.4-2931	0.1084	$3.09^{+0.10}_{-0.10}$	$44.247^{+0.005}_{-0.005}$	0.93	Pratt et al. (2009)
RXC J0145.0-5300	0.1168	$5.53^{+0.13}_{-0.13}$	$44.696^{+0.003}_{-0.003}$	1.23	Pratt et al. (2009)
RXC J0211.4-4017	0.1008	$2.07^{+0.07}_{-0.00}$	$43.905^{+0.005}_{-0.005}$	1.33	Pratt et al. (2009)
RXC J0225.1-2928	0.0604	$2.47^{+0.15}_{-0.06}$	$43.704^{+0.008}_{-0.009}$	0.91	Pratt et al. (2009)
RXC J0345.7-4112	0.0603	$2.19^{+0.04}_{-0.04}$	$43.883^{+0.006}_{-0.006}$	0.89	Pratt et al. (2009)
RXC J0547.6-3152	0.1483	$6.02^{+0.11}_{-0.11}$	$44.951^{+0.002}_{-0.002}$	1.32	Pratt et al. (2009)

Table C.2: Continued

Name	z	T^{a} (keV)	$\log L_{\mathrm{X},500}{}^{\mathrm{b}}$ (erg s^{-1})	$R_{\mathrm{det}}{}^{\mathrm{c}}$	Reference
RXC J0605.8-3518	0.1392	$4.56^{+0.05}_{-0.05}$	$44.977^{+0.002}_{-0.002}$	1.17	Pratt et al. (2009)
RXC J0616.8-4748	0.1164	$4.22^{+0.10}_{-0.10}$	$44.374^{+0.004}_{-0.004}$	1.12	Pratt et al. (2009)
RXC J0645.4-5413	0.1644	$6.95^{+0.13}_{-0.13}$	$45.274^{+0.002}_{-0.002}$	1.28	Pratt et al. (2009)
RXC J0821.8+0112	0.0822	$2.68^{+0.09}_{-0.09}$	$43.883^{+0.006}_{-0.006}$	0.93	Pratt et al. (2009)
RXC J0958.3-1103	0.1669	$5.34^{+0.21}_{-0.21}$	$45.061^{+0.006}_{-0.006}$	0.78	Pratt et al. (2009)
RXC J1044.5-0704	0.1342	$3.41^{+0.03}_{-0.03}$	$44.868^{+0.001}_{-0.001}$	1.09	Pratt et al. (2009)
RXC J1141.4-1216	0.1195	$3.31^{+0.03}_{-0.03}$	$44.571^{+0.001}_{-0.001}$	1.25	Pratt et al. (2009)
RXC J1236.7-3354	0.0796	$2.70^{+0.05}_{-0.05}$	$44.009^{+0.004}_{-0.004}$	0.99	Pratt et al. (2009)
RXC J1302.8-0230	0.0847	$2.97^{+0.06}_{-0.07}$	$44.136^{+0.003}_{-0.003}$	1.22	Pratt et al. (2009)
RXC J1311.4-0120	0.1832	$8.91^{+0.08}_{-0.08}$	$45.555^{+0.001}_{-0.001}$	1.31	Pratt et al. (2009)
RXC J1516.3+0005	0.1181	$4.51^{+0.06}_{-0.06}$	$44.612^{+0.002}_{-0.002}$	1.29	Pratt et al. (2009)
RXC J1516.5-0056	0.1198	$3.55^{+0.07}_{-0.07}$	$44.361^{+0.004}_{-0.004}$	1.37	Pratt et al. (2009)
RXC J2014.8-2430	0.1538	$4.78^{+0.05}_{-0.05}$	$45.321^{+0.001}_{-0.001}$	1.09	Pratt et al. (2009)
RXC J2023.0-2056	0.0564	$2.71^{+0.09}_{-0.09}$	$43.781^{+0.007}_{-0.007}$	0.86	Pratt et al. (2009)
RXC J2048.1-1750	0.1475	$4.65^{+0.13}_{-0.07}$	$44.708^{+0.003}_{-0.003}$	1.48	Pratt et al. (2009)
RXC J2129.8-5048	0.0796	$3.81^{+0.15}_{-0.15}$	$44.161^{+0.006}_{-0.006}$	0.93	Pratt et al. (2009)
RXC J2149.1-3041	0.1184	$3.26^{+0.04}_{-0.04}$	$44.549^{+0.002}_{-0.002}$	1.26	Pratt et al. (2009)
RXC J2157.4-0747	0.0579	$2.46^{+0.08}_{-0.08}$	$43.649^{+0.010}_{-0.010}$	0.97	Pratt et al. (2009)
RXC J2217.7-3543	0.1486	$4.86^{+0.09}_{-0.09}$	$44.785^{+0.002}_{-0.002}$	1.33	Pratt et al. (2009)
RXC J2218.6-3853	0.1411	$5.84^{+0.11}_{-0.11}$	$44.972^{+0.003}_{-0.003}$	1.04	Pratt et al. (2009)
RXC J2234.5-3744	0.1510	$7.78^{+0.15}_{-0.15}$	$45.280^{+0.002}_{-0.003}$	1.15	Pratt et al. (2009)
RXC J2319.6-7313	0.0984	$2.22^{+0.03}_{-0.03}$	$44.298^{+0.004}_{-0.004}$	1.11	Pratt et al. (2009)
XLSS J022023.5-025027	0.2300	$1.30^{+0.30}_{-0.10}$	$42.981^{+0.087}_{-0.176}$	0.46	Pacaud et al. (2007)
XLSS J022205.5-043247	0.3200	$1.60^{+1.10}_{-0.30}$	$43.229^{+0.051}_{-0.058}$	1.20	Pacaud et al. (2007)
XLSS J022348.1-025131	0.1700	$1.20^{+0.10}_{-0.10}$	$42.914^{+0.038}_{-0.041}$	1.15	Pacaud et al. (2007)
XLSS J022356.5-030558	0.3000	$1.30^{+0.20}_{-0.20}$	$43.201^{+0.054}_{-0.062}$	0.65	Pacaud et al. (2007)
XLSS J022402.0-050525	0.3200	$2.00^{+0.70}_{-0.40}$	$43.139^{+0.062}_{-0.073}$	0.65	Pacaud et al. (2007)
XLSS J022433.8-041405	0.2600	$1.30^{+0.20}_{-0.10}$	$43.105^{+0.035}_{-0.038}$	2.88	Pacaud et al. (2007)
XLSS J022456.2-050802	0.0800	$0.68^{+0.04}_{-0.02}$	$42.071^{+0.038}_{-0.041}$	0.37	Pacaud et al. (2007)
XLSS J022520.8-034805	0.3000	$1.30^{+0.70}_{-0.20}$	$43.104^{+0.067}_{-0.046}$	0.62	Pacaud et al. (2007)
XLSS J022524.7-044039	0.2600	$2.00^{+0.20}_{-0.20}$	$43.689^{+0.018}_{-0.019}$	1.12	Pacaud et al. (2007)
XLSS J022530.6-041420	0.1400	$1.34^{+0.14}_{-0.06}$	$43.409^{+0.018}_{-0.018}$	0.86	Pacaud et al. (2007)
XLSS J022540.6-031121	0.1400	$3.50^{+0.60}_{-0.50}$	$43.997^{+0.023}_{-0.029}$	0.52	Pacaud et al. (2007)
XLSS J022559.5-024935	0.2800	$1.20^{+0.10}_{-0.10}$	$42.980^{+0.087}_{-0.051}$	0.61	Pacaud et al. (2007)
XLSS J022609.9-045805	0.0500	$0.64^{+0.06}_{-0.04}$	$42.072^{+0.038}_{-0.041}$	1.51	Pacaud et al. (2007)
XLSS J022616.3-023957	0.0600	$0.63^{+0.03}_{-0.03}$	$42.428^{+0.033}_{-0.036}$	0.40	Pacaud et al. (2007)
XLSS J022726.0-043216	0.3100	$1.00^{+0.10}_{-0.10}$	$43.139^{+0.032}_{-0.035}$	5.43	Pacaud et al. (2007)
XLSS J022739.9-045127	0.2900	$1.70^{+0.10}_{-0.10}$	$43.818^{+0.014}_{-0.014}$	1.53	Pacaud et al. (2007)

Table C.2: Continued

Name	z	T[a] (keV)	$\log L_{\mathrm{X},500}$[b] (erg s^{-1})	R_{det}[c]	Reference
XLSS J022803.4-045103	0.2900	$2.80^{+0.60}_{-0.50}$	$43.707^{+0.035}_{-0.028}$	0.80	Pacaud et al. (2007)
Zw 3146	0.2910	$6.40^{+0.10}_{-0.10}$	$45.648^{+0.004}_{-0.004}$	1.00[d]	Maughan et al. (2008)
ZwCl J1953	0.3200	$7.30^{+0.70}_{-0.70}$	$45.194^{+0.011}_{-0.011}$	1.00[d]	Maughan et al. (2008)

Note: Values shown include conversion to the XIS cosmology.

[a] Full spectral temperature ($r < R_s$, where R_s is the spectral extraction radius of the source).

[b] Derived luminosity in the radius $r < R_{500}$. Values in parentheses have been extrapolated to R_{500} in this research using their best-fit surface brightness profiles and masses from the $M_{500} - T$ relation.

[c] Radius of detection or extraction of the surface brightness profile as a fraction of R_{500}. Shown as an indicator of the quality of the data. Values in parentheses have been estimated using masses from the $M - T$ relation.

[d] Only the radius of centroid shift fitting was available.

Table C.3: X-ray sources and their properties as used for the $r_{cf} - T$ and $\beta - T$ relations, including references for the original data.

Name	z	T[a] (keV)	$\log r_{cf}$[b]	β	$R_{\rm det}$[c]	Reference[e]
3C 129	0.0223	$5.60^{+0.70}_{-0.60}$	$(-0.710^{+0.090}_{-0.094})$	$0.601^{+0.260}_{-0.131}$	(0.99)	Chen et al. (2007); (1)
A119	0.0440	$5.80^{+0.60}_{-0.60}$	$(-0.512^{+0.086}_{-0.093})$	$0.675^{+0.026}_{-0.023}$	(1.65)	Chen et al. (2007); (2)
A133	0.0569	$3.80^{+2.00}_{-0.90}$	$(-1.454^{+0.193}_{-0.147})$	$0.530^{+0.004}_{-0.004}$	(1.19)	Chen et al. (2007); (1)
A1413	0.1427	$7.32^{+0.26}_{-0.24}$	$(-0.976^{+0.078}_{-0.078})$	$0.660^{+0.017}_{-0.015}$	(1.42)	Chen et al. (2007); (3)
A1644	0.0474	$4.70^{+0.90}_{-0.70}$	$(-0.685^{+0.104}_{-0.108})$	$0.579^{+0.111}_{-0.074}$	(1.28)	Chen et al. (2007); (4)
A1650	0.0845	$5.60^{+0.60}_{-0.60}$	$(-0.738^{+0.087}_{-0.094})$	$0.704^{+0.131}_{-0.081}$	(2.06)	Chen et al. (2007); (2)
A1651	0.0860	$6.30^{+0.50}_{-0.50}$	$(-0.959^{+0.082}_{-0.086})$	$0.643^{+0.014}_{-0.013}$	(1.24)	Chen et al. (2007); (2)
A1689	0.1840	$9.23^{+0.28}_{-0.28}$	$(-1.055^{+0.077}_{-0.078})$	$0.690^{+0.011}_{-0.011}$	(1.28)	Chen et al. (2007); (3)
A1736	0.0461	$3.50^{+0.40}_{-0.40}$	$(-0.519^{+0.088}_{-0.096})$	$0.542^{+0.147}_{-0.092}$	(2.00)	Chen et al. (2007); (2)
A1775	0.0757	$3.69^{+0.20}_{-0.11}$	$(-0.679^{+0.079}_{-0.078})$	$0.673^{+0.026}_{-0.023}$	(1.63)	Chen et al. (2007); (3)
A1795	0.0616	$6.00^{+0.30}_{-0.30}$	$(-1.320^{+0.079}_{-0.081})$	$0.596^{+0.003}_{-0.002}$	(1.31)	Chen et al. (2007); (2)
A1914	0.1712	$10.53^{+0.51}_{-0.50}$	$(-0.939^{+0.079}_{-0.080})$	$0.751^{+0.018}_{-0.017}$	(1.18)	Chen et al. (2007); (3)
A2029	0.0767	$8.70^{+0.30}_{-0.30}$	$(-1.374^{+0.078}_{-0.078})$	$0.582^{+0.004}_{-0.005}$	(1.41)	Chen et al. (2007); (2)
A2052	0.0348	$3.03^{+0.04}_{-0.04}$	$(-1.507^{+0.077}_{-0.077})$	$0.526^{+0.005}_{-0.005}$	(0.99)	Chen et al. (2007); (3)
A2142	0.0899	$8.80^{+0.60}_{-0.60}$	$(-1.106^{+0.081}_{-0.084})$	$0.591^{+0.006}_{-0.006}$	(1.58)	Chen et al. (2007); (2)
A2151w	0.0369	$2.40^{+0.06}_{-0.06}$	$(-1.175^{+0.077}_{-0.078})$	$0.564^{+0.014}_{-0.013}$	(1.43)	Chen et al. (2007); (3)
A2163	0.2010	$13.29^{+0.64}_{-0.64}$	$(-0.628^{+0.079}_{-0.080})$	$0.796^{+0.030}_{-0.028}$	(1.43)	Chen et al. (2007); (3)
A2204	0.1523	$7.21^{+0.25}_{-0.25}$	$(-1.393^{+0.078}_{-0.079})$	$0.597^{+0.008}_{-0.007}$	(1.99)	Chen et al. (2007); (3)
A2244	0.0970	$7.10^{+5.00}_{-2.20}$	$(-1.141^{+0.238}_{-0.187})$	$0.607^{+0.016}_{-0.015}$	(1.53)	Chen et al. (2007); (4)
A2255	0.0800	$6.87^{+0.20}_{-0.20}$	$(-0.464^{+0.077}_{-0.078})$	$0.797^{+0.035}_{-0.030}$	(1.87)	Chen et al. (2007); (3)
A2256	0.0601	$7.50^{+0.40}_{-0.40}$	$(-0.497^{+0.079}_{-0.081})$	$0.914^{+0.054}_{-0.047}$	(1.68)	Chen et al. (2007); (2)
A2319	0.0564	$9.20^{+0.70}_{-0.70}$	$(-0.861^{+0.082}_{-0.086})$	$0.591^{+0.013}_{-0.012}$	(1.73)	Chen et al. (2007); (2)
A2589	0.0416	$3.70^{+2.20}_{-1.10}$	$(-1.035^{+0.211}_{-0.179})$	$0.596^{+0.013}_{-0.012}$	(1.14)	Chen et al. (2007); (1)
A2597	0.0852	$3.60^{+0.20}_{-0.20}$	$(-1.327^{+0.079}_{-0.081})$	$0.633^{+0.008}_{-0.008}$	(1.18)	Chen et al. (2007); (2)
A2657	0.0404	$3.70^{+0.30}_{-0.30}$	$(-1.032^{+0.083}_{-0.087})$	$0.556^{+0.008}_{-0.007}$	(1.19)	Chen et al. (2007); (2)
A2877	0.0241	$3.50^{+2.20}_{-1.10}$	$(-0.825^{+0.219}_{-0.189})$	$0.566^{+0.029}_{-0.025}$	(0.84)	Chen et al. (2007); (4)
A3112	0.0750	$4.70^{+0.40}_{-0.40}$	$(-1.364^{+0.083}_{-0.088})$	$0.576^{+0.006}_{-0.006}$	(1.54)	Chen et al. (2007); (2)
A3158	0.0590	$5.77^{+0.10}_{-0.05}$	$(-0.776^{+0.077}_{-0.077})$	$0.661^{+0.025}_{-0.022}$	(1.21)	Chen et al. (2007); (3)
A3266	0.0594	$7.70^{+0.80}_{-0.80}$	$(-0.521^{+0.086}_{-0.093})$	$0.796^{+0.020}_{-0.019}$	(1.60)	Chen et al. (2007); (2)
A3391	0.0531	$5.70^{+0.70}_{-0.70}$	$(-0.835^{+0.089}_{-0.099})$	$0.579^{+0.026}_{-0.024}$	(1.24)	Chen et al. (2007); (2)
A3395n	0.0498	$4.80^{+0.40}_{-0.40}$	$(-0.338^{+0.083}_{-0.087})$	$0.981^{+0.619}_{-0.244}$	(0.94)	Chen et al. (2007); (2)
A3395s	0.0498	$4.80^{+0.40}_{-0.40}$	$(-0.384^{+0.083}_{-0.087})$	$0.964^{+0.275}_{-0.167}$	(0.99)	Chen et al. (2007); (2)
A3526	0.0103	$3.68^{+0.06}_{-0.06}$	$(-1.551^{+0.077}_{-0.077})$	$0.495^{+0.011}_{-0.010}$	(1.25)	Chen et al. (2007); (4)
A3528n	0.0540	$3.40^{+1.66}_{-0.64}$	$(-0.834^{+0.183}_{-0.124})$	$0.621^{+0.034}_{-0.030}$	(1.25)	Chen et al. (2007); (4)
A3528s	0.0551	$3.15^{+0.89}_{-0.59}$	$(-1.064^{+0.128}_{-0.123})$	$0.463^{+0.013}_{-0.012}$	(1.17)	Chen et al. (2007); (4)
A3530	0.0544	$3.89^{+0.27}_{-0.25}$	$(-0.491^{+0.081}_{-0.083})$	$0.773^{+0.114}_{-0.085}$	(1.19)	Chen et al. (2007); (4)
A3532	0.0539	$4.58^{+0.19}_{-0.17}$	$(-0.704^{+0.078}_{-0.079})$	$0.653^{+0.034}_{-0.029}$	(1.16)	Chen et al. (2007); (4)

Table C.3: Continued

Name	z	T[a] (keV)	$\log r_{cf}$[b]	β	$R_{\rm det}$[c]	Reference[e]
A3558	0.0480	$5.50^{+0.30}_{-0.30}$	$(-0.849^{+0.079}_{-0.081})$	$0.580^{+0.006}_{-0.006}$	(1.34)	Chen et al. (2007); (2)
A3562	0.0499	$5.16^{+0.16}_{-0.16}$	$(-1.191^{+0.078}_{-0.078})$	$0.472^{+0.006}_{-0.006}$	(1.32)	Chen et al. (2007); (3)
A3571	0.0397	$6.90^{+0.30}_{-0.30}$	$(-0.996^{+0.078}_{-0.080})$	$0.613^{+0.010}_{-0.010}$	(1.31)	Chen et al. (2007); (2)
A3581	0.0214	$1.83^{+0.04}_{-0.04}$	$(-1.406^{+0.077}_{-0.077})$	$0.543^{+0.024}_{-0.022}$	(0.72)	Chen et al. (2007); (4)
A3627	0.0163	$6.02^{+0.08}_{-0.08}$	$(-0.756^{+0.077}_{-0.077})$	$0.555^{+0.056}_{-0.044}$	(1.29)	Chen et al. (2007); (3)
A3667	0.0560	$7.00^{+0.60}_{-0.60}$	$(-0.805^{+0.083}_{-0.088})$	$0.541^{+0.008}_{-0.008}$	(1.58)	Chen et al. (2007); (2)
A3921	0.0936	$5.73^{+0.24}_{-0.23}$	$(-0.673^{+0.078}_{-0.079})$	$0.762^{+0.036}_{-0.030}$	(1.57)	Chen et al. (2007); (3)
A399	0.0715	$7.40^{+0.70}_{-0.70}$	$(-0.605^{+0.085}_{-0.090})$	$0.713^{+0.137}_{-0.095}$	(1.76)	Chen et al. (2007); (2)
A401	0.0748	$8.30^{+0.50}_{-0.50}$	$(-0.894^{+0.080}_{-0.082})$	$0.613^{+0.010}_{-0.010}$	(1.98)	Chen et al. (2007); (2)
A4038	0.0283	$3.15^{+0.03}_{-0.03}$	$(-1.311^{+0.077}_{-0.077})$	$0.541^{+0.009}_{-0.008}$	(1.14)	Chen et al. (2007); (3)
A4059	0.0460	$4.10^{+0.30}_{-0.30}$	$(-1.180^{+0.081}_{-0.085})$	$0.582^{+0.010}_{-0.010}$	(1.28)	Chen et al. (2007); (2)
A478	0.0900	$7.10^{+0.40}_{-0.40}$	$(-1.249^{+0.080}_{-0.082})$	$0.613^{+0.004}_{-0.004}$	(1.79)	Chen et al. (2007); (2)
A548e	0.0410	$3.10^{+0.10}_{-0.10}$	$(-0.994^{+0.078}_{-0.078})$	$0.480^{+0.013}_{-0.013}$	(1.82)	Chen et al. (2007); (3)
A576	0.0381	$4.02^{+0.07}_{-0.07}$	$(-0.533^{+0.077}_{-0.077})$	$0.825^{+0.432}_{-0.185}$	(1.73)	Chen et al. (2007); (3)
A644	0.0704	$7.10^{+0.60}_{-0.60}$	$(-0.943^{+0.083}_{-0.087})$	$0.700^{+0.011}_{-0.011}$	(2.27)	Chen et al. (2007); (2)
A754	0.0528	$9.00^{+0.50}_{-0.50}$	$(-0.933^{+0.079}_{-0.081})$	$0.698^{+0.027}_{-0.024}$	(0.93)	Chen et al. (2007); (2)
A85	0.0556	$6.10^{+0.20}_{-0.20}$	$(-1.305^{+0.078}_{-0.078})$	$0.532^{+0.004}_{-0.004}$	(1.29)	Chen et al. (2007); (2)
C11054-1145	0.7000	$3.50^{+0.80}_{-0.60}$	$(-0.394^{+0.114}_{-0.117})$	$0.700^{+0.000}_{-0.000}$	(0.56)[d]	Johnson et al. (2006)
C11216-1201	0.7900	$4.80^{+0.80}_{-0.60}$	$(-0.652^{+0.099}_{-0.099})$	$0.680^{+0.060}_{-0.050}$	(0.42)[d]	Johnson et al. (2006)
C11216-South	0.7000	$5.00^{+0.60}_{-0.60}$	$(-0.988^{+0.089}_{-0.098})$	$0.480^{+0.100}_{-0.060}$	(0.46)[d]	Johnson et al. (2006)
CI J0046.3+8530	0.6200	$4.40^{+0.50}_{-0.40}$	$(-0.739^{+0.088}_{-0.089})$	$0.600^{+0.080}_{-0.030}$	(0.80)	Maughan et al. (2006)
CI J0152.7-1357N	0.8300	$5.60^{+1.00}_{-0.80}$	$(-0.483^{+0.101}_{-0.106})$	$0.730^{+0.130}_{-0.060}$	(0.49)	Maughan et al. (2006)
CI J0152.7-1357S	0.8300	$4.80^{+1.10}_{-1.00}$	$(-0.753^{+0.114}_{-0.133})$	$0.660^{+0.080}_{-0.060}$	(0.40)	Maughan et al. (2006)
CI J1008.7+5342	0.8700	$3.60^{+0.80}_{-0.60}$	$(-0.535^{+0.112}_{-0.115})$	$0.680^{+0.100}_{-0.080}$	(1.30)	Maughan et al. (2006)
CI J1103.6+3555	0.7800	$6.00^{+0.90}_{-0.70}$	$(-0.759^{+0.095}_{-0.097})$	$0.580^{+0.030}_{-0.030}$	(0.87)	Maughan et al. (2006)
CI J1113.1-2615	0.7300	$4.70^{+0.90}_{-0.70}$	$(-0.838^{+0.104}_{-0.108})$	$0.670^{+0.030}_{-0.050}$	(0.49)	Maughan et al. (2006)
CI J1226.9+3332	0.8900	$10.60^{+1.10}_{-1.10}$	$(-0.961^{+0.086}_{-0.093})$	$0.660^{+0.020}_{-0.020}$	(0.75)	Maughan et al. (2006)
CI J1342.9+2828	0.7100	$3.70^{+0.50}_{-0.40}$	$(-0.577^{+0.092}_{-0.094})$	$0.700^{+0.060}_{-0.050}$	(1.21)	Maughan et al. (2006)
CI J1415.1+3612	1.0300	$5.70^{+1.20}_{-0.70}$	$(-0.860^{+0.109}_{-0.099})$	$0.670^{+0.060}_{-0.040}$	(0.71)	Maughan et al. (2006)
CI J1429.0+4241	0.9200	$6.20^{+1.50}_{-1.00}$	$(-0.894^{+0.117}_{-0.113})$	$0.670^{+0.060}_{-0.060}$	(0.51)	Maughan et al. (2006)
CI J1559.1+6353	0.8500	$4.10^{+1.40}_{-1.00}$	$(-0.975^{+0.144}_{-0.150})$	$0.590^{+0.060}_{-0.110}$	(0.89)	Maughan et al. (2006)
CL 0016+16	0.5400	$8.90^{+0.30}_{-0.30}$	$-0.648^{+0.021}_{-0.023}$	$0.760^{+0.010}_{-0.010}$	0.84[d]	Kotov & Vikhlinin (2005)
CL 0024+17	0.3900	$3.50^{+0.10}_{-0.10}$	$-0.920^{+0.039}_{-0.027}$	$0.590^{+0.020}_{-0.010}$	0.68[d]	Kotov & Vikhlinin (2005)
EXO 422	0.0390	$2.90^{+0.90}_{-0.60}$	$(-0.899^{+0.135}_{-0.132})$	$0.722^{+0.104}_{-0.098}$	(1.17)	Chen et al. (2007); (1)
HCG 22	0.0091	$0.26^{+0.04}_{-0.04}$	$-2.335^{+0.658}_{-3.665}$	$0.440^{+0.200}_{-0.200}$	0.16	Osmond & Ponman (2004)
HCG 42	0.0150	$0.75^{+0.04}_{-0.04}$	$-2.010^{+0.062}_{-0.072}$	$0.560^{+0.020}_{-0.020}$	0.23	Osmond & Ponman (2004)
HCG 48	0.0094	$2.56^{+2.40}_{-0.75}$	$(-1.897^{+0.292}_{-0.180})$	$0.560^{+0.010}_{-0.010}$	(0.09)	Mulchaey et al. (2003)
HCG 57	0.0304	$1.14^{+1.93}_{-0.31}$	$(-1.736^{+0.439}_{-0.310})$	$0.340^{+0.020}_{-0.020}$	(0.59)	Mulchaey et al. (2003)

Table C.3: Continued

Name	z	T[a] (keV)	$\log r_{cf}$[b]	β	$R_{\rm det}$[c]	Reference[e]
HCG 67	0.0270	$0.68^{+0.08}_{-0.08}$	$-1.984^{+0.124}_{-0.173}$	$0.540^{+0.070}_{-0.070}$	0.48	Osmond & Ponman (2004)
HCG 68	0.0096	$0.58^{+0.06}_{-0.06}$	$-1.857^{+0.197}_{-0.371}$	$0.450^{+0.050}_{-0.050}$	0.28	Osmond & Ponman (2004)
HCG 94	0.0417	$3.45^{+0.30}_{-0.30}$	$(-1.156^{+0.083}_{-0.088})$	$0.514^{+0.007}_{-0.006}$	(1.70)	Chen et al. (2007); (4)
Hydra-A	0.0538	$3.80^{+0.20}_{-0.20}$	$(-1.410^{+0.079}_{-0.081})$	$0.573^{+0.003}_{-0.003}$	(1.29)	Chen et al. (2007); (2)
IC 1459	0.0057	$0.63^{+0.06}_{-0.06}$	$(-2.483^{+0.087}_{-0.095})$	$0.660^{+0.010}_{-0.010}$	(0.23)	Mulchaey et al. (2003)
IC 1860	0.0231	$1.26^{+0.14}_{-0.17}$	$(-1.932^{+0.089}_{-0.105})$	$0.460^{+0.010}_{-0.010}$	(0.96)	Mulchaey et al. (2003)
IC 4296	0.0125	$0.85^{+0.33}_{-0.24}$	$(-0.905^{+0.216}_{-0.287})$	$0.350^{+0.030}_{-0.030}$	(0.54)	Mulchaey et al. (2003)
M49	0.0044	$0.95^{+0.02}_{-0.02}$	$(-1.804^{+0.077}_{-0.077})$	$0.592^{+0.007}_{-0.007}$	(0.42)	Chen et al. (2007); (4)
MKW 3S	0.0450	$3.50^{+0.20}_{-0.20}$	$(-1.273^{+0.080}_{-0.082})$	$0.581^{+0.008}_{-0.007}$	(1.12)	Chen et al. (2007); (2)
MKW 8	0.0270	$3.29^{+0.23}_{-0.22}$	$(-1.060^{+0.081}_{-0.084})$	$0.511^{+0.098}_{-0.059}$	(1.56)	Chen et al. (2007); (4)
MS 0302.5+1717	0.4200	$4.50^{+0.50}_{-0.40}$	$-0.818^{+0.078}_{-0.085}$	$0.650^{+0.060}_{-0.050}$	0.64[d]	Kotov & Vikhlinin (2005)
NGC 1332	0.0054	$0.56^{+0.03}_{-0.03}$	$-3.778^{+0.517}_{-2.222}$	$0.520^{+0.010}_{-0.010}$	0.07	Osmond & Ponman (2004)
NGC 1407	0.0061	$1.02^{+0.04}_{-0.04}$	$-3.853^{+0.459}_{-2.147}$	$0.460^{+0.010}_{-0.010}$	0.18	Osmond & Ponman (2004)
NGC 1550	0.0123	$1.43^{+0.04}_{-0.03}$	$(-1.243^{+0.077}_{-0.077})$	$0.554^{+0.049}_{-0.037}$	(0.90)	Chen et al. (2007); (4)
NGC 1587	0.0122	$0.92^{+0.15}_{-0.15}$	$(-1.943^{+0.259}_{-0.722})$	$0.470^{+0.060}_{-0.060}$	(0.20)	Helsdon & Ponman (2000)
NGC 2563	0.0171	$1.05^{+0.04}_{-0.04}$	$-2.425^{+0.024}_{-0.025}$	$0.370^{+0.010}_{-0.010}$	0.63	Osmond & Ponman (2004)
NGC 3091	0.0128	$0.71^{+0.03}_{-0.03}$	$(-1.615^{+0.078}_{-0.078})$	$0.600^{+0.020}_{-0.020}$	(0.36)	Helsdon & Ponman (2000)
NGC 315	0.0164	$0.81^{+0.19}_{-0.12}$	$(-1.956^{+0.119}_{-0.117})$	$0.770^{+0.020}_{-0.020}$	(0.24)	Mulchaey et al. (2003)
NGC 326	0.0477	$1.41^{+0.47}_{-0.24}$	$(-0.693^{+0.144}_{-0.123})$	$0.360^{+0.010}_{-0.010}$	(1.93)	Mulchaey et al. (2003)
NGC 3557	0.0091	$0.24^{+0.02}_{-0.02}$	$-2.378^{+0.074}_{-0.089}$	$0.520^{+0.030}_{-0.030}$	0.35	Osmond & Ponman (2004)
NGC 3607	0.0037	$0.41^{+0.04}_{-0.04}$	$(-1.119^{+0.119}_{-0.153})$	$0.520^{+0.180}_{-0.180}$	(0.15)	Helsdon & Ponman (2000)
NGC 3647	0.0495	$2.21^{+0.98}_{-0.49}$	$(-0.684^{+0.174}_{-0.143})$	$0.400^{+0.010}_{-0.010}$	(1.48)	Mulchaey et al. (2003)
NGC 3665	0.0069	$0.45^{+0.11}_{-0.11}$	$(-2.438^{+0.288}_{-1.202})$	$0.490^{+0.030}_{-0.030}$	(0.17)	Helsdon & Ponman (2000)
NGC 383	0.0173	$1.53^{+0.07}_{-0.07}$	$(-1.810^{+0.093}_{-0.104})$	$0.362^{+0.003}_{-0.003}$	(1.08)	Helsdon & Ponman (2000)
NGC 3923	0.0051	$0.52^{+0.03}_{-0.03}$	$-2.803^{+0.040}_{-0.043}$	$0.550^{+0.010}_{-0.010}$	0.08	Osmond & Ponman (2004)
NGC 4065	0.0235	$1.22^{+0.08}_{-0.08}$	$(-0.647^{+0.094}_{-0.107})$	$0.470^{+0.040}_{-0.040}$	(0.83)	Helsdon & Ponman (2000)
NGC 4073	0.0204	$1.59^{+0.06}_{-0.06}$	$(-2.382^{+0.085}_{-0.092})$	$0.431^{+0.002}_{-0.002}$	(0.75)	Helsdon & Ponman (2000)
NGC 4104	0.0286	$1.48^{+0.24}_{-0.14}$	$(-1.243^{+0.101}_{-0.098})$	$0.380^{+0.010}_{-0.010}$	(1.02)	Mulchaey et al. (2003)
NGC 4261	0.0071	$0.94^{+0.03}_{-0.03}$	$(-3.713^{+0.305}_{-2.287})$	$0.446^{+0.004}_{-0.004}$	(0.29)	Helsdon & Ponman (2000)
NGC 4325	0.0252	$0.86^{+0.03}_{-0.03}$	$(-1.643^{+0.084}_{-0.090})$	$0.600^{+0.010}_{-0.010}$	(0.73)	Helsdon & Ponman (2000)
NGC 4636	0.0044	$0.72^{+0.01}_{-0.01}$	$(-2.429^{+0.079}_{-0.081})$	$0.476^{+0.003}_{-0.003}$	(0.30)	Helsdon & Ponman (2000)
NGC 4697	0.0047	$0.32^{+0.03}_{-0.03}$	$-2.408^{+0.091}_{-0.115}$	$0.460^{+0.020}_{-0.020}$	0.17	Osmond & Ponman (2004)
NGC 4761	0.0146	$1.04^{+0.02}_{-0.02}$	$(-1.949^{+0.081}_{-0.083})$	$0.502^{+0.005}_{-0.005}$	(0.59)	Helsdon & Ponman (2000)
NGC 499	0.0147	$0.72^{+0.03}_{-0.02}$	$(-1.373^{+0.078}_{-0.078})$	$0.722^{+0.034}_{-0.030}$	(0.55)	Chen et al. (2007); (4)
NGC 5044	0.0082	$1.05^{+0.01}_{-0.02}$	$(-1.569^{+0.077}_{-0.077})$	$0.520^{+0.010}_{-0.010}$	(0.76)	Mulchaey et al. (2003)
NGC 507	0.0170	$1.30^{+0.05}_{-0.05}$	$(-1.306^{+0.078}_{-0.080})$	$0.460^{+0.010}_{-0.010}$	(1.28)	Mulchaey et al. (2003)
NGC 5129	0.0232	$0.81^{+0.06}_{-0.06}$	$(-1.993^{+0.160}_{-0.245})$	$0.440^{+0.020}_{-0.020}$	(0.61)	Helsdon & Ponman (2000)
NGC 5171	0.0232	$1.25^{+0.40}_{-0.25}$	$(-1.823^{+0.188}_{-0.275})$	$0.320^{+0.020}_{-0.020}$	(0.75)	Mulchaey et al. (2003)

Table C.3: Continued

Name	z	T[a] (keV)	$\log r_{cf}$[b]	β	$R_{\rm det}$[c]	Reference[e]
NGC 524	0.0083	$0.56^{+0.08}_{-0.08}$	$(-3.524^{+0.305}_{-2.476})$	$0.450^{+0.010}_{-0.010}$	(0.32)	Helsdon & Ponman (2000)
NGC 533	0.0181	$1.06^{+0.04}_{-0.04}$	$(-1.736^{+0.082}_{-0.085})$	$0.482^{+0.005}_{-0.005}$	(0.93)	Helsdon & Ponman (2000)
NGC 5353	0.0081	$0.68^{+0.05}_{-0.05}$	$(-1.449^{+0.090}_{-0.100})$	$0.580^{+0.030}_{-0.030}$	(0.25)	Helsdon & Ponman (2000)
NGC 5846	0.0061	$0.82^{+0.01}_{-0.01}$	$(-1.990^{+0.077}_{-0.077})$	$0.599^{+0.016}_{-0.015}$	(0.36)	Chen et al. (2007); (4)
NGC 6109	0.0312	$2.43^{+1.28}_{-0.53}$	$(-0.906^{+0.200}_{-0.166})$	$0.430^{+0.020}_{-0.020}$	(1.25)	Mulchaey et al. (2003)
NGC 6269	0.0353	$1.92^{+0.44}_{-0.26}$	$(-0.903^{+0.119}_{-0.116})$	$0.480^{+0.020}_{-0.020}$	(1.47)	Mulchaey et al. (2003)
NGC 6329	0.0274	$1.03^{+0.09}_{-0.10}$	$(-1.146^{+0.096}_{-0.112})$	$0.450^{+0.010}_{-0.010}$	(1.12)	Mulchaey et al. (2003)
NGC 6338	0.0283	$1.69^{+0.16}_{-0.16}$	$(-2.479^{+0.099}_{-0.115})$	$0.428^{+0.004}_{-0.004}$	(0.76)	Helsdon & Ponman (2000)
NGC 720	0.0054	$0.52^{+0.03}_{-0.03}$	$-2.541^{+0.070}_{-0.083}$	$0.470^{+0.010}_{-0.010}$	0.16	Osmond & Ponman (2004)
NGC 741	0.0185	$1.21^{+0.09}_{-0.09}$	$-2.431^{+0.033}_{-0.035}$	$0.440^{+0.010}_{-0.010}$	0.62	Osmond & Ponman (2004)
NGC 7619	0.0116	$1.05^{+0.05}_{-0.05}$	$(-1.819^{+0.082}_{-0.085})$	$0.440^{+0.010}_{-0.010}$	(0.68)	Mulchaey et al. (2003)
NGC 7777	0.0229	$0.62^{+0.15}_{-0.15}$	$(-3.112^{+0.305}_{-2.888})$	$0.350^{+0.020}_{-0.020}$	(0.51)	Helsdon & Ponman (2000)
Ophiuchus	0.0280	$10.26^{+0.32}_{-0.32}$	$(-0.908^{+0.078}_{-0.078})$	$0.747^{+0.035}_{-0.032}$	(1.02)	Chen et al. (2007); (4)
PKS0745	0.1028	$7.21^{+0.11}_{-0.11}$	$(-1.388^{+0.077}_{-0.077})$	$0.608^{+0.006}_{-0.006}$	(1.41)	Chen et al. (2007); (3)
RX J0505.3+2849	0.5100	$2.50^{+0.40}_{-0.50}$	$-0.601^{+0.110}_{-0.121}$	$0.690^{+0.140}_{-0.100}$	1.54[d]	Kotov & Vikhlinin (2005)
RX J1120.1+4318	0.6000	$4.90^{+0.30}_{-0.30}$	$-0.664^{+0.042}_{-0.048}$	$0.810^{+0.040}_{-0.040}$	1.06[d]	Kotov & Vikhlinin (2005)
RX J1334.3+5030	0.6200	$4.60^{+0.40}_{-0.30}$	$-0.786^{+0.037}_{-0.038}$	$0.610^{+0.020}_{-0.020}$	1.03[d]	Kotov & Vikhlinin (2005)
S1101	0.0580	$3.00^{+1.20}_{-0.70}$	$(-1.311^{+0.160}_{-0.145})$	$0.639^{+0.006}_{-0.007}$	(1.46)	Chen et al. (2007); (1)
Triangulum	0.0510	$9.50^{+0.70}_{-0.70}$	$(-0.880^{+0.082}_{-0.085})$	$0.610^{+0.010}_{-0.010}$	(1.20)	Chen et al. (2007); (2)
W J1342.8+4028	0.7000	$3.50^{+0.30}_{-0.30}$	$-1.020^{+0.107}_{-0.095}$	$0.490^{+0.030}_{-0.020}$	1.02[d]	Kotov & Vikhlinin (2005)

Note: Values shown include conversion to the XIS cosmology.

[a] Full spectral temperature ($r < R_s$, where R_s is the spectral extraction radius of the source).

[b] Core radius as a fraction of R_{500}. Values in parentheses have been estimated using masses from the $M_{500} - T$ relation. Errors have been propagated from the r_c fit and the scatter in $M_{500} - T$ relation.

[c] Radius of detection or extraction of the surface brightness profile as a fraction of R_{500}. Shown as an indicator of the quality of the data. Values in parentheses have been estimated using masses from $M_{500} - T$ relation.

[d] Only the radius of spectral extraction was available.

[e] Temperature data was from the following references: (1) Edge & Stewart (1991); (2) Markevitch et al. (1998); (3) White (2000); (4) Reiprich & Böhringer (2002).

APPENDIX D

XIS Data Structures

X-ray observations are affected by a large number of factors relating to both the observatory and the universe it is observing. To organise these factors into meaningful groups, XIS uses IDL structures. Some of these are contained within object classes. The following classes are defined in XIS:

- options (for general set-up and cosmology),
- relation (for determining cluster properties),
- telescope (for mirror-related effects),
- detector (for CCD related effects),
- pointing (for observing direction and time).

Three additional structures are defined to represent the X-ray source types used in the simulator, and are detailed in their respective sections in Chapter 2. Pointing objects can be formed into an array for a batch of simulations to be performed. Each pointing object contains the following information:

- angular coordinates of the pointing centre (arcsec),
- exposure time (ks),
- energy band (keV),
- galactic neutral hydrogen column density n_H (cm^2),
- results file name.

Default settings include simulating the $0.5 - 2$ keV energy band and a column density $n_H = 10^{20}$ cm^{-2}. This n_H represents a fairly low level of galactic absorption and is used for all simulations in this research.

The following three tables give the source properties for clusters, galaxies and AGN that are stored during the simulation process. The final table lists the variables that have been amended to the previous tables by the conclusion of the source identification process.

Table D.1: The properties stored for each simulated cluster and what other properties they are derived from.

Property	Unit	Derived from / value	Description
name			Optional label.
RA	arcsec	N-body simulation	Angular co-ordinate.
Dec	arcsec	N-body simulation	As above but for the other position axis.
x	pixels	RA, observatory	Pixel co-ordinate on the final image. Based on 1 being the centre of the image origin pixel, that with the highest RA and lowest Dec.
y	pixels	Dec, observatory	As above but for the other position axis.
D	h^{-1} Mpc	N-body simulation	Comoving distance to the cluster.
z		D	Redshift.
M_{200}	h^{-1} $M_\odot$	N-body simulation	Mass within R_{200}.
M_{500}	h^{-1} $M_\odot$	M_{200}, z	Mass within R_{500}.
T	keV	M_{500}, z	Isothermal temperature.
Z	$Z_\odot$	0.3	Metallicity.
L_{500}	erg s^{-1}	T, evolution model (z, cosmology)	Bolometric X-ray luminosity within R_{500}.
S_{500}	erg cm^{-2} s^{-1}	L_{500}, z, cosmology	Bolometric X-ray flux within R_{500}.
S_{SX}	counts s^{-1}	S_{500}, observatory	$0.5-2$ keV X-ray flux within R_{500}.
R_{200}	kpc	M_{200}, z, cosmology	Radius where the overdensity $\Delta = 200$ times the critical density of the Universe.
	arcsec	R_{200}, z, cosmology	
	pixels	R_{200}, observatory	
R_{500}	kpc	M_{500}, z, cosmology	As above but for $\Delta = 500$.
	arcsec	R_{500}, z, cosmology	
	pixels	R_{500}, observatory	
r_{cf}		T, z[a]	Surface brightness profile core radius as a fraction of R_{500}.
r_c	kpc	r_{cf}, R_{500}	Surface brightness profile core radius.
	arcsec	r_{cf}, R_{500}, z, cosmology	
	pixels	R_{cf}, observatory	
β		T	Surface brightness profile slope.
ϵ			1 minus the surface brightness profile minor to major axis ratio.
rotation			Rotation of the surface brightness profile as a fraction of a full circle.

[a] Only a factor when core cores are modelled.

Table D.2: The properties stored for each simulated galaxy and what other properties they are derived from.

Property	Unit	Derived from / value	Description
name			Optional label.
RA	arcsec	Cluster-weighted random distribution	Angular co-ordinate.
Dec	arcsec	Cluster-weighted random distribution	As above but for the other position axis.
x	pixels	RA, observatory	Pixel co-ordinate on the final image. Based on 1 being the centre of the image origin pixel, that with the highest RA and lowest Dec.
y	pixels	Dec, observatory	As above but for the other position axis.
D	h^{-1} Mpc	z	Comoving distance to the galaxy.
z		$N(S_{\rm SX}, z)$ distribution	Redshift.
T	keV	0.6	Isothermal temperature.
Z	$Z_\odot$	0.8	Metallicity.
Γ		2.1	Power law spectral index.
$L_{\rm SX}$	erg s^{-1}	$S_{\rm SX}$, z, cosmology	$0.5-2$ keV X-ray luminosity.
$S_{\rm SX}$	erg cm^{-2} s^{-1} counts s^{-1}	$N(S_{\rm SX}, z)$ distribution $S_{\rm SX}$, observatory	$0.5-2$ keV X-ray flux.

Table D.3: The properties stored for each simulated AGN and what other properties they are derived from.

Property	Unit	Derived from / value	Description
name			Optional label.
RA	arcsec	Cluster-weighted random distribution	Angular co-ordinate.
Dec	arcsec	Cluster-weighted random distribution	As above but for the other position axis.
x	pixels	RA, observatory	Pixel co-ordinate on the final image. Based on 1 being the centre of the image origin pixel, that with the highest RA and lowest Dec.
y	pixels	Dec, observatory	As above but for the other position axis.
D	h^{-1} Mpc	z	Comoving distance to the galaxy.
z		$N(S_{\rm SX}, z, n_H)$ distribution	Redshift.
Γ		Normal distribution	Power law spectral index.
n_H	cm^{-2}	$N(S_{\rm SX}, z, n_H)$	Neutral hydrogen column density of obscuration component.
$L_{\rm SX}$	erg s^{-1}	$S_{\rm X}$, z, cosmology	$0.5-2$ keV X-ray luminosity.
$S_{\rm SX}$	erg cm^{-2} s^{-1} counts s^{-1}	$N(S_{\rm SX}, z, n_H)$ distribution $S_{\rm X}$, observatory	$0.5-2$ keV X-ray flux.

Table D.4: The additional properties stored for each simulated source.

Property	Unit	Derived from / value	Description
$r_{\rm ext}$	pixels	Wavelet decomposition	Extraction radius.
$r_{\rm con}$	pixels	Wavelet decomposition	Contamination radius.
$\mathcal{M}$	counts	Wavelet decomposition	Sum of the amplitude of the candidate within the scale radius on each scale.
$n_{\rm fit}$		$r_{\rm ext}$, $r_{\rm con}$ of other sources	Number of pixels in fitting region.
$N_{\rm cts}$	counts	$r_{\rm ext}$, $r_{\rm con}$ of other sources	Number of counts in fitting region.
$N_{\rm con}$		$r_{\rm ext}$, $r_{\rm con}$ of other sources	Number of contaminating sources.
fit x	pixels	exposed β-model fit	Fit of pixel co-ordinate relative to the final image. Based on 1 being the centre of the image origin pixel, that with the highest RA and lowest Dec.
	pixels	exposed PSF model fit	
fit y	pixels	exposed β-model fit	As above but for the other position axis.
	pixels	exposed PSF model fit	
fit S	counts/s	exposed β-model fit, N, exposure time	Fit of flux within $r_{\rm ext}$.
	counts/s	exposed PSF model fit	
fit r_c	pixels	exposed β-model fit,	Fit of core radius.
σ_{r_c}	pixels	exposed β-model fit	1σ upper and lower errors on the fitted core radius.
fit β		exposed β-model fit	Fit of β.
σ_β		exposed β-model fit	1σ upper and lower errors on the fitted core radius.
C_β		exposed β-model fit	Cash statistic for the best-fit exposed β-model.
$C_{\rm PSF}$		exposed PSF model fit	Cash statistic for the best-fit exposed PSF model.
$C_{\rm Bkg}$		Bkg	Cash statistic for the background model.
$B_{\rm s}$		Marginal likelihood calculations	Existence statistic. Bayes factor of best-fit model to exposed background model.
$B_{\rm x}$		Marginal likelihood calculations	Extent statistic. Bayes factor of exposed β-model to exposed PSF model.

APPENDIX E

Simulated Images

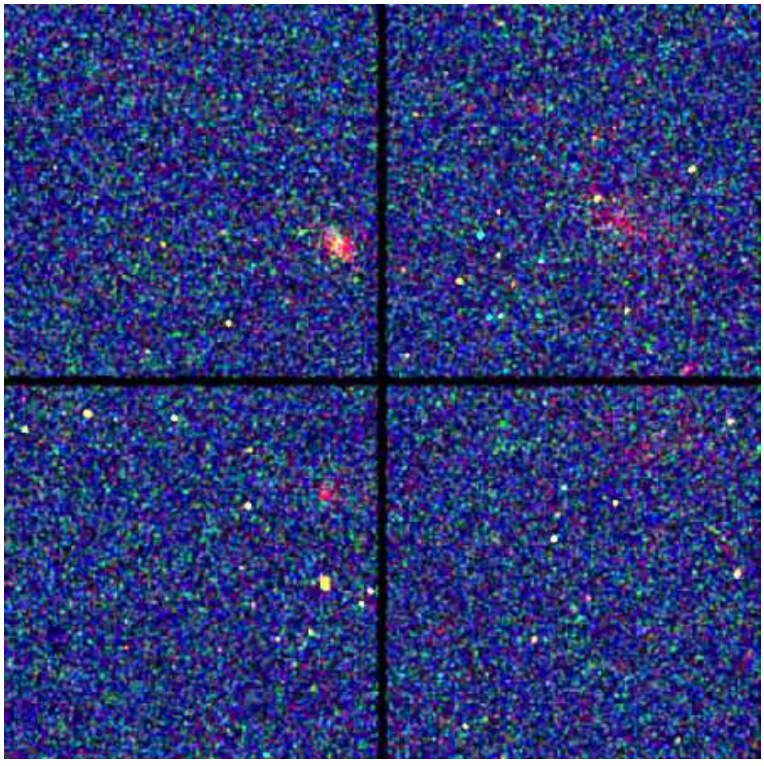

Figure E.1: Simulated 100 ks, true-colour image of Chandra ACIS-I, re-binned by a pixel length of 4:1. It is a composite of the soft, medium and hard band simulated images at the same coordinates as Figure 2.36, Section 2.4.9. Gaussian smoothing of 2 pixel radius has been applied to improve clarity.

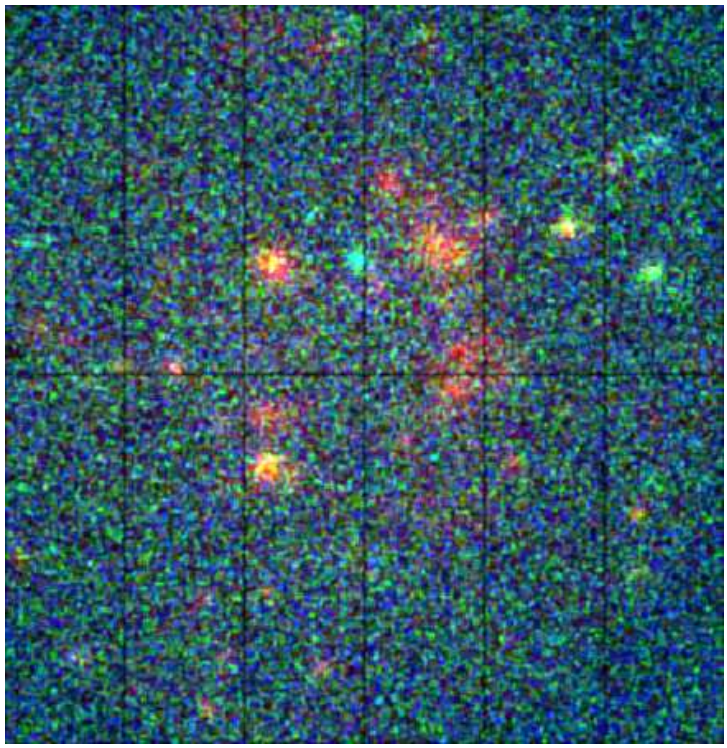

Figure E.2: Simulated 100 ks, true-colour image of XMM-Newton EPIC pn. Image processing is the same as for Figure E.1, but without any re-binning.

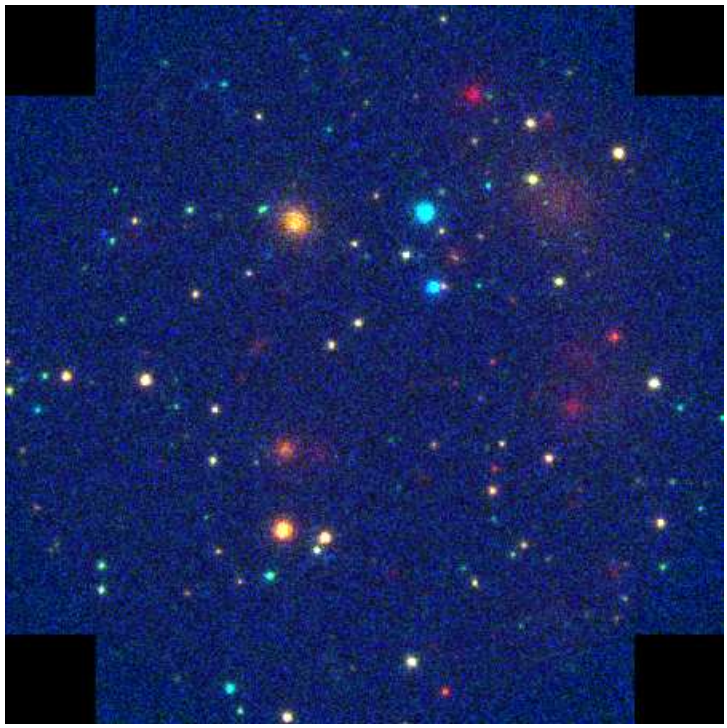

Figure E.3: Simulated 100 ks, true-colour image of IXO-10. Image processing is the same as for Figure E.2.

APPENDIX F

Selection Function

r_c[a]	log S[b]														
	- 2.50	- 2.25	- 2.00	- 1.75	- 1.50	- 1.25	- 1.00	- 0.75	- 0.50	- 0.25	0.00	0.25	0.50	0.75	1.00
	$\beta = 0.3$														
0.1000	0.00	0.03	0.02	0.03	0.02	0.04	0.02	0.03	0.02	0.01	0.09	0.21	0.56	0.92	1.00
0.1585	0.00	0.00	0.03	0.01	0.04	0.04	0.04	0.17	0.30	0.71	0.99	1.00	1.00	1.00	1.00
0.2512	0.00	0.02	0.02	0.04	0.10	0.26	0.56	0.94	1.00	1.00	1.00	1.00	1.00	1.00	1.00
0.3981	0.00	0.02	0.10	0.20	0.64	0.95	1.00	1.00	1.00	1.00	1.00	1.00	1.00	1.00	1.00
0.6310	0.00	0.09	0.45	0.80	0.94	1.00	1.00	1.00	1.00	1.00	1.00	1.00	1.00	1.00	1.00
1.0000	0.00	0.08	0.65	0.87	0.90	0.98	1.00	1.00	1.00	1.00	1.00	1.00	1.00	1.00	1.00
1.5849	0.00	0.02	0.27	0.87	0.94	0.97	0.95	1.00	1.00	1.00	0.99	1.00	1.00	1.00	1.00
2.5119	0.00	0.00	0.03	0.12	0.61	0.83	0.92	0.96	0.95	1.00	1.00	0.99	1.00	1.00	1.00
3.9811	0.00	0.01	0.01	0.09	0.43	0.72	0.94	0.92	0.97	0.96	0.98	0.96	1.00	1.00	1.00
6.3096	0.01	0.02	0.00	0.02	0.03	0.20	0.68	0.90	0.97	0.99	1.00	0.99	0.99	1.00	1.00
10.000	0.00	0.00	0.00	0.00	0.01	0.04	0.11	0.55	0.78	0.93	0.98	0.97	0.99	1.00	1.00
15.849	0.00	0.00	0.00	0.00	0.00	0.00	0.02	0.02	0.21	0.58	0.80	0.89	0.95	1.00	0.99
25.119	0.00	0.00	0.00	0.00	0.00	0.00	0.00	0.00	0.00	0.00	0.22	0.59	0.78	0.89	0.96
39.811	0.00	0.00	0.00	0.00	0.00	0.00	0.00	0.00	0.00	0.01	0.01	0.00	0.02	0.09	0.35
63.096	0.00	0.00	0.00	0.00	0.00	0.00	0.00	0.00	0.00	0.00	0.00	0.01	0.02	0.00	0.02
100.00	0.00	0.00	0.00	0.00	0.00	0.00	0.00	0.00	0.00	0.00	0.00	0.00	0.00	0.00	0.01

r_c[a]	log S[b]														
	- 2.50	- 2.25	- 2.00	- 1.75	- 1.50	- 1.25	- 1.00	- 0.75	- 0.50	- 0.25	0.00	0.25	0.50	0.75	1.00
							$\beta = 0.4$								
0.1000	0.00	0.05	0.07	0.04	0.07	0.07	0.10	0.03	0.03	0.01	0.02	0.04	0.16	0.40	0.78
0.1585	0.00	0.08	0.05	0.06	0.08	0.10	0.07	0.12	0.08	0.19	0.59	0.91	1.00	1.00	1.00
0.2512	0.00	0.00	0.08	0.08	0.06	0.12	0.28	0.49	0.87	1.00	1.00	1.00	1.00	1.00	1.00
0.3981	0.00	0.05	0.10	0.12	0.34	0.58	0.96	1.00	1.00	1.00	1.00	1.00	1.00	1.00	1.00
0.6310	0.00	0.07	0.17	0.47	0.87	0.99	0.99	1.00	1.00	1.00	1.00	1.00	1.00	1.00	1.00
1.0000	0.01	0.04	0.30	0.69	0.92	0.94	0.98	1.00	1.00	1.00	1.00	1.00	1.00	1.00	1.00
1.5849	0.00	0.03	0.27	0.71	0.92	0.96	0.96	1.00	1.00	1.00	1.00	1.00	1.00	1.00	1.00
2.5119	0.00	0.01	0.08	0.46	0.88	0.89	0.98	1.00	0.99	1.00	1.00	1.00	1.00	1.00	1.00
3.9811	0.00	0.02	0.08	0.39	0.80	0.94	0.93	0.99	1.00	1.00	1.00	1.00	0.97	1.00	1.00
6.3096	0.00	0.00	0.04	0.11	0.45	0.83	0.86	0.96	0.99	1.00	1.00	1.00	0.98	1.00	1.00
10.000	0.00	0.01	0.00	0.01	0.11	0.45	0.83	0.90	0.92	0.98	0.98	1.00	0.98	1.00	1.00
15.849	0.00	0.00	0.00	0.00	0.00	0.02	0.22	0.60	0.82	0.93	0.97	0.97	0.98	1.00	1.00
25.119	0.00	0.01	0.00	0.00	0.00	0.00	0.04	0.07	0.37	0.68	0.75	0.93	0.93	1.00	1.00
39.811	0.00	0.00	0.00	0.00	0.00	0.00	0.00	0.00	0.01	0.03	0.03	0.27	0.49	0.68	0.93
63.096	0.00	0.00	0.00	0.00	0.00	0.00	0.00	0.00	0.00	0.01	0.00	0.00	0.03	0.12	0.34
100.00	0.00	0.00	0.00	0.00	0.00	0.00	0.00	0.00	0.00	0.00	0.00	0.00	0.01	0.03	0.04
							$\beta = 0.5$								
0.1000	0.01	0.06	0.08	0.12	0.17	0.05	0.06	0.03	0.04	0.02	0.04	0.02	0.02	0.11	0.21
0.1585	0.00	0.07	0.09	0.04	0.10	0.06	0.02	0.04	0.01	0.05	0.07	0.29	0.65	0.91	1.00
0.2512	0.00	0.07	0.12	0.17	0.11	0.10	0.13	0.14	0.36	0.55	0.92	1.00	1.00	1.00	1.00
0.3981	0.00	0.11	0.15	0.15	0.18	0.14	0.51	0.82	1.00	1.00	1.00	1.00	1.00	1.00	1.00
0.6310	0.01	0.10	0.16	0.32	0.49	0.81	0.99	1.00	1.00	1.00	1.00	1.00	1.00	1.00	1.00
1.0000	0.01	0.13	0.27	0.48	0.85	0.98	0.98	0.98	1.00	1.00	1.00	1.00	1.00	1.00	1.00
1.5849	0.01	0.07	0.25	0.52	0.88	0.94	1.00	0.97	0.98	1.00	1.00	1.00	1.00	1.00	1.00
2.5119	0.01	0.07	0.17	0.49	0.88	0.94	1.00	0.99	0.99	1.00	1.00	1.00	1.00	1.00	1.00
3.9811	0.00	0.03	0.07	0.23	0.70	0.90	0.98	1.00	0.98	1.00	1.00	1.00	1.00	1.00	1.00
6.3096	0.00	0.02	0.05	0.21	0.86	0.93	0.99	0.98	1.00	1.00	1.00	1.00	1.00	1.00	1.00
10.000	0.00	0.03	0.00	0.06	0.51	0.81	0.96	0.95	0.99	0.94	1.00	1.00	1.00	1.00	1.00
15.849	0.00	0.00	0.03	0.01	0.06	0.31	0.78	0.93	0.87	0.97	0.98	1.00	1.00	1.00	1.00
25.119	0.00	0.00	0.00	0.00	0.01	0.04	0.25	0.60	0.77	0.91	0.98	0.99	1.00	0.99	0.99
39.811	0.00	0.00	0.00	0.00	0.00	0.00	0.00	0.00	0.04	0.27	0.53	0.67	0.95	0.97	1.00
63.096	0.00	0.00	0.00	0.00	0.00	0.00	0.00	0.00	0.00	0.01	0.00	0.17	0.46	0.42	0.83
100.00	0.00	0.00	0.00	0.00	0.00	0.00	0.00	0.00	0.00	0.00	0.00	0.03	0.03	0.02	0.10

r_c[a]	log S[b]														
	- 2.50	- 2.25	- 2.00	- 1.75	- 1.50	- 1.25	- 1.00	- 0.75	- 0.50	- 0.25	0.00	0.25	0.50	0.75	1.00
							$\beta = 0.6$								
0.1000	0.00	0.07	0.06	0.03	0.08	0.05	0.04	0.02	0.03	0.01	0.01	0.02	0.02	0.02	0.07
0.1585	0.01	0.07	0.06	0.08	0.08	0.10	0.09	0.05	0.01	0.02	0.03	0.04	0.04	0.20	0.32
0.2512	0.01	0.09	0.10	0.10	0.11	0.06	0.05	0.03	0.03	0.07	0.24	0.52	0.89	1.00	1.00
0.3981	0.01	0.08	0.14	0.12	0.13	0.11	0.10	0.13	0.53	0.79	1.00	1.00	1.00	1.00	1.00
0.6310	0.01	0.10	0.18	0.20	0.16	0.35	0.53	0.85	1.00	1.00	1.00	1.00	1.00	1.00	1.00
1.0000	0.01	0.11	0.14	0.22	0.35	0.76	0.98	1.00	1.00	1.00	1.00	1.00	1.00	1.00	1.00
1.5849	0.01	0.08	0.17	0.28	0.70	0.98	1.00	1.00	1.00	1.00	1.00	1.00	1.00	1.00	1.00
2.5119	0.02	0.07	0.18	0.42	0.69	0.98	1.00	0.99	1.00	1.00	1.00	1.00	1.00	1.00	1.00
3.9811	0.01	0.06	0.06	0.37	0.79	0.93	0.98	0.99	1.00	0.99	0.99	1.00	1.00	1.00	1.00
6.3096	0.00	0.03	0.05	0.26	0.75	0.94	0.99	1.00	1.00	1.00	0.99	1.00	1.00	1.00	1.00
10.000	0.00	0.00	0.04	0.29	0.79	0.89	0.96	0.94	1.00	1.00	1.00	1.00	1.00	1.00	1.00
15.849	0.00	0.00	0.02	0.02	0.30	0.71	0.88	0.97	0.99	1.00	0.98	1.00	1.00	1.00	1.00
25.119	0.00	0.00	0.00	0.00	0.04	0.16	0.64	0.82	0.90	0.93	0.98	0.99	0.99	1.00	1.00
39.811	0.00	0.00	0.00	0.01	0.01	0.01	0.03	0.11	0.36	0.57	0.74	0.94	0.97	0.99	0.99
63.096	0.00	0.00	0.00	0.00	0.00	0.00	0.00	0.01	0.02	0.03	0.25	0.43	0.71	0.93	0.94
100.00	0.00	0.00	0.00	0.00	0.00	0.00	0.00	0.00	0.00	0.00	0.01	0.04	0.09	0.27	0.26
							$\beta = 0.7$								
0.1000	0.01	0.00	0.00	0.02	0.01	0.02	0.01	0.04	0.02	0.02	0.00	0.02	0.02	0.01	0.00
0.1585	0.00	0.01	0.03	0.02	0.05	0.03	0.03	0.02	0.04	0.01	0.00	0.00	0.04	0.02	0.01
0.2512	0.01	0.03	0.02	0.02	0.05	0.01	0.05	0.03	0.04	0.08	0.01	0.06	0.09	0.28	0.66
0.3981	0.00	0.01	0.01	0.03	0.06	0.08	0.04	0.04	0.05	0.14	0.35	0.71	0.97	1.00	1.00
0.6310	0.01	0.02	0.04	0.04	0.08	0.10	0.10	0.13	0.54	0.88	1.00	1.00	1.00	1.00	1.00
1.0000	0.01	0.02	0.04	0.02	0.16	0.27	0.50	0.88	1.00	1.00	1.00	1.00	1.00	1.00	1.00
1.5849	0.01	0.02	0.06	0.10	0.30	0.53	0.94	0.99	1.00	1.00	1.00	1.00	1.00	1.00	1.00
2.5119	0.01	0.04	0.06	0.27	0.61	0.93	1.00	1.00	1.00	1.00	1.00	1.00	1.00	1.00	1.00
3.9811	0.01	0.01	0.10	0.40	0.75	0.99	1.00	1.00	1.00	1.00	1.00	1.00	1.00	1.00	1.00
6.3096	0.00	0.00	0.11	0.35	0.86	0.99	1.00	1.00	1.00	1.00	1.00	1.00	1.00	1.00	1.00
10.000	0.00	0.03	0.08	0.37	0.90	0.93	0.97	0.99	1.00	1.00	0.99	1.00	1.00	1.00	1.00
15.849	0.01	0.00	0.02	0.15	0.58	0.88	0.89	1.00	0.98	1.00	1.00	1.00	1.00	1.00	1.00
25.119	0.00	0.00	0.00	0.03	0.10	0.70	0.85	0.97	0.97	0.93	0.98	0.99	1.00	1.00	1.00
39.811	0.00	0.00	0.00	0.00	0.00	0.00	0.09	0.30	0.61	0.71	0.81	0.98	1.00	1.00	1.00
63.096	0.00	0.00	0.00	0.00	0.00	0.00	0.00	0.00	0.10	0.29	0.56	0.72	0.91	0.96	1.00
100.00	0.00	0.00	0.00	0.00	0.00	0.00	0.00	0.00	0.00	0.01	0.01	0.12	0.30	0.40	0.63

r_c[a]	$\log S$[b]														
	- 2.50	- 2.25	- 2.00	- 1.75	- 1.50	- 1.25	- 1.00	- 0.75	- 0.50	- 0.25	0.00	0.25	0.50	0.75	1.00
							$\beta = 0.8$								
0.1000	0.02	0.00	0.03	0.02	0.06	0.02	0.02	0.02	0.03	0.02	0.04	0.03	0.01	0.01	0.01
0.1585	0.02	0.01	0.00	0.01	0.01	0.01	0.03	0.02	0.02	0.03	0.02	0.00	0.00	0.00	0.04
0.2512	0.00	0.01	0.01	0.02	0.04	0.01	0.03	0.01	0.01	0.01	0.00	0.01	0.05	0.01	0.06
0.3981	0.02	0.00	0.04	0.01	0.02	0.04	0.03	0.04	0.02	0.02	0.05	0.05	0.24	0.59	0.93
0.6310	0.01	0.01	0.01	0.02	0.09	0.04	0.02	0.04	0.08	0.29	0.75	0.96	1.00	1.00	1.00
1.0000	0.01	0.02	0.01	0.04	0.06	0.07	0.17	0.22	0.67	0.97	1.00	1.00	1.00	1.00	1.00
1.5849	0.00	0.04	0.02	0.11	0.13	0.28	0.54	0.97	1.00	1.00	1.00	1.00	1.00	1.00	1.00
2.5119	0.00	0.01	0.04	0.10	0.40	0.82	0.97	1.00	1.00	1.00	1.00	1.00	1.00	1.00	1.00
3.9811	0.01	0.04	0.09	0.32	0.87	1.00	1.00	1.00	1.00	1.00	1.00	1.00	1.00	1.00	1.00
6.3096	0.02	0.00	0.12	0.49	0.90	0.98	1.00	1.00	1.00	1.00	1.00	1.00	1.00	1.00	1.00
10.000	0.00	0.00	0.02	0.37	0.86	0.98	0.99	1.00	1.00	1.00	1.00	1.00	1.00	1.00	1.00
15.849	0.00	0.00	0.01	0.24	0.74	0.95	0.98	0.97	1.00	1.00	1.00	1.00	1.00	1.00	1.00
25.119	0.00	0.00	0.00	0.04	0.40	0.78	0.89	0.93	0.98	0.99	1.00	1.00	1.00	1.00	1.00
39.811	0.00	0.00	0.00	0.00	0.01	0.07	0.30	0.59	0.75	0.82	0.93	0.99	0.99	1.00	1.00
63.096	0.00	0.00	0.00	0.00	0.00	0.01	0.02	0.03	0.18	0.42	0.60	0.88	0.98	1.00	1.00
100.00	0.01	0.00	0.00	0.00	0.00	0.00	0.01	0.00	0.01	0.03	0.12	0.27	0.40	0.75	0.85

[a] Units of arcsec.

[b] S is in units of cts s^{-1}. Minus signs above a value of $\log S$ indicate a negative value.

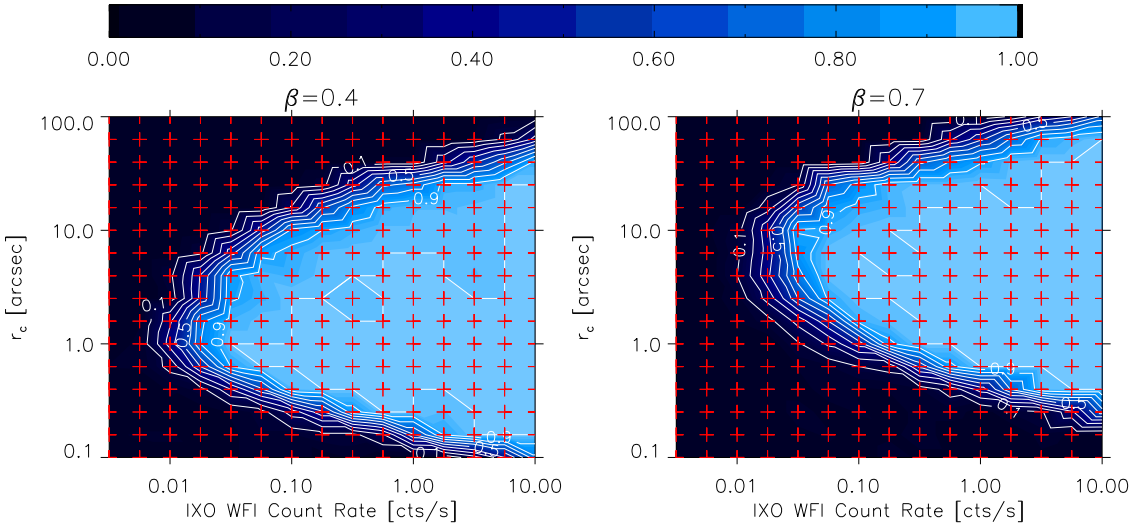

Figure F.1: Two cross-sections of the IXO-09 10 ks selection function before smoothing. Lighter blue represents higher detection probability. Red crosses mark the locations which are sampled using simulations. *Left:* $\beta = 0.3$. *Right:* $\beta = 0.8$.

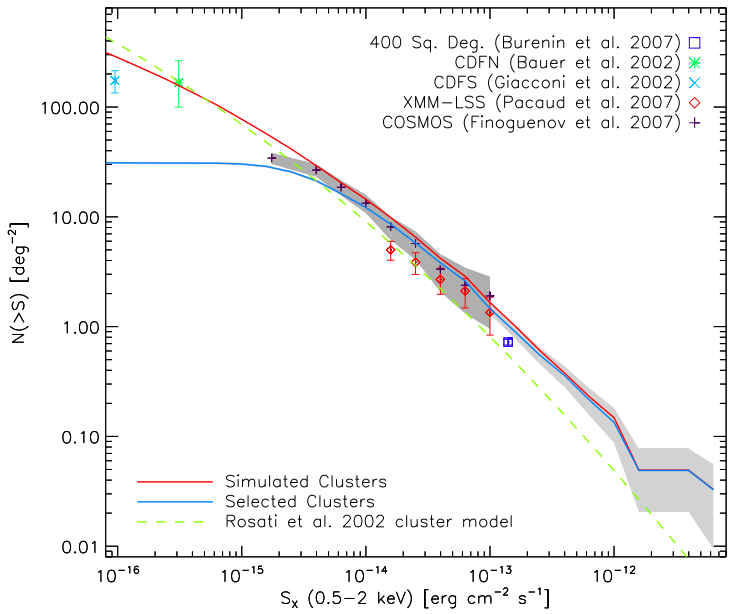

Figure F.2: Cumulative $\log N - \log S$ plot for a compilation of 4 cluster sky fields. The solid red line shows the simulated clusters, whilst the solid blue lines shows the predicted detections from the IXO-09 10 ks SBSF (see Figure 4.1, Section 4.1.2). The points show the results of cluster surveys by Bauer et al. (2002); Giacconi et al. (2002); Burenin et al. (2007); Finoguenov et al. (2007); Pacaud et al. (2007). Error bars give Poissonian 1σ confidence levels for the observational data. The light shaded area shows the 1σ confidence interval around the selected clusters, while the dark shaded area shows that around the Finoguenov et al. (2007) clusters.

Table F.2: *Top:* Predicted number of detected clusters as a function of temperature and redshift in the 10 ks exposure survey covering 6.77 degree^2 with IXO-09, with no $L_{\rm X} - T$ evolution. The predictions are made using the smoothed SBSF in its $f(S, r_c, \beta)$ form on all of the simulated clusters. Uses 7 temperature and 6 redshift bins of equal size from $-0.6 < \log T \leq 0.8$ and $0 < z \leq 3$, respectively. Three statistics are shown for each (z, T) bin: the predicted fraction of detections as a fraction of the total number of simulated clusters (i.e. the predicted completeness, in italics), and the predicted completeness minus the detected completeness in the survey. Errors are Poissonian, based on the number of detections in each bin. *Bottom:* As above but with predictions made from the $f(L_{\rm X}, T, z, r_c, \beta)$ SBSF as used for the evolutionary study in Section 4.2.2.

T (keV)	z 0.0 − 0.5		0.5 − 1.0		1.0 − 1.5		1.5 − 2.0		2.0 − 2.5		2.5 − 3.0	
0.3 − 0.4	*0.01*	0.01 ± 0.00	*0.00*	0.00 ± 0.00	*0.00*	0.00 ± 0.00	*0.00*	0.00 ± 0.00	*0.00*	0.00 ± 0.00	*0.00*	0.00 ± 0.00
0.4 − 0.6	*0.04*	0.02 ± 0.01	*0.00*	0.00 ± 0.00	*0.00*	0.00 ± 0.00	*0.00*	0.00 ± 0.00	*0.00*	0.00 ± 0.00	*0.00*	0.00 ± 0.00
0.6 − 1.0	*0.22*	0.06 ± 0.03	*0.02*	0.00 ± 0.00	*0.00*	0.00 ± 0.00	*0.00*	0.00 ± 0.00	*0.00*	0.00 ± 0.00	*0.00*	0.00 ± 0.00
1.0 − 1.6	*0.64*	0.18 ± 0.07	*0.19*	−0.04 ± 0.03	*0.02*	−0.02 ± 0.01	*0.00*	0.00 ± 0.00	*0.00*	0.00 ± 0.00	*0.00*	0.00 ± 0.00
1.6 − 2.5	*0.93*	0.24 ± 0.16	*0.58*	−0.03 ± 0.08	*0.28*	−0.08 ± 0.07	*0.07*	−0.13 ± 0.07	*0.02*	−0.11 ± 0.09	*0.00*	−0.10 ± 0.10
2.5 − 4.0	*0.96*	−0.04 ± 0.35	*0.81*	0.01 ± 0.20	*0.62*	−0.04 ± 0.33	*0.26*	−0.74 ± 0.58	*0.00*	0.00 ± 0.00	*0.00*	0.00 ± 0.00
4.0 − 6.3	*0.00*	0.00 ± 0.00	*0.56*	0.06 ± 0.50	*0.72*	−0.28 ± 1.00	*0.00*	0.00 ± 0.00	*0.00*	0.00 ± 0.00	*0.00*	0.00 ± 0.00
T (keV)	z 0.0 − 0.5		0.5 − 1.0		1.0 − 1.5		1.5 − 2.0		2.0 − 2.5		2.5 − 3.0	
0.3 − 0.4	*0.00*	0.00 ± 0.00	*0.00*	0.00 ± 0.00	*0.00*	0.00 ± 0.00	*0.00*	0.00 ± 0.00	*0.00*	0.00 ± 0.00	*0.00*	0.00 ± 0.00
0.4 − 0.6	*0.04*	0.02 ± 0.01	*0.00*	0.00 ± 0.00	*0.00*	0.00 ± 0.00	*0.00*	0.00 ± 0.00	*0.00*	0.00 ± 0.00	*0.00*	0.00 ± 0.00
0.6 − 1.0	*0.22*	0.05 ± 0.03	*0.03*	0.00 ± 0.00	*0.00*	0.00 ± 0.00	*0.00*	0.00 ± 0.00	*0.00*	0.00 ± 0.00	*0.00*	0.00 ± 0.00
1.0 − 1.6	*0.64*	0.18 ± 0.07	*0.20*	−0.03 ± 0.03	*0.04*	0.01 ± 0.01	*0.00*	0.00 ± 0.00	*0.00*	0.00 ± 0.00	*0.00*	0.00 ± 0.00
1.6 − 2.5	*0.93*	0.24 ± 0.16	*0.57*	−0.05 ± 0.08	*0.33*	−0.03 ± 0.07	*0.08*	−0.12 ± 0.07	*0.05*	−0.08 ± 0.09	*0.00*	−0.10 ± 0.10
2.5 − 4.0	*0.96*	−0.04 ± 0.35	*0.79*	−0.01 ± 0.20	*0.64*	−0.03 ± 0.33	*0.20*	−0.80 ± 0.58	*0.00*	0.00 ± 0.00	*0.00*	0.00 ± 0.00
4.0 − 6.3	*0.00*	0.00 ± 0.00	*0.58*	0.08 ± 0.50	*0.74*	−0.26 ± 1.00	*0.00*	0.00 ± 0.00	*0.00*	0.00 ± 0.00	*0.00*	0.00 ± 0.00

APPENDIX G

Survey Strategy Table

Table G.1: Results of fits to the $L_{\rm X} - T$ enhancement factor $F(z)$ for the wide-field survey and 3 deep surveys with and without the SBSF correction. $F(z) = (1+z)^u E(z)^v$. Fitting parameters are limited to the range between $-6 \leq u \leq 6$.

Survey		No sel. fn.	SBSF	SBSF with fits
Wide-field survey	u	4.00 ± 0.14	$3.00^{+0.17}_{-0.18}$	-0.10 ± 0.21
(Cooling threshold 10 ks)	v	-3.49 ± 0.19	-3.57 ± 0.24	$-0.07^{+0.28}_{-0.29}$
Deep survey 1	u	$4.99^{+0.25}_{-0.22}$	$3.47^{+0.26}_{-0.25}$	2.53 ± 0.27
	v	$-5.43^{+0.33}_{-0.28}$	$-4.34^{+0.34}_{-0.33}$	-3.28 ± 0.35
Deep survey 2	u	$2.95^{+0.18}_{-0.66}$	$1.76^{+0.39}_{-0.37}$	0.65 ± 0.39
	v	$-1.86^{+0.21}_{-0.94}$	$-1.53^{+0.51}_{-0.50}$	-0.33 ± 0.52
Deep survey 3	u	4.45 ± 0.27	$3.13^{+0.30}_{-0.29}$	$2.45^{+0.31}_{-0.32}$
	v	-4.71 ± 0.34	$-3.82^{+0.38}_{-0.37}$	$-3.18^{+0.40}_{-0.41}$

APPENDIX H

Instrument Trade-off Figures

Table H.1: Results of fits to the $L_X - T$ enhancement factor $F(z)$ for an 80×100 ks pointing IXO-10 survey for each evolution model, PSF width and selection function correction. $F(z) = (1+z)^u E(z)^v$. Surveys have the following $L_X - T$ evolution models: BD and TC. Fitting parameters are limited to the range between $-6 \leq u \leq 6$.

Survey		No correction	SBSF	SBSF with fits
BD 5 arcsec	u	3.19 ± 0.09	1.57 ± 0.09	0.99 ± 0.10
	v	-1.16 ± 0.11	0.23 ± 0.11	0.80 ± 0.12
BD 9 arcsec	u	3.57 ± 0.10	1.54 ± 0.11	0.64 ± 0.11
	v	-1.61 ± 0.12	0.08 ± 0.13	0.96 ± 0.14
TC 5 arcsec	u	$3.32^{+0.14}_{-0.12}$	1.89 ± 0.14	1.03 ± 0.14
	v	-3.06 ± 0.17	-2.02 ± 0.18	-1.04 ± 0.19
TC 9 arcsec	u	5.07 ± 0.14	2.55 ± 0.15	1.00 ± 0.16
	v	-5.30 ± 0.18	-3.04 ± 0.20	-1.31 ± 0.21

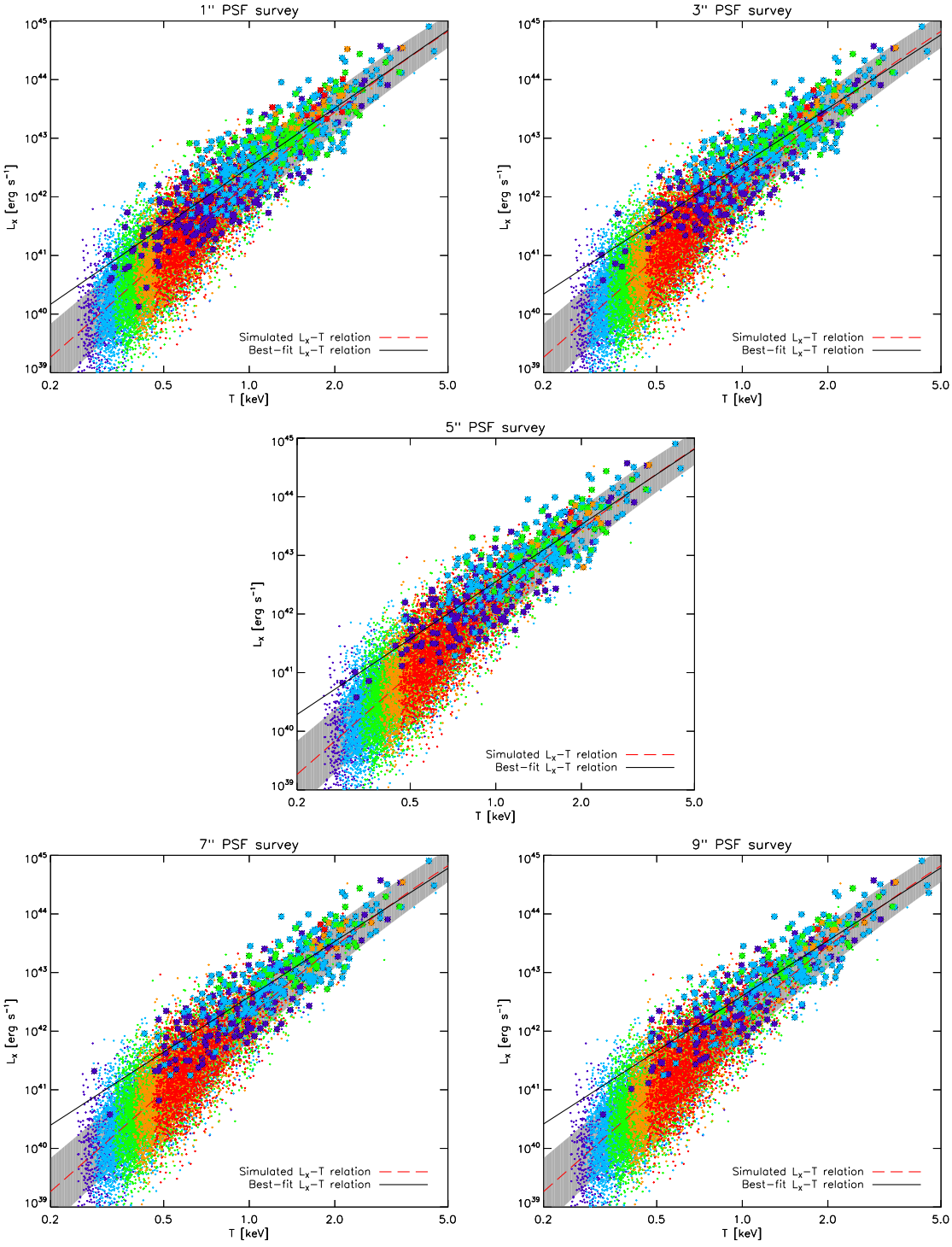

Figure H.1: $L_{\rm X} - T$ relation for an 80 × 100 ks pointing IXO-10 survey, with 5 different PSF FWHM. *From top-left to bottom right:* 1, 3, 5, 7 and 9 arcsec. Large points show the detected clusters, whilst dots represent undetected clusters. Symbol colours represent the following sequential redshift ranges: $z \leq 0.5$ dark blue, $z \leq 1$ light blue, $z \leq 1.5$ green, $z \leq 2$ orange, $z \leq 3$ red. The red long dashed line shows the XIS $L_{\rm X} - T$ relation. A power law fit to the detected clusters (black solid line) used to illustrate bias caused by detection of only the brightest low T systems.

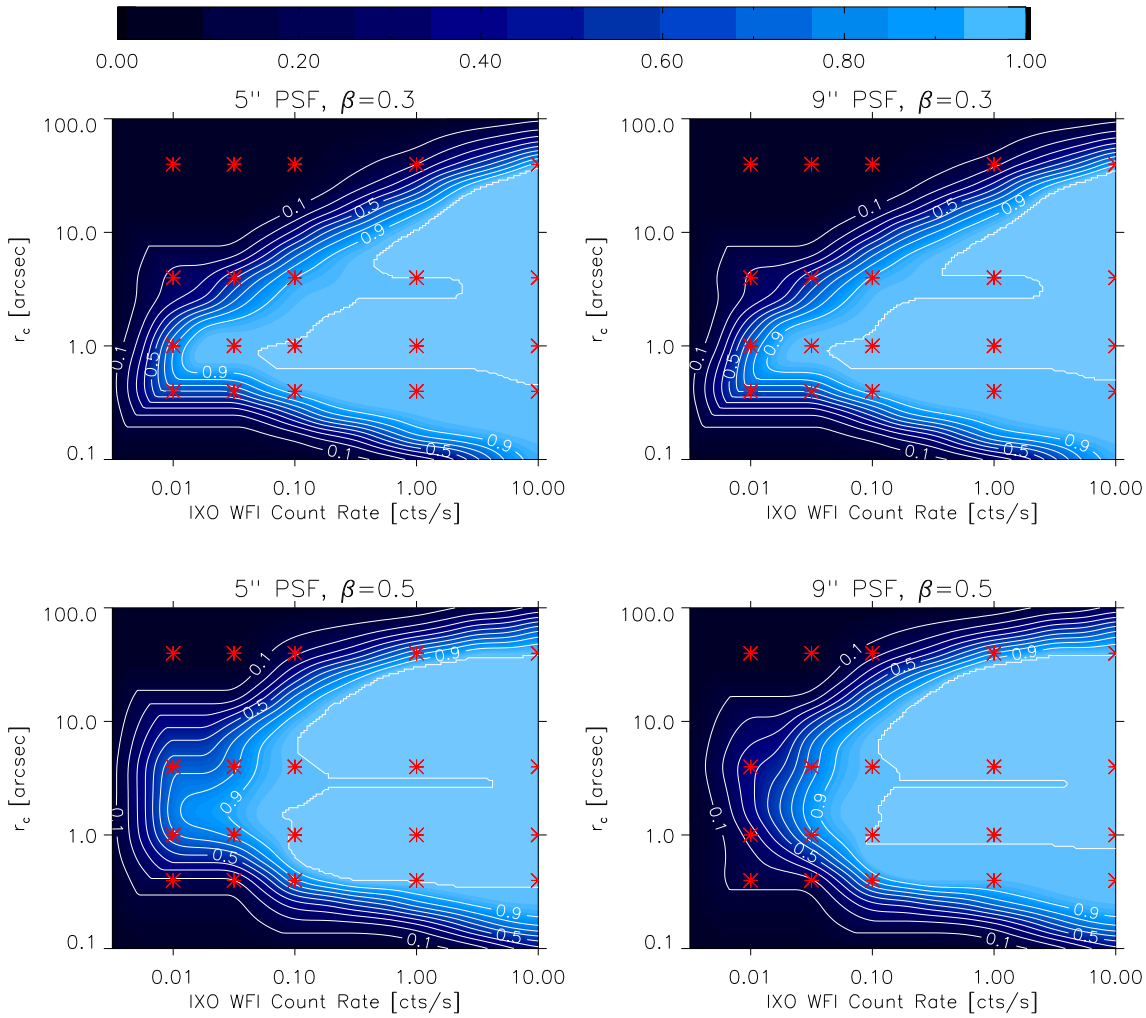

Figure H.2: Cross-sections of the IXO-10 100 ks selection function scaled from that of IXO-09 10 ks, with PSF widths of 5 arcsec (*left*) and 9 arcsec (*right*) FWHM. Lighter blue represents higher detection probability. Red crosses mark the locations which are sampled using simulations for the interpolation. *Top:* $\beta = 0.3$. *Bottom:* $\beta = 0.5$.

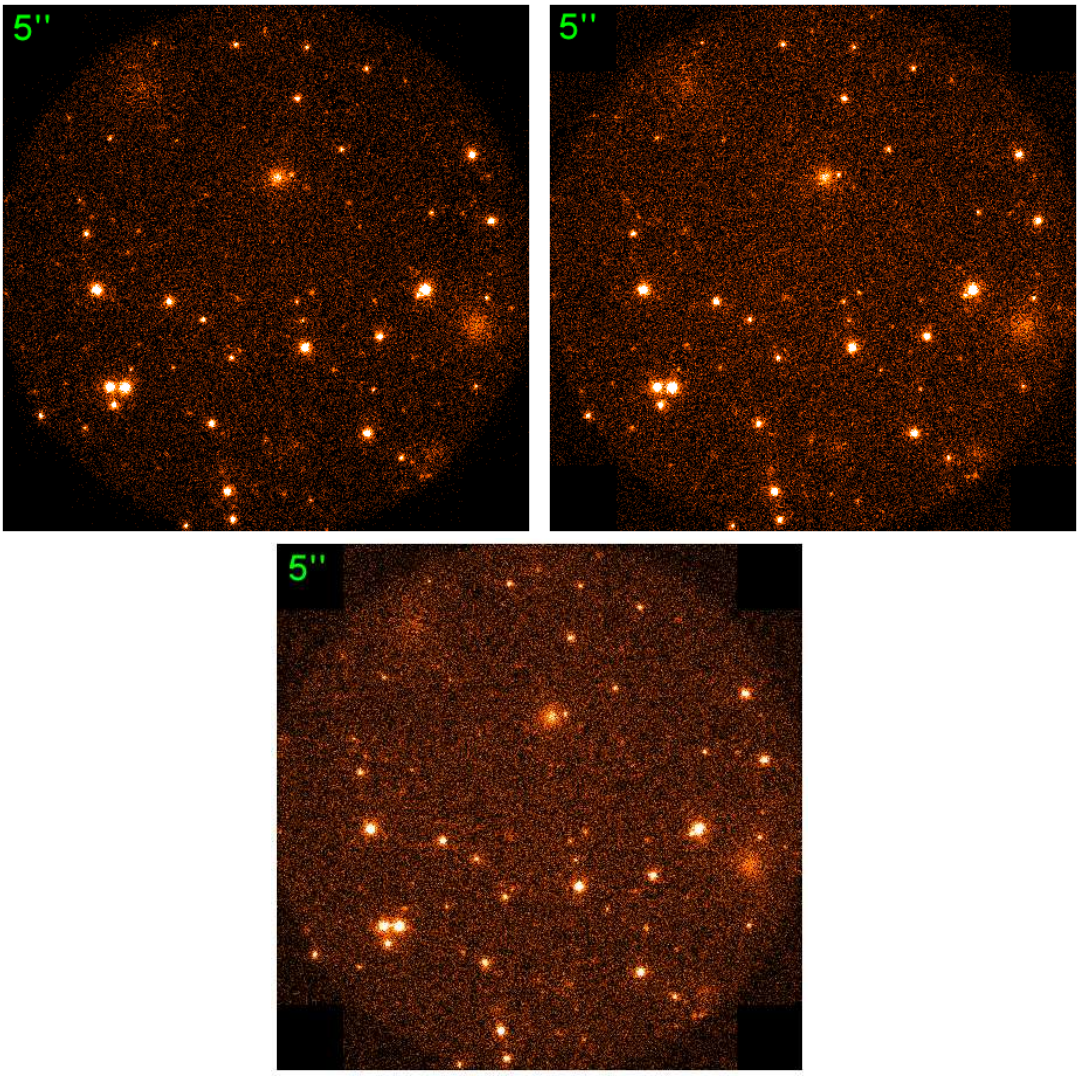

Figure H.3: 100 ks, $0.5 - 2$ keV IXO-10 images covering the same area but with 3 different particle background levels. *From top-left to bottom right:* no particle background, normal particle rate and double particle rate. Each image has a PSF of 5 arcsec FWHM and is scaled separately with a 99.5% linear scale.

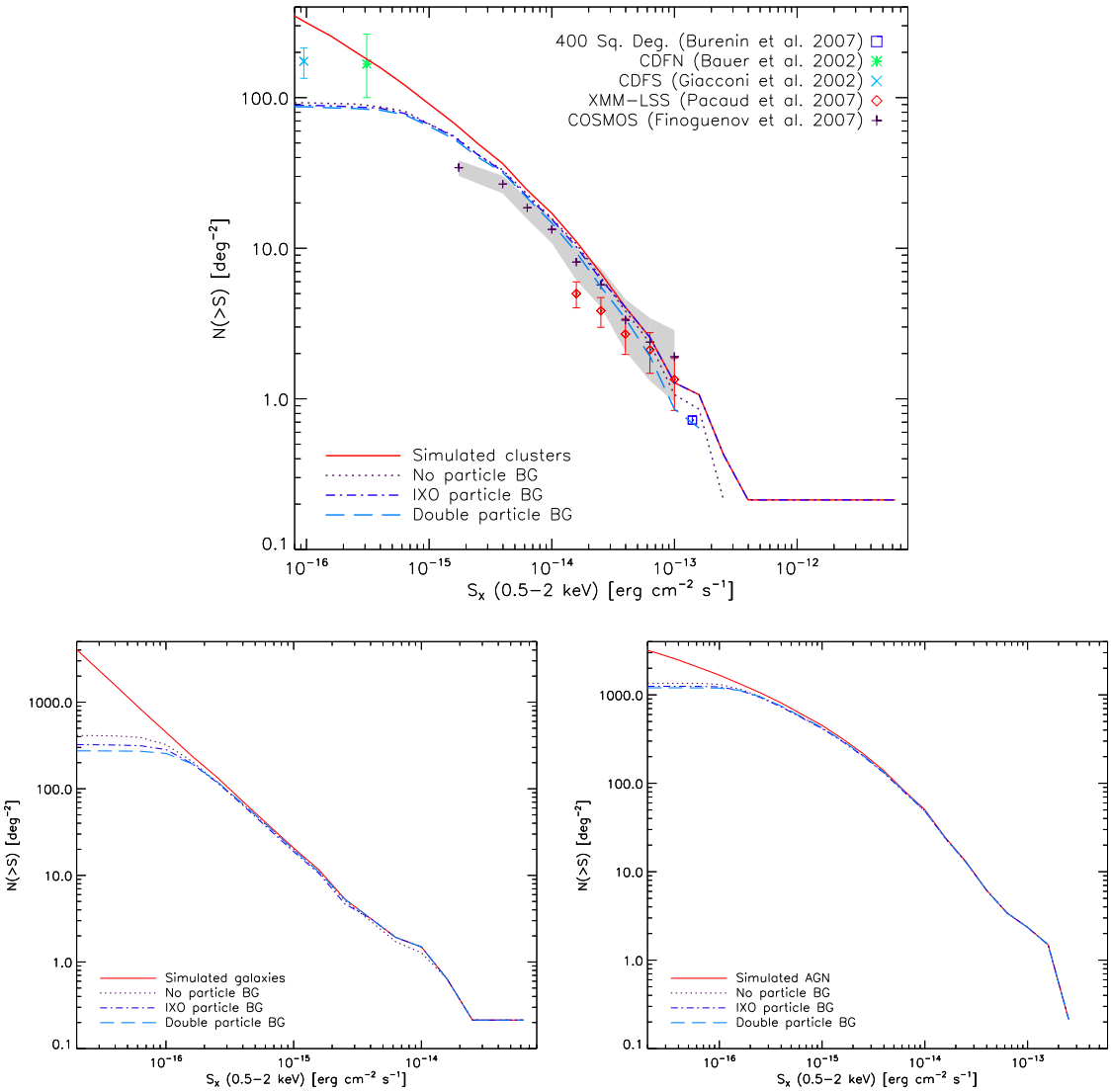

Figure H.4: *Top:* Cumulative $\log N - \log S$ plot comparing the simulated clusters (red solid line) in an 80×100 ks pointing IXO-10 survey to the detected clusters with 3 different particle background levels (blue lines): no particle background (dotted), normal particle rate (dot-dash) and double particle rate (dashed). The points show the results of cluster surveys by Bauer et al. (2002); Giacconi et al. (2002); Burenin et al. (2007); Finoguenov et al. (2007); Pacaud et al. (2007). Error bars give Poissonian 1σ confidence levels for the observational data. The shaded area shows the 1σ confidence interval around the Finoguenov et al. (2007) clusters. *Bottom-left:* As above, but comparing the galaxies. *Bottom-right:* As above, but comparing the AGN.

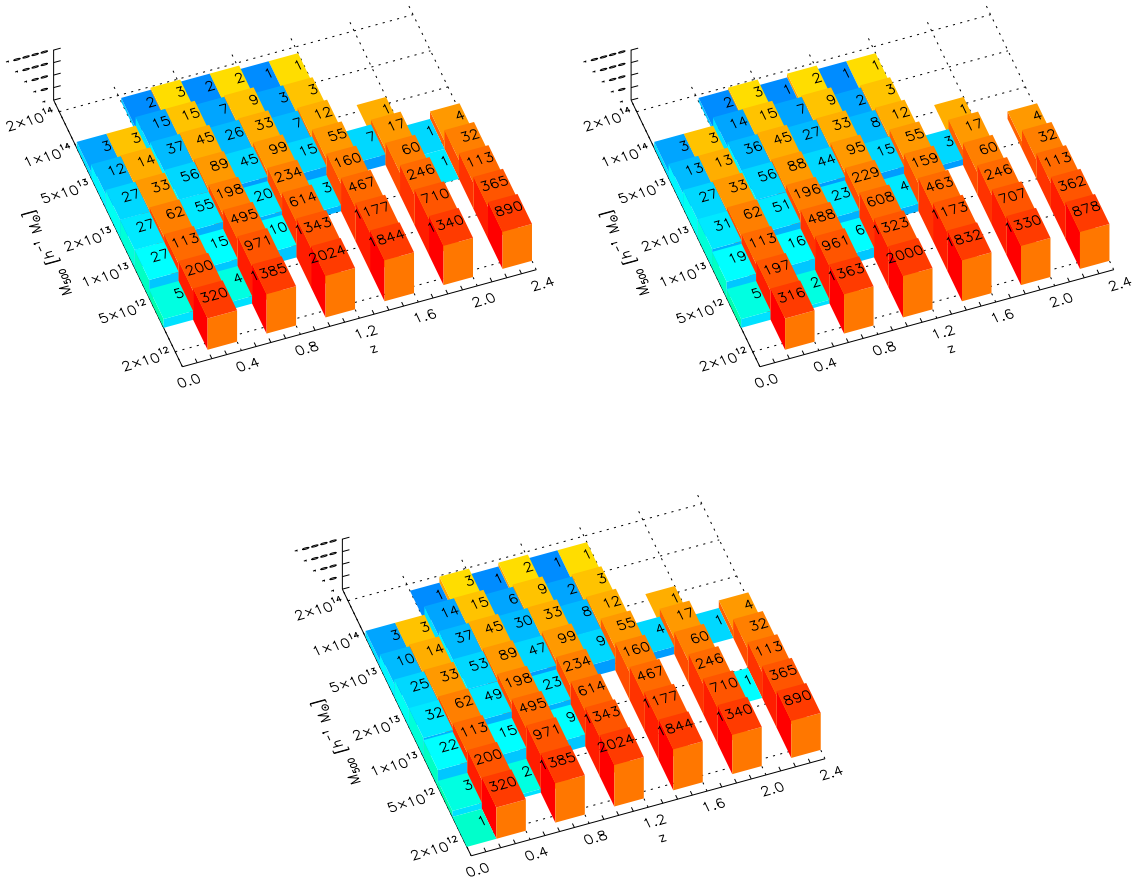

Figure H.5: Number of detected clusters (blue) and total clusters (orange) as a function of mass and redshift in an 80 × 100 ks pointing IXO-10 survey, with 3 different particle background levels. *From top-left to bottom right:* no particle background, normal particle rate and double particle rate.

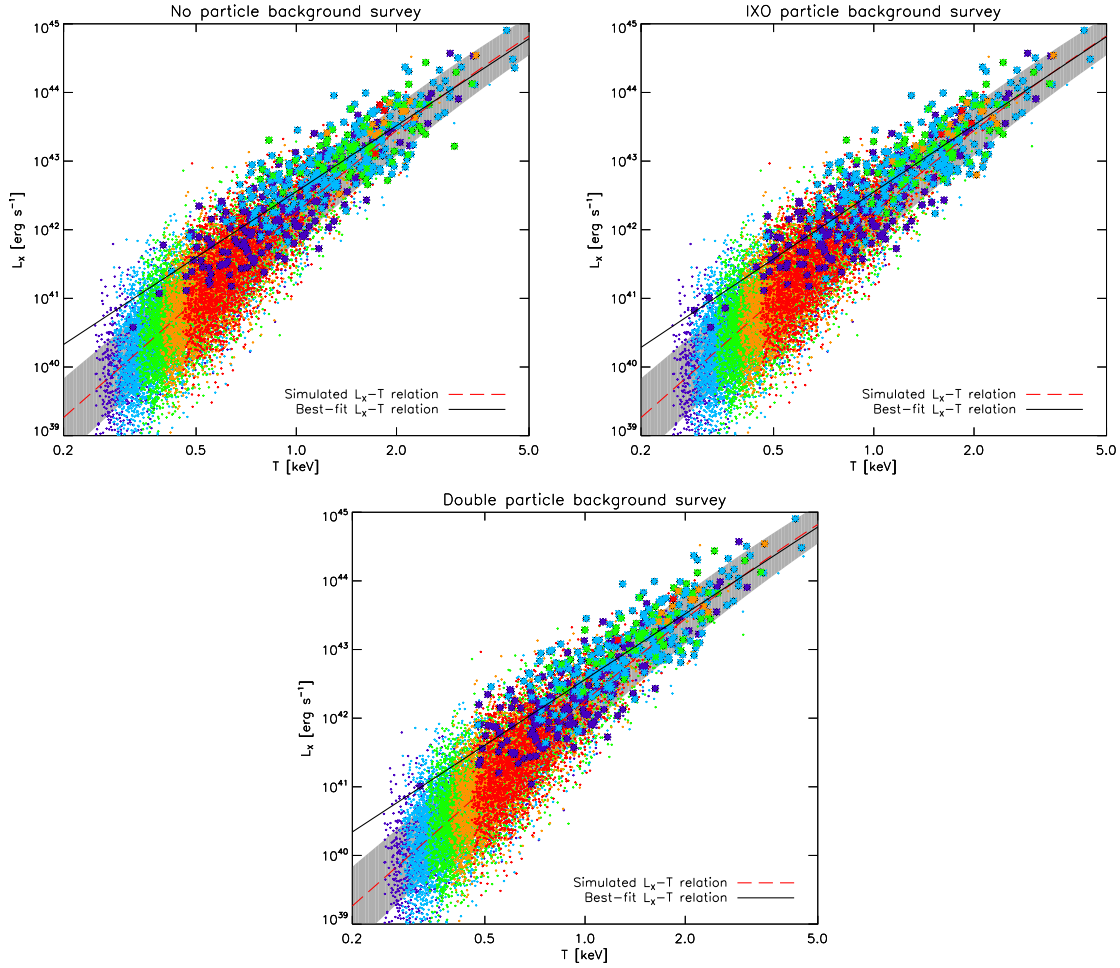

Figure H.6: $L_{\rm X}-T$ relation for an 80×100 ks pointing IXO-10 survey, with 3 different particle background levels. *From top-left to bottom right:* no particle background, normal particle rate and double particle rate. Large points show the detected clusters, whilst dots represent undetected clusters. Symbol colours represent the following sequential redshift ranges: $z \leq 0.5$ dark blue, $z \leq 1$ light blue, $z \leq 1.5$ green, $z \leq 2$ orange, $z \leq 3$ red. The red long dashed line shows the XIS $L_{\rm X}-T$ relation. A power law fit to the detected clusters (black solid line) used to illustrate bias caused by detection of only the brightest low T systems.

List of Acronyms

160d 160 square degree.

400d 400 square degree.

ACIS Advanced CCD Imaging Spectrometer.

AEGIS All-wavelength Extended Goth strip International Survey.

AGN Active Galactic Nuclei.

AIC Akaike Information Criterion.

APEC Astrophysical Plasma Emission Code.

ARF Ancillary Response File.

ASCA Advanced Satellite for Cosmology and Astrophysics.

ASDC ASI Science Data Center.

ASI Italian Space Agency.

AUL Astronomy User's Library.

BCG Brightest Cluster Galaxy.

BCS Brightest Cluster Sample.

BD self-similar with respect to the background density.

BIC Bayesian Information Criterion.

CC Cool Core.

CCD Charge-Coupled Device.

CD self-similar with respect to the critical density.

CDFN Chandra Deep Field North.

CDFS Chandra Deep Field South.

CDM Cold Dark Matter.

CdTe Cadmium-Telluride.

CIAO Chandra Interactive Analysis of Observations.

CMB Cosmic Microwave Background.

COSMOS Cosmic Evolution Survey.

Dec Declination.

DePFET Depleted P-channel Field Effect Transistor.

DID Descendant Identification.

DL90 Dickey & Lockman (1990).

DSB Diffuse Soft Background.

DSSD Double-sided Silicon Strip Detector.

EMSS Einstein Extended Medium Sensitivity Survey.

EPIC European Photon Imaging Camera.

EPL Extragalactic Power-Law.

ESA European Space Agency.

EXOSAT European X-ray Observatory Satellite.

FFT Fast Fourier Transform.

FITS Flexible Image Transport System.

FWHM Full Width at Half Maximum.

GCA Growth Curve Analysis.

GCH07 Gilli, Comastri, & Hasinger (2007).

GSFC Goddard Space Flight Center.

HDF Hubble Deep Field.

HMS05 Hasinger, Miyaji, & Schmidt (2005).

HRC High Resolution Camera.

HTRS High Time Resolution Spectrometer.

HXI Hard X-ray Imager.

ICM Intracluster Medium.

ID Identification.

IDL Interactive Data Language.

IMF Initial Mass Function.

IXO International X-ray Observatory.

JAXA Japan Aerospace Exploration Agency.

K-S Kolmogorov-Smirnov.

L2 2nd Lagrange.

LDDE Luminosity Dependent Density Evolution.

MCMC Markov Chain Monte Carlo.

MEKAL Mewe-Kaastra-Liedahl.

MGS Millennium Gas Simulations.

MIP Mobile Instrument Platform.

MOS Metal Oxide Semi-conductor.

MS Millennium Simulation.

NASA National Aeronautics and Space Administration.

NCC Non Cool Core.

NE no evolution.

NEP North Ecliptic Pole.

PDF Probability Density Function.

PSF Point Spread Function.

QSO Quasi-stellar Object.

RA Right Ascension.

RASS ROSAT All Sky Survey.

RCS03 Ranalli, Comastri, & Setti (2003).

RDCS ROSAT Deep Cluster Survey.

REFLEX ROSAT ESO Flux-Limited X-Ray.

REXCESS Representative XMM-Newton Cluster Structure Survey.

RGS Reflection Grating Spectrometers.

RIXOS ROSAT International X-ray Optical Survey.

RMF Redistribution Matrix File.

RXTE Rossi X-ray Timing Explorer.

SASS Standard Analysis Software System.

SBSF Surface Brightness Selection Function.

SHARC Serendipitous High-redshift Archival ROSAT Cluster.

SRT Steepness Ratio Technique.

SXLF Soft X-ray Luminosity Function.

SZ Sunyaev-Zel'dovich.

TC similarity linked to the threshold for radiative cooling.

VTP Voronoi Tessellation and Percolation.

WARPS Wide-Angle ROSAT Pointed X-Ray Survey.

WFI Wide Field Imager.

WVT Weighted Voronoi Tessellation.

X-MAS X-ray Map Simulator.

XBACs X-ray-Brightest Abell-type Clusters of galaxies.

XCS XMM Cluster Survey.

XEUS X-ray Evolving Universe Spectroscopy.

XGS X-ray Grating Spectrometer.

XIS X-ray Image Suite.

XLF X-ray Luminosity Function.

XMM-LSS XMM Large Scale Structure.

XMS X-ray Microcalorimeter Spectrometer.

XRB X-ray Background.

List of References

Abell, G. O., Corwin, Jr., H. G., & Olowin, R. P. 1989, ApJS, 70, 1

Akaike, H. 1981, Journal of Econometrics, 16, 3

Alshino, A., Ponman, T., Pacaud, F., & Pierre, M. 2010, MNRAS, 407, 2543

Ambrosi, R. M., Holland, A. D., Smith, D. R., Hutchinson, I. B., & Denby, M. 2005, Planet. Space Sci., 53, 1449

Anderson, J. L. & Cohen, J. M. 1970, Ap&SS, 9, 146

Arida, M. 2001, QuickSim Version 2.0, NASA
`http://heasarc.gsfc.nasa.gov/docs/xmm/quicksim/quicksim.html`

Arnaud, K. A. 1996, in Astronomical Society of the Pacific Conference Series, Vol. 101, Astronomical Data Analysis Software and Systems V, ed. G. H. Jacoby & J. Barnes, 17–+

Arnaud, M. & Evrard, A. E. 1999, MNRAS, 305, 631

Arnaud, M., Pointecouteau, E., & Pratt, G. W. 2005, A&A, 441, 893

Arnaud, M., Pointecouteau, E., & Pratt, G. W. 2007, A&A, 474, 37

Ballet, J. 1999, A&AS, 135, 371

Balogh, M. L., Babul, A., & Patton, D. R. 1999, MNRAS, 307, 463

Balogh, M. L., Pearce, F. R., Bower, R. G., & Kay, S. T. 2001, MNRAS, 326, 1228

Barret, D., Belloni, T., Bhattacharyya, S., Gilfanov, M., Gogus, E., Homan, J., Méndez, M., Miller, J. M., Miller, M. C., Mereghetti, S., Paltani, S., Poutanen, J., Wilms, J., & Zdziarski, A. A. 2008, in Presented at the Society of Photo-Optical Instrumentation Engineers (SPIE) Conference, Vol. 7011, Society of Photo-Optical Instrumentation Engineers (SPIE) Conference Series

Barth, J. L., Isaacs, J. C., & Poivey, C. 2000, The radiation environment for the Next Generation Telescope, Tech. rep., NASA Report

Barthel, P. D. 1989, ApJ, 336, 606

Barvainis, R. 1987, ApJ, 320, 537

Basilakos, S., Plionis, M., Georgakakis, A., & Georgantopoulos, I. 2005, MNRAS, 356, 183

Bauer, F. E., Alexander, D. M., Brandt, W. N., Hornschemeier, A. E., Miyaji, T., Garmire, G. P., Schneider, D. P., Bautz, M. W., Chartas, G., Griffiths, R. E., & Sargent, W. L. W. 2002, AJ, 123, 1163

Bauer, F. E., Fabian, A. C., Sanders, J. S., Allen, S. W., & Johnstone, R. M. 2005, MNRAS, 359, 1481

Best, P. N., Kauffmann, G., Heckman, T. M., Brinchmann, J., Charlot, S., Ivezić, Ž., & White, S. D. M. 2005, MNRAS, 362, 25

Binney, J. & Tabor, G. 1995, MNRAS, 276, 663

Birkinshaw, M. & Lancaster, K. 2007, New Astron. Rev., 51, 346

Blanchard, A., Valls-Gabaud, D., & Mamon, G. A. 1992, A&A, 264, 365

Böhringer, H., Schuecker, P., Guzzo, L., Collins, C. A., Voges, W., Cruddace, R. G., Ortiz-Gil, A., Chincarini, G., De Grandi, S., Edge, A. C., MacGillivray, H. T., Neumann, D. M., Schindler, S., & Shaver, P. 2004, A&A, 425, 367

Böhringer, H., Schuecker, P., Pratt, G. W., Arnaud, M., Ponman, T. J., Croston, J. H., Borgani, S., Bower, R. G., Briel, U. G., Collins, C. A., Donahue, M., Forman, W. R., Finoguenov, A., Geller, M. J., Guzzo, L., Henry, J. P., Kneissl, R., Mohr, J. J., Matsushita, K., Mullis, C. R., Ohashi, T., Pedersen, K., Pierini, D., Quintana, H., Raychaudhury, S., Reiprich, T. H., Romer, A. K., Rosati, P., Sabirli, K., Temple, R. F., Viana, P. T. P., Vikhlinin, A., Voit, G. M., & Zhang, Y. 2007, A&A, 469, 363

Böhringer, H., Voges, W., Huchra, J. P., McLean, B., Giacconi, R., Rosati, P., Burg, R., Mader, J., Schuecker, P., Simiç, D., Komossa, S., Reiprich, T. H., Retzlaff, J., & Trümper, J. 2000, ApJS, 129, 435

Bookbinder, J. 2010, ArXiv e-prints, 1003.2847

Borgani, S., Murante, G., Springel, V., Diaferio, A., Dolag, K., Moscardini, L., Tormen, G., Tornatore, L., & Tozzi, P. 2004, MNRAS, 348, 1078

Borgani, S., Rosati, P., Tozzi, P., Stanford, S. A., Eisenhardt, P. R., Lidman, C., Holden, B., Della Ceca, R., Norman, C., & Squires, G. 2001, ApJ, 561, 13

Bosma, A. 1981, AJ, 86, 1825

Bothun, G., ed. 1998, Modern cosmological observations and problems, `http://nedwww.ipac.caltech.edu/level5/Bothun2/Bothun3_2_2.html`

Brandt, W. N., Alexander, D. M., Hornschemeier, A. E., Garmire, G. P., Schneider, D. P., Barger, A. J., Bauer, F. E., Broos, P. S., Cowie, L. L., Townsley, L. K., Burrows, D. N., Chartas, G., Feigelson, E. D., Griffiths, R. E., Nousek, J. A., & Sargent, W. L. W. 2001, AJ, 122, 2810

Brinkman, A., Aarts, H., den Boggende, A., Bootsma, T., Dubbeldam, L., den Herder, J., Kaastra, J., de Korte, P., van Leeuwen, B., Mewe, R., Paerels, F., de Vries, C., Cottam, J., Decker, T., Kahn, S., Rasmussen, A., Spodek, J., Branduardi-Raymont, G., Guttridge, P., Thomsen, K., Zehnder, A., & Guedel, M. 1998, in Science with XMM

Bryan, G. L. & Norman, M. L. 1998, ApJ, 495, 80

Burenin, R. A., Vikhlinin, A., Hornstrup, A., Ebeling, H., Quintana, H., & Mescheryakov, A. 2007, ApJS, 172, 561

Burke, D. J., Collins, C. A., Sharples, R. M., Romer, A. K., Holden, B. P., & Nichol, R. C. 1997, ApJ, 488, L83+

Calderwood, T., Dobrzycki, A., Jessop, H., & Harris, D. E. 2001, in Astronomical Society of the Pacific Conference Series, Vol. 238, Astronomical Data Analysis Software and Systems X, ed. F. R. Harnden Jr., F. A. Primini, & H. E. Payne, 443–+

Cappellari, M. & Copin, Y. 2003, MNRAS, 342, 345

Cappelluti, N., Böhringer, H., Schuecker, P., Pierpaoli, E., Mullis, C. R., Gioia, I. M., & Henry, J. P. 2007, A&A, 465, 35

Cappi, M., Mazzotta, P., Elvis, M., Burke, D. J., Comastri, A., Fiore, F., Forman, W., Fruscione, A., Green, P., Harris, D., Hooper, E. J., Jones, C., Kaastra, J. S., Kellogg, E., Murray, S., McNamara, B., Nicastro, F., Ponman, T. J., Schlegel, E. M., Siemiginowska, A., Tananbaum, H., Vikhlinin, A., Virani, S., & Wilkes, B. 2001, ApJ, 548, 624

Caroli, E., Stephen, J. B., Di Cocco, G., Natalucci, L., & Spizzichino, A. 1987, Space Sci. Rev., 45, 349

Carrera, F. J., Barcons, X., & Fabian, A. C. 1996, in Roentgenstrahlung from the Universe, ed. H. U. Zimmermann, J. Trümper, & H. Yorke, 571–572

Cash, W. 1979, ApJ, 228, 939

Cattaneo, A. & Teyssier, R. 2007, MNRAS, 261

Cavaliere, A. & Fusco-Femiano, R. 1976, A&A, 49, 137

Cen, R. & Ostriker, J. P. 1999, ApJ, 514, 1

Chen, Y., Reiprich, T. H., Böhringer, H., Ikebe, Y., & Zhang, Y.-Y. 2007, A&A, 466, 805

Cole, S. 1991, ApJ, 367, 45

Collins, C. A., Burke, D. J., Romer, A. K., Sharples, R. M., & Nichol, R. C. 1997, ApJ, 479, L117+

Collon, M. J., Guenther, R., Ackermann, M., Partapsing, R., Kelly, C., Beijersbergen, M. W., Bavdaz, M., Wallace, K., Olde Riekerink, M., Mueller, P., & Krumrey, M. 2009, in Presented at the Society of Photo-Optical Instrumentation Engineers (SPIE) Conference, Vol. 7437, Society of Photo-Optical Instrumentation Engineers (SPIE) Conference Series

Crawford, C. S., Allen, S. W., Ebeling, H., Edge, A. C., & Fabian, A. C. 1999, MNRAS, 306, 857

Croston, J. H., Kraft, R. P., & Hardcastle, M. J. 2006, ArXiv Astrophysics e-prints, astro-ph/0610889

Croston, J. H., Pratt, G. W., Böhringer, H., Arnaud, M., Pointecouteau, E., Ponman, T. J., Sanderson, A. J. R., Temple, R. F., Bower, R. G., & Donahue, M. 2008, A&A, 487, 431

Culhane, J. L. & P W Sanford, P. W. 1981, X-ray Astronomy (Faber and Faber)

Davis, M., Efstathiou, G., Frenk, C. S., & White, S. D. M. 1985, ApJ, 292, 371

de Grandi, S., Molendi, S., Boehringer, H., Chincarini, G., & Voges, W. 1997, ApJ, 486, 738

Dickey, J. M. & Lockman, F. J. 1990, ARA&A, 28, 215

Diehl, S. & Statler, T. S. 2006, MNRAS, 368, 497

Domainko, W., Gitti, M., Schindler, S., & Kapferer, W. 2004, A&A, 425, L21

Ebeling, H., Edge, A. C., Fabian, A. C., Allen, S. W., Crawford, C. S., & Boehringer, H. 1997, ApJ, 479, L101+

Ebeling, H., Voges, W., Bohringer, H., Edge, A. C., Huchra, J. P., & Briel, U. G. 1996, MNRAS, 281, 799

Ebeling, H. & Wiedenmann, G. 1993, Phys. Rev. E, 47, 704

Eddington, A. S. 1913, MNRAS, 73, 359

Edge, A. C. 2001, MNRAS, 328, 762

Edge, A. C. & Stewart, G. C. 1991, MNRAS, 252, 414

Ehle, M., Breitfellner, M., Díaz Trigo, M., González Riestra, R., Guainazzi, M., Loiseau, N., Rodríguez, P., Santos-Lleó, M., Schartel, N., Tomás, E., Verdugo, L., & Dahlem, M. 2007, XMM-Newton Users' Handbook, European Space Agency
`http://heasarc.gsfc.nasa.gov/docs/xmm/uhb/XMM_UHB.html`

Ettori, S., Tozzi, P., Borgani, S., & Rosati, P. 2004, A&A, 417, 13

Evrard, A. E. 2004, An Overview of Growth and Structure. In: Mulchaey J S, Dressler A and Oemler A (Eds.), Clusters of Galaxies: Probes of Cosmological Structure and Galaxy Evolution, Vol. 3 (Cambridge University Press), pp 1-23

Fabbiano, G. 1989, ARA&A, 27, 87

Fabian, A. C. 1994, ARA&A, 32, 277

Fabian, A. C., Crawford, C. S., Ettori, S., & Sanders, J. S. 2001, MNRAS, 322, L11

Fabian, A. C., Nulsen, P. E. J., & Canizares, C. R. 1982, MNRAS, 201, 933

Fabian, A. C., Sanders, J. S., Crawford, C. S., Conselice, C. J., Gallagher, J. S., & Wyse, R. F. G. 2003, MNRAS, 344, L48

Fabian, A. C., Sanders, J. S., Ettori, S., Taylor, G. B., Allen, S. W., Crawford, C. S., Iwasawa, K., Johnstone, R. M., & Ogle, P. M. 2000, MNRAS, 318, L65

Finoguenov, A., Borgani, S., Tornatore, L., & Böhringer, H. 2003, A&A, 398, L35

Finoguenov, A., Guzzo, L., Hasinger, G., Scoville, N. Z., Aussel, H., Böhringer, H., Brusa, M., Capak, P., Cappelluti, N., Comastri, A., Giodini, S., Griffiths, R. E., Impey, C., Koekemoer, A. M., Kneib, J., Leauthaud, A., Le Fèvre, O., Lilly, S., Mainieri, V., Massey, R., McCracken, H. J., Mobasher, B., Murayama, T., Peacock, J. A., Sakelliou, I., Schinnerer, E., Silverman, J. D., Smolčić, V., Taniguchi, Y., Tasca, L., Taylor, J. E., Trump, J. R., & Zamorani, G. 2007, ApJS, 172, 182

Finoguenov, A., Reiprich, T. H., & Böhringer, H. 2001a, A&A, 368, 749

Finoguenov, A., Reiprich, T. H., & Böhringer, H. 2001b, A&A, 368, 749

Fraser, G. W., Barstow, M. A., Whiteley, M. J., & Wells, A. 1982, Nature, 300, 509

Freedman, W. L., Madore, B. F., Gibson, B. K., Ferrarese, L., Kelson, D. D., Sakai, S., Mould, J. R., Kennicutt, Jr., R. C., Ford, H. C., Graham, J. A., Huchra, J. P., Hughes, S. M. G., Illingworth, G. D., Macri, L. M., & Stetson, P. B. 2001, ApJ, 553, 47

Freeman, P. E., Kashyap, V., Rosner, R., & Lamb, D. Q. 2002, ApJS, 138, 185

Fujimoto, M. Y. & Taam, R. E. 1986, ApJ, 305, 246

Gardini, A., Rasia, E., Mazzotta, P., Tormen, G., De Grandi, S., & Moscardini, L. 2004, MNRAS, 351, 505

Gazzola, L. & Pearce, F. R. 2007, in Heating versus Cooling in Galaxies and Clusters of Galaxies, ed. H. Böhringer, G. W. Pratt, A. Finoguenov, & P. Schuecker, 412–+

Gehrels, N. 1986, ApJ, 303

Georgakakis, A., Nandra, K., Laird, E. S., Gwyn, S., Steidel, C. C., Sarajedini, V. L., Barmby, P., Faber, S. M., Coil, A. L., Cooper, M. C., Davis, M., & Newman, J. A. 2006, MNRAS, 371, 221

Giacconi, R., Gursky, H., Paolini, F. R., & Rossi, B. B. 1962, Physical Review Letters, 9, 439

Giacconi, R., Zirm, A., Wang, J., Rosati, P., Nonino, M., Tozzi, P., Gilli, R., Mainieri, V., Hasinger, G., Kewley, L., Bergeron, J., Borgani, S., Gilmozzi, R., Grogin, N., Koekemoer, A., Schreier, E., Zheng, W., & Norman, C. 2002, ApJS, 139, 369

Gilli, R. 2003, Astronomische Nachrichten, 324, 165

Gilli, R., Comastri, A., & Hasinger, G. 2007, A&A, 463, 79

Gilli, R., Daddi, E., Zamorani, G., Tozzi, P., Borgani, S., Bergeron, J., Giacconi, R., Hasinger, G., Mainieri, V., Norman, C., Rosati, P., Szokoly, G., & Zheng, W. 2005, A&A, 430, 811

Gilmour, R., Best, P., & Almaini, O. 2009, MNRAS, 392, 1509

Gioia, I. M., Henry, J. P., Maccacaro, T., Morris, S. L., Stocke, J. T., & Wolter, A. 1990a, ApJ, 356, L35

Gioia, I. M., Maccacaro, T., Schild, R. E., Wolter, A., Stocke, J. T., Morris, S. L., & Henry, J. P. 1990b, ApJS, 72, 567

Giommi, P. 2000, X-ray events simulator Version 3.0, ASDC
`http://www.asdc.asi.it/simulator/`

Giommi, P. 2005, Swift-XRT Data Simulator, ASDC
`http://www.asdc.asi.it/simulator/swift/`

Giommi, P., Angelini, L., Jacobs, P., & Tagliaferri, G. 1992, in Astronomical Society of the Pacific Conference Series, Vol. 25, Astronomical Data Analysis Software and Systems I, ed. D. M. Worrall, C. Biemesderfer, & J. Barnes, 100–+

Grebenev, S. A., Forman, W., Jones, C., & Murray, S. 1995, ApJ, 445, 607

Gunn, J. E. 1977, ApJ, 218, 592

Gunn, J. E. & Gott, III, J. R. 1972, ApJ, 176, 1

Guseinov, O. K. 1971, Soviet Astronomy, 14, 912

Guzzo, L., Böhringer, H., Schuecker, P., Collins, C. A., Schindler, S., Neumann, D. M., de Grandi, S., Cruddace, R., Chincarini, G., Edge, A. C., Shaver, P. A., & Voges, W. 1999, The Messenger, 95, 27

Hall, D. 2007, private communication

Hall, D., Holland, A., & Turner, M. 2008, in Society of Photo-Optical Instrumentation Engineers (SPIE) Conference Series, Vol. 7021, Society of Photo-Optical Instrumentation Engineers (SPIE) Conference Series

Hardcastle, M. J., Evans, D. A., & Croston, J. H. 2006, MNRAS, 370, 1893

Hardcastle, M. J., Evans, D. A., & Croston, J. H. 2007, MNRAS, 376, 1849

Hartley, W. G., Gazzola, L., Pearce, F. R., Kay, S. T., & Thomas, P. A. 2008, MNRAS, 386, 2015

Hasinger, G., Cappelluti, N., Brunner, H., Brusa, M., Comastri, A., Elvis, M., Finoguenov, A., Fiore, F., Franceschini, A., Gilli, R., Griffiths, R. E., & Lehmann, I. 2006, arXiv.org, e-Print Arch. Astrophys.

Hasinger, G., Miyaji, T., & Schmidt, M. 2005, A&A, 441, 417

Helsdon, S. F. & Ponman, T. J. 2000, MNRAS, 315, 356

Hendry, M. A., Simmons, J. F. L., & Newsam, A. M. 1993, in Cosmic Velocity Fields, ed. F. Bouchet & M. Lachieze-Rey, 23–+

Henry, J. P. & Briel, U. G. 1991, A&A, 246, L14

Henry, J. P., Gioia, I. M., Maccacaro, T., Morris, S. L., Stocke, J. T., & Wolter, A. 1992, ApJ, 386, 408

Henry, J. P., Kellogg, E. M., Murray, S. S., van Speybroeck, L. P., Bjorkholm, P. J., & Briel, U. G. 1977, in Presented at the Society of Photo-Optical Instrumentation Engineers (SPIE) Conference, Vol. 106, Society of Photo-Optical Instrumentation Engineers (SPIE) Conference Series, ed. R. C. Chase & G. W. Kuswa, 196–205

Hicks, A. K. & Mushotzky, R. 2005, ApJ, 635, L9

Hogg, D. W. 1999, ArXiv Astrophysics e-prints, arXiv:astro-ph/9905116

Horner, D. J., Mushotzky, R. F., & Scharf, C. A. 1999, ApJ, 520, 78

Horner, D. J., Perlman, E. S., Ebeling, H., Jones, L. R., Scharf, C. A., Wegner, G., Malkan, M., & Maughan, B. 2008, ApJS, 176, 374

Hubble, E. 1929, Proceedings of the National Academy of Science, 15, 168

ISAS/JAXA. 2010, The Suzaku Technical Description, Institute of Space and Astronautical Science (ISAS/JAXA) and NASA/GSFC
`http://heasarc.nasa.gov/docs/suzaku/prop_tools/suzaku_td/suzaku_td.html`

Ishibashi, B. 2006, Marx Home Page, MIT/CXC group
`http://space.mit.edu/ASC/MARX/`

Johnson, O., Best, P., Zaritsky, D., Clowe, D., Aragón-Salamanca, A., Halliday, C., Jablonka, P., Milvang-Jensen, B., Pelló, R., Poggianti, B. M., Rudnick, G., Saglia, R., Simard, L., & White, S. 2006, MNRAS, 371, 1777

Jones, C. & Forman, W. 1984, ApJ, 276, 38

Joye, W. A. & Mandel, E. 2003, in Astronomical Society of the Pacific Conference Series, Vol. 295, Astronomical Data Analysis Software and Systems XII, ed. H. E. Payne, R. I. Jedrzejewski, & R. N. Hook, 489–+

Kaastra, J. S., Ferrigno, C., Tamura, T., Paerels, F. B. S., Peterson, J. R., & Mittaz, J. P. D. 2001, A&A, 365, L99

Kaastra, J. S. & Mewe, R. 1993, A&AS, 97, 443

Kafatos, M. 1973, ApJ, 182, 433

Kaiser, N. 1986, MNRAS, 222, 323

Katz, N. & White, S. D. M. 1993, ApJ, 412, 455

Kay, S. T., Thomas, P. A., Jenkins, A., & Pearce, F. R. 2004, MNRAS, 355, 1091

Kelly, B. C. 2007, ApJ, 665, 1489

Kilbourne, C. A., Bandler, S. R., Brown, A., Chervenak, J. A., Figueroa-Feliciano, E., Finkbeiner, F. M., Iyomoto, N., Kelley, R. L., Porter, F. S., & Smith, S. J. 2007, in Presented at the Society of Photo-Optical Instrumentation Engineers (SPIE) Conference, Vol. 6686, Society of Photo-Optical Instrumentation Engineers (SPIE) Conference Series

Kim, W.-T., El-Zant, A. A., & Kamionkowski, M. 2005, ApJ, 632, 157

King, I. R. 1972, ApJ, 174, L123+

Kitzbichler, M. G. & White, S. D. M. 2007, MNRAS, 376, 2

Kobulnicky, H. A. & Martin, C. L. 2010, ApJ, 718, 724

Komatsu, E., Smith, K. M., Dunkley, J., Bennett, C. L., Gold, B., Hinshaw, G., Jarosik, N., Larson, D., Nolta, M. R., Page, L., Spergel, D. N., Halpern, M., Hill, R. S., Kogut, A., Limon, M., Meyer, S. S., Odegard, N., Tucker, G. S., Weiland, J. L., Wollack, E., & Wright, E. L. 2010, ArXiv e-prints

Kormendy, J. & Richstone, D. 1995, ARA&A, 33, 581

Kotov, O. & Vikhlinin, A. 2005, ApJ, 633, 781

Kotov, O. & Vikhlinin, A. 2006, ApJ, 641, 752

Kravtsov, A. V., Vikhlinin, A., & Nagai, D. 2006, ApJ, 650, 128

Kuntz, K. D. & Snowden, S. L. 2000, ApJ, 543, 195

Laird, E. S., Nandra, K., Georgakakis, A., Aird, J. A., Barmby, P., Conselice, C. J., Coil, A. L., Davis, M., Faber, S. M., Fazio, G. G., Guhathakurta, P., Koo, D. C., Sarajedini, V., & Willmer, C. N. A. 2009, ApJS, 180, 102

Lamastra, A., Perola, G. C., & Matt, G. 2006, A&A, 449, 551

Lampton, M., Margon, B., & Bowyer, S. 1976, ApJ, 208, 177

Landsman, W. B. 1993, in Astronomical Society of the Pacific Conference Series, Vol. 52, Astronomical Data Analysis Software and Systems II, ed. R. J. Hanisch, R. J. V. Brissenden, & J. Barnes, 246–+

Liddle, A. R. 2003, An introduction to modern cosmology (An introduction to modern cosmology, 2nd ed., by Andrew R. Liddle. Chichester, UK: Wiley, 2003, ISBN 0470848340.)

Liedahl, D. A., Osterheld, A. L., & Goldstein, W. H. 1995, ApJ, 438, L115

Lilje, P. B. & Efstathiou, G. 1988, MNRAS, 231, 635

Lin, Y., Mohr, J. J., & Stanford, S. A. 2003, ApJ, 591, 749

Lloyd-Davies, E. J., Ponman, T. J., & Cannon, D. B. 2000, MNRAS, 315, 689

Lumb, D. H., Bartlett, J. G., Romer, A. K., Blanchard, A., Burke, D. J., Collins, C. A., Nichol, R. C., Giard, M., Marty, P. B., Nevalainen, J., Sadat, R., & Vauclair, S. C. 2004, A&A, 420, 853

Lynden-Bell, D. 1967, MNRAS, 136, 101

Malmquist, K. G. 1920, Medd. Lund. Astron. Obs., 22, 1

Markevitch, M. 1998, ApJ, 504, 27

Markevitch, M., Bautz, M. W., Biller, B., Butt, Y., Edgar, R., Gaetz, T., Garmire, G., Grant, C. E., Green, P., Juda, M., Plucinsky, P. P., Schwartz, D., Smith, R., Vikhlinin, A., Virani, S., Wargelin, B. J., & Wolk, S. 2003, ApJ, 583, 70

Markevitch, M., Forman, W. R., Sarazin, C. L., & Vikhlinin, A. 1998, ApJ, 503, 77

Markevitch, M., Randall, S., Clowe, D., Gonzalez, A., & Bradac, M. 2006, in COSPAR, Plenary Meeting, Vol. 36, 36th COSPAR Scientific Assembly, 2655–+

Markwardt, C. B. 2009, ArXiv e-prints, 0902.2850

Maughan, B. J. 2007, ApJ, 668, 772

Maughan, B. J., Jones, C., Forman, W., & Van Speybroeck, L. 2008, ApJS, 174, 117

Maughan, B. J., Jones, L. R., Ebeling, H., & Scharf, C. 2006, MNRAS, 365, 509

McHardy, I. M., Jones, L. R., Merrifield, M. R., Mason, K. O., Newsam, A. M., Abraham, R. G., Dalton, G. B., Carrera, F., Smith, P. J., Rowan-Robinson, M., Wegner, G. A., Ponman, T. J., Lehto, H. J., Branduardi-Raymont, G., Luppino, G. A., Efstathiou, G., Allan, D. J., & Quenby, J. J. 1998, MNRAS, 295, 641

McNamara, B. R. The Riddle of Cooling Flows in Galaxies and Clusters of galaxies, ed. , T. ReiprichJ. Kempner & N. Soker, 177–+

McNamara, B. R., Nulsen, P. E. J., Wise, M. W., Rafferty, D. A., Carilli, C., Sarazin, C. L., & Blanton, E. L. 2005, Nature, 433, 45

McNamara, B. R., Wise, M. W., & Murray, S. S. 2004, ApJ, 601, 173

Mellier, Y. 1999, ARA&A, 37, 127

Menou, K., Quataert, E., & Narayan, R. 1997, ArXiv Astrophysics e-prints, astro-ph/9712015

Mewe, R., Gronenschild, E. H. B. M., & van den Oord, G. H. J. 1985, A&AS, 62, 197

Mo, H. J., Peacock, J. A., & Xia, X. Y. 1993, MNRAS, 260, 121

Mohr, J. J. & Evrard, A. E. 1997, ApJ, 491, 38

Mohr, J. J., Evrard, A. E., Fabricant, D. G., & Geller, M. J. 1995, ApJ, 447, 8

Mohr, J. J., Mathiesen, B., & Evrard, A. E. 1999, ApJ, 517, 627

Morrison, R. & McCammon, D. 1983, ApJ, 270, 119

Motl, P. M., Burns, J. O., Loken, C., Norman, M. L., & Bryan, G. 2004, ApJ, 606, 635

Muanwong, O., Kay, S. T., & Thomas, P. A. 2006, ApJ, 649, 640

Mulchaey, J. S., Davis, D. S., Mushotzky, R. F., & Burstein, D. 2003, ApJS, 145, 39

Muleri, F., Soffitta, P., Baldini, L., Bellazzini, R., Bregeon, J., Brez, A., Costa, E., Frutti, M., Latronico, L., Minuti, M., Negri, M. B., Omodei, N., Pesce-Rollins, M., Pinchera, M., Razzano, M., Rubini, A., Sgró, C., & Spandre, G. 2008, Nuclear Instruments and Methods in Physics Research A, 584, 149

Mullis, C. R., Henry, J. P., Gioia, I. M., Böhringer, H., Briel, U. G., Voges, W., & Huchra, J. P. 2004a, ApJ, 617, 192

Mullis, C. R., Vikhlinin, A., Henry, J. P., Forman, W., Gioia, I. M., Hornstrup, A., Jones, C., McNamara, B. R., & Quintana, H. 2004b, ApJ, 607, 175

Nash, S. G. 2000, Journal of Computational and Applied Mathematics, 124, 45

Navarro, J. F., Frenk, C. S., & White, S. D. M. 1995, MNRAS, 275, 720

Navarro, J. F., Frenk, C. S., & White, S. D. M. 1997, ApJ, 490, 493

Nenkova, M., Ivezić, Ž., & Elitzur, M. 2002, ApJ, 570, L9

Neumann, D. M. & Arnaud, M. 2001, A&A, 373, L33

Nevalainen, J., Markevitch, M., & Forman, W. 2000, ApJ, 536, 73

O'Dea, C. P., Baum, S. A., Mack, J., Koekemoer, A. M., & Laor, A. 2004, ApJ, 612, 131

Ogle, P., Whysong, D., & Antonucci, R. 2006, ApJ, 647, 161

Osmond, J. P. F. & Ponman, T. J. 2004, MNRAS, 350, 1511

Pacaud, F., Pierre, M., Adami, C., Altieri, B., Andreon, S., Chiappetti, L., Detal, A., Duc, P., Galaz, G., Gueguen, A., Le Fèvre, J., Hertling, G., Libbrecht, C., Melin, J., Ponman, T. J., Quintana, H., Refregier, A., Sprimont, P., Surdej, J., Valtchanov, I., Willis, J. P., Alloin, D., Birkinshaw, M., Bremer, M. N., Garcet, O., Jean, C., Jones, L. R., Le Fèvre, O., Maccagni, D., Mazure, A., Proust, D., Röttgering, H. J. A., & Trinchieri, G. 2007, MNRAS, 382, 1289

Pacaud, F., Pierre, M., Refregier, A., Gueguen, A., Starck, J., Valtchanov, I., Read, A. M., Altieri, B., Chiappetti, L., Gandhi, P., Garcet, O., Gosset, E., Ponman, T. J., & Surdej, J. 2006, MNRAS, 372, 578

Parmar, A. 2009, in High Resolution X-ray Spectroscopy: Towards IXO

Pascarelle, S. M., Windhorst, R. A., Keel, W. C., & Odewahn, S. C. 1996, Nature, 383, 45

Peebles, P. J. E. 1965, ApJ, 142, 1317

Peebles, P. J. E. 1968, ApJ, 153, 1

Pen, U. 1999, ApJ, 510, L1

Perlman, E. S., Horner, D. J., Jones, L. R., Scharf, C. A., Ebeling, H., Wegner, G., & Malkan, M. 2002, ApJS, 140, 265

Peterson, J. R., Kahn, S. M., Paerels, F. B. S., Kaastra, J. S., Tamura, T., Bleeker, J. A. M., Ferrigno, C., & Jernigan, J. G. 2003, ApJ, 590, 207

Peterson, J. R., Paerels, F. B. S., Kaastra, J. S., Arnaud, M., Reiprich, T. H., Fabian, A. C., Mushotzky, R. F., Jernigan, J. G., & Sakelliou, I. 2001, A&A, 365, L104

Pillitteri, I., Micela, G., Damiani, F., & Sciortino, S. 2006, A&A, 450, 993

Pointecouteau, E., Arnaud, M., & Pratt, G. W. 2005, A&A, 435, 1

Ponman, T. J., Allan, D. J., Jones, L. R., Merrifield, M., McHardy, I. M., Lehto, H. J., & Luppino, G. A. 1994, Nature, 369, 462

Ponman, T. J., Sanderson, A. J. R., & Finoguenov, A. 2003, MNRAS, 343, 331

Pratt, G. W. & Arnaud, M. 2003, A&A, 408, 1

Pratt, G. W., Arnaud, M., Piffaretti, R., Böhringer, H., Ponman, T. J., Croston, J. H., Voit, G. M., Borgani, S., & Bower, R. G. 2010, A&A, 511, A85+

Pratt, G. W., Böhringer, H., Croston, J. H., Arnaud, M., Borgani, S., Finoguenov, A., & Temple, R. F. 2007, A&A, 461, 71

Pratt, G. W., Croston, J. H., Arnaud, M., & Böhringer, H. 2009, A&A, 498, 361

Press, W. H. & Schechter, P. 1974, ApJ, 187, 425

Price, R., Duric, N., Burns, J. O., & Newberry, M. V. 1991, AJ, 102, 14

Ranalli, P., Comastri, A., & Setti, G. 2003, A&A, 399, 39

Raymond, J. C. & Smith, B. W. 1977, ApJS, 35, 419

Read, A. M. 2004, PSF of the X-ray telescopes, XMM-CCF-REL-167

Read, A. M. & Ponman, T. J. 2003, A&A, 409, 395

Reed, D. S., Bower, R., Frenk, C. S., Jenkins, A., & Theuns, T. 2007, MNRAS, 374, 2

Reiprich, T. H. & Böhringer, H. 2002, ApJ, 567, 716

Richards, E. A. 2000, ApJ, 533, 611

Riess, A. G., Filippenko, A. V., Challis, P., Clocchiatti, A., Diercks, A., Garnavich, P. M., Gilliland, R. L., Hogan, C. J., Jha, S., Kirshner, R. P., Leibundgut, B., Phillips, M. M., Reiss, D., Schmidt, B. P., Schommer, R. A., Smith, R. C., Spyromilio, J., Stubbs, C., Suntzeff, N. B., & Tonry, J. 1998, AJ, 116, 1009

Romer, A. K., Nichol, R. C., Holden, B. P., Ulmer, M. P., Pildis, R. A., Merrelli, A. J., Adami, C., Burke, D. J., Collins, C. A., Metevier, A. J., Kron, R. G., & Commons, K. 2000, ApJS, 126, 209

Rosati, P., Borgani, S., & Norman, C. 2002, ARA&A, 40, 539

Rosati, P., Della Ceca, R., Burg, R., Norman, C., & Giacconi, R. 1995, ApJ, 445, L11

Rosati, P., della Ceca, R., Norman, C., & Giacconi, R. 1998, ApJ, 492, L21+

Rubin, V. C., Ford, W. K. J., & . Thonnard, N. 1980, ApJ, 238, 471

Sahlén, M., Viana, P. T. P., Liddle, A. R., Romer, A. K., Davidson, M., Hosmer, M., Lloyd-Davies, E., Sabirli, K., Collins, C. A., Freeman, P. E., Hilton, M., Hoyle, B., Kay, S. T., Mann, R. G., Mehrtens, N., Miller, C. J., Nichol, R. C., Stanford, S. A., & West, M. J. 2009, MNRAS, 397, 577

Samuele, R., McNamara, B. R., Vikhlinin, A., & Mullis, C. R. 2011, ApJ, 731, 31

Sánchez, A. G., Lambas, D. G., Böhringer, H., & Schuecker, P. 2005, MNRAS, 362, 1225

Sanderson, A. J. R. & Ponman, T. J. 2003, MNRAS, 345, 1241

Sanderson, A. J. R., Ponman, T. J., Finoguenov, A., Lloyd-Davies, E. J., & Markevitch, M. 2003, MNRAS, 340, 989

Santos, J. S., Rosati, P., Tozzi, P., B"Ohringer, H., Ettori, S., & Bignamini, A. 2008, in Astronomical Society of the Pacific Conference Series, Vol. 399, Astronomical Society of the Pacific Conference Series, ed. T. Kodama, T. Yamada, & K. Aoki, 375–+

Santos, J. S., Tozzi, P., Rosati, P., & Böhringer, H. 2010, A&A, 521, A64+

Santos-Lleo, M., Schartel, N., Tananbaum, H., Tucker, W., & Weisskopf, M. C. 2010, ArXiv e-prints

Scharf, C. A., Jones, L. R., Ebeling, H., Perlman, E., Malkan, M., & Wegner, G. 1997, ApJ, 477, 79

Schindler, S. 1999, A&A, 349, 435

Schmidt, M. & Green, R. F. 1983, ApJ, 269, 352

Schulz, H. & Komossa, S. 1999, ArXiv Astrophysics e-prints

Schulze, A., Wisotzki, L., & Husemann, B. 2009, A&A, 507, 781, 0909.5112

Schwarz, G. 1978, Annals of Statistics, 6, 461

Sefusatti, E., Vale, C., Kadota, K., & Frieman, J. 2006, ArXiv Astrophysics e-prints

Sheth, R. K. & Tormen, G. 1999, MNRAS, 308, 119

Shrader, C. R. & Titarchuk, L. 2003, ApJ, 598, 168

Slezak, E., Bijaoui, A., & Mars, G. 1990, A&A, 227, 301

Slezak, E., Durret, F., & Gerbal, D. 1994, AJ, 108, 1996

Smith, R. K., Brickhouse, N. S., Liedahl, D. A., & Raymond, J. C. 2001, ApJ, 556, L91

Smithsonian Institution. 2008, About Chandra, NASA
`http://cxc.harvard.edu/cdo/about_chandra/`

Snowden, S. L., Freyberg, M. J., Plucinsky, P. P., Schmitt, J. H. M. M., Truemper, J., Voges, W., Edgar, R. J., McCammon, D., & Sanders, W. T. 1995, ApJ, 454, 643

Springel, V., White, S. D. M., Jenkins, A., Frenk, C. S., Yoshida, N., Gao, L., Navarro, J., Thacker, R., Croton, D., Helly, J., Peacock, J. A., Cole, S., & Thomas, P. 2005, Nature, 435, 629

Stanek, R., Rudd, D., & Evrard, A. E. 2009, MNRAS, 394, L11

Staniszewski, Z., Ade, P. A. R., Aird, K. A., Benson, B. A., Bleem, L. E., Carlstrom, J. E., Chang, C. L., Cho, H., Crawford, T. M., Crites, A. T., de Haan, T., Dobbs, M. A., Halverson, N. W., Holder, G. P., Holzapfel, W. L., Hrubes, J. D., Joy, M., Keisler, R., Lanting, T. M., Lee, A. T., Leitch, E. M., Loehr, A., Lueker, M., McMahon, J. J., Mehl, J., Meyer, S. S., Mohr, J. J., Montroy, T. E., Ngeow, C., Padin, S., Plagge, T., Pryke, C., Reichardt, C. L., Ruhl, J. E., Schaffer, K. K., Shaw, L., Shirokoff, E., Spieler, H. G., Stalder, B., Stark, A. A., Vanderlinde, K., Vieira, J. D., Zahn, O., & Zenteno, A. 2009, ApJ, 701, 32

Stark, A. A., Gammie, C. F., Wilson, R. W., Bally, J., Linke, R. A., Heiles, C., & Hurwitz, M. 1992, ApJS, 79, 77

Strüder, L., Briel, U., Dennerl, K., Hartmann, R., Kendziorra, E., Meidinger, N., Pfeffermann, E., Reppin, C., Aschenbach, B., Bornemann, W., Bräuninger, H., & Burkert, W. 2001, A&A, 365, L18

Sun, M., Voit, G. M., Donahue, M., Jones, C., Forman, W., & Vikhlinin, A. 2009, ApJ, 693, 1142

Sunyaev, R. A. & Zeldovich, I. B. 1980, ARA&A, 18, 537

Swartz, D. A., Wolk, S. J., & Fruscione, A. 2010, Proceedings of the National Academy of Science, 107, 7127

Tadayuki, T., Nakazawa, K., Wanatanabe, S., Goro, S., Mitani, T., Tanaka, T., Oonuki, K., Tamura, K., Hiroyasu, T., & Kamae, T. 2005, in , 332–341

Tamura, T., Kaastra, J. S., Peterson, J. R., Paerels, F. B. S., Mittaz, J. P. D., Trudolyubov, S. P., Stewart, G., Fabian, A. C., Mushotzky, R. F., Lumb, D. H., & Ikebe, Y. 2001, A&A, 365, L87

Tananbaum, H. & Kellogg, E. M. 1970, IEEE Transactions on Nuclear Science, 17, 97

Tinker, J., Kravtsov, A. V., Klypin, A., Abazajian, K., Warren, M., Yepes, G., Gottlöber, S., & Holz, D. E. 2008, ApJ, 688, 709

Tornatore, L., Borgani, S., Springel, V., Matteucci, F., Menci, N., & Murante, G. 2003, MNRAS, 342, 1025

Treis, J., Bombelli, L., Fiorini, C., Herrmann, S., Lauf, T., Lechner, P., Lutz, G., Majewski, P., Porro, M., Richter, R. H., Stefanescu, A., Strüder, L., & de Vita, G. 2009, in Presented at the Society of Photo-Optical Instrumentation Engineers (SPIE) Conference, Vol. 7435, Society of Photo-Optical Instrumentation Engineers (SPIE) Conference Series

Turner, M. J. L., Abbey, A., Arnaud, M., Balasini, M., Barbera, M., Belsole, E., Bennie, P. J., Bernard, J. P., Bignami, G. F., Boer, M., Briel, U., Butler, I., Cara, C., Chabaud, C., Cole, R., Collura, A., Conte, M., Cros, A., Denby, M., Dhez, P., Di Coco, G., Dowson, J., Ferrando, P., Ghizzardi, S., Gianotti, F., Goodall, C. V., Gretton, L., Griffiths, R. G., Hainaut, O., Hochedez, J. F., Holland, A. D., Jourdain, E., Kendziorra, E., Lagostina, A., Laine, R., La Palombara, N., Lortholary, M., Lumb, D., Marty, P., Molendi, S., Pigot, C., Poindron, E., Pounds, K. A., Reeves, J. N., Reppin, C., Rothenflug, R., Salvetat, P., Sauvageot, J. L., Schmitt, D., Sembay, S., Short, A. D. T., Spragg, J., Stephen, J., Strüder, L., Tiengo, A., Trifoglio, M., Trümper, J., Vercellone, S., Vigroux, L., Villa, G., Ward, M. J., Whitehead, S., & Zonca, E. 2001, A&A, 365, L27

Ueda, Y., Akiyama, M., Ohta, K., & Miyaji, T. 2003, ApJ, 598, 886

Valdarnini, R. 2003, MNRAS, 339, 1117

Vikhlinin, A. 1999, Part of ZHTOOLS
`http://hea-www.harvard.edu/RD/zhtools/`

Vikhlinin, A. 2006, ApJ, 640, 710

Vikhlinin, A., Burenin, R., Forman, W. R., Jones, C., Hornstrup, A., Murray, S. S., & Quintana, H. H. Böhringer, G. W. PrattA. Finoguenov & P. Schuecker, 48–+

Vikhlinin, A., Burenin, R. A., Ebeling, H., Forman, W. R., Hornstrup, A., Jones, C., Kravtsov, A. V., Murray, S. S., Nagai, D., Quintana, H., & Voevodkin, A. 2009a, ApJ, 692, 1033

Vikhlinin, A., Kravtsov, A., Forman, W., Jones, C., Markevitch, M., Murray, S. S., & Van Speybroeck, L. 2006, ApJ, 640, 691

Vikhlinin, A., Kravtsov, A. V., Burenin, R. A., Ebeling, H., Forman, W. R., Hornstrup, A., Jones, C., Murray, S. S., Nagai, D., Quintana, H., & Voevodkin, A. 2009b, ApJ, 692, 1060

Vikhlinin, A., Markevitch, M., Murray, S. S., Jones, C., Forman, W., & Van Speybroeck, L. 2005, ApJ, 628, 655

Vikhlinin, A., McNamara, B. R., Forman, W., Jones, C., Quintana, H., & Hornstrup, A. 1998, ApJ, 502, 558

Vikhlinin, A., VanSpeybroeck, L., Markevitch, M., Forman, W. R., & Grego, L. 2002, ApJ, 578, L107

Vikhlinin, A., Voevodkin, A., Mullis, C. R., van Speybroeck, L., Quintana, H., McNamara, B. R., Gioia, I., Hornstrup, A., Henry, J. P., Forman, W. R., & Jones, C. 2003, ApJ, 590, 15

Voges, W. 1993, Advances in Space Research, 13, 391

Voigt, L. M. & Fabian, A. C. 2004, MNRAS, 347, 1130

Voit, G. M. 2005a, Advances in Space Research, 36, 701

Voit, G. M. 2005b, Reviews of Modern Physics, 77, 207

Voit, G. M. & Bryan, G. L. 2001, Nature, 414, 425

Volonteri, M. 2006, ArXiv Astrophysics e-prints, astro-ph/0602630

Weisskopf, M. C., Brinkman, B., Canizares, C., Garmire, G., Murray, S., & Van Speybroeck, L. P. 2002, PASP, 114, 1

White, D. A. 2000, MNRAS, 312, 663

White, S. D. M. & Frenk, C. S. 1991, ApJ, 379, 52

Wilman, R. J., Edge, A. C., & Swinbank, A. M. 2006, MNRAS, 371, 93

Wilson, A., ed. 2003, X-ray Evolving-Universe Spectroscopy - The XEUS Instruments (European Space Agency)

Windhorst, R., Mathis, D., & Neuschaefer, L. 1990, in Astronomical Society of the Pacific Conference Series, Vol. 10, Evolution of the Universe of Galaxies, ed. R. G. Kron, 389–403

XMM-Newton Team. 2005, XMM-Newton Science Simulator, ESA `http://xmm.vilspa.esa.es/scisim/`

Xue, Y.-J. & Wu, X.-P. 2000, ApJ, 538, 65

Zentsova, A. S. 1980, Astrophysics, 16, 445

Zhang, W. W., Bolognese, J., Byron, G., Chan, K. W., Content, D. A., Hadjimichael, T. J., Hewitt, C., Hill, M. D., Hong, M., Lehan, J. P., Lozipone, L., Mazzarella, J. M., McClelland, R., Nguyen, D. T., Olsen, L., Petre, R., Robinson, D., Rohrbach, S. O., Russell, R., Saha, T. T., Sharpe, M., Gubarev, M. V., Jones, W. D., O'Dell, S. L., Davis, W., Caldwell, D. R., Freeman, M., Podgorski, W., & Reid, P. B. 2009, in Presented at the Society of Photo-Optical Instrumentation Engineers (SPIE) Conference, Vol. 7360, Society of Photo-Optical Instrumentation Engineers (SPIE) Conference Series

Zheng, Z., Tinker, J. L., Weinberg, D. H., & Berlind, A. A. 2002, ApJ, 575, 617